



**Georgia Institute
of Technology**

School of Civil and Environmental Engineering

**Durability of Precast Prestressed Concrete Piles
in Marine Environment:
Reinforcement Corrosion and Mitigation – Part 1**

Final Report

Prepared for

**Office of Materials and Research
Georgia Department of Transportation**

**GDOT Research Project No. 07-30
Task Order No. 02-55**

by

**Robert Moser, Brett Holland,
Lawrence Kahn, Preet Singh, and Kimberly Kurtis**

June 2011

Contract Research

GDOT Research Project No. 07-30
Task Order No. 02-55

Durability of Precast Prestressed Concrete Piles in Marine
Environment: Reinforcement Corrosion and Mitigation
Part 1

Final Report

Prepared for

Office of Materials and Research
Georgia Department of Transportation

By

Robert Moser, Brett Holland,
Lawrence Kahn, Preet Singh, and Kimberly Kurtis,

June 2011

The contents of this report reflect the views of the authors who are responsible for the facts and the accuracy of the data presented herein. The contents do not necessarily reflect the official views or policies of the Georgia Department of Transportation. This report does not constitute a standard, specification or regulation.

Executive Summary

Research conducted in Part 1 has verified that precast prestressed concrete piles in Georgia's marine environment are deteriorating. The concrete is subjected to sulfate and biological attack and the prestressed and nonprestressed reinforcement is corroding. Concrete is reported as "soft" in many bridges; and exterior cracking indicates reinforcement corrosion.

Researchers reviewed concrete durability and reinforcement corrosion research and experiences. These reviews gave the necessary background to evaluate the condition of Georgia's prestressed concrete piles and to establish future tests for strand corrosion and for concrete mix design experiments.

Based on discussions with the Bridge Maintenance Engineer, four 40-ft lengths of piles were removed from the Turtle River Bridge and transported to Georgia Institute of Technology. The forensic examination of the piles indicated that after 32 years in service, the concrete within the water had suffered from biological attack by sponges which consumed the limestone aggregate, and the cement had deteriorated due to sulfate attack. Prestressing strands and tie reinforcement had severely corroded in splash zones due to high levels of chloride. Concrete above water was in good condition.

Experiments on the corrosion resistance of typical A416 prestressing strand wire and on 7-wire prestressing strands were conducted. Solutions represented various chloride conditions; concentrations varied from none to twice that of seawater. Georgia marsh conditions have an average chloride content about one-half that of open seawater. For wire in good quality, non-carbonated concrete, corrosion is very limited. In carbonated concrete, corrosion starts quickly at low chloride concentrations.

The experiments further showed that prestressing strands exhibit a 60-70% reduction in corrosion resistance when compared with wires and reinforcing bars because of crevices created in the stranded geometry. Future experiments must consider such crevice corrosion. Most of the past corrosion research did not consider this effect of crevice corrosion due to stranding.

Six alloys of stainless steel were considered for potential use as prestressing wire and strand. Most stainless steels are not capable of developing the high strength needed for prestressing applications. Change in structure of the steel due to cold drawing has the potential for making the steel very susceptible to corrosion. Further, stainless steels such as the nitronic 33 used in older Navy piles have high stress relaxation. While all six will be investigated in Part 2, the most promising alloys are 2205 and 2304. Such stainless steel prestressing strands seem to be the best solution for providing durable piles in the marine environment.

Based on the research conducted in Part 1, research in Part 2 will concentrate on (1) concrete mixes which have improved sulfate resistance, resist biological attack and have the ability to self-heal cracks caused by pile driving, and (2) determination of stainless steel

properties including corrosion resistance, stress relaxation, yield strength, ultimate strength and ductility. The result of the research will be recommendations for high-performance concrete for marine piles and for corrosion-resistant high-strength stainless steel prestressing reinforcement.

Acknowledgements

The research reported herein was sponsored by the Georgia Department of Transportation through Research Project Number 07-30, Task Order Number 02-55. Mr. Paul Liles, Assistant State Preconstruction Engineer, Mr. Myron Banks, Concrete Engineer, Mr. Mike Clements, Bridge Maintenance Engineer, Ms. Supriya Kamatkar, Research Engineer, Mr. Kevin Schwartz, Bridge Inspection Engineer, Mrs. Lisa Sikes, Bridge Liasson, Mr. Michael Garner, Bridge Liasson, Mr. Andy Doyle, State Bridge Inspection Engineer, Mr. Jeff Carroll, Materials and Research Branch, Mr. Brian Scarbrough, Area Engineer, and Mr. Slade Cole, Assistant Area Engineer of GDOT provided many valuable suggestions throughout the study. The opinions and conclusions expressed herein are those of the authors and do not represent the opinions, conclusions, policies, standards or specifications of the Georgia Department of Transportation or of other cooperating organizations.

Mr. Daniel Schuetz assisted with the production of the corrosion test specimens, and Mr. Jamshad Mahmood helped with the corrosion experimental setups and potentiostats. Messrs. Fred Aguayo, Robert Heusel, and Armin Vosough assisted with the forensic investigation of piling from the Turtle River Bridge. Mr. Jeremy Mitchell provided help and expertise with equipment and research tasks at the Georgia Tech Structures Laboratory. Messrs. Richard Potts and Alan Pritchard of Standard Concrete Products provided expertise and valuable suggestions throughout the study. Mr. Bill McClenathan, Brian Burr, Jon Cornelius, and colleagues from Sumiden Wire Products Corporation provided valuable insights into the production of materials for stainless steel prestressing wire and strand; their assistance and expertise are gratefully acknowledged.

Table of Contents

Executive Summary	ii
Acknowledgments	iii
Table of Contents	iv
Chapter	
1. Introduction	1-1
2. Background – Corrosion Mechanisms in Reinforced and Prestressed Concrete Structures	2-1
3. Background – Concrete for Marine Piles	3-1
4. Background – Interviews	4-1
5. Georgia Coastal Bridge Inspections	5-1
6. Forensic Investigation of Turtle River Bridge Piles	6-1
7. Preliminary Corrosion Studies on Carbon Steel A416 Prestressing Strand	7-1
8. Preliminary Corrosion Studies on Stainless Steel Prestressing Strand	8-1
9. Future Studies Planned for Part 2	9-1
10. Conclusions	10-1
Appendix A: Inspection Reports	A-1
Combined References	R-1

1. Introduction

1.1 Purpose and Objectives

The purpose of the overall research project is to determine methods which may be applied economically to mitigate corrosion of reinforcement in precast prestressed concrete piles in Georgia's marine environments. The overall goal is to improve the durability of bridge piles so that a design life of 100 years may be achieved.

The research has four specific objectives. The first objective is to determine the extent of corrosion damage in Georgia's structural concrete bridge piling and the success of methods used to improve the durability of bridge piles in Georgia.

The second objective is to fully document past research and investigations on the durability of structural concrete in the marine environment with particular emphasis on the corrosion of reinforcement and its mitigation. The latter includes learning from state departments of transportation: finding from their experiences with corrosion mitigation including the effect of concrete quality and cover and with regard to types of reinforcement, their metallurgy and coatings.

The third objective is to perform a preliminary experimental investigation on the corrosion of reinforcement in concrete piles in Georgia by measuring corrosion potential and by characterization of concrete, steel, and reinforced concrete, including samples obtained from the field. The durability of these field and laboratory samples will be compared to the findings from the literature study to see how Georgia's marine environment and construction matches that found from the other states.

The fourth objective is to identify what, if any, further research needs to be undertaken to determine improved methods to increase the durability of piles in Georgia's marine environment.

1.2 Need for Research

The maintenance costs for Georgia bridges are growing. There is a need to reduce maintenance costs. Further, the Federal Highway Administration has mandated that the design life of new bridges be between 75 and 100 years; the Georgia State Bridge Engineer has suggested that the design life be 100 years.

Some prestressed concrete piles in the coastal region of Georgia have been shown to have severe corrosion damage in the splash zone after less than 25 years of service. Therefore, the current design standards for assuring durability of new structures are not sufficient if the 100-year design life is to be achieved. New standards must be developed and implemented; but what those standards are is unknown. One suggestion is to require that concrete for precast prestressed piles be High-Performance Concrete (HPC) with a rapid chloride ion permeability of less than 2000 coulombs. While it is probable that this standard will improve the durability of

piles, it is unknown if it is sufficient or if it is “overkill”. Further, piles are sometimes cracked during driving. If an HPC pile is cracked, it is unknown if the 2000 coulomb requirement will still protect the reinforcement from corrosion. Thus, an understanding of the influence of crack width, including the role of self-healing, will be important in determining the durability of HPC piles.

If cracking prestressed piles does lead to early corrosion of the reinforcement, then there should be changes in pile composition and construction and driving techniques to prevent or minimize cracking. Those compositional changes (e.g., fiber reinforcement) and construction techniques need to be identified, their economic implications need to be defined, and sample construction specifications need to be developed.

At one time it was thought that epoxy coating of reinforcement would indefinitely protect reinforcement from corrosion damage. Recent studies have shown that this hypothesis is not true, yet other studies indicate that changing the metallurgy of reinforcement can diminish corrosion potential. There is a need to determine if there is any economical method associated with the composition of non-prestressed and/or prestressed reinforcement to mitigate its corrosion. Of especial benefit might be the use of stainless steel prestressing strand with nonprestressed ties.

Significant corrosion of prestressing steels has been reported on concrete bridges in coastal environments, particularly in precast prestressed concrete piles used in bridge substructures (Griggs, 1987, and Hamilton, 2007). Figure 1-1 shows typical reinforcement corrosion on a coastal concrete bridge substructure.

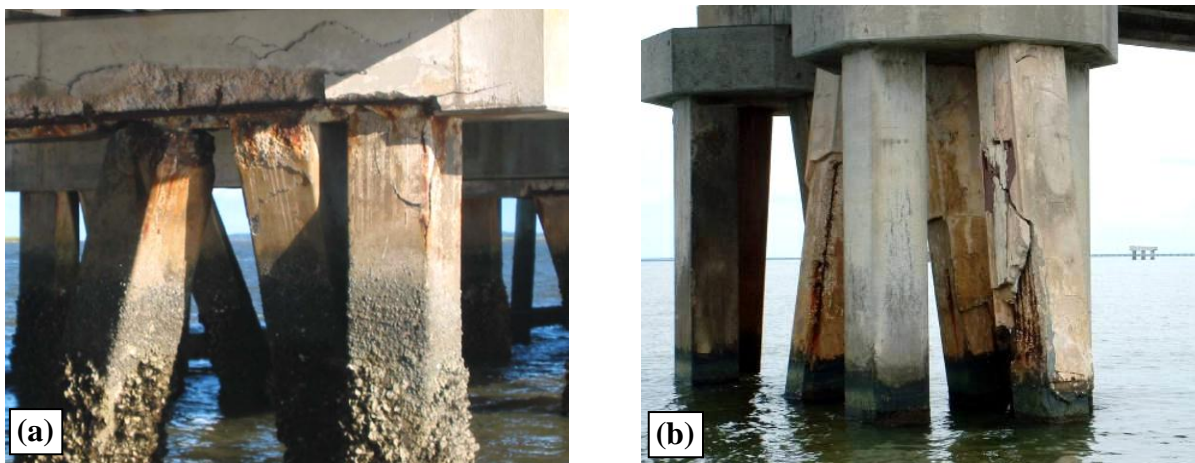


Figure 1-1: Corrosion of (a) concrete pile cap and (b) precast prestressed concrete piles (from Hamilton, 2007)

1.3 Report Organization

Past research on pile durability is reported in chapters 2 and 3, literature surveys of reinforcement corrosion and concrete durability, respectively. Particular attention is paid to the

potential application of stainless steel for prestressing reinforcement and its corrosion resistance.

Chapter 4 discusses the findings from interviews with Georgia DOT personnel. Chapter 5 presents an inspection report which identifies typical pile performance in Georgia's marine environment. Based on the interviews and inspections, deteriorated piles from the Turtle River Bridge were withdrawn and transported to Georgia Tech for forensic analysis. Chapter 6 presents the forensic analysis which includes investigation of concrete and corrosion of the prestressed and nonprestressed reinforcement.

Preliminary experimental corrosion studies on typical A416 prestressing strands are given in Chapter 7, while the potential for use of stainless steel alloys for prestressing reinforcement is given in Chapter 8.

Based on the background investigations, the forensic pile investigation and the corrosion experiments, studies planned for Part 2 of the research is presented in Chapter 9. Chapter 10 gives the conclusions based on Part 1 of the overall study.

References for each chapter are given in each chapter. All references are repeated in the Combined References.

1.4 References for Chapter 1

Griggs, R.D. (1987), *Structural Concrete in the Georgia Coastal Environment*. 1987, GDOT: Atlanta, GA.

Hamilton III, H.R. (2007), *St. George Island Bridge Pile Testing*. 2007, FDOT.

2. Background – Corrosion Mechanisms in Reinforced and Prestressed Concrete Structures

Corrosion of steel in reinforced and prestressed concrete structures has been one of the prevalent deterioration mechanisms since their introduction in the early 1900's. Previously thought to occur due to stray currents, we know today that most corrosion in reinforced concrete is caused by the ingress of aggressive agents such as Cl^- and CO_2 . The corrosion of reinforcing steels became especially prevalent in the 1960's with the increased use of deicing salts, causing extensive corrosion of bridge decks in areas with harsh winters (Hartt, et al., 2004). Today, reinforcement corrosion affects all types of concrete elements, including bridge girders and decks, exposed members of buildings, concrete pavements, and substructure members such as precast concrete piles.

Steel embedded in concrete is typically very durable and resistant to corrosion. Calcium, potassium, and sodium hydroxides present in the pore solution of the hydrated cement paste provide the high pH (12-14) necessary for mild carbon steels to develop a protective passive film on their surface. This passive film is only degraded in the presence of chlorides or when pH falls due to carbonation of the cover concrete (Revie, 2000). In most cases, corrosion caused by the ingress of chlorides is the main concern, as carbonation rates are typically low in modern structures with higher quality concretes. Structures exposed to severe marine environments, industrial conditions, and/or deicing salts are at the greatest risk of reinforcement corrosion caused by the ingress of Cl^- .

Corrosion of steel can lead to a variety of different modes of failure in a concrete structure. As corrosion occurs, its products are bulky hydrated metal oxides, which occupy a volume much greater than that of the reacted metal. Expansion due to oxide formation eventually results in the spalling of concrete as expansive stresses exceed the tensile strength of the cover concrete. Spalling of the cover concrete results in an autocatalytic form of deterioration, where more cracking and spalling further accelerate Cl^- ingress and reinforcement corrosion. Another result of corrosion is loss of reinforcement cross section and in turn member strength. This is generally not a large concern in reinforced concrete structures, as corrosion will be very apparent by staining and cracking before a large loss of strength occurs (Young, et al., 1998). Section loss is however a great concern in prestressed concrete structures. The small diameter of wires used for prestressing strands and their high initial stress makes them susceptible to fracture if corrosion occurs. Other forms of failure such as environmentally induced cracking are also a concern in prestressed concrete structure, and will be discussed further in subsequent chapters (Hope, et al., 2001).

Failures of structures due to reinforcement corrosion can be seen throughout recent history. Almost all bridges include reinforced concrete decks, with 50% of new bridges being all concrete, including precast prestressed concrete girders. Approximately 13% of the nations 595,000 bridges have been classified as structurally deficient according to the Federal Highway Administration's 2006 Report to Congress (Federal Highway Administration, 2006). The

projected average annual cost of just maintaining these bridges in their current state is \$8.3 Billion, with a cost of upwards of \$150 Billion to improve the condition of existing infrastructure. Many of the deficiencies in these bridges are due to the corrosion of reinforcement from the use of deicing salts and/or exposure to coastal environments. In addition to direct costs of corrosion, indirect costs stemming from increased traffic congestion, bridge closures, affected businesses, and off-system structures like parking decks and piers have been estimated to be between \$50 and \$200 Billion annually (NACE, 2008).

Bridges and other coastal structures here in Georgia and throughout the Southeast are deteriorating prematurely due to corrosion (Griggs, 1987, Hamilton III, 2007). Numerous failures have occurred in substructure members such as piles and pile caps, leading to the costly repair and replacement of either the entire bridge or the affected members, if possible. Figures 2-1 and 2-2 show typical corrosion related degradation of a bridge structure.



Figure 2-1: Typical Corrosion of Precast Prestressed Concrete Piles (NACE, 2007)



Figure 2-2: Corrosion of Pier Cap on Steel Girder Bridge (Inc., 2008)

Reinforcement corrosion can also be found all over the globe. Severe distress was found in over 100 bridges only 20 years after their construction in the Arabian Gulf due to the combined effects of a harsh environment and poor construction practices (Matta, 1993). The 70 year old Progresso Pier was constructed with stainless steel reinforcement to replace a conventionally reinforced pier which failed after only a few years in the same exposure (Knudson, et al., 1999). Collapse of the roof of the Berlin Congress Hall in 1980 was caused by corrosion (environmentally induced cracking) of the prestressing strands because of poor construction practices (Isecke, 1982). Many other examples of reinforcement corrosion can be found throughout the literature. In today's society, it is believed that numerous corrosion-related failures go undocumented and are settled through litigation before any investigation or research is conducted (Hope, et al., 2001).

While reinforcement corrosion can occur in all types of structures and exposures, the main focus of this chapter is to provide an in-depth discussion of the relevant corrosion mechanisms in reinforced and prestressed (focus will be given to precast pretensioned members) concrete members in marine environments. Concrete structures in coastal areas are especially prone to corrosion due to three main factors, (1) high Cl^- content in seawater, (2) potential for high temperature and relative humidity, and (3) cyclic wetting due to tidal and splash action (Mehta, 1991). In order to achieve the now required 75-100+ year design life in new bridges, changes must be made in the design and materials used for new construction.

2.1 Electrochemistry and Corrosion Theory

The production of most structural metals, including iron (the main constituent of steel), involves the creation of a pure metal from its respective ore. As an ore, most metals are in their most stable form. Corrosion of a metal is its natural breakdown into a more stable state, as a metal oxide (Singh, 2008). For a corrosion cell to form, five main components are required:

- (1) an anode where metal is oxidized, example: $Fe \rightarrow Fe^{+2} + 2e^{-}$
- (2) a cathode to accept (reduce) electrons, example: $2H_2O + O_2 + 4e^{-} \rightarrow 4OH^{-}$
- (3) an electrical connection between the anode and cathode to transfer electrons
- (4) an electrolytic environment to transfer ions and complete the circuit
- (5) availability of reactants at the site of corrosion such as O_2 , Cl^{-} , H_2O

For corrosion reactions to proceed, each one of the five components must be present. Corrosion reactions are controlled mainly by electrochemical phenomena, that is, the interchange of chemical and electrical energy at the interface between a material and an ionically conductive electrolyte. Just as a metal naturally “wants” to become an ore, electrochemically reactive surfaces naturally want to react with their surrounding environment.

The main focus of this section is the corrosion of metals which exhibit metallic bonding. Metallic bonding occurs due to the atomic orbital morphology of most structural metals. The large amount of electrons residing in high energy d-orbital levels makes the promotion of electrons to the conduction band from the valence band relatively easy. Due to the high electron mobility of metals, when atoms come close together, as in a close packed face centered cubic or body centered cubic (FCC or BCC) crystal structure, valence electrons have an increased tendency to delocalize and be shared randomly by all of the metal atoms in the structure. While the more complicated Band Theory is typically employed to describe metallic bonding, most elementary texts describe metallic bonding as consisting of positively charged metal nuclei which are surrounded by an electron gas (Zumdahl, 2000).

The electrochemical reactivity of surfaces and interfaces is mainly a result of changes in bonding present at the surface compared to in the bulk of the material due to edge effects. In the bulk of the material, the atoms will coordinate themselves to achieve the lowest energy structure with charge neutrality. As the structure present in the bulk approaches the surface, the lack of atoms to complete the periodic crystal structure results in unsatisfied bonds at the surface – which in most cases leads to some buildup of charge (Skorchelletti, 1976). Figure 2-3 shows the surface of an FCC metallic crystal structure.

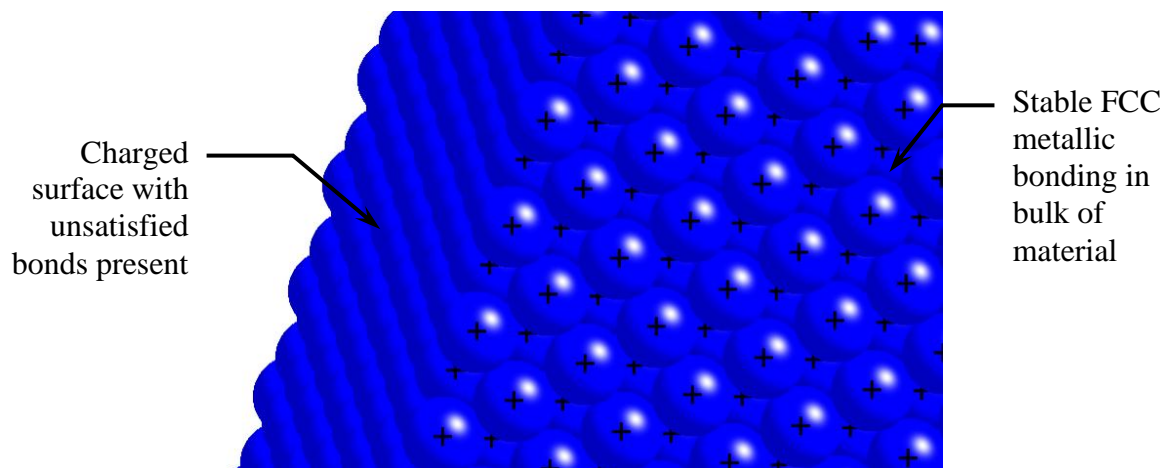


Figure 2-3: Surface of FCC Metallic Crystal Structure

In order to achieve energetic stability and charge neutrality at the surface the material will either alter its structure (a high activation energy process) or it will react with the environment. Reactions with the environment for a surface to achieve energetic stability are the main cause of corrosion in metals. In the case of metallic corrosion, the charged surface will cause the adsorption of solvated compounds from the electrolyte, forming a double layer at the surface as shown in Figure 2-4. The adsorbed compounds and ions at the surface react with the metallic substrate to stabilize the surface (Young, et al., 1998). It is these surface-interface reactions which result in metallic corrosion.

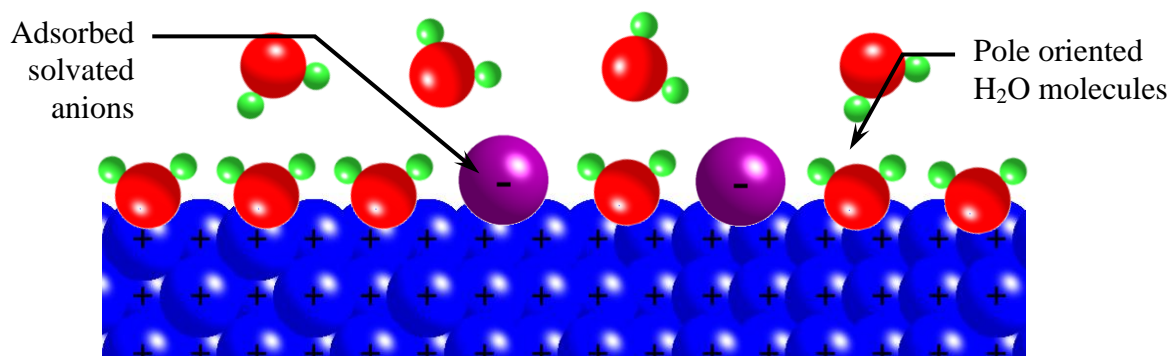


Figure 2-4: Double Layer on Charged Metallic Surface

Corrosion reactions occur in localized cells where all five components of the electrochemical circuit are present. For an electrochemical cell to form a surface inhomogeneity must be present to initiate an anodic and cathodic site for oxidation and reduction reactions to occur, respectively. Due to the inherent defects present on material surfaces caused by processing, surface inhomogeneities will undoubtedly be present (Singh, 2008). Anodic sites will typically exhibit more unsatisfied bonds while cathodic sites will have a more stable / less reactive structure. Thus, the presence of defects such as slip steps, scratches, grain boundaries, dislocations, and vacancies has a large effect on the electrochemical reactivity of the surface (Morrison, 1990). An example of a surface defect is given in Figure 2-5.

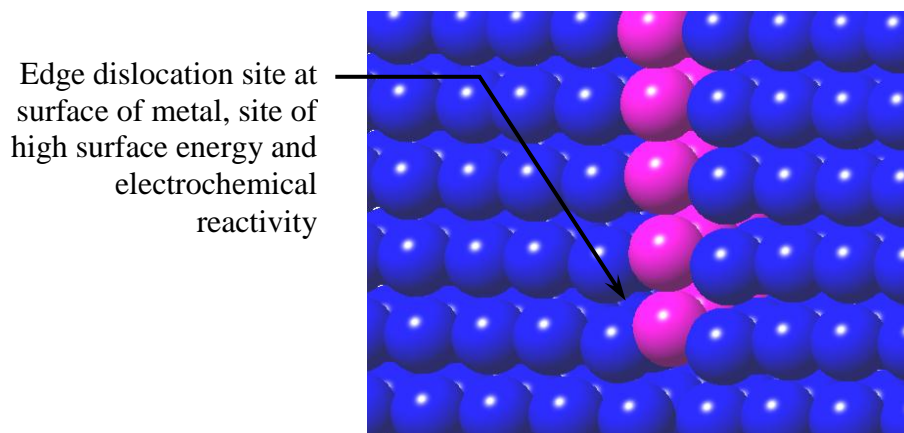


Figure 2-5: Electrochemically Reactive Defect Sites on Metal Surface

Once an electrochemical circuit is complete on the surface of the metal a corrosion cell can form. Corrosion cells can exist as microcells as shown in Figure 2-6, or macrocells as shown

in Figure 2-7. Microcells occur when the anode and cathode of the corrosion cell are very close in proximity, usually on the same reinforcing bar in the case of reinforced concrete. Macrocells are created when there is a large separation between the anode and cathode. A typical example of a corrosion macrocell is when the top mat of reinforcement in a bridge deck has begun corrosion due to Cl^- exposure from deicing salts and acts as the anode, while the unaffected bottom mat of reinforcing acts as the cathode, both being electrically connected by ties, stands, or stirrups, with ionic transfer occurring through the hydrated cement paste's (HCP) pore solution (Kurtis, 2007). Limitations in the distance between anodic and cathodic sites are controlled mainly by Ohmic resistance present in the material and the electrolyte. Metals generally have low resistivity and do not greatly limit the transfer of electrons between the anode and the cathode of an electrochemical cell. However, concrete, being a high resistivity medium, can limit distance of effective ionic transfer between the anode and the cathode (Bohni, 2005).

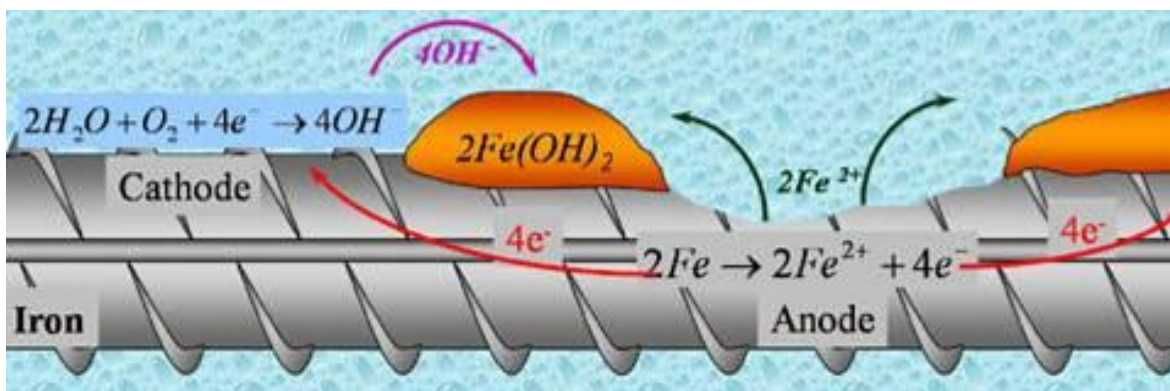


Figure 2-6: Anode & Cathode in Corrosion Microcell on Reinforcement (PCA, 2007)

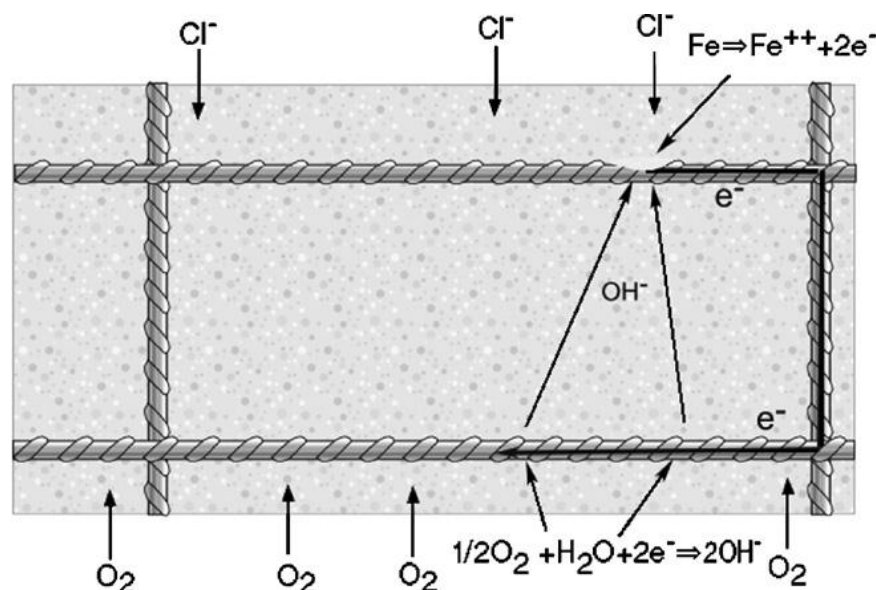


Figure 2-7: Typical Corrosion Macrocell (Hansson, et al., 2006)

2.1.1 Thermodynamics of Corrosion

The tendency for a corrosion reaction to initiate is determined by the electrochemical reactivity of the surface on which it will occur. The spontaneity of a corrosion reaction is proportional to the change in Gibbs free energy which occurs due to the reactions (Perez, 2004). From thermodynamics, it can be shown that:

$$\Delta G = \Delta H - T\Delta S + \Delta W \quad (2.1)$$

Where:

ΔG = Change in Gibbs free energy

ΔH = Change in enthalpy

T = Temperature

ΔS = Change in entropy

ΔW = Change in additional external work

However, in the case of a typical corrosion reaction, environmental conditions are relatively constants and changes in entropy and enthalpy tend towards zero (Thomas, 2003). Therefore, equation (2.1) reduces to:

$$\Delta G = \Delta W \quad (2.2)$$

Equation (2.2) can be used to correlate the change in Gibbs free energy of a system resulting from a corrosion reaction to the work done by the reaction. In an electrochemical system, $\Delta W = -Q \cdot E$, where E is the electrochemical potential difference formed by the spatial distribution of ions in the double layer as shown in Figure 2-4, Q is the charge / ion transfer present at the interface between the metal and the electrolyte, and the negative sign is included by convention for electrochemical potential measurements. According to Faraday, $Q = n \cdot F$, where n is the number of electrons transferred in the reaction and F is Faraday's constant (96,500 C/mol). Thus, equation (2.3) shown below, can be used to relate the change in Gibbs free energy to the electrochemical potential present at the surface (Thomas, 2003).

$$\Delta G = -n \cdot F \cdot E \quad (2.3)$$

Using equation (2.3) and a measured value of the electrochemical potential, E , the spontaneity of a corrosion reaction can be determined. Negative values of ΔG indicate a reduction in free energy, and thus a spontaneous reaction. Positive values of ΔG indicate an increase in the free energy of the system and a thermodynamically unstable condition (Jones, 1996).

Like any thermodynamic quantity, values of the electrochemical potential cannot be determined against an "absolute" reference point. Therefore, a standard non-polarizable reference electrode, the standard hydrogen electrode (SHE), has been adopted as a reference point for the measurement of electrochemical potentials. In many cases, more durable reference electrodes are used for laboratory and field work, such as the saturated calomel electrode (SCE), the silver / silver chloride electrode (Ag – AgCl), and the copper / copper sulfate electrode (Cu –

CuSO_4) (Landolt, 2007). Potential measurements taken against an alternate reference electrode are adjusted to match the SHE potential reference level. The electrochemical potential is typically measured in the laboratory using a Daniell cell, shown in Figure 2-8.

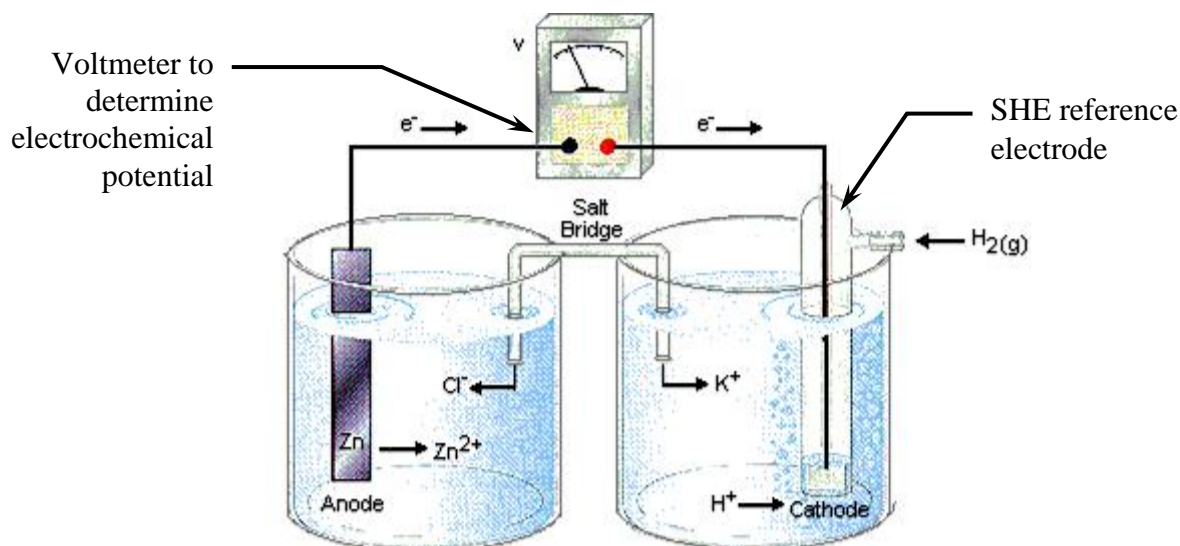


Figure 2-8: Daniell Cell with SHE Reference Electrode

Values of the electrochemical potential vs. SHE have been experimentally measured for a variety of materials and collected in the electromotive force series (EMF series). An example EMF series for a variety of different metals is shown in Table 2-1. Reactions in the EMF series are written as reduction reactions by convention. Therefore, according to equation (2.3), positive values of E_{SHE} will proceed as reduction reactions (results in negative ΔG) and negative values of E_{SHE} will force the reaction to proceed in the opposite direction, as an oxidation reaction.

Table 2-1: EMF Series vs. Standard Hydrogen Electrode

	Reaction	Standard Potential E_{SHE} (V)
<div style="display: flex; align-items: center;"> <div style="margin-right: 10px;"> Noble ↑ ↓ Active </div> </div>	$\text{O}_2 + 4\text{H}^+ + 4\text{e}^- = 2\text{H}_2\text{O}$ (pH 0)	+1.358
	$\text{Pt}^{2+} + 3\text{e}^- = \text{Pt}$	+1.118
	$\text{O}_2 + 2\text{H}_2\text{O} + 4\text{e}^- = 4\text{OH}^-$ (pH 7)	+0.820
	$\text{Fe}^{3+} + \text{e}^- = \text{Fe}^{2+}$	+0.771
	$\text{O}_2 + 2\text{H}_2\text{O} + 4\text{e}^- = 4\text{OH}^-$ (pH 14)	+0.401
	$\text{Cu}^{2+} + 2\text{e}^- = \text{Cu}$	+0.342
	$2\text{H}^+ + 2\text{e}^- = \text{H}_2$ (SHE Reference)	0.000
	$\text{Ni}^{2+} + 2\text{e}^- = \text{Ni}$	-0.250
	$2\text{H}_2\text{O} + 2\text{e}^- = \text{H}_2 + 2\text{OH}^-$ (pH 7)	-0.413
	$\text{Fe}^{2+} + 2\text{e}^- = \text{Fe}$	-0.447
	$\text{Cr}^{3+} + 3\text{e}^- = \text{Cr}$	-0.744
	$\text{Zn}^{2+} + 2\text{e}^- = \text{Zn}$	-0.762
	$2\text{H}_2\text{O} + 2\text{e}^- = \text{H}_2 + 2\text{OH}^-$ (pH 14)	-0.828

It should be noted that all values in standard EMF series are calculated at standard temperature and pressure (STP, 25°C and 1 atm) with an activity of all reaction components of 1.0. According to chemical potential theory:

$$\Delta G_i = \Delta G_o + RT \ln(a) \quad (2.4)$$

Where:

ΔG_o = Initial change in Gibb's free energy at STP

ΔG_i = Change in Gibb's free energy at non-standard state

T = Temperature

R = Universal gas constant (8.314472 J/mol*K)

a = Activity coefficient of reactant

Combining equations (2.3) and (2.4) yields:

$$(-n \cdot F \cdot E)_i = (-n \cdot F \cdot E)_o + RT \ln(Q) \quad (2.5)$$

where Q is the activity of the products over the reactants. Therefore, a relation has been made to calculate electrochemical potentials when conditions differ from that of the standard state. This relation is given by the Nernst equation (Perez, 2004). For the half-cell reaction written in the cathodic direction as $aA + mH^+ + ne^- = bB + dH_2O$:

$$E_i = E^o - \frac{RT}{nF} \ln \left[\frac{[B]^b [H_2O]^d}{[A]^a [H^+]^m} \right] \quad (2.6)$$

Where:

E_i = Non-standard state electrochemical potential

E^o = Standard state electrochemical potential from EMF series

$[X]^x$ = Activity / concentration (mol/L) of component X raised to its reaction coefficient

A, B, a, b, m, d = chemical variable of the half cell reaction

Assuming standard conditions with a temperature of 25°C, activity of H₂O of 1.0, and converting the natural logarithm to a base ten logarithm yields (Jones, 1996):

$$E_i = E^o + \frac{0.059}{n} \log \left[\frac{[A]^a}{[B]^b} \right] - \frac{m}{n} \cdot 0.059 \cdot pH \quad (2.7)$$

Equation (2.7) can be used to construct Pourbaix diagrams, which map regions of stability for products formed by corrosion reactions for various electrochemical potentials and values of pH. A basic Pourbaix diagram is shown in Figure 2.9. Active regions represent reactions where the product formed is not protective and corrosion reactions act continuously. Passive regions represent reactions where the product form is protective to the surface, causing corrosion reactions to slow greatly. Immune regions represent reactions where the pure metal is

stable and corrosion reactions will not occur (i.e. ΔG for the reaction is positive). More detail on active – passive behavior will be given in Section 2.1.3. It should be noted that Pourbaix diagrams are only valid for aqueous environments with little resistivity. Therefore, their application to corrosion in reinforced and prestressed concrete is limited and should only be used to approximate behavior (Kurtis, et al., 1997).

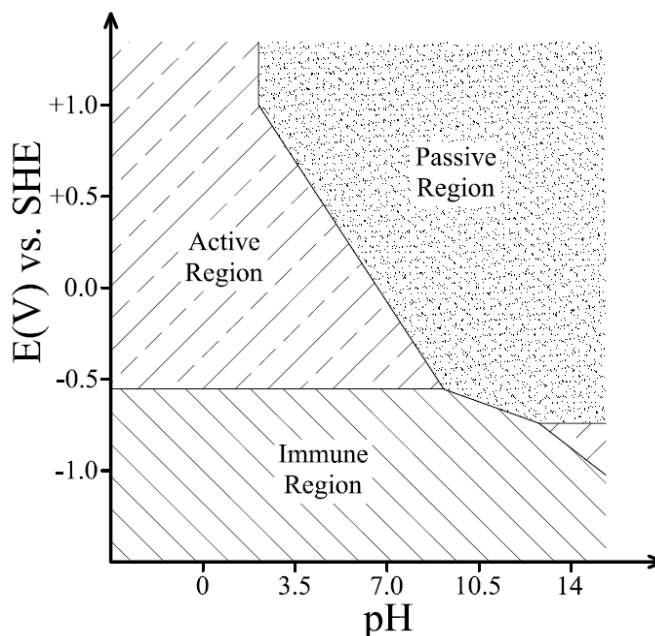


Figure 2-9: Example E vs. pH Pourbaix Diagram

Section 2.1.1 has provided an introduction to the thermodynamics of corrosion reactions. However, thermodynamics relations can only be used to compute the spontaneity of a corrosion reaction in a given environment and in no way can predict the kinetics of these reactions. Therefore, we must investigate reaction kinetics, as these control the degradation caused by corrosion.

2.1.2 Kinetics of Corrosion

The occurrence of an electrochemical reaction due to its spontaneity does not dictate the rate at which it proceeds. The rate of a reaction is controlled by its environment, resistivity of the electrolyte transferring ions, the availability of reactants, conductivity of the metal transferring electrons, and the nature of the product which is formed during the reaction which may be rate limiting.

Many experimentalists use conventional mass loss measurements to determine corrosion penetration rates. Equation (2.8), shown below, is easily derived and can be used for simple experimental measurements (Jones, 1996).

$$r_p = \frac{K \cdot \Delta m}{\rho \cdot A \cdot t} \quad (2.8)$$

Where:

r_p = Penetration rate of the surface corrosion

K = Constant for unit consistency

Δm = Change in mass of the sample

ρ = Density of the material

A = Exposed surface area

t = Exposure time

While this is useful for long term testing, in many instances an “instantaneous” measurement of the corrosion rate is needed. As discussed in Section 2.1, electrochemical reactions occur as a circuit with mass transfer (formation of ion) and electron transfer. By Faraday’s law, we can develop an equation to relate mass transfer (chemical energy) to electron transfer (electrical energy) (Devine, 1997).

$$r_p = \frac{K \cdot I \cdot a}{A \cdot \rho \cdot n \cdot F} \quad (2.9)$$

Where:

I = Measured current between anodic and cathodic sites

a = Atomic weight of the material

Thus, a relation has been made between mass and electron transfer, which can be used to quantify corrosion rates by current measurements using simple electrochemical testing techniques. It should be noted that equations (2.8) and (2.9) assume a uniform reaction of the surface which may not occur if corrosion is of a localized morphology, as is the case with pitting corrosion.

At equilibrium between the metal surface and the electrolyte, the surface will exhibit a rest potential, E_o , and exchange current density (current present between anode and cathode at equilibrium), i_o . By polarizing the material from its equilibrium potential, E_o , and measuring current, the corrosion behavior of the material can be determined for a wide range of electrochemical potentials. Electrochemical polarization is given by:

$$\eta = E_i - E_o \quad (2.10)$$

Where:

E_i = Polarized electrochemical potential

E_o = Equilibrium electrochemical potential

η = Electrochemical polarization from equilibrium

$\eta > 0$ Anodic polarization

$\eta < 0$ Cathodic polarization

Behavior resulting from polarization from equilibrium is most easily visualized using E vs. log(i) polarization diagrams, where i is the current density (I/A). Figure 2-10 shows a basic polarization curve in a region near equilibrium. Although a detailed explanation is beyond the scope of this chapter, a brief discussion of Maxwell reaction rate / chemical potential relations is warranted. According to Maxwell's Distribution Law (Singh, 2008):

$$K \approx C \cdot \exp \left[\frac{-\Delta G}{RT} \right] \quad (2.11)$$

Where:

R = Universal gas constant

K = Reaction rate

C = Constant

T = Temperature

Combining equations (2.11) and (2.3) yields:

$$\eta = \beta \log \left[\frac{i_i}{i_o} \right] \quad (2.12)$$

Where:

η = Polarization overpotential

$\beta = 2.3 \frac{RT}{\alpha n F}$ = Tafel constant / slope of polarization curve

i_i = Polarized corrosion current density

i_o = Exchange current density

α = Constant related to surface geometry

R = Universal gas constant

F = Faraday's constant, 96485 C/mol

n = Number of electrons transferred in anodic reaction

T = Temperature

Equation (2.12) provides a relationship between the applied polarization and the change in corrosion current density of a material. In addition, equation (2.12) verifies the experimentally observed linearity in the relationship between current and polarization when curves are plotted using a log scale for the current component. Tafel constants β_a and β_c used in equation (2.12) typically range between 0.05 and 0.2 V/decade and represent the ~constant linear slope of the anodic and cathodic portions of a polarization curve (Jones, 1996).

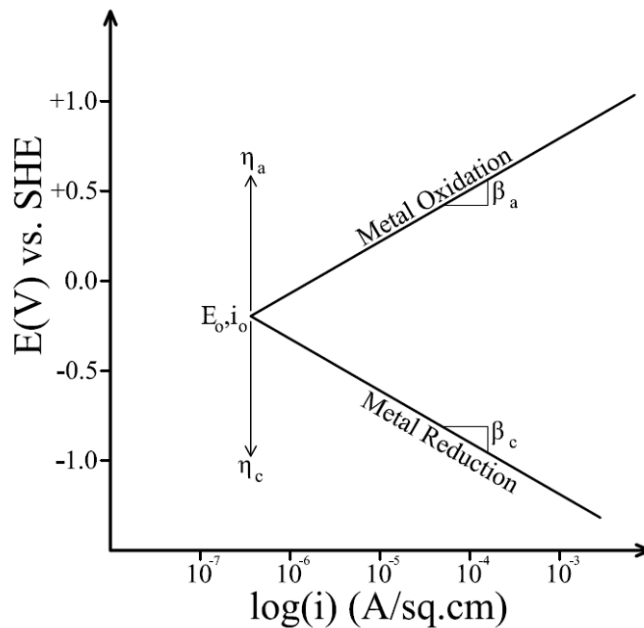


Figure 2-10: Example Polarization Curve

For corrosion reactions to proceed, chemical and electrical energy exchange between anodic and cathodic sites must occur at the same rate. By plotting anodic and cathodic polarization curves on the same diagram their interaction can be observed. These combined interaction diagrams are typically the subject of Mixed Potential Theory.

In many cases complete linearity is observed when plotted against the logarithm of current, indicating the reaction is activation controlled (rate of reactions controls corrosion according to equation (2.12)). An example corrosion reaction exhibiting activation control is shown in Figure 2-11. In some instances nonlinearity may be observed and is known as concentration control. Concentration control may result from high rates of reaction causing reactant depletion at the surface and/or the buildup of reaction products on the surface limiting the availability of reactants (Jones, 1996). Figure 2-12 shows a corrosion reaction in which the cathodic portion of the electrochemical cell exhibits concentration polarization induced nonlinearity.

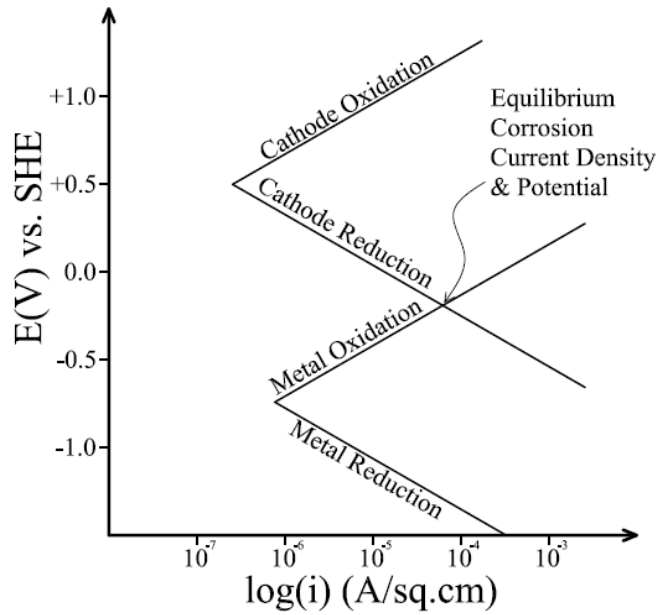


Figure 2-11: Activation Controlled Polarization Diagram

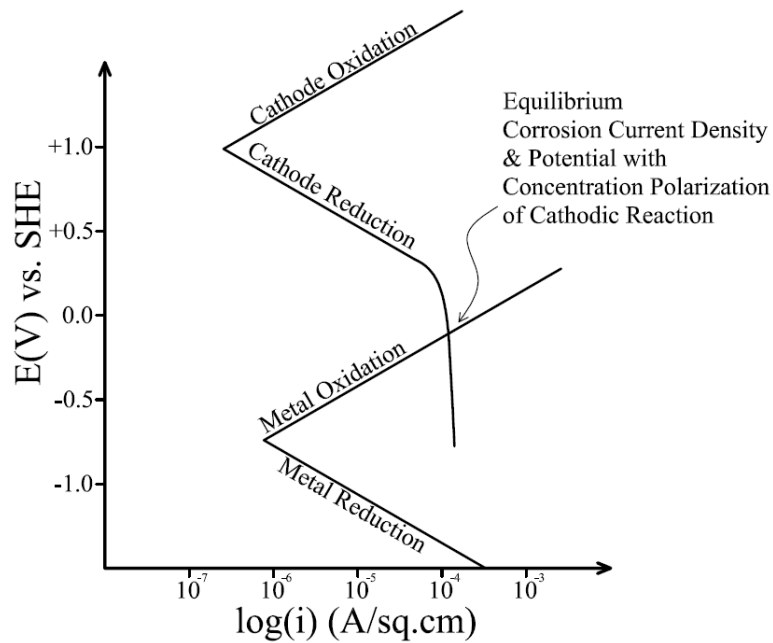


Figure 2-12: Concentration Controlled Polarization Diagram

In addition to its use for simple systems, Mixed Potential Theory can also be used to describe the interactions associated with crevice corrosion, galvanic coupling of dissimilar metals, concentration cells corrosion, and systems where there may be multiple anodic and cathodic reactions occurring simultaneously.

2.1.3 Active – Passive Behavior of Metals

While the kinetics discussed in Section 2.1.2 are theoretically applicable to all corrosion reactions, consideration of the reaction products formed on the surface should also be given, as they have a great influence on the corrosion behavior of the material. In the case of concrete reinforcement, we are mainly concerned with conventional carbon and stainless steel alloys. Shown in Figures 2-13 to 2-15 for Fe, Cr, and Ni, respectively, the Pourbaix diagrams indicate regions of phase / structure stability with respect to E and pH. Depending on E and pH, a surface may exhibit passive behavior by the buildup of a nanometer thick passive metal-oxide layer, active behavior by continuous dissolution of metal ions into the electrolyte, or immune behavior if the surface is thermodynamically stable in its pure form. The passive condition is shown in the aqua shaded regions on Figures 2-13 to 2-15.

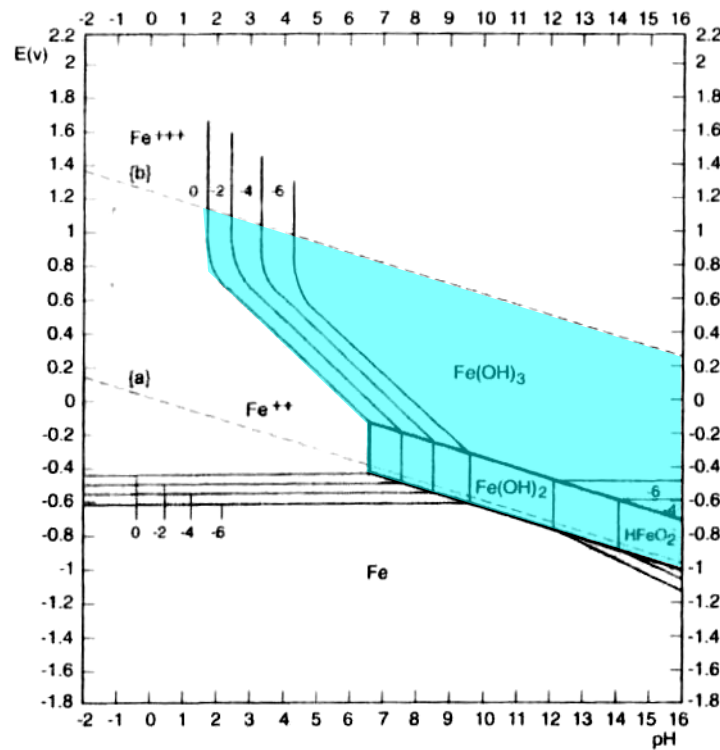


Figure 2-13: Iron E vs. pH Pourbaix Diagram (Pourbaix, 1974)

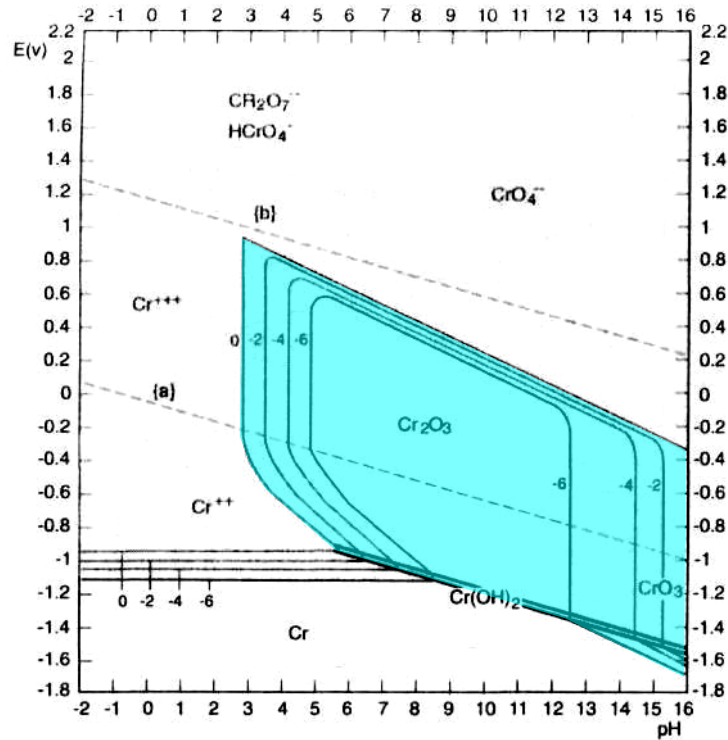


Figure 2-14: Chromium E vs. pH Pourbaix Diagram (Pourbaix, 1974)

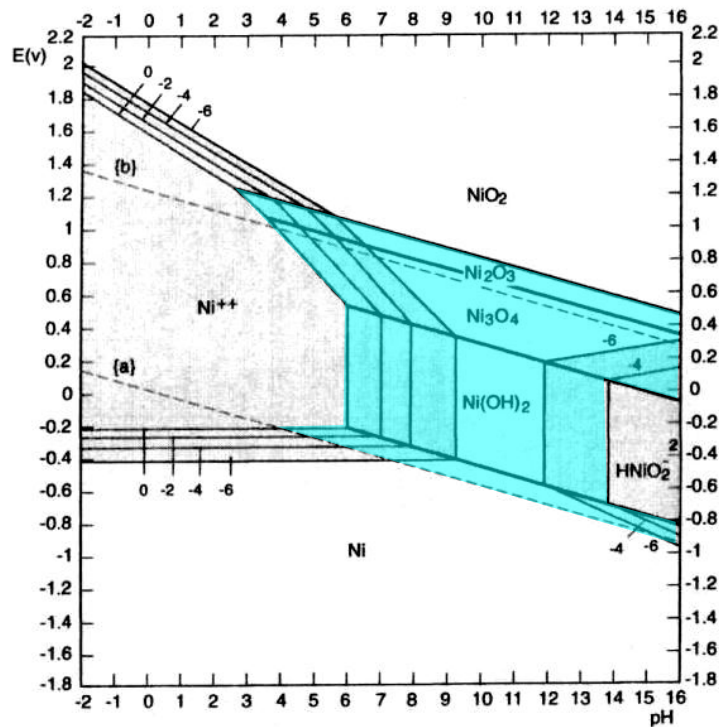


Figure 2-15: Nickel E vs. pH Pourbaix Diagram (Pourbaix, 1974)

In order to effectively explain passivity of metallic concrete reinforcement, a description of the environment present at the surface for the embedded reinforcement is necessary. Normal

Portland cement concrete (PCC) consists of fine and coarse aggregates, cement, and water. In many cases, additional chemical and mineral admixtures may be used to produce concretes with higher strength and durability. Hydration of cement produces a porous hydrated cement paste (HCP) structure of calcium silicate hydrate (C-S-H), calcium hydroxide (CH), ettringite (A_{ft}), and monosulfate hydrate (A_{fm}). In addition, a pore solution rich in KOH, NaOH, and $Ca(OH)_2$ exists in the HCP. The presence of hydroxides in the pore solution raises its pH to approximately 12.5 to 14 (Kurtis, 2007, Mehta, et al., 2006).

As indicated in Figure 2-13 and experimentally observed, in the highly alkaline pore solution, normal steel reinforcement develops a strongly protective passive film on its surface, resulting in a high resistance to corrosion (Ahmad, 2003, Jones, 1996, Mehta, 1991, PCA, 2007). Many mechanisms, which will be discussed in subsequent chapters, may degrade the protection offered by the passive film. For example, if a process results in a drop of pH to near neutral conditions or the stability of the film is jeopardized, corrosion may be initiated.

To achieve increased resistance to corrosion, alloys which develop a passive film over a wider range of E and pH may be utilized. For civil infrastructure applications, stainless steels are the typical alternative alloys used for concrete reinforcement to provide high corrosion resistance (Hartt, et al., 2007). Stainless steels are comprised mainly of Fe, Cr, and Ni. As shown in Figures 2-13 to 2-15, each of these alloys develops a passive film in an alkaline environment under ranges of potential which are typical in reinforced and prestressed concrete. When passive regions are superimposed, the effectiveness of adding Cr to the alloy is indicated by a much wider range of passivity. Figure 2-16 shows the regions of passivity in a Fe-Cr-Ni alloy, with Fe shaded red, Ni, shaded aqua, and Cr shaded blue.

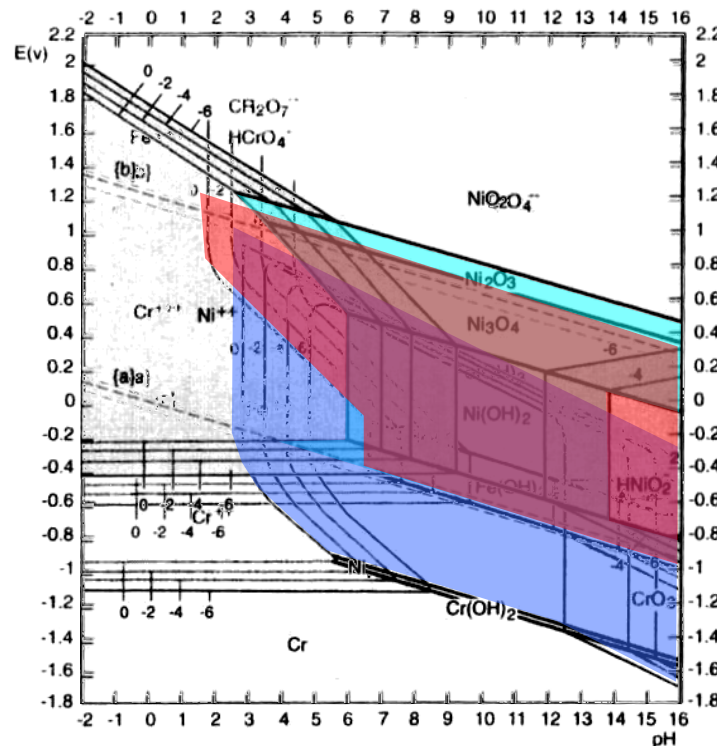


Figure 2-16: Superposition of Fe, Cr, and Ni E vs. pH Pourbaix Diagrams (Pourbaix, 1974)

In most stainless steels, Cr is the main contributor to increased passivity. However, the effectiveness of Cr is only gained if addition is upwards of 10% in the stainless steel, as evidenced in Figure 2-17. At lower alloying percentages, Cr only participates in metallic bonding of the Fe-Cr-Ni structure. Its ability to form a stable Cr_2O_3 passive film structure over a wide range E and pH provides stainless steels with a high resistance to corrosion once a passive film has formed (Skorchelletti, 1976).

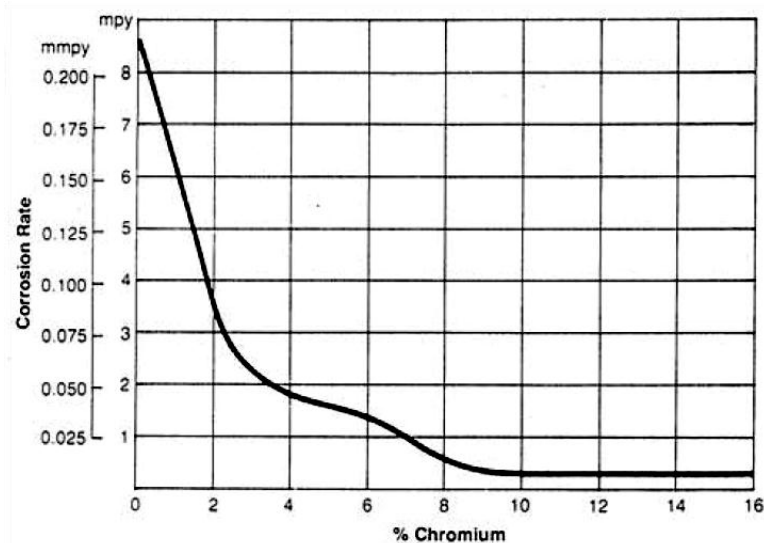


Figure 2-17: Effect of Cr Addition on Corrosion Rate

Nickel shows little benefit beyond that given by Fe in the formation of a passive film. The primary function of Ni is to stabilize the FCC structure of Fe present in typical austenitic (e.g. Types 304 and 316) stainless steels. Further information on the use of stainless steels (including austenitic, duplex, and new innovative alloys) for concrete reinforcement will be presented in subsequent chapters.

Experimentally, the presence of a protective passive film may be shown on a polarization diagram, where corrosion current density remains constant or decreases over a wide range of E, indicating the presence of a reaction limiting product being formed on the surface. Figure 2-18 depicts the typical behavior of an active – passive metal with the large region in which corrosion rates are constant with increasing values of E (Singh, 2008). The active region represents dissolution of the metal to solvated cations in the electrolyte. The passive region represents the buildup of a stable passive film on the surface. Once potentials reach the transpassive level, corrosion protection is lost as the passive film's structure begins to degrade (or O_2 may be evolved), particularly at defect sites such as scratches and grains boundaries.

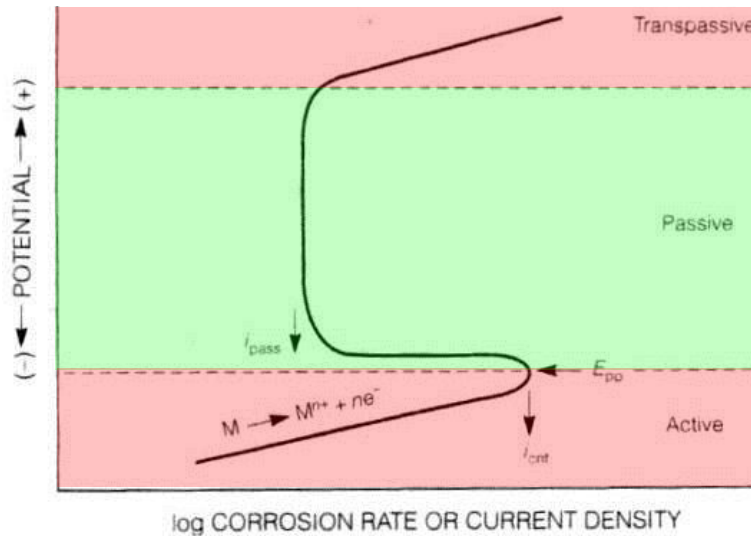


Figure 2-18: Polarization Curve for Active – Passive Metal (Jones, 1996)

The effect of alloy composition, solution / electrolyte aggressiveness, temperature, and many other factors all alter the behavior of polarization curves (Jones, 1996). For example, Figure 2-19 illustrates the increase in passivity resulting from addition of 10.5% Cr to a normal Fe steel in an aqueous alkaline environment. It should be noted that polarization curves are specific to the material and environment tested and cannot be used for broad applications of electrochemical behavior.

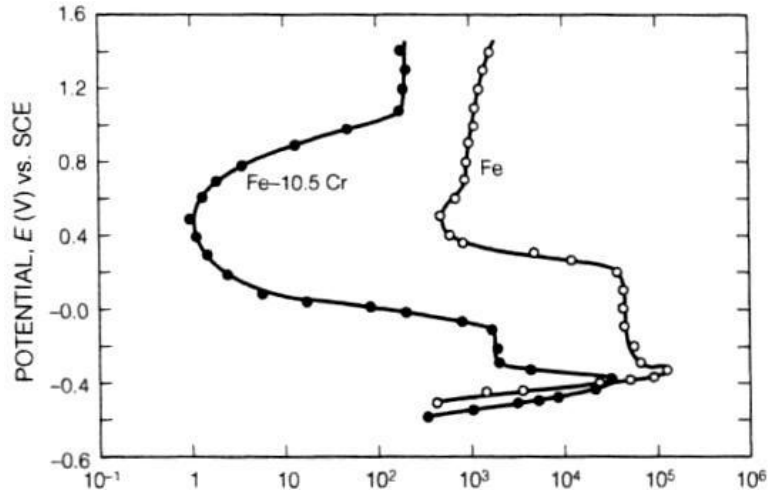


Figure 2-19: Polarization Curve for Fe & Fe + 10.5% Cr Alloys (Jones, 1996)

2.2 Corrosion Mechanisms in Concrete

2.2.1 Carbonation Corrosion

Corrosion of reinforcement caused carbonation of the cover concrete occurs with the ingress of CO_2 from the atmosphere and its subsequent reaction with phases present in the HCP.

For corrosion to occur, carbonation of the HCP must occur to the level of the reinforcing steel. Ingress of CO₂ has been shown to follow (Bertolini, et al., 2004):

$$d = K \cdot t^{1/n} \quad (2.13)$$

Where:

d = Depth of carbonation

K = Experimentally curve fitted constant

t = time

n = Curve fitting factor (2 in PCC and >2 in HPC)

The ingress of CO₂ is greatly affected by environmental conditions such as relative humidity (RH) and temperature. As shown in Figure 2-20, maximum CO₂ ingress occurs approximately at a RH of 60-70% and moderate temperature of 20-25°C. Lower carbonation rates may occur when concrete is saturated by rain or dry due to little exposure.

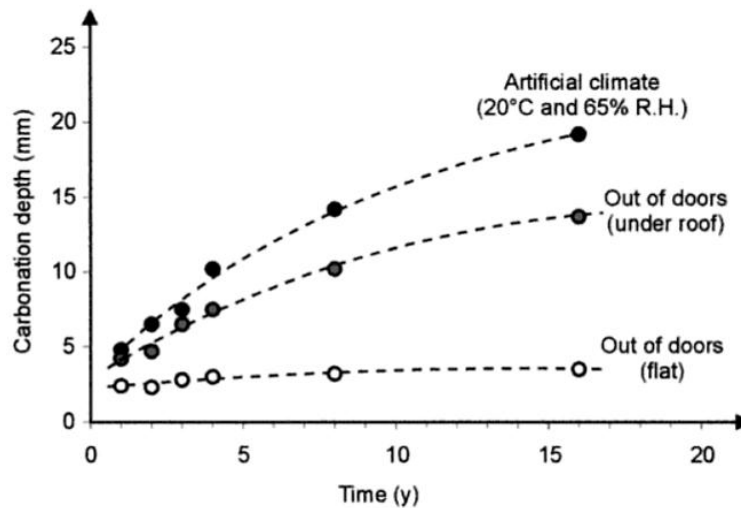


Figure 2-20: Carbonation Depth vs. Time (Wierig, 1984)

Once the carbonation front reaches the surface of the reinforcement, pH falls as CO₂ reacts with the components of the concrete pore solution (Bohni, 2005), as shown below:



Each carbonation reaction requires H₂O to complete. This requirement is the reason a moderate RH of 60-70% is required for carbonation rates to be at a maximum. Too high of a RH will limit the ingress of CO₂ gas, while too low of a RH will limit the availability of H₂O. Cyclic wet/dry cycles can also increase carbonation rates. Dry cycles allow CO₂ to permeate into the concrete, while wet cycles provide the H₂O needed for carbonation reactions to occur. CO₂ concentration can also have a large impact on carbonation rates. Under normal conditions CO₂ concentrations are in the order of 0.03%, with up to 10X higher concentrations in industrial or

urban areas, and up to 100X higher concentrations in areas such as highway tunnels or power plants (Hope, et al., 2001). As would be expected, increased temperatures also increase rates of carbonation and carbonation related corrosion.

The products of the carbonation reactions, sodium and potassium carbonates have a high solubility, therefore, they stay in solution while the calcium carbonate has a low solubility and precipitates out of solution, often filling the pore space and reducing CO₂ ingress rates. The consumption of the sodium, potassium, and calcium hydroxides leads to a reduction in the pH of the pore solution to approximately 7 to 9. At the neutral pH, the protection offered by the passive film is lost, and uniform corrosion of the reinforcing steel begins (Broomfield, 2007). Figure 2-21 illustrates the typical distribution of pH with carbonation depth.

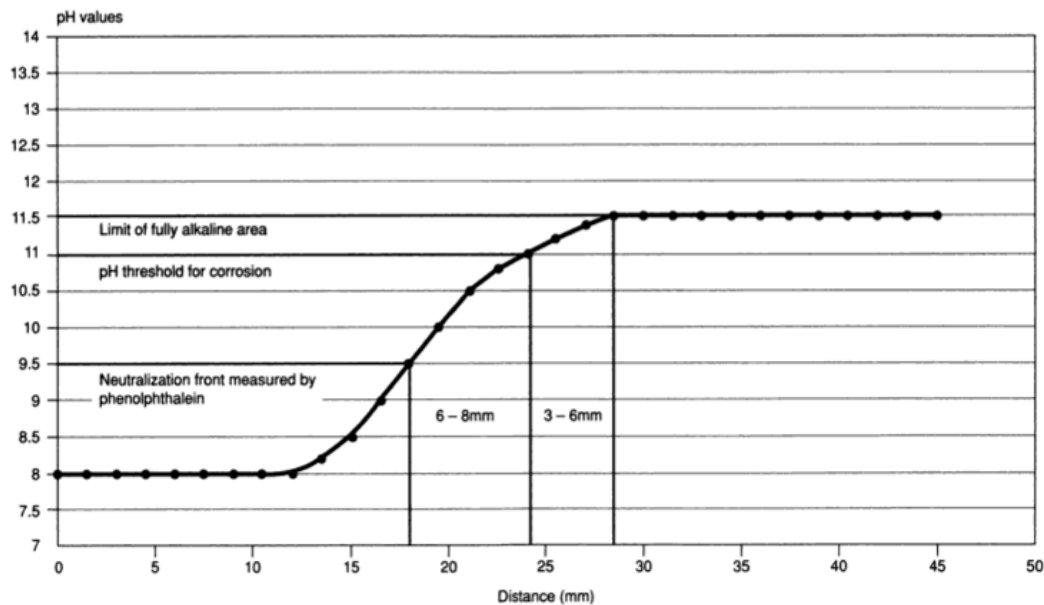


Figure 2-21: Typical pH Distribution during Carbonation (Broomfield, 2007)

Determination of carbonation depth is typically made with the use of a Phenothalene / alcohol indicator which turns pink at a pH greater than 9. As shown in Figure 2-22, the cover concrete has been carbonated, while the inner concrete is still highly alkaline. In this case, carbonation has reached the surface of the reinforcement inclusion in the core.



Figure 2-22: Carbonation of Cover Concrete

In the U.S., corrosion due to carbonation is of little concern in most modern structures which utilize low w/c ratios, cover concrete thicknesses greater than 1", supplementary cementitious materials, proper curing, and high cement contents provided that proper consolidation of the concrete occurs (Bertolini, et al., 2004). In these structures, carbonation rates are typically in the order of $1\text{--}5^{\text{mm}}/\text{yr}$ (Hartt, et al., 2004). Many regions around the globe where climates are more favorable to accelerated carbonation rates (moderate temperature with frequent wet / dry cycles) are subject to corrosion induced by carbonation of the cover concrete (Broomfield, 2007). However, as service lives extend beyond 75-100 years, carbonation may be an additional mechanism which must be considered in order to assess the corrosion resistance of a concrete structure.

In addition, carbonation of the cover concrete may also liberate bound chlorides in the HCP. Monosulfate hydrate and ettringite phases present in the HCP have the capability to bind Cl^- to form Friedel's Salts ($3\text{CaO} \cdot \text{Al}_2\text{O}_3 \cdot \text{CaCl}_2 \cdot 10\text{H}_2\text{O}$). Once the cover concrete has been carbonated and bound Cl^- released, a "front" of high Cl^- concentration results. Once the Cl^- front reaches the level of the reinforcing steel corrosion may be initiated by Cl^- interaction with the passive film as will be discussed in the following section.

2.2.2 Chloride Induced Corrosion

In modern structures, ingress of Cl^- ions from the environment is the predominant cause of corrosion in reinforced and prestressed concrete members. Because corrosion by chloride ions is of utmost importance, this section will discuss the effect of marine and deicing salt exposure, Cl^- corrosion mechanisms, transport mechanisms including the effect of Cl^- binding, the effect of cracking, and a discussion of accepted Cl^- threshold values.

2.2.2.1 Marine and Deicing Salt Exposure

The most destructive component of a salt bearing environment is the Cl^- ion. In seawater, salt content ranges from 33-38 parts per thousand (ppt) and is usually considered to be 35 ppt in open ocean water (Mehta, 1991). While the salts are made up of various elements including sodium, potassium, and magnesium, the main ion present in seawater is the chloride ion. Table 2-2 shows the typical anion and cation content in open ocean water. Chlorides can also ingress into concrete through the use of deicing salts in regions with severe winters, resulting in extensive corrosion of bridge decks and concrete pavements. Degradation can also be accelerated in tropical regions, where marine conditions are accompanied by increased temperatures and relative humidity (Hartt, et al., 2004).

Table 2-2: Seawater Ion Content (Chandler, 1984)

Seawater Ions	Content (g/kg)
Total Salts	35.10
Sodium	10.77
Magnesium	1.30
Calcium	0.409
Potassium	0.338
Chloride	19.37

Another important consideration in both bridge decks and marine exposures is the potential for periodic wet and dry cycling. Periodic wetting due to tidal or splash action in marine structures, or periods of rain/snow and dry on bridge decks can allow chlorides to ingress at high rates during wet periods and then precipitate and deposit during dry periods. Examples of this can be seen in Figures 2-23 and 2-24, showing the increased Cl^- concentration occurring in the splash zone and submerged areas relative to the dry regions. Even though Cl^- contents can be very high in submerged areas, corrosion is of little concern due to the lack of O_2 to carry out reactions at the cathodic site. It is only in the wet/dry areas of the splash and tidal zone where a supply of both chlorides and oxygen is present and corrosion rates are accelerated (Sandberg, et al., 1998).

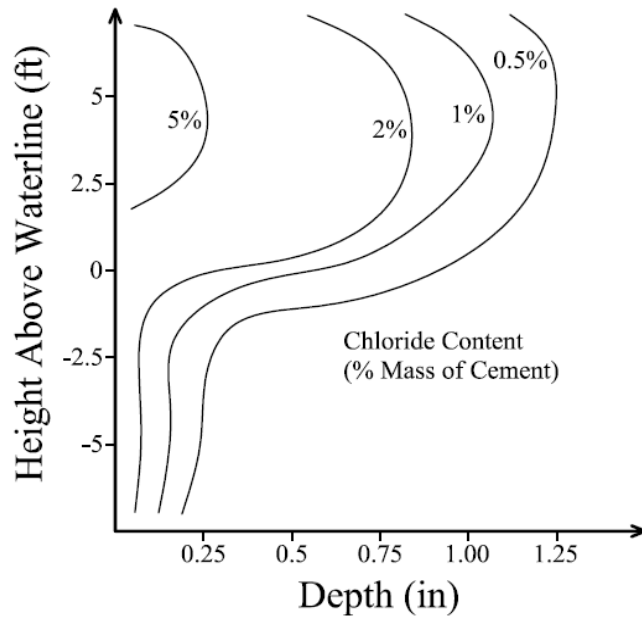


Figure 2-23: Typical Cl^- Profile at Waterline (Nuernberger, 1995)

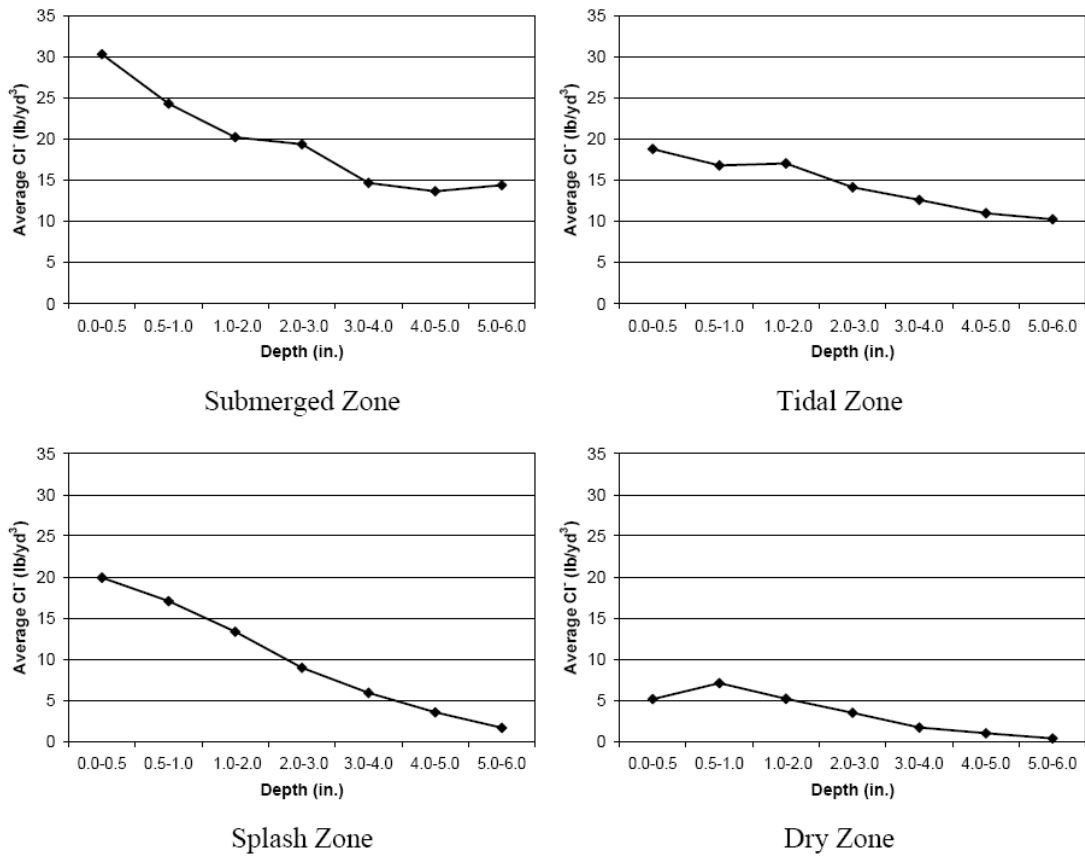
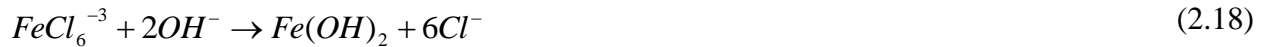


Figure 2-24: Cl^- Concentration vs. Depth for Coastal Piles (Hamilton III, 2007)

2.2.2.2 Chloride Induced Corrosion Mechanisms

As discussed in Section 2.1.3, steel typically does not corrode in concrete as portland cement-based concrete has a high pH and causes passivation of the steel surface. In Cl^- bearing environments, the main danger of corrosion is the localized breakdown of the passive film. Once Cl^- has reached a sufficient concentration at the level of the reinforcement, passivity can be lost locally, initiating corrosion. Breakdown of the passive film is caused primarily by diffusion of Cl^- into the passive film (Jones, 1996).

Under normal conditions the passive film dissolves at a slow and steady rate. Cl^- at the passive layer – electrolyte interface can dissociate hydroxyl ions in the passive film, forming metal chlorides (halides) which dissolve into the electrolyte (pore solution in this case). Degradation of the passive film occurs according to equations 2.16 to 2.18 (Kurtis, et al., 1997). It should be noted that the reaction shown in equation 2.18 involves the formation of $\text{Fe}(\text{OH})_2$ corrosion product and, most importantly, the release of the Cl^- . Thus, the breakdown of the passive film is an autocatalytic reaction, with the Cl^- reactant not being bound into the corrosion products (Kurtis, et al., 1997).



Reactions will occur preferentially at defect sites in the passive film. Defects can be due to grain boundaries in the underlying metal, slip planes at the surface, or scratches and imperfections. From the localized sites of dissolution, larger pits will eventually be formed leading to corrosion damage. A typical corrosion pit is shown in Figure 2-25. Inside of the pit Cl^- are concentrated and pH falls to very acidic levels approaching 1 due to the formation of H^+ (Revie, 2000).

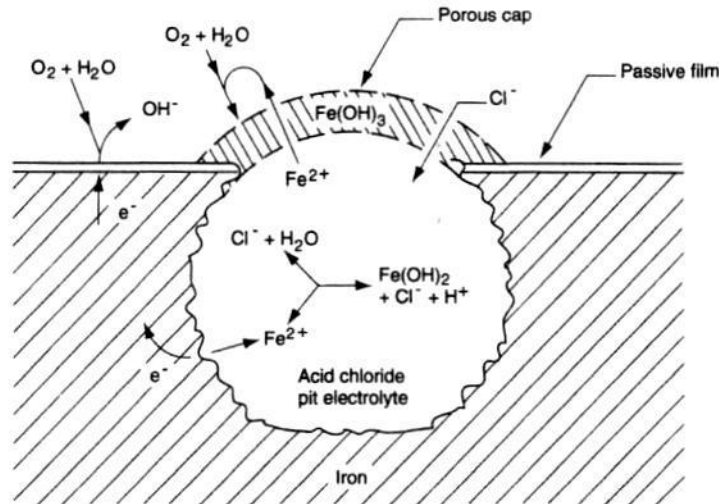


Figure 2-25: Typical Corrosion Pit Morphology (Jones, 1996)

Because the ingress of Cl^- is typically fairly uniform, breakdown of the passive film occurs uniformly across the surface of the reinforcing steel. Once pitting has become extensive on the surface of the reinforcement, pits will eventually coalesce and transgress into general / uniform corrosion, causing the typical cracking and spalling of the cover concrete.

2.2.2.3 Cl^- Transport Mechanisms in Concrete

For Cl^- induced corrosion to occur, Cl^- must reach the depth of steel by transport from the surface. The ingress of chlorides is controlled by many different mechanisms including diffusion, capillary suction, and chloride binding. Diffusion is defined as transport (in this case of Cl^-) into a material due to a concentration gradient. Capillary suction is the absorption of a fluid into a material due to capillary tension forces (also known as capillary action). When concrete is saturated, diffusion is the dominant transport mechanism, and when dry, capillary suction upon first wetting is the main mode of transport for chlorides (Thomas, et al., 1999). Concrete which is completely dry has almost no ability to absorb Cl^- and is resistant to corrosion.

Most research performed on chloride ingress utilizes Fick's second law for diffusion to model the non-steady state transport phenomena found in concrete. Fick's second law states that:

$$\frac{\partial C}{\partial t} = -\text{div}(\bar{J}) \quad (2.19)$$

Where:

C = Concentration

t = Time

\bar{J} = Diffusional flux across a boundary

Using Fick's first law, $\bar{J} = -D\nabla\bar{C}$ and taking D (the diffusion coefficient) to be constant, we obtain the usual form of Fick's second law, a 2nd order partial differential equation (2.20).

$$\frac{\partial C}{\partial t} = D \frac{\partial^2 C}{\partial x^2} \quad (2.20)$$

Where:

D = Diffusion coefficient

x = Depth of ingress

Through Boltzman substitution, $\eta = x/\sqrt{2Dt}$, equation can be transformed from a partial differential equation to an easily solved 2nd order homogeneous ordinary differential equation of the form:

$$\frac{\partial^2 C}{\partial \eta^2} + 2\eta \frac{\partial C}{\partial \eta} = 0 \quad (2.21)$$

Solution to equation (2.21), incorporating boundary conditions and an error function to simplify calculations yields (Kreyszig, 1967):

$$C(x, t) = C_s \left(1 - \operatorname{erf} \frac{x}{2\sqrt{Dt}} \right) \quad (2.22)$$

Where:

$C(x, t)$ = Concentration at depth x and time t

C_s = Concentration at surface

Many researchers have used normal diffusion models to predict Cl^- ingress successfully (Bertolini, et al., 2004). *Thomas et. al* used a normal Fickian model to test the effectiveness of supplementary cementitious materials (SCMs) at limiting Cl^- ingress effectively, accurately predicting chloride concentrations, as shown in Figure 2-26.

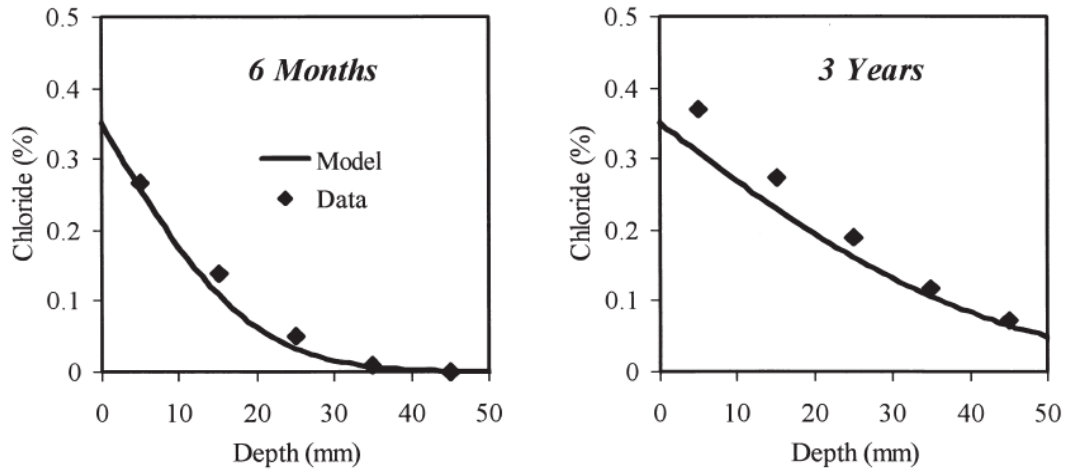


Figure 2-26: Comparison between Diffusion Model and Data (Thomas, et al., 1999)

To accurately model Cl^- ingress, capillary suction should also be considered. When concrete is dry, at first wetting liquid is absorbed quickly into the matrix due to the action of capillary suction. Capillary absorption of water is typically modeled according to the equation:

$$A = R + S \cdot t^{1/2} \quad (2.23)$$

Where:

A = Water uptake capacity of the concrete

R = A constant to account for surface roughness

where A represents the water uptake capacity of the concrete, S is the sorptivity, t the elapsed time, and C a constant to consider the disturbance (roughness) of the surface (Basheer, et al., 2001).

For a complete transport model the effect of Cl^- binding must also be considered. Chloride binding occurs due to the formation of Friedel's salts ($3\text{CaO} \cdot \text{Al}_2\text{O}_3 \cdot \text{CaCl}_2 \cdot 10\text{H}_2\text{O}$) by reaction Monosulfate hydrate (A_{fm}), ettringite (A_{ft}), and Cl^- (Mehta, et al., 2006). Two accepted mechanisms are responsible for the chloride binding capacity of Friedel's salts, the adsorption theory and the anion-exchange theory. In the adsorption theory, it is theorized that Cl^-

penetrates the lattice structure of the A_{fm} and A_{ft} phases and is physically bound to the crystal structure through bonding. The anion-exchange theory speculates that Cl^- physically bonds to the surface of the A_{fm} and A_{ft} phases to form Friedel's salt (Suryavanshi, et al., 1996). Whether these theories are completely accurate does not invalidate the fact that Cl^- binding does occur in the HCP. As would be expected, an increase in C_3A content in cement, resulting in an increased amount of Monosulfate hydrate and ettringite present in the HCP, has been shown to increase a concrete's ability to bind chlorides (Glass, et al., 2000). It is important to note that only free Cl^- present in the HCP can participate in corrosion reactions.

Many models have been proposed which consider all of the transport effects present in concrete, including Cl^- binding. *Boddy et. al* have developed a transport model for computer implementation which follows (Boddy, et al., 1999):

$$\frac{dC}{dt} = D \cdot \frac{d^2C}{dx^2} - v \frac{dC}{dx} + \frac{\rho \cdot dC_b}{n \cdot dt} \quad (2.24)$$

Where:

$v = Q/nA$ = Flow velocity according to Darcy's Law

Q = Flowrate

n = Porosity

A = Area of fluid flux

ρ = Density

t = Time

x = Distance from exposed surface

C_b = Concentration of bound Cl^-

C = Concentration of free Cl^-

Glass et. al also developed a transport model based on the Langmuir adsorption theory to account for the effect of chloride binding. Equation (2.25) shown below, is used to determine the concentration of bound Cl^- present in the HCP.

$$C_b = \frac{\alpha \cdot C}{1 + \beta \cdot C} \quad (2.25)$$

Where:

α, β = Experimentally fitted constants

When equation (2.25) is input into a Fickian non-steady state diffusion model the following results (Glass, et al., 2000):

$$\left[1 + \frac{\alpha}{w \cdot (1 + \beta C)^2} \right] \cdot \frac{dC}{dt} = D \cdot \frac{d^2C}{dx^2} \quad (2.26)$$

Where:

w = Constant related to the ratio of free to bound Cl^-

The effect of including chloride binding in a transport model can be seen in the concentration vs. depth graph shown in Figure 2-27. While many researchers have sufficiently relied on diffusion models to predict Cl^- ion transport, much controversy still exists as to their accuracy with respect to newer models which take into account all effects. One important consideration which is neglected in these models is the increase in Cl^- concentration which can occur at the splash/tidal zone in marine structures and the presence of cracks. In addition, each model relies on experimental data to fit theoretical equations using variable constants. While empirical curve fitting results in an acceptable prediction of Cl^- ingress, applying these models without any specific experimental data to a material as variable as concrete is ineffective given current technologies.

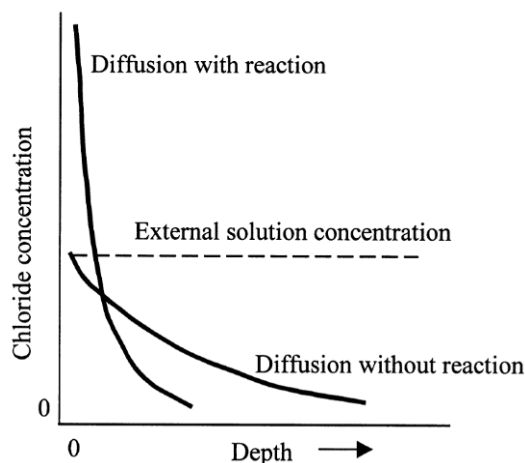


Figure 2-27: Concentration Profile With and Without Cl^- Binding (Basheer, et al., 2001)

2.2.2.4 Effect of Cracking on Chloride Ingress

While much debate exists over the influence of cracking on Cl^- ingress, it is universally accepted that the presence of cracks will increase permeability. Numerous studies have been conducted to determine the effect of cracking, and evaluate at which size a crack begins to affect the ingress of Cl^- . Most studies indicate that if a detectable crack is present, it will greatly increase the ingress of Cl^- , and the width of the crack has little effect on the rate of ingress (Rodriguez, et al., 2003, Schiebl, et al., 1997). Others, such as *Hansson et. al.*, indicate that crack width can effect the ingress of Cl^- , finding that cracks less than $\sim 0.5\text{mm}$ in width have little influence on the ingress of Cl^- (Hansson, 2005). Cracking of cover concrete not only allows for Cl^- to reach a direct point on the surface of the reinforcement, but also allows for additional ingress of Cl^- into the HCP through the interior surfaces of the crack. Figure 2-28 illustrates the typical progression of Cl^- through a crack in the cover concrete.

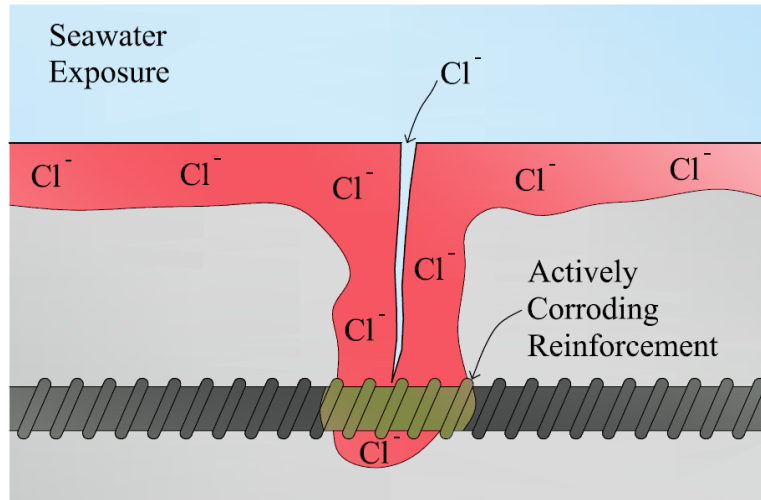


Figure 2-28: Effect of Cracking on Cl^- Ingress

Much research has also been conducted on the possibility of autogenous self healing of cracks to limit permeability. Self healing is possible due to the combined effects of swelling and additional hydration of cement paste, precipitation of carbonates, such as CaCO_3 , and crack blocking by impurities or broken concrete. While self healing of cracks was not found to be possible when widths are large, healing was found to occur when crack widths were less than $\sim 0.1\text{mm}$, with almost a full recovery in permeability (Edvardsen, 1999). While larger crack widths will experience some self healing, their rate of recovery is limited as evidenced in Figure 2-29. In any case, researchers agree that over a long design life (as is the case in current bridges with a 100+ year design life) the presence of cracks only accelerates the initiation of corrosion (Ahern, 2005).

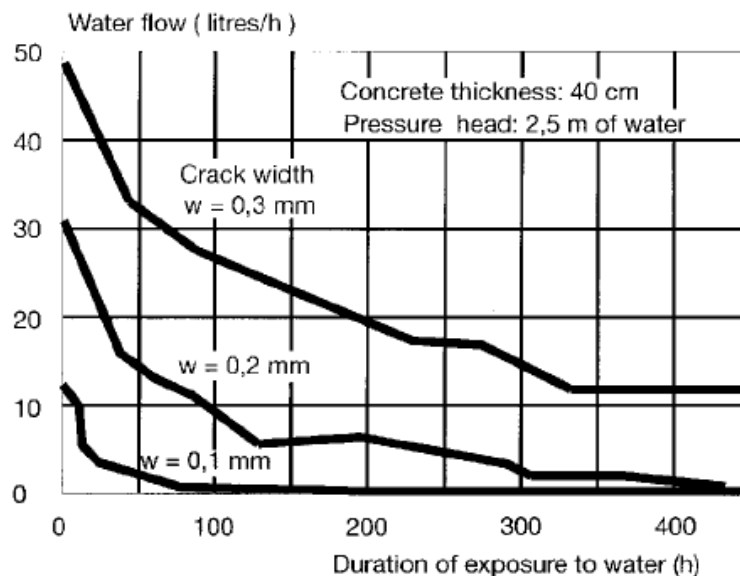


Figure 2-29: Relationship Between Crack Width and Self healing (Edvardsen, 1999)

In the case of prestressed concrete structures, the possibility of crack closure and subsequent self healing due to the presence of precompression forces has received little

investigation. It has been shown that the self healing of cracks to restore original permeability properties is greatly accelerated at early ages by the presence of compressive stress to close the crack. In addition, it was found that only enough compressive stress to close the faces of the crack was needed to initiate self healing (Heide, 2005). Figure 2-30 shows the results of crack self healing in the presence of compressive stress imaged using fluorescent epoxy impregnation. Self healing experiments conducted in compression are typically performed at early ages when hydration is still occurring. Further research is warranted which investigates the effect of cracks in compression in fully hydrated concrete exposed to realistic non-laboratory environments.

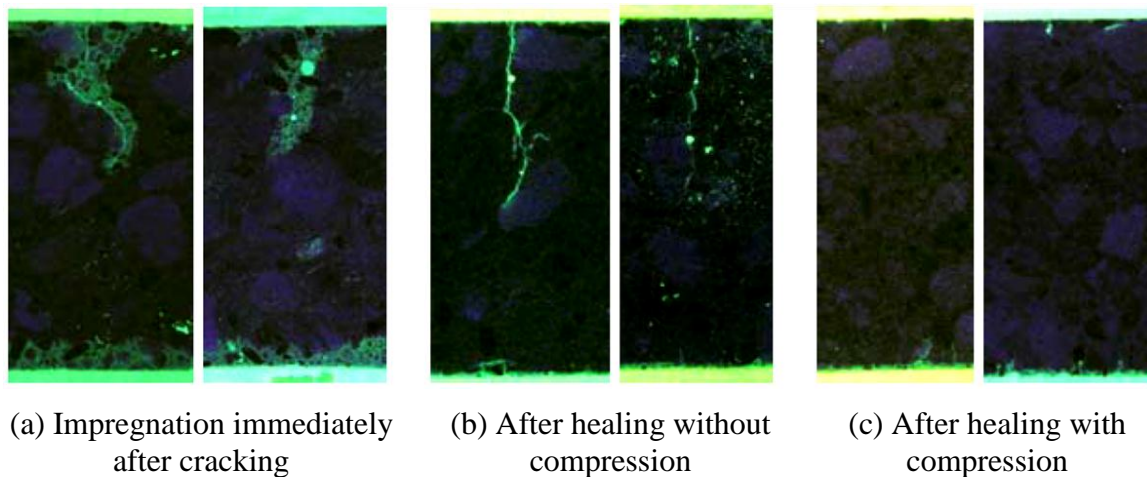


Figure 2-30: Self Healing of Cracks With and Without Compressive Stress (Heide, 2005)

2.2.2.5 Chloride Threshold Level

The parameter utilized by most engineers for Cl^- limits is the chloride threshold level, commonly known as the CTL. This value is typically expressed as the weight percent of chloride vs. the weight of cement in a concrete mixture, or weight of chlorides per cubic volume of concrete and represents the concentration of Cl^- when corrosion is expected to initiate. In the United States, a CTL value of 1 to 1.5 lb/yd^3 (.6 to .9 kg/m^3) has been agreed upon by most researchers for mild steel reinforcement in concrete (Ann, et al., 2007, Manera, et al., 2007). Due to the large variability in values for the CTL reported by researchers, the American Concrete Institute (ACI) has taken a conservative stance on CTL values. CTL values given in the ACI 318-05 Building Code Requirements for Structural Concrete and Commentary are shown in Table 2-3. ACI 318-05 CTL values are much less than those of 0.4 to 0.6 % used in Europe and Canada (Hope, et al., 2001).

Table 2-3: CTL Values Recommended in ACI 318-05 (Wight, 2005)

Type of member	Maximum water soluble Cl^- in concrete, percent by weight of cement
Prestressed Concrete	0.06
Reinforced concrete exposed to Cl^- in service	0.15
Reinforced concrete that will be dry or protected from moisture in service	1.00
Other reinforced concrete construction	0.30

Another measure of chloride content recommended by researchers is the use of a molar chloride-to-hydroxide ratio, $[Cl^-]:[OH^-]$ (Ann, et al., 2007). Researchers indicate that this value is more inclusive of the corrosion inhibiting behavior of concretes with higher OH^- contents. While ratios of 1 to 3 are typical, variability from 0.5 to 40 seems to make the $[Cl^-]:[OH^-]$ ratio an unreliable indicator of the CTL (Ann, et al., 2007, Thangavel, et al., 1998).

In both the cases of the typical weight % measure of CTL and the $[Cl^-]:[OH^-]$ ratio, variability in laboratory and field conditions and concrete placement techniques makes any measure of CTL inherently unreliable (Hope, et al., 2001). The CTL is affected by numerous factors, including concrete quality, the presence of voids, temperature, relative humidity, cracking, and oxygen availability. Therefore, there is a synergistic relationship present between the many possible variables which interact differently to give the true CTL of a particular reinforced concrete element. Figure 2-31 illustrates these interdependent relationships as determined by the CEB-FIP committee on Durable Concrete Structures.

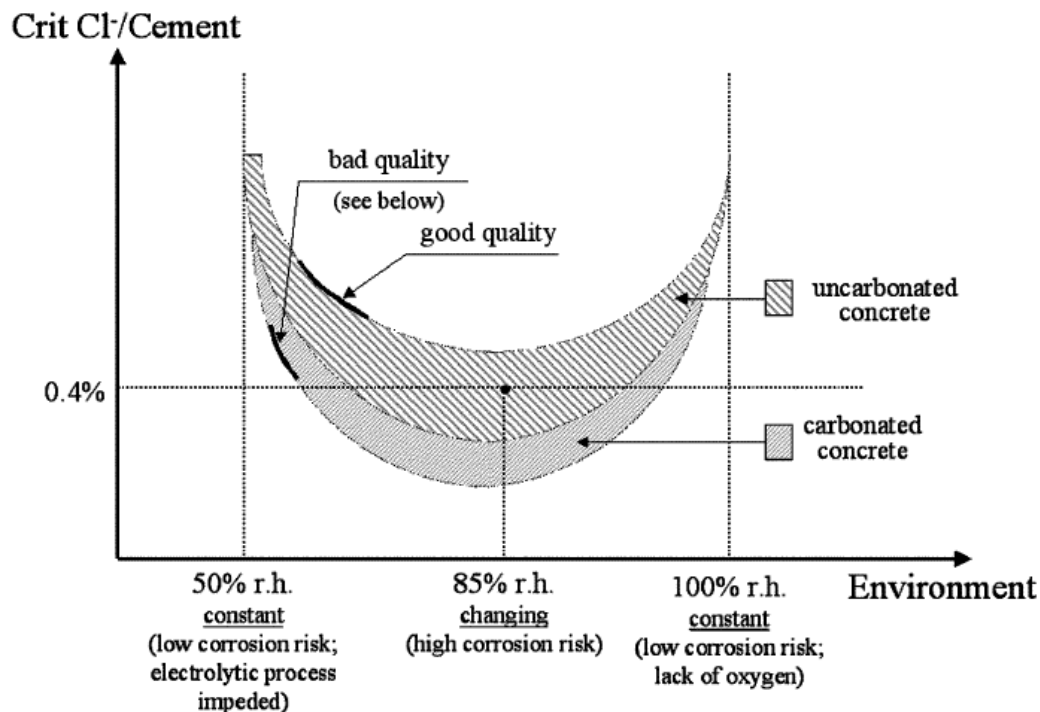


Figure 2-31: CTL Recommendations by CEB – FIP (FIP, 1992)

2.2.3 Consequences of Carbonation and Cl^- Induced Corrosion

Damage to structures caused by corrosion occurs over an extended period of time. Depending on the quality of the concrete, the environment, cover, and many other factors, the time until failure of the structure occurs and/or rehabilitation is needed can vary greatly. Corrosion timelines include an initiation period where carbonation of the cover concrete or ingress of Cl^- to the level of the reinforcing steel occurs and a propagation period as corrosion is initiated and damage to the structure begins. As explained in Figure 2-32, the length of each period is affected by many factors.

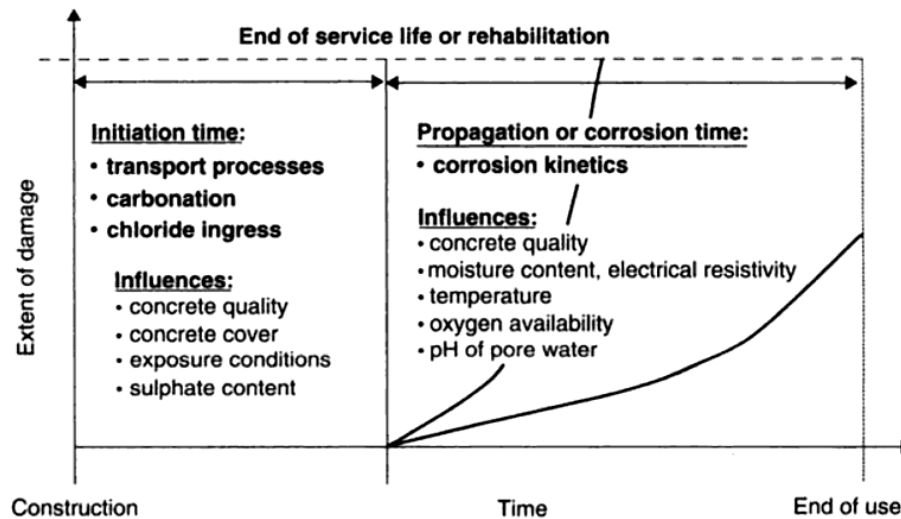


Figure 2-32: Corrosion Damage Timeline (Bohni, 2005)

Once corrosion of the reinforcement has initiated, it is the reaction itself and the corrosion products formed which degrade the integrity of the concrete structure. Corrosion reactions result in dissolution of metal, in this case Fe, from the surface of the reinforcement, resulting in a loss of cross sectional area. Due to decreased cross section, the design strength of the member may be decreased. However, in most cases general reinforcement corrosion is noted by cracks and brown rust stains like those depicted in Figure 2-33 well before strength is degraded to dangerously low levels (Bertolini, et al., 2004).



Figure 2-33: Cracks and Rust Staining on Concrete Member

The far greater impact of corrosion is the formation of corrosion products on the surface of the reinforcement. As shown in Figure 2-34, products formed by corrosion reactions when hydrated can occupy up to 7 times the volume when compared to that of the reacted metal (Mehta, et al., 2006).

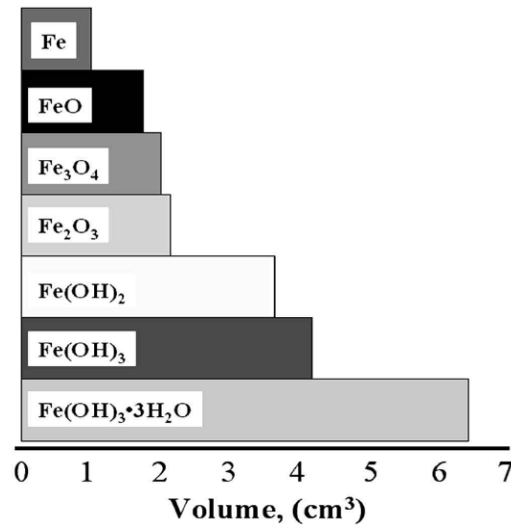


Figure 2-34: Relative Volumes of Fe Oxides (Hope, et al., 2001)

Expansive corrosion products develop tensile hoop stresses around the perimeter of the reinforcing bar. With concrete being weak in tension, cracks develop perpendicular to the tensile hoop stresses, as shown in Figure 2-35. Eventually, cracks will become extensive and spalling of the cover concrete occurs (see Figures 2-1 and 2-2). In addition to reducing the member's strength, cracking and spalling greatly lowers the concrete's resistance to the ingress of Cl^- and other reactants such as CO_2 and O_2 , leading to accelerated corrosion (Broomfield, 2007). The formation of corrosion products at the steel / concrete interface may also lead to bond degradation (Kurtis, et al., 1997).

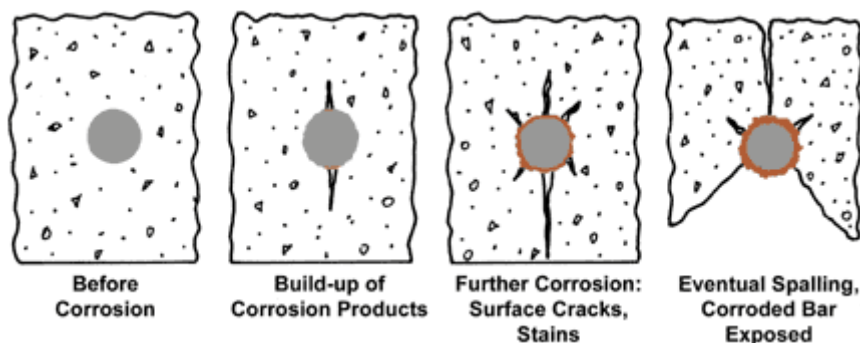


Figure 2-35: Cracking and Spalling of Concrete Caused by Corrosion (Rourke, 2008)

2.3 DEGRADATION OF PRESTRESSING STEELS

In addition to the corrosion mechanisms discussed in section 2.2 present in reinforced and prestressed concrete, other dangers exist in prestressed concrete structures. Due to their high level of initial stress and inherent metallurgical properties, prestressing steels may be susceptible to environmentally induced cracking (EIC) and strength and fatigue degradation in the presence of a corrosive environment.

In the case of prestressed concrete structures, two modes of EIC are of particular concern, stress corrosion cracking (SCC) and hydrogen embrittlement (HE) (Hope, et al., 2001). In many cases, SCC and HE mechanisms may occur simultaneously and interact with each other. The main danger of EIC is a reduction in both strength and ductility of the affected metal resulting in brittle failure modes at lower than anticipated loadings, as shown in Figure 2-36.

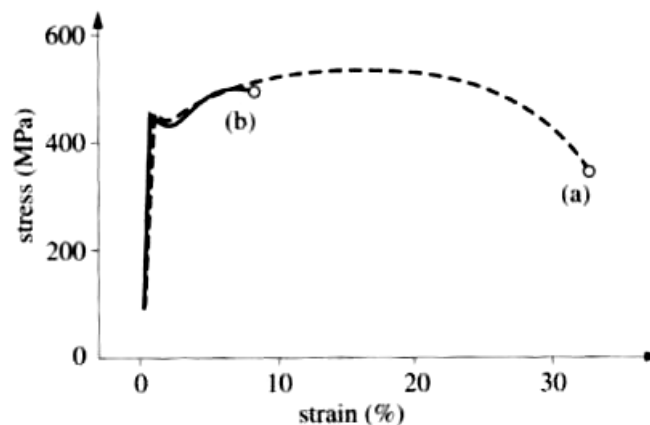


Figure 2-36: Slow Strain Rate Testing of Steel (a) in Air, and (b) in Seawater (Landolt, 2007)

Much like the timeline for Cl^- corrosion initiation, EIC includes an initiation period when cracks begin to form, a propagation period as cracks grow through the microstructure, and a damage period when fast fracture and failure of the metal occurs (Landolt, 2007). Corrosion of prestressing steels may also result in a loss of strength, ductility, and fatigue resistance through what is referred to as corrosion fatigue. For background, the following section will review the properties of prestressing steels.

2.3.1 Properties of Prestressing Steels

Steels used for prestressing are high-strength carbon steel Fe alloys with approximately 0.85% C, 0.65% Mn, 0.23% Si, and other trace elements such as S, P, Al, Mo, Cr, Cu, Ni, and V (Schroeder, et al., 2003). Prestressing steels are manufactured in a continuous process, producing a coil of wire which can then be manufactured into various forms for use in prestressing systems. Finishing of the wire during the first phase of manufacture is done using the Stelmor process. This process uses a quick quenching of the steel from 1500°F to room temperature to create the fine pearlitic microstructure of prestressing steels (Hope, et al., 2001). Wire produced using this process has strength of approximately 160ksi (1100MPa).

In order to achieve the desired 250-270ksi (1720-1860MPa), wires produced at the mill are cold drawn and heat treated. Cold drawing is done by reducing the diameter of the wire by approximately 25% at each stage until the desired wire diameter is obtained. Following cold drawing, post processing of the wires to reduce residual stresses created during cold drawing is done to produce a linear stress vs. strain relationship and to limit stress relaxation of the wire. Figure 2-37 shows the strand production process at Insteel's Jacksonville, FL production facility, one of the largest prestressing wire, strand, and bar producers in the country. The stress relieving process is performed at approximately 700°F, allowing residual stresses in the wire from the drawing process to “relax”, resulting in improved material properties. The currently used low-relaxation method combines the high temperature of stress relieving with stress of approximately 40% ultimate tensile strength (ASTM, 2006). The resulting product possesses an alternating α -Fe and Fe_3C pearlitic microstructure (shown in Figure 2-38), with high-strength (250-270ksi), moderate ductility (of ~5%), and low stress relaxation (typically less than 2% to 3% by ASTM A416 specifications (ASTM, 2006)) (Hope, et al., 2001, Lewis, 1969, Nawy, 2000).

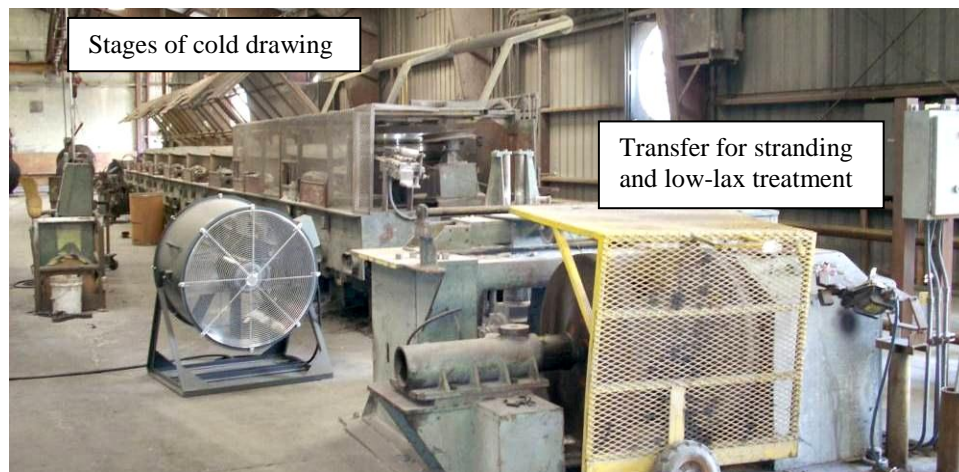


Figure 2-37: Prestressing Strand Production Process

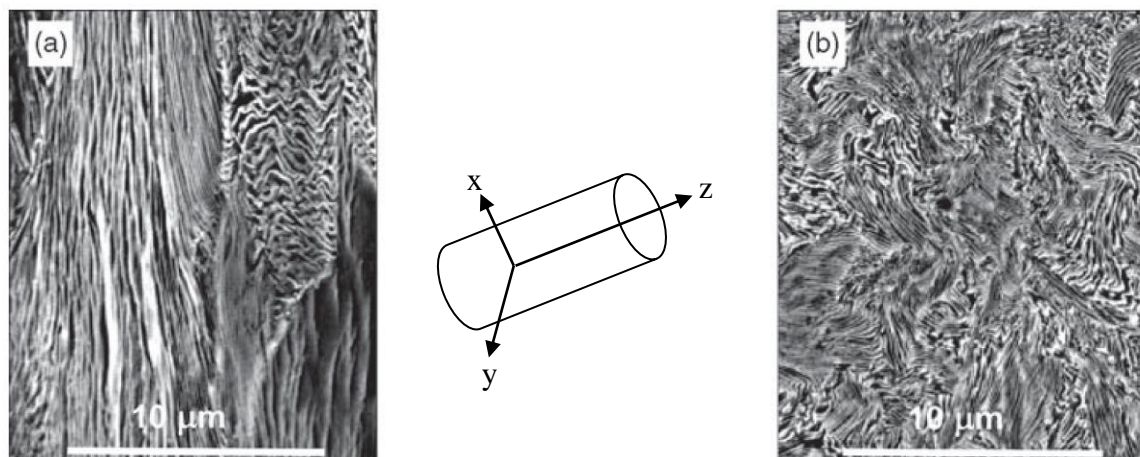


Figure 2-38: Pearlitic Microstructure (a) Parallel to z-axis, and (b) Normal to z-axis (Elices, et al., 2008)

Wires manufactured for use as prestressing are processed into three different configurations; single indented wires, multi-wire strands, and threaded bars. Single indented wires are typically used for specialty pretensioning applications such as precast concrete pipes, where a large amount of prestressing force is not required. Multi-wire strands are by far the most popular material used in prestressing systems. Strands are typically manufactured in a 7-wire configuration, although 3, 19, and many other configurations are available. 7-wire prestressing strands are available in 3/8", 7/16", 1/2", and 0.6" diameters, with the most common "1x7" configuration shown in Figure 2-39. 1x7 prestressing strand is used in both pre and post-tensioning systems in prestressed concrete. Threaded bars used for prestressing are typically used in post-tensioning operations. Prestressing bars are manufactured with lower strengths of 150-160ksi (1000-1100MPa) and in a variety of diameters (Nawy, 2000).

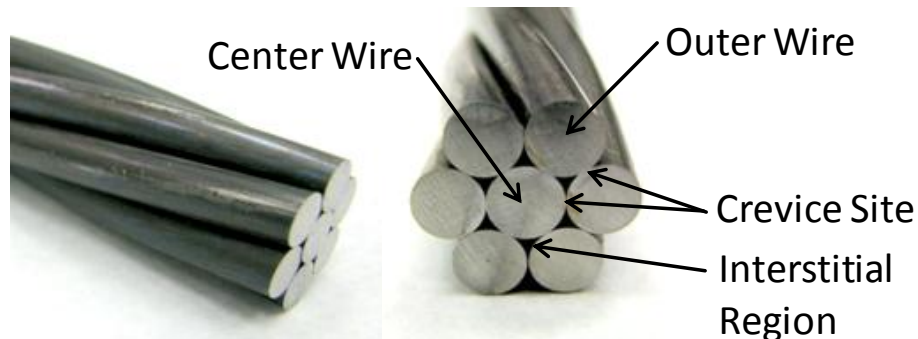


Figure 2-39: 1x7 Prestressing Strand Configuration

2.3.2 Stress Corrosion Cracking

Brittle failures caused by SCC may result when a susceptible alloy is placed in a corrosive environment while under a constant tensile loading (Schweitzer, 2003). In many cases, only specific alloy / environment combinations may be susceptible to damage by SCC. High strength alloys are at the greatest risk of SCC, owed to their high defect density and possible microstructural inhomogeneities resulting from production (Jones, 1996).

SCC may be intergranular or transgranular, as shown in Figure 2-40. Transgranular cracking results from reaction with the alloy itself along specific crystal planes and directions. Intergranular cracking results from inhomogeneities present at the surface causing cracks to be initiated preferentially at sites such as grain boundaries and defects (e.g. dislocations and vacancies) which have reached the surface. This is especially prevalent in cases where metal processing has resulted in undesirable precipitates (such as chromic carbides) being formed at grain boundary sites due to improper heat treatment (Jones, 1996, Mietz, et al., 1997, Singh, 2008).

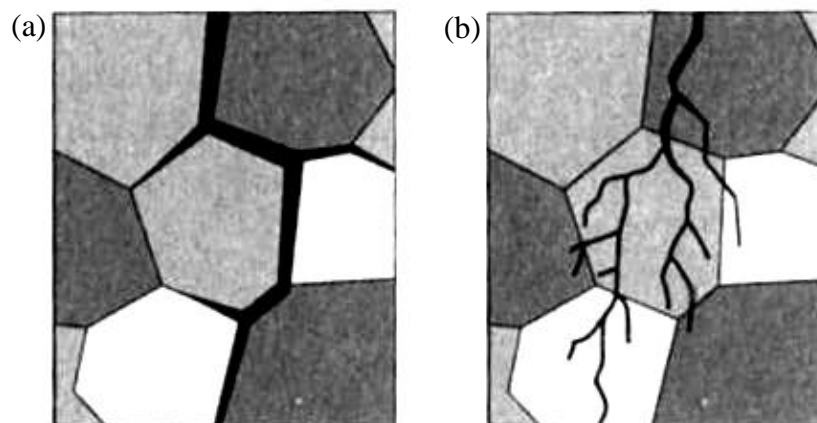


Figure 2-40: SCC (a) Intergranular, and (b) Transgranular (Landolt, 2007)

SCC is mainly limited to active – passive alloy / environment combinations, with damage occurring primarily in regions where passive film stability is easily jeopardized. Figure 2-41 shows zone 1 and 2 potential regions where SCC will most likely occur. In the transpassive region zone 1, the passive film is becoming weak as pitting occurs and the film begins to breakdown. As will be discussed later, pitting corrosion has also been shown to assist in the initiation of SCC, although it is not the only mechanism responsible for SCC. In zone 2, a stable passive film is just beginning to be formed and is not stable. Therefore, the metal's surface can easily transfer between active and passive states, resulting in randomly distributed local anodic sites with large cathodic regions driving the formation of electrochemically active crack tips (Jones, 1996, Landolt, 2007).

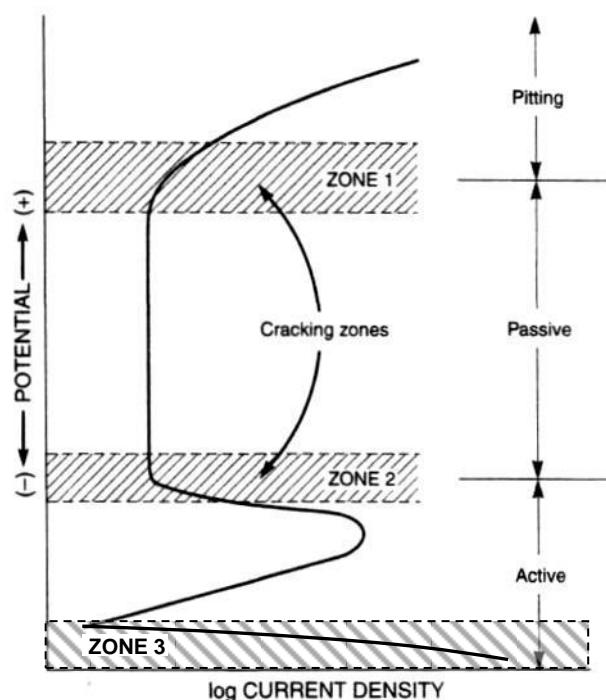


Figure 2-41: Regions of SCC and HE Susceptibility (from (Jones, 1996))

While most theories of SCC attribute anodic dissolution of metal at the crack tip to be the driving force for damage, examination of fracture surfaces shows little anodic dissolution of the faces of cracks, indicating combined SCC and mechanical modes of fracture. An example of intergranular SCC induced cracking in a prestressing steel is shown in Figure 2-42. In Figure 2-42, note the intergranular cracking which is adjacent to the region of ductile fracture of the prestressing steel.

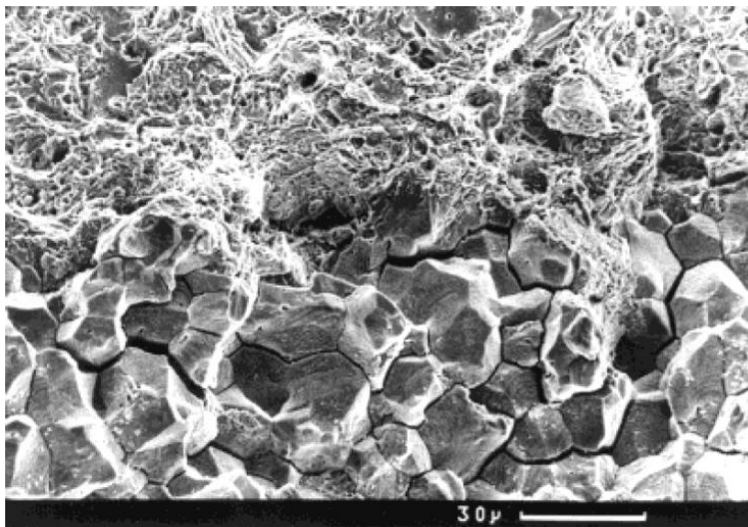


Figure 2-42: Intergranular SCC Cracking in Prestressing Steel (Mietz, 2000)

2.3.4 Hydrogen Embrittlement of Metals

Damage of metals due to hydrogen diffusing into the crystal structure of an alloy is referred to as hydrogen embrittlement. Much like SCC, HE results in brittle modes of failure with cracking of the microstructure upon tensile loading. Cracks formed by HE are mainly transgranular, as HE typically results in the most damage when occurring in the lattice structure and not at defects and grain boundaries where porosity is relatively high compared to the bulk. HE may occur only when atomic hydrogen is present due to high pressure hydrogen gas, generation at cathodic reaction sites, or by corrosion reactions (Nuernberger, 2002). Thus, in civil infrastructure applications, atomic hydrogen may only be generated at sufficient levels of cathodic polarization through excessive cathodic protection, as shown in Zone 3 of Figure 2-41; or when corrosion potentials are such that cathodic reactions result in the formation of atomic hydrogen (below H_2 stability line on Pourbaix diagram, see Figure 2-43) (Bertolini, et al., 2004).

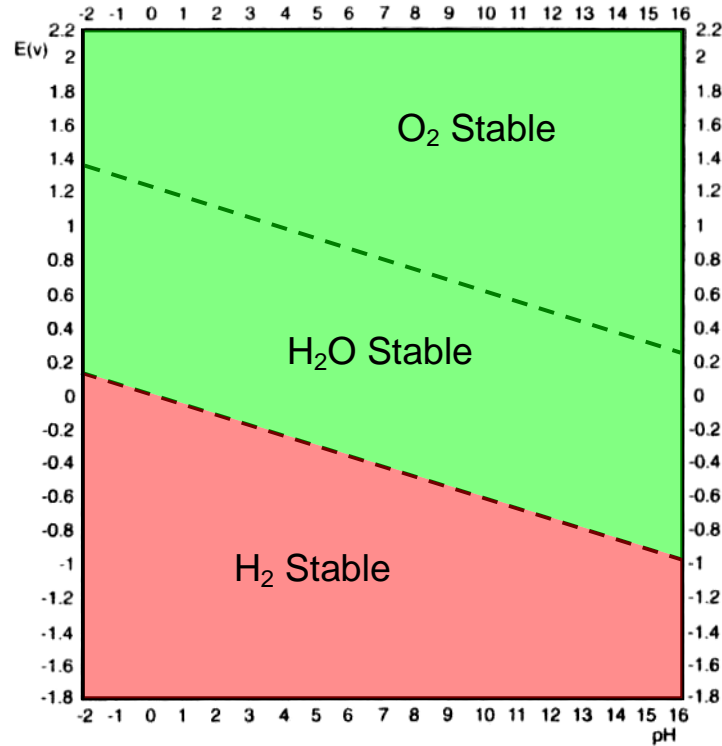


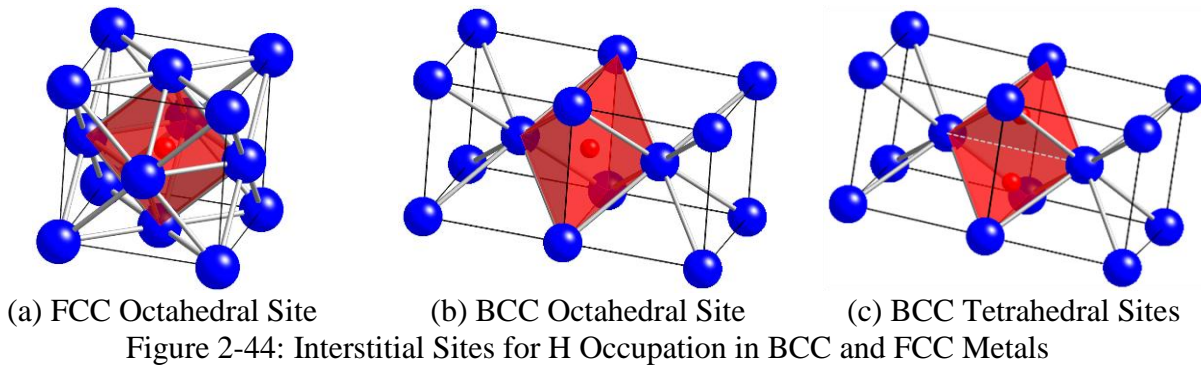
Figure 2-43: Regions of Stability for Cathodic Reactions (from (Pourbaix, 1974) and (Bertolini, et al., 2004))

Atomic hydrogen may be present at the surface by reduction of water or hydrogen cations in neutral and acidic solutions (Landolt, 2007), respectively:



Because hydrogen exhibits a +1 oxidation state, it will normally react to form covalently bonded molecular hydrogen by $H + H \rightarrow H_2$. However, reactions to form molecular hydrogen may be slow, allowing atomic hydrogen present on the surface of the metal to penetrate the lattice before reaction to form H_2 (Skorchelletti, 1976). Reaction times may be significantly slowed by the presence of doping agents in the alloy such as S, As, Sb, and P. The formation of expansive hydrides by reaction with Ti, Zn, Hf, V, Nb, Ta, and Pd are also mechanisms for HE (Jones, 1996), but these elements are not typically present in great quantities in alloys used for civil engineering applications.

Once atomic hydrogen has entered the lattice, it will occupy interstitial sites and other regions of high porosity, such as grain boundaries and defect / dislocation regions. Interstitial sites for H occupation in BCC and FCC metals are shown in Figure 2-44 below.



With atomic hydrogen present in the crystal lattice, reaction to form molecular H_2 results in expansion and dilation of the lattice as the larger molecule is formed at interstitial and defect sites (Jones, 1996, Skorchelletti, 1976). Dilation of the lattice from HE results in weakening of metallic bonding, resulting in a structure which is susceptible to crack formation upon tensile loading.

FCC structures with larger interstitial sites and higher ductility are generally less affected than BCC metals which have lower H solubility and restricted slip capabilities. Cracks formed by HE are generally transgranular, as the lattice structure itself is most affected by the formation of molecular H_2 (Landolt, 2007). An example of transgranular HE induced cracking in prestressing steel is shown in Figure 2-45.

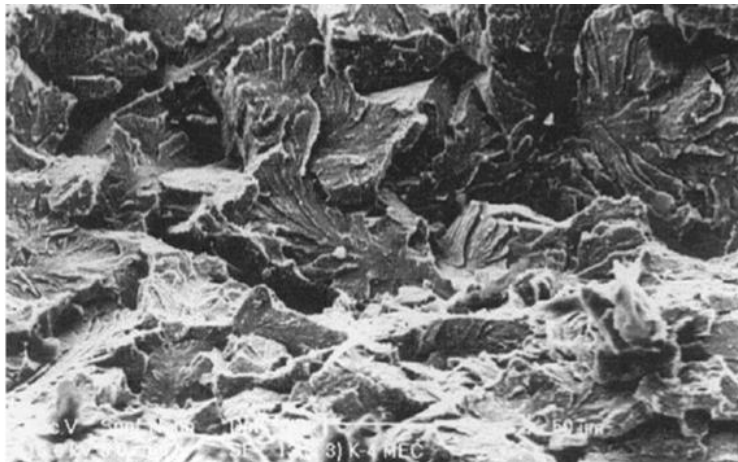


Figure 2-45: Transgranular HE Fracture of Prestressing Steel (Schroeder, et al., 2003)

2.3.5 Mechanisms of SCC and HE Crack Formation

The degradation of a metal caused by SCC and HE can be explained by many mechanisms. While an in depth examination of each possible mechanism is beyond the scope of this report, Figure 2-46 shows 6 accepted mechanisms which may lead to SCC and HE cracking.

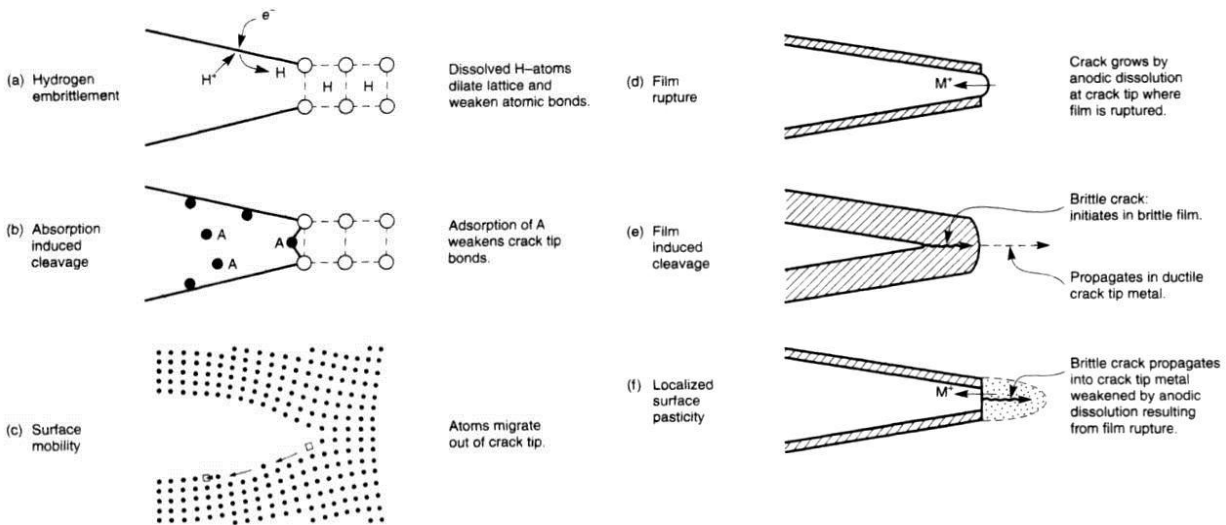


Figure 2-46: Proposed SCC and HE Crack Propagation Mechanisms (Jones, 1996)

Most popular mechanisms used to describe SCC include electrochemical dissolution at the crack tip in conjunction with mechanical fracture to model crack propagation through the metal. Cracks initiate at preferential sites of corrosion, such as corrosion pits, grain boundaries, slip steps, and other defects or dislocations present on the surface (Jones, 1996, Landolt, 2007). Anodic dissolution of metal occurs at the crack tip with large cathodic areas forming on the inner faces of the crack as the crack progresses through the metal. In addition to anodic dissolution, stress concentrations and degradation of bonding at the crack tip / corrosion pit lead to brittle mechanical fracture in front of the crack (Singh, 2008). Other mechanisms, including film rupture at slip lane intersections shown in Figure 2-47, may lead to accelerated dissolution and crack velocity in the metal.

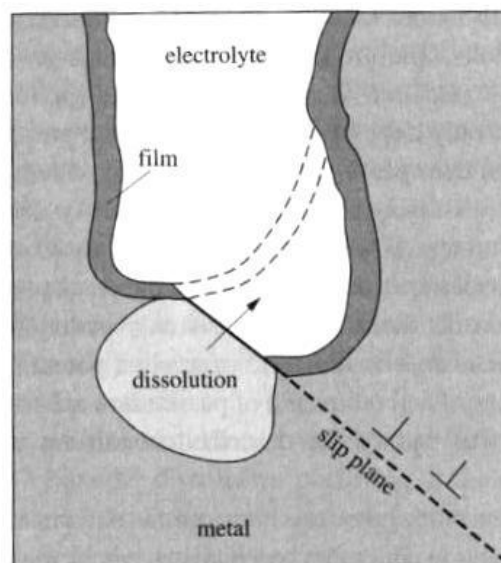


Figure 2-47: Film Rupture of Passive Film at Slip Plane Intersection (Landolt, 2007)

Degradation caused by HE is mainly due to bond weakening at the crack tip from the buildup of H_2 . As H_2 forms in the lattice, the structure is dilated and bonds between adjacent metals atoms weaken. In addition to weakening bonds, regions in front of the crack tip may be brittle due to the dilation causing solution hardening of the metal, increasing its tendency to fracture in a brittle manner (Nuernberger, 2002).

2.3.6 SCC and HE in Prestressing Steels

With an applied tensile stress of 55 to 75% ultimate tensile strength, cracking and embrittlement caused by SCC and HE may result in catastrophic failures of prestressed concrete structures with little to no warning. Therefore, prestressing steels should be carefully evaluated to determine their susceptibility to SCC and HE. Previously used quenched and tempered prestressing steels showed significant SCC and HE problems and resulted in a switch to cold drawn production. Currently used cold drawn and stabilized prestressing steels have shown exceptional resistance to SCC and HE (Lewis, 1969, Mietz, 2000).

Many test methods are available to determine resistance to SCC and HE, most focusing on HE and hydrogen induced stress corrosion cracking (HI-SCC). The most popular tests are those developed by the International Federation of Prestressed Concrete (FIP test) and Deutsches Institut für Bautechnik (DIBt test) (Elices, et al., 2008). Both tests utilize a wire specimen tested at 80% ultimate tensile strength while exposed to a corrosion solution. A typical constant load experimental setup used for FIP and DIBt testing is shown in Figure 2-48. Many alterations to the setup shown in Figure 2-48 may be used, including actuators for loading, various frame configurations, and instrumentation to monitor times to failure. The FIP test, developed in 1978, uses a 20% aqueous solution of ammonium thiocyanate (NH_4SCN) maintained at $50^\circ C$. The DIBt test, developed in 1982, uses what is thought to be a more “realistic” test solution of 0.014M KCl, 0.052M K_2SO_4 , and 0.017M KSCN maintained at $50^\circ C$. The main purpose of Thiocyanate compounds is to promote the uptake of hydrogen into the lattice, accelerating damage caused by HE and HI-SCC (Hartt, et al., 1993).

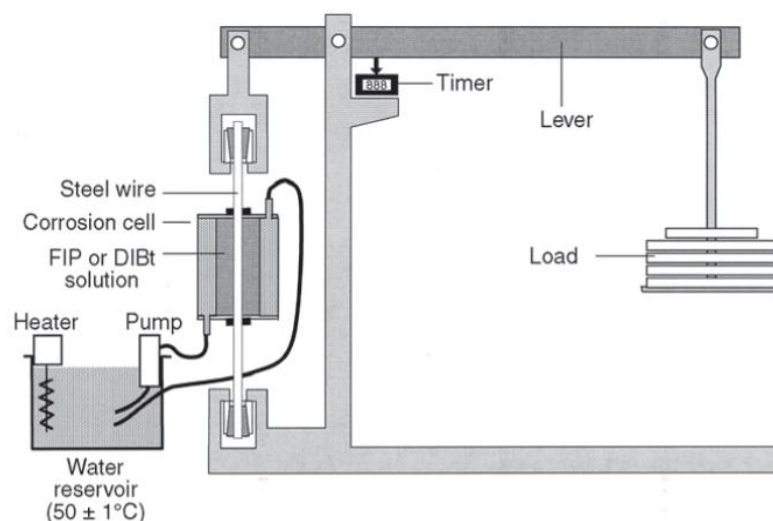


Figure 2-48: Experimental Setup Used for FIP and DIBt Tests (Elices, et al., 2008)

Most researchers state that the DIBt test is much more realistic than the solution exposure used for FIP testing, which is seen as an extremely conservative accelerated test procedure (Elices, et al., 2008, Schroeder, et al., 2003). The main disadvantage of DIBt testing is that it can take weeks to years for fracture of the wire specimen to occur, while FIP testing typically only requires a few hours to a few days before fracture occurs (Elices, et al., 2008). Acceptable environmentally induced cracking (EIC) behavior of a prestressing steel is indicated by times to failure greater than 2000 hours in the DIBt test and 10 hours for the FIP test (no clear delineation for FIP test though). However, it should be noted that good correlation has been found between the results of FIP and DIBt testing. Figure 2-49 shows the results of both test methods performed on prestressing steel of varying tensile strength. Note that as tensile strengths rise above 1900 MPa and DIBt values drop below 2000 hours, FIP times to failure drop accordingly. Also, recent work to compare the two tests has shown that fracture surfaces of wires used in both tests, shown in Figure 2-50, show the same behavior.

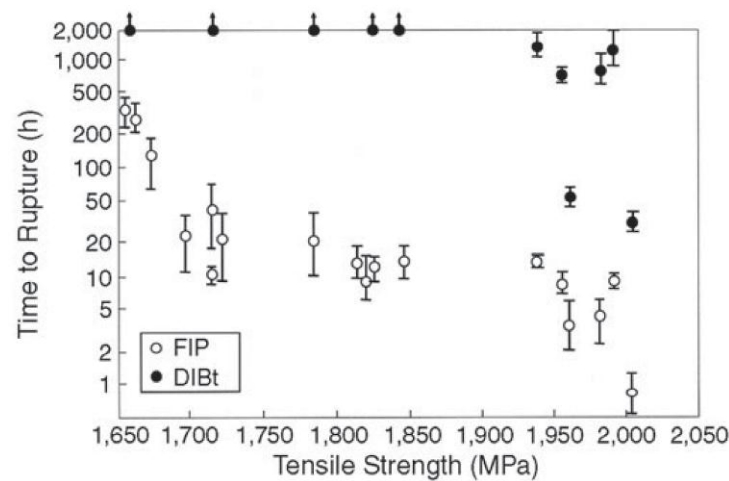
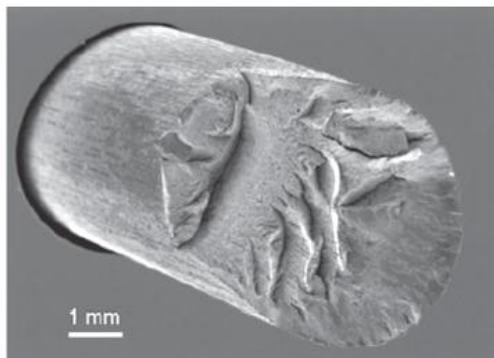
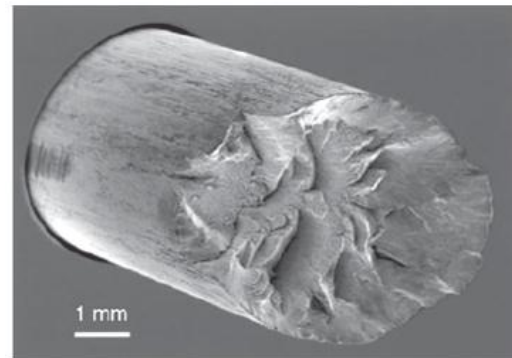


Figure 2-49: Times to Failure vs. U.T.S. Using FIP and DIBt Tests (Elices, et al., 2008)



(a) FIP Fracture Surface



(b) DIBt Fracture Surface

Figure 2-50: SEM Micrograph of FIP and DIBt Test Fracture Surfaces (Elices, et al., 2008)

Both the FIP and DIBt tests have been used with success to conservatively determine the susceptibility of prestressing steels to EIC. However, many researchers state that both the FIP and DIBt tests do not accurately represent an accurate environment for prestressing steels embedded in concrete (Elices, et al., 2008, Mietz, 2000, Schroeder, et al., 2003). Therefore, many recent experiments have begun to utilize more modern EIC testing techniques, including

slow strain rate testing (SSRT) and fracture mechanics testing. These new test methods are being conducted in more accurate environments modeled after concrete pore solutions with addition of Cl^- and in some cases thiocyanate to promote hydrogen uptake (Hartt, et al., 1993, Schroeder, et al., 2003).

In general, research has shown that cold drawn eutectoid prestressing steels used in current construction are resistant to EIC given proper construction practices (Nuernberger, 2002). While it has been shown that EIC is possible when tested in the lab, very few failures in actual structures have been attributed to EIC, with most being caused by the general and pitting corrosion mechanisms. However, newly developed alloys for use as prestressing steels should be thoroughly evaluated for their EIC resistance. A good summary of the possible effects which may initiate EIC in prestressing steels is given by Dr. Ulf Nürnberg, noted expert on EIC of prestressing steels, who states that:

“Major issues which strongly influence the level of durability actually achieved are insufficient design (poor construction), incorrect execution of planned design (poor workmanship), unsuitable mineral building materials (e.g. concretes, grouts, and mortars), unsuitable post-tensioning components (e.g. anchorages, ducts), including prestressing steels. Insufficient design and incorrect work execution will mean that the necessary corrosion control is not guaranteed from the beginning in all areas or that as a result of natural influences (i.e. carbonation and Cl^- ingress) it will get lost soon within the time frame of the originally anticipated life time. Unsuitable materials or inappropriate substances in materials will further corrosion and/or stress corrosion cracking. Sensitive prestressing steels cannot withstand even inevitable building-site influences and will fail while in use (Nuernberger, 2002).” - Dr. Ulf Nürnberg

2.3.7 Strength and Fatigue Resistance Degradation

The mechanical properties and performance of prestressing steels have been shown to be degraded when corrosion occurs on the steel's surface. Of particular concern is pitting corrosion, which may lead to losses in strength and fatigue resistance. Relatively little research has been performed in this area, but it is one which deserves attention. Figure 2-51 shows the deterioration of tensile strength, ductility, and fatigue loading (for $N = 2 \times 10^6$ cycles) versus the depth of localized corrosion present on the surface of the prestressing steels (Nuernberger, 2002). Note in Figure 2-51, it takes approximately a 0.5 to 0.6mm depth of localized corrosion for fracture to occur in an 1860MPa prestressing steel stressing to 70% ultimate tensile strength. Also, a depth of 0.2mm of localized corrosion may decrease fatigue resistance from approximately 400MPa to 100MPa, a 75% reduction. While the large reduction in fatigue resistance seems to be a “dangerous” concern, in most cases large loads (e.g. heavy trucks on bridges) will occur at very low frequencies, with only small vibrations (from wind and light vehicles) occurring at high frequencies (Nuernberger, 2002).

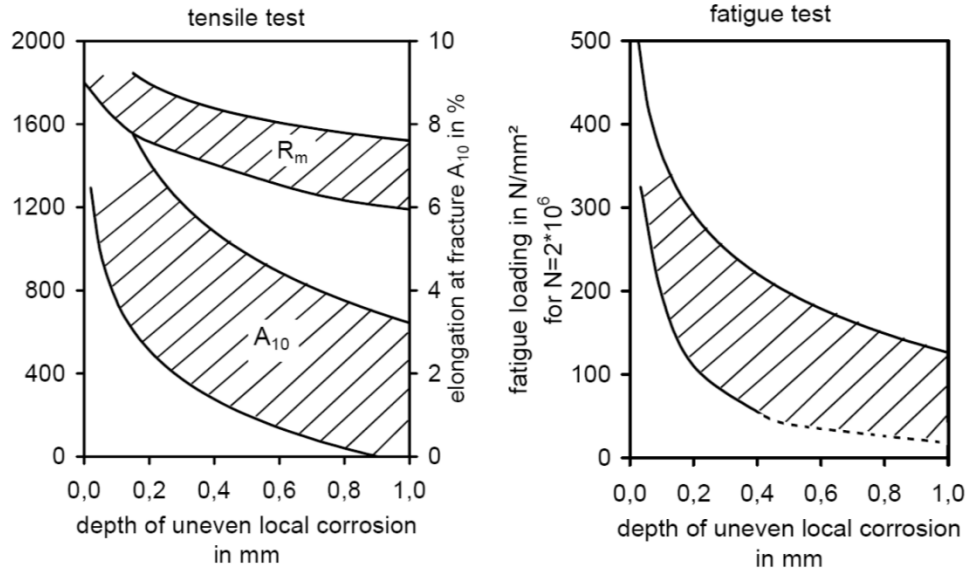


Figure 2-51: Deterioration of Mechanical Performance by Corrosion (Nuernberger, 2002)

In the same research, Professor Nürnberg also tested the effect of surface corrosion on EIC using the FIP. Figure 2-52 shows the time to failure of FIP prestressing steel test specimens when local surface corrosion has occurred on the surface. Localized corrosion depths of as little as 0.2mm were found to reduce times to failure by up to 75%.

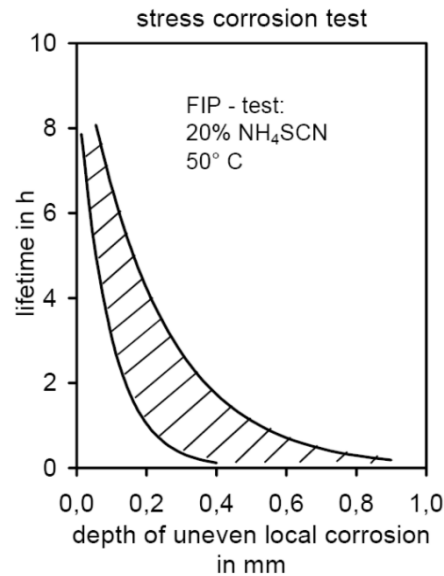


Figure 2-52: Effect of Surface Corrosion on FIP Times to Failure (Nuernberger, 2002)

2.4 References

- Ahern, M. E. (2005). "Design and Fabrication of a Compact Specimen for Evaluation of Corrosion Resistance of New Post-Tensioning Systems." MS Thesis, University of Texas at Austin, Austin, TX.
- Ahmad, S. (2003). "Reinforcement Corrosion in Concrete Structures, its Monitoring and Service Life Prediction - A Review." *Cement & Concrete Composites*, V. 25, pp. 459-471.
- Ann, K. Y., and Song, H.-W. (2007). "Chloride Threshold Level for Corrosion of Steel in Concrete." *Corrosion Science*, V. 49 (11), pp. 4113-4133.
- ASTM A416 / A416M - 06 Standard Specification for Steel Strand, Uncoated Seven-Wire for Prestressed Concrete. American Society of Testing and Materials, West Conshohocken, PA.
- Basheer, L., Kropfb, J., and Clelandc, D. J. (2001). "Assessment of the durability of concrete from its permeation properties: a review." *Construction and Building Materials*, V. (15), pp. 93-103.
- Bertolini, L., Elsener, B., Pedferri, P., and Polder, R. (2004). *Corrosion of Steel in Concrete*, Wiley-VCH.
- Boddy, A., Bentz, E., Thomas, M. D. A., and Hooton, R. D. (1999). "An overview and sensitivity study of a multimechanistic chloride transport model." *Cement & Concrete Research*, V. (29), pp. 827-837.
- Bohni, H. (2005). *Corrosion in Reinforced Concrete Structures*, Woodhead Publishing Ltd.
- Broomfield, J. P. (2007). *Corrosion of Steel in Concrete*, Taylor and Francis Group.
- Chandler, K. A. (1984). *Marine and Offshore Corrosion*, Butterworth & Company Ltd.
- Devine, T. M. (1997). "Corrosion Science." University of California Berkeley.
- Edvardsen, C. (1999). "Water Permeability and Autogenous Healing of Cracks in Concrete." *ACI Materials Journal*, V. 96 (4), pp. 448-456.
- Elices, M., Cabllero, L., Valiente, A., Ruiz, J., and Martin, A. (2008). "Hydrogen Embrittlement of Steel for Prestressing Concrete: The FIP and DIBt Tests." *CORROSION* V. 64 (2), pp. 164-174.
- Federal Highway Administration (2006). "Status of the Nation's Highways, Bridges, and Transit: Report to Congress." FHWA, 436.
- FIP, C.-. (1992). "Design Guide for Durable Concrete Structures." T. T. Publishers, ed., Comité Euro-International du Béton - Fédération Internationale du Béton, Lausanne, Switzerland.

- Glass, G. K., and Buenfeld, N. R. (2000). "The influence of chloride binding on the chloride induced corrosion risk in reinforced concrete." *Corrosion Science*, V. (42), pp. 329-344.
- Griggs, R. D. (1987). "Structural Concrete in the Georgia Coastal Environment." GDOT, Atlanta, GA.
- Hamilton III, H. R. (2007). "St. George Island Bridge Pile Testing." FDOT.
- Hansson, C. M. (2005). "Effects of High Performance Concrete on Corrosion of Reinforcement." PCA, ed., Portland Cement Association, Skokie, IL.
- Hansson, C. M., Poursaei, A., and Laurent, A. (2006). "Macrocell and Microcell Corrosion of Steel in Ordinary Portland Cement and High Performance Concretes." *Cement and Concrete Research*, V. 36, pp. 2098-2102.
- Hartt, W. H., Kumria, C. C., and Kessler, R. J. (1993). "Influence of Potential, Chlorides, pH, and Precharging Time on Embrittlement of Cathodically Polarized Prestressing Steel." *CORROSION*, V. 49 (5).
- Hartt, W. H., and Nam, J. (2004). "Critical Parameters for Corrosion Induced Deterioration of Marine Bridge Substructures in Florida." Florida Atlantic University, 69.
- Hartt, W. H., Powers, R. G., Leroux, V., and Lysogorski, D. K. (2004). "Critical Literature Review of High-Performance Corrosion Reinforcements in Concrete Bridge Applications." Florida Atlantic University, 53.
- Hartt, W. H., Powers, R. G., Lysogorski, D. K., Liroux, V., and Virmani, Y. P. (2007). "Corrosion Resistant Alloys for Reinforced Concrete." Florida Atlanta University, 135.
- Heide, N. t. (2005). "Crack healing in hydrating concrete." M.S. , Delft University of Technology, Delft, Netherlands.
- Hope, B. B., and Nmai, C. K. (2001). "Corrosion of Prestressing Steels." American Concrete Institute Committee 222, 43.
- Hope, B. B., and Nmai, C. K. (2001). "Protection of Metals in Concrete Against Corrosion." American Concrete Institute Committee 222, 41.
- Matco Inc. (2008). "Pier Cap Spalling of Cover Concrete." <http://www.matcoinc.com/files/New/Home/WhatsNew/Bridge3.jpg>
- Isেকে, B. (1982). "Collapse of the Berlin Congress Hall Prestressed Concrete Roof." *Materials Performance*, V. 21 (12), pp. 36-39.
- Jones, D. A. (1996). *Principles and Prevention of Corrosion*, Prentice Hall.
- Knudson, A., and Skovsgaard, T. (1999). "The Optimal Use of Stainless Steel Reinforcement in Concrete Structures." Ramboll Arminox, 8.

- Kreyszig, E. (1967). *Advanced Engineering Mathematics*, John Wiley & Sons, Inc., New York, NY.
- Kurtis, K. E. (2007). "Materials Science of Concrete." Georgia Institute of Technology.
- Kurtis, K. E., and Mehta, K. "A Critical Review of Deterioration of Concrete Due to Corrosion of Reinforcing Steel." *Proc., Durability of Concrete*, ACI, 535-554.
- Landolt, D. (2007). *Corrosion and Surface Chemistry of Metals*, EPFL Press, Lausanne, Switzerland.
- Lewis, A. F. G. (1969). *Steel for Prestressing*, Lowe & Brydone Limited, London, UK.
- Manera, M., Vennesland, Ø., and Bertolini, L. (2008). "Chloride Threshold for Rebar Corrosion in Concrete with Addition of Silica Fume." *Corrosion Science*, V. 50 (2), pp. 554-560.
- Matta, Z. G. (1993). "More Deterioration of Concrete in the Arabian Gulf." *Concrete International*, V. November, pp. 50-51.
- Mehta, P. K. (1991). *Corrosion in the Marine Environment*, Elsevier Applied Science.
- Mehta, P. K., and Monteiro, P. J. M. (2006). *Concrete: Microstructure, Properties, and Materials*, McGraw-Hill Companies Ltd.
- Mietz, J. (2000). "Investigations on Hydrogen-Induced Embrittlement of Quench and Tempered Prestressing Steels." *Materials and Corrosion*, V. 51, pp. 80-90.
- Mietz, J., Elsener, B., and Polder, R. (1997). *Corrosion of Reinforcement in Concrete - Monitoring, Prevention, and Rehabilitation*, The Institute of Materials, London, UK.
- Morrison, S. R. (1990). *The Chemical Physics of Surfaces*, Plenum Press, New York, NY.
- NACE (2007). "Corrosion of Concrete Pier."
<http://www.nace.org/nace/content/library/photogallery/showLarge.asp?PhotoID=145>
- NACE (2008). "How Much Can a Bridge Take?", National Association of Corrosion Engineers.
- Nawy, E. G. (2000). *Prestressed Concrete - A Fundamental Approach*, Prentice Hall, Upper Saddle River, NJ.
- Nuernberger, U. (2002). "Corrosion Induced Failures of Prestressing Steels." *Otto-Graf Journal*, V. 13.
- Nuernberger, U. (1995). *Korrosion und Korrosionsschutz im Bauwesen*, GmbH, Berlin.
- PCA (2007). "Corrosion of Embedded Metals." Portland Cement Association.
- Perez, N. (2004). *Electrochemistry and Corrosion Science*, Kluwer Academic Publishers, Norwell, MA.

- Pourbaix, M. (1974). *Atlas of Electrochemical Equilibria in Aqueous Solutions*, NACE International, Houston, TX.
- Revie, R. W. (2000). *Uhlig's Corrosion Handbook*, John Wiley & Sons Inc.
- Rodriguez, O. G., and Hooton, R. D. (2003). "Influence of Cracks on Chloride Ingress into Concrete." *ACI Materials Journal*, V. 100 (2), pp. 120-126.
- Rourke, D. (2008). "Galvanized Rebar Resource Center." <http://www.galvanizedrebar.com/>
- Sandberg, P., Tang, L., and Andersen, A. (1998). "Recurrent Studies of Chloride Ingress in Uncracked Marine Concrete at Various Exposure Times and Elevations." *Cement and Concrete Research*, V. 28 (10), pp. 1489-1503.
- Schiessl, P., and Raupach, M. (1997). "Laboratory Studies and Calculations on the Influence of Crack Width on Chloride-Induced Corrosion of Steel in Concrete." *ACI Materials Journal*, V. 94 (1), pp. 56-62.
- Schroeder, R. M., and Müller, I. L. (2003). "Stress Corrosion Cracking and Hydrogen Embrittlement Susceptibility of an Eutectoid Steel Employed in Prestressed Concrete." *Corrosion Science*, V. 45, pp. 1969-1983.
- Schweitzer, P. A. (2003). *Metallic Materials: Physical, Mechanical, and Corrosion Properties*, Marcel Dekker, Inc., New York, NY.
- Singh, P. M. (2008). "Environmental Degradation." Georgia Institute of Technology.
- Skorchelletti, V. V. (1976). *Theory of Metal Corrosion*, Israel Program for Scientific Translations, Jerusalem, Israel.
- Suryavanshi, A., Scantlebury, J. D., and Lyon, S. B. (1996). "Mechanism of Friedel's Salt Formation in Cements Rich in Tri-Calcium Aluminate." *Cement & Concrete Research*, V. 26 (5), pp. 717-727.
- Thangavel, K., and Rengaswamy, N. S. (1998). "Relationship Between Chloride/Hydroxide Ratio and Corrosion Rate of Steel in Concrete." *Cement & Concrete Composites*, V. 20, pp. 283-292.
- Thomas, D. (2003). "Fundamentals of Electrochemistry." University of Guelph.
- Thomas, M. D. A., Bamforth, P. B., and Banerjee, M. K. (1999). "Modelling chloride diffusion in concrete effect of fly ash and slag." *Cement & Concrete Research*, V. (29), pp. 487-495.
- Wierig, H. J. (1984). "Long-Time Studies on the Carbonation of Concrete Under Normal Outdoor Exposure." *Durability of Concrete Structures Under Normal Outdoor Exposure*, RILEM, Hannover.

Wight, J. K. (2005). "ACI 318-05 Building Code Requirement for Structural Concrete and Commentary." American Concrete Institute Farmington Hills, MI.

Young, J. F., Mindess, S., Gray, R. J., and Bentur, A. (1998). *The Science and Technology of Civil Engineering Materials*, Prentice Hall, Upper Saddle River, NJ.

Zumdahl, S. S. (2000). *Chemistry*, Houghton Mifflin Company, Boston, MA.

3. Background – Concrete for Marine Piles

3.1 Deterioration Mechanisms of Concrete Piles in Marine Environments

Concrete structures exposed to marine environments are subjected to multiple deterioration mechanism. Prestressed concrete piling in coastal exposures is subjected to biological, physical, and chemical attack. The reinforcement steel, aggregate, and paste all have the potential for degradation under the environmental conditions present. Figure 3.1 shows the typical degradation mechanisms that occur in marine environments. Chloride ingress and chloride induced corrosion is discussed in section 3.2, carbonation of concrete and carbonation induced corrosion in section 3.3, sulfate attack of concrete in section 3.4, and biological attack of concrete in section 3.5.

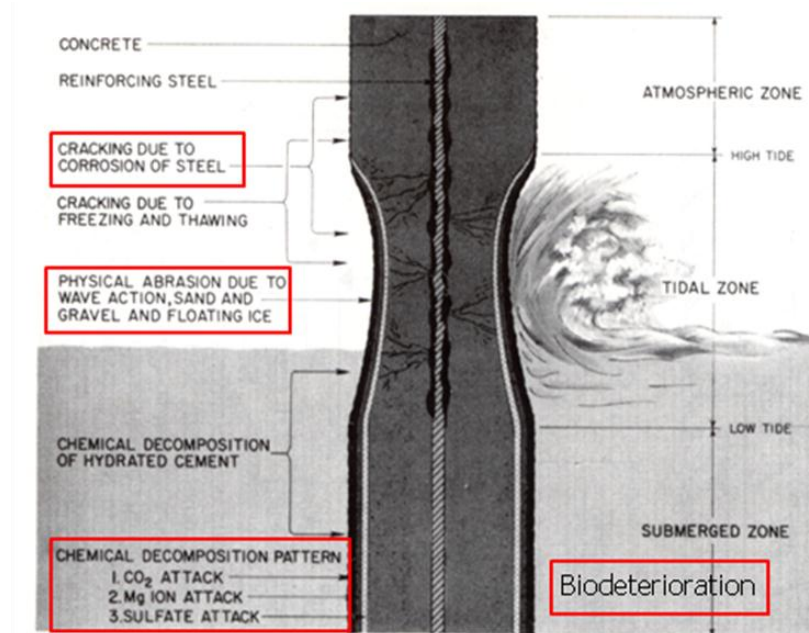


Figure 3.1: Typical degradation mechanisms in coastal concrete piling (Mehta, 1991)

3.2 Chlorides in Concrete

The ingress of chlorides into reinforced concrete is an important concern for the durability of prestressed concrete piles. The rate of ingress and concentration of chlorides at the steel reinforcement depth can dictate the usable service lives of structures by induced damage by the corrosion of prestressing steel.

3.2.1 Sources of Chlorides

Chlorides can be introduced into concrete from either internal or external sources. Internal sources of chlorides could include the use of sea water for mixing water, dredged aggregate, aggregate washed with sea water, and chloride containing admixtures (Bertolini, et. al., 2004). External chlorides typically occur from environmental factors. Typical external sources are from the ingress of seawater in marine environments, and from the use of deicing salts containing chlorides in colder climates (Bertolini, et. al., 2004). Additionally, concrete may be exposed to chlorides if used in industrial applications where chemicals may contain chlorides, like dry-cleaning facilities, paper mills, and aquariums (Bertolini, et. al., 2004).

3.2.2 Transport Mechanisms

External chlorides ingress into concrete occurs through several transport mechanisms. Three primary forms of transport occur in concrete: diffusion, permeation, and absorption (Stanish, et. al, 1997). Additionally, the binding of chlorides can affect these transport mechanisms (Bertolini, et. al., 2004).

3.2.2.1 Chloride Diffusion

The primary form of ingress is through diffusion, which is the flow of ions due to a concentration gradient. The behavior and modeling of chloride diffusion is discussed in Section 2.2.2.3.

3.2.2.2 Chloride Binding

Within the concrete, chlorides exist in a free or uncombined form and in bound forms, where they may combine with existing hydration products or unhydrated cementitious phases. The bound chlorides do not contribute to corrosion initiation in concrete (Mohammed and Hamada, 2003). In the bound form, the most common product formed is Friedel's salt $[\text{Ca}_2\text{Al}(\text{OH})_6\text{Cl}\cdot 2\text{H}_2\text{O}]$. The extent of chloride binding that can occur in a mix depends upon the cementitious materials contained in the mix (Mohammed and Hamada, 2003).

3.2.2.3 Chloride Permeation

Permeation occurs due to the presence of a pressure gradient. If an applied hydraulic head exists on one face of the concrete and chlorides are present, they may permeate into the concrete under the pressure gradient. This mechanism requires a large pressure head to cause the flow of chlorides to the depth of reinforcement (Stanish, et. al., 1997).

3.2.2.4 Chloride Absorption

As a concrete surface is exposed to the environment, it will undergo wetting and drying cycles. When water, potentially containing chlorides, encounters a dry surface, it will be drawn into the pore structure through capillary suction. Absorption is driven by moisture gradients, and

for wetting and drying cycles the depth of drying is small. Therefore, absorption is not able to bring chlorides to the depth of reinforcement for a good quality concrete (Stanish, et. al., 1997).

3.2.3 Effects of Mix Design on Chloride Durability

Alterations to concrete mix design can drastically affect the chloride ingress properties. Polder (1995), Luping (1992, 1995), Bamforth (1993), Collepardi (1972), Diab (1988), Dhir (1990), and Johnson (1996) each investigated the effect of varying water-to-cement ratios on the diffusion coefficient of concrete. The results of these investigations are shown in Figure 3.2. The data shows that the diffusion coefficient increases with the water-to-cement ratio. The large spread of values on the graph for the same water to cement ratio is due to differences in the mix designs, including aggregate type and content, type of cement used, and age of curing before exposure.

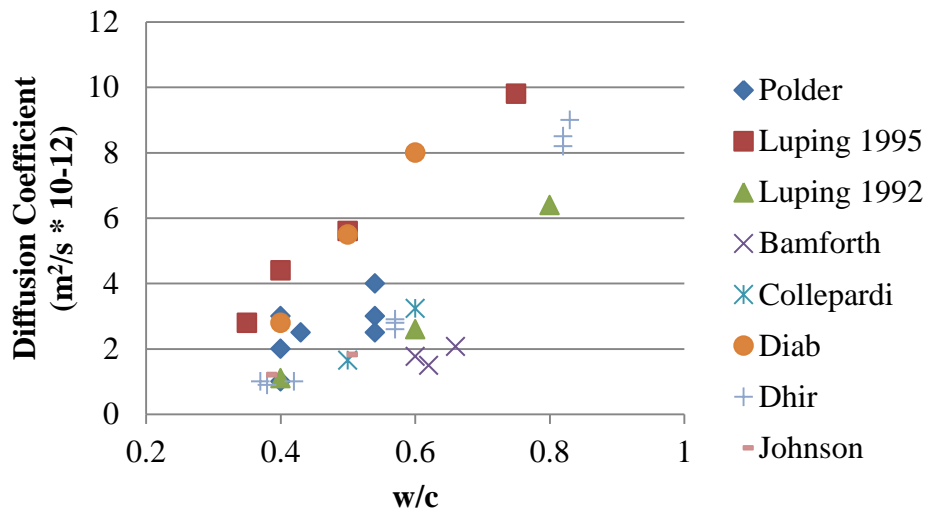


Figure 3.2: Effect of water to cement ratio on diffusion coefficient in Portland Cement Concrete

The effect of age of exposure on the diffusion coefficient was investigated by Polder (1995), Luping (1992), Kanaya (1998), Pedersen (1998), and Mangat (1994), and the results of their studies are shown in Figure 3.3. The data suggests that the diffusion coefficient decreases as the chloride exposure is initiated at later concrete ages. Stanish (2003) developed Eq. 3.1 to predict the diffusion coefficient of concrete at any age given that it is known through testing for at least one age.

$$D_{avg} = D_{ref} \left(\frac{t_{ref}}{t_{eff}} \right)^m \quad (\text{Eq. 3.1})$$

Where,

D_{avg} = average diffusion coefficient at t_{eff}

D_{ref} = diffusion coefficient at reference age
 t_{ref} = reference age of concrete
 t_{eff} = effective age of concrete
 m = coefficient based upon mix parameters
 = 0.32 for OPC, 0.66 for 25% fly ash replacement

Figure 3.4 shows Stanish's estimator equation plotted with the experimental results for diffusion coefficients of OPC concrete mixes. The data suggests the estimator equation provides an accurate estimate of how the diffusion coefficient varies with time. The decreased diffusion coefficient with time suggests that longer curing periods would lead to decreased rates of chloride ingress.

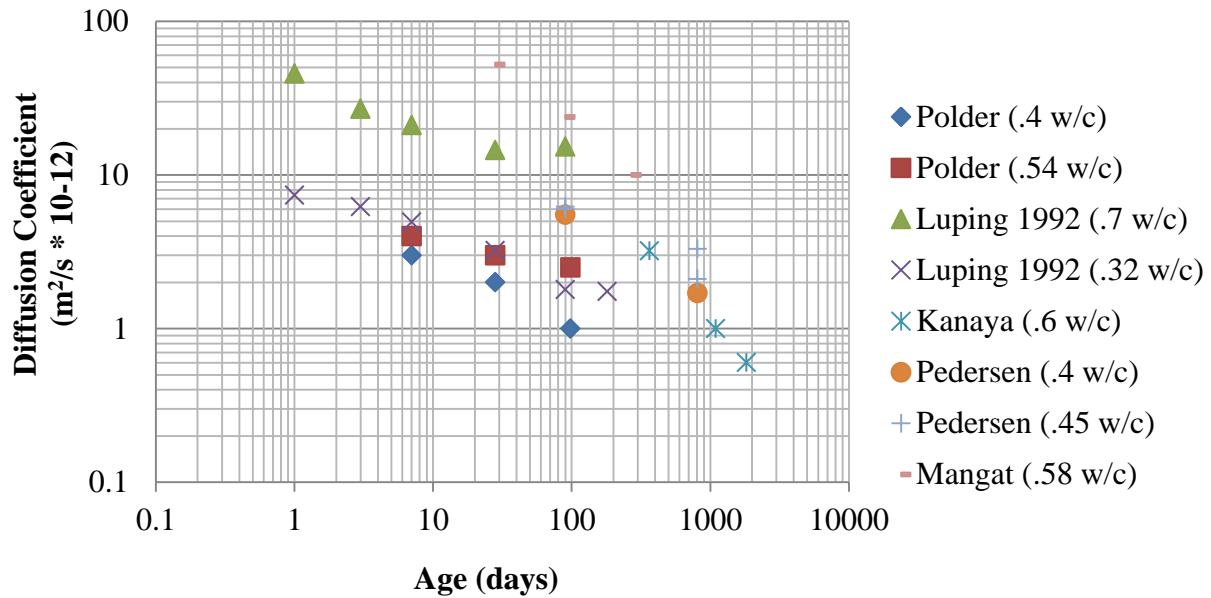


Figure 3.3: Effect of age of exposure on diffusion coefficient in OPC Concrete

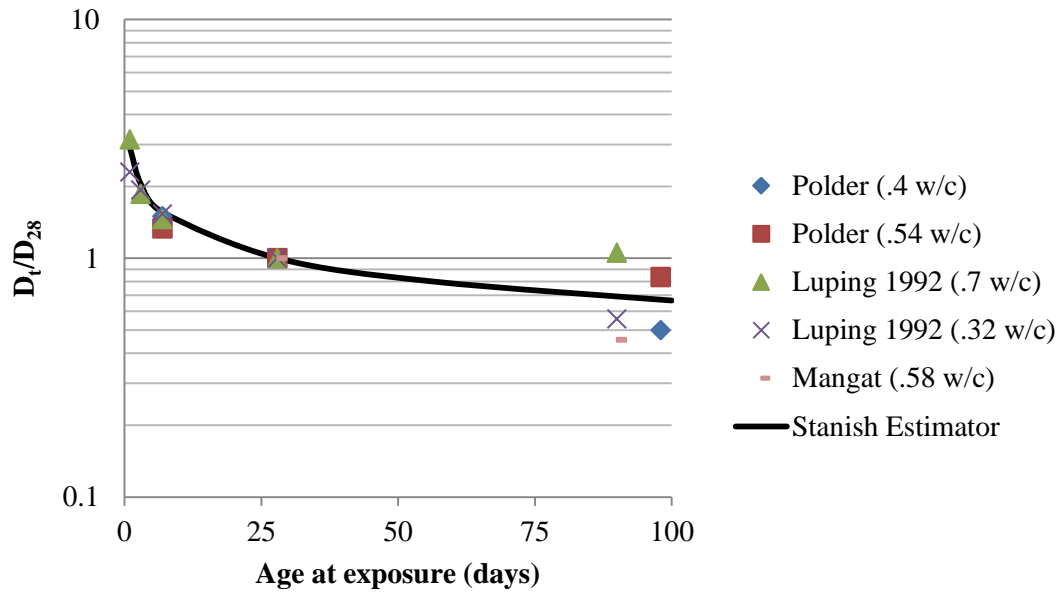


Figure 3.4: Comparison of time dependent diffusion coefficients with estimator equation

The effect of using supplementary cementitious materials (SCMs) on the diffusion coefficient has been investigated by Bentz (2000), Basheer (2001), and Thomas (1999). The results of the Basheer study are shown in Figure 3.5. The results show that the use of SCMs decreases the diffusion coefficient, with fly ash, slag, and metakaolin having larger effects than silica fume. This result is in contradiction to the research performed by Bentz. Bentz's research, which is shown in Figure 3.6, showed that the diffusion coefficient with 10% silica fume replacement was an order of magnitude smaller than the OPC mix with the same parameters.

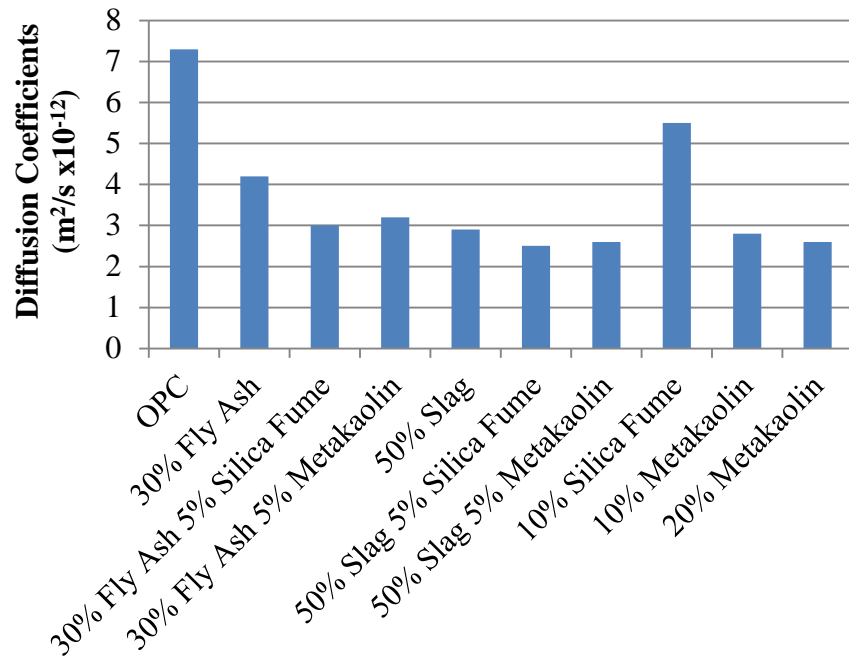


Figure 3.5: Effect of SCM's on diffusion coefficient

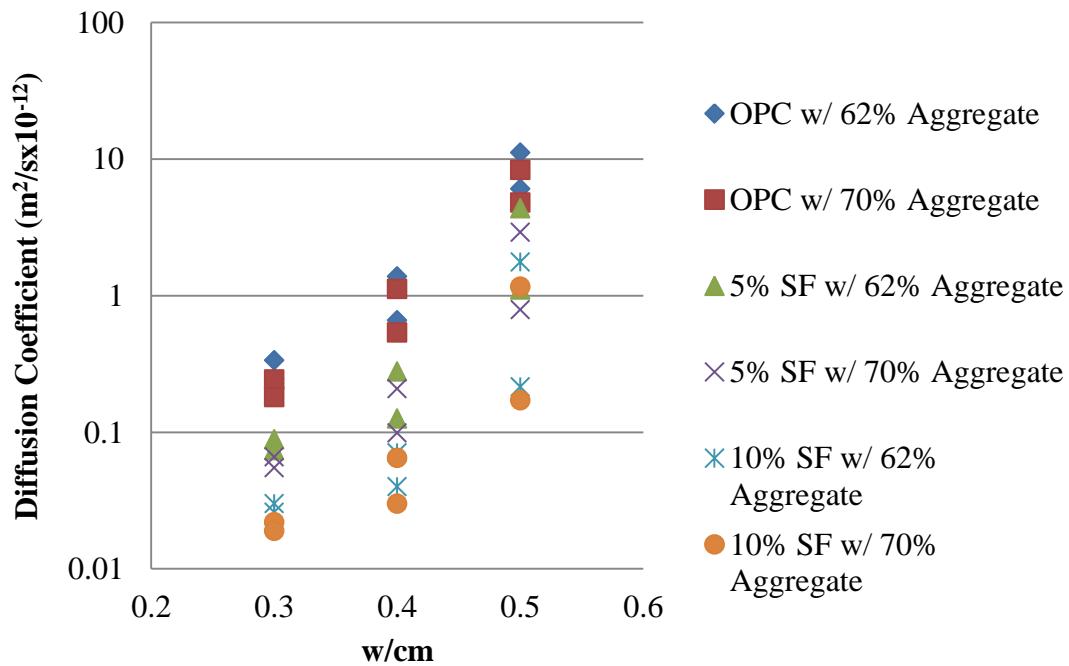


Figure 3.6: Effect of silica fume content on diffusion coefficient

3.3 Carbonation of Concrete

Carbonation of concrete can occur due to the diffusion of carbon dioxide through the pores of concrete. Carbonation of concrete can cause strength loss of the concrete and initiate corrosion of reinforcing steel (as discussed in section 2.2.1). Carbonation of concrete leads to the depletion of calcium hydroxide, which causes the decrease in pH, and can lead to a loss of calcium silicate hydrate (C-S-H), which is the primary strength giving component of hydrated cement paste (Neville, 1997). The decreased pH can lead to the initiation of general corrosion of reinforcement. The rate of carbonation is affected by environmental factors (humidity, temperature, and CO₂ concentration) and concrete properties (Bertolini, et. al, 2004).

The effect of humidity on carbonation rate is shown in Figure 3.7. The maximum carbonation rate has been shown by Papadakis (1991) and Bertolini (2004) to occur at approximately 60-70% relative humidity. An increase in temperature will also cause the carbonation rate to increase (Bertolini, et. al., 2004).

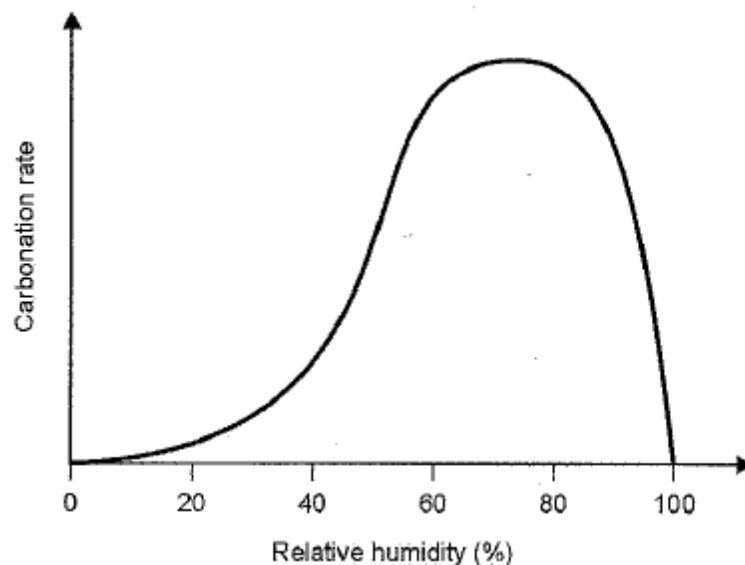


Figure 3.7: Effect of relative humidity on carbonation rate (Bertolini, et. al., 2004)

The permeability of concrete has a large influence on the rate of carbonation. Decreasing the water to cement ratio (w/c) can vary the permeability by orders of magnitude (Papadakis, et. al., 1991). Figure 3.8 shows the effect of water to cement ratio on depth of carbonation. Also, the binder composition has a large influence on the carbonation resistance. The use of SCM's may decrease the initial pH of the concrete, but decreases the permeability (Bertolini, et. al., 2004). The effect of binder composition on carbonation depth is shown in Figure 3.9.

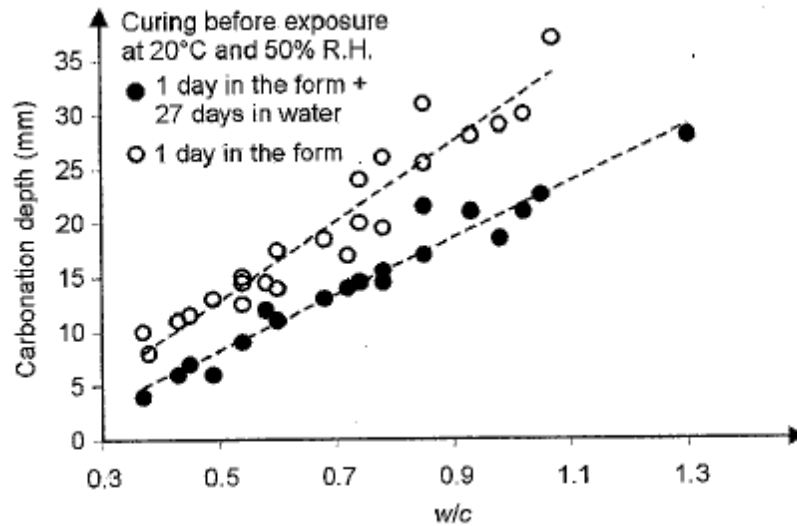


Figure 3.8: Effect of water to cement ratio on carbonation depth (Bertolini, et. al., 2004)

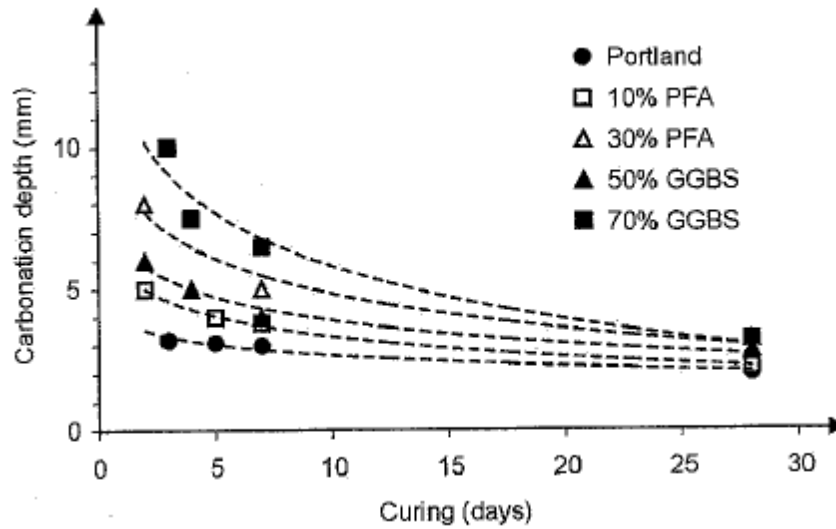


Figure 3.9: Effect of binder composition on carbonation depth (Bertolini, et. al., 2004)

3.4 Sulfate Attack

3.4.1 Degradation Mechanisms

Concrete piling in seawater and brackish water can be exposed to high concentrations of sulfates. In addition to sulfates present in the water, it is being investigated if additional sulfates may be produced by bacteria on the surface of the piles. The primary forms of sulfates present are NaSO_4 and MgSO_4 (Skalny, et. al., 2002). Damage to the concrete due to various reactions between the ingressing sulfate ions and hydration products and anhydrous cement phases in the cement paste is termed “sulfate attack”. Two primary mechanisms are associated with sulfate attack. First, sulfate ions can react with monosulfoaluminate or available tricalcium aluminate to form ettringite. The formation of ettringite can be expansive and lead to cracking and spalling. The calcium consumed in this reaction comes from the dissolution of available

portlandite. In addition, sulfate ions may react with available calcium hydroxide to form gypsum. If there is no portlandite present, then the calcium comes from the decomposition of the calcium silicate hydrate phase (C-S-H). The loss of calcium from the C-S-H leads to a reduction in strength (Skalny, et. al., 2002).

In the case of magnesium sulfate attack, additional reaction mechanisms are possible. Magnesium sulfate reacts with portlandite to form brucite, in addition to gypsum. Simultaneously, C-S-H is decomposed and converted to an amorphous hydrous silica or magnesium silicate hydrate phase. The decomposition of C-S-H is significantly faster with exposure to magnesium sulfate compared to sodium sulfate (Skalny, et. al., 2002).

3.4.2 Effect of Concrete Mix Designs

Alterations to the binder composition has been shown to improve sulfate resistance of concretes. ACI 318 (2008) requires the use of an ASTM C 150 Type V cement in areas with high sulfate concentrations in the water or soils. This cement has a decreased C_3A content, which will decrease damage due to sulfates reacting with it to form ettringite (Skalny, et. al., 2002). The use of SCM's was investigated by Kaid (2009), Torii (1994), Mangat (1992), and Khatib (1998). Their results showed that the use of fly ash, silica fume, and metakaolin improved sulfate resistance. Slag provided only marginal improvements (Mangat and El-Khatib, 1992).

3.5 Biological Attack

Biological attack may be a concern in prestressed concrete piles, specifically the effect of the boring sponge, *Cliona*. There have been reports of *Cliona* sponges at Gardiner's Island, New York (Nicol and Reisman, 1976), along the coast of Virginia (Hopkins, 1962), Corpus Christi, Texas (Miller, et. al., 2010), and off the coast of Jamaica (Scott, et. al., 1988).

A reported case of boring sponge attack was reported in Jamaica due to *Cliona lampa* (Scott, et. al., 1988). The sponges burrowed through the limestone aggregate of concrete masonry blocks manufactured with limestone aggregate. The damage was primarily at the corners, and irregular shaped bore holes occurred in the aggregate. The sponges use etching secretions to penetrate calcium carbonate and form the boreholes (Nicol and Reisman, 1976). The genus *Cliona* sponges leave silicate spicules near the surface of their borings. The length of the spicules varies by species but is typically between 200 μm to 400 μm (Zea and Weil, 2003). Studies on the erosion rate of the sponge show that the rate may exceed 1 mm (0.04 in.) per year of ingress in solid limestone (Neumann, 1966). Further research is needed on biological attack of concrete piles including a foundation of knowledge on the species causing attack, the rate and effects of their ingress, as well as methods of preventing and mitigating damage to existing piles need to be assessed.

3.6 References for Chapter 3

Bamforth, P. (1993). "Concrete Classification for R.C. Structures Exposed to Marine and Other Salt-Laden Environments," *Structural Faults and Repair Conference*, Edinburgh, UK.

Basheer, L., et. al. (2001). "Assessment of the durability of concrete from its permeation properties: a review." *Construction and Building Materials*, V. 15, pp. 93-103.

Bentz, D.P. (2000). "Influence of Silica Fume on Diffusivity in Cement-Based Materials II. Multi-Scale Modeling of Concrete Diffusivity," *Cement and Concrete Research*, V. 30, pp. 1121-1129.

Bertolini, L., et. al. (2004). *Corrosion of Steel in Concrete: Prevention Diagnosis, Repair*, Wiley-VCH, pp. 392.

Colleparidi, M., et. al. (1972). "Penetration of Chloride Ions into Cement Pastes and Concrete," *Journal of the American Ceramic Society*, V. 55, pp.534-535.

Dhir, R.K., et. al. (1990). "Rapid Estimation of Chloride Diffusion Coefficient in Concrete," *Magazine of Concrete Research*, V. 42, pp. 177-185.

Diab, H., et. al. (1988). "The Diffusion of Cl- Ions Through Portland Cement and Portland Cement-Polymer Pastes," *Cement and Concrete Research*, V. 18, pp. 715-722.

Hopkins, S.E. (1962). "Distribution of the species of *Cliona* (boring sponge) on the eastern shore of Virginia in relation to salinity," *Chesapeake Science*, V. 3, pp. 121-125.

Johnson, D., et. al. (1996). "Determining Chloride Diffusion Coefficients for Concrete using Accelerated Test Methods," *Proceedings on Performance of Concrete in a Marine Environment*, New Brunswick, Canada.

Kaid, H., Cyr, M., Julien, S., and Khelafi, H. (2009). "Durability of concrete containing a natural pozzolan as defined by a performance-based approach." *Construction and Building Materials*, V. 23, pp. 3457-3467.

Kanaya, M., et. al. (1998). "Diffusion of Chloride Ions in Concrete Exposed in the Coastal Area," *Concrete Under Severe Conditions 2: Environment and Loading*, E & FN Spon, pp. 242-249.

Khatib, J. M. and Wild, S. (1998). "Sulphate resistance of metakaolin mortar." *Cement and Concrete Research*, V. 28, pp. 83-92.

Luping, T., and Nilsson, L.O. (1992). "Chloride Diffusivity in High Strength Concrete at Different Ages," *Nordic Concrete Research*, V. 11, pp. 162-171.

- Luping, T. (1995). "On Chloride Diffusion Coefficients Obtained by Using the Electrically Accelerated Methods," *Rilem International Conference*, Paris, France.
- Mangat, P. S. and El-Khatib, J. M. (1992). "Influence of initial curing on sulphate resistance of blended cement concrete." *Cement and Concrete Research*, V. 22, pp. 1089-1100.
- Mangat, P.S., and Molloy, B.T. (1994). "Prediction of Long Term Chloride Concentration in Concrete," *Materials and Structures*, V. 27, pp. 338-346.
- Mehta, P.K. (1991). *Concrete in the Marine Environment*, Elsevier Science Publishers, New York, NY, pp. 214.
- Miller, A.N., et. al. (2010). "Effects of Heat and Salinity Stress on the Sponge *Cliona celata*," *International Journal of Biology*, V. 2, pp. 3-16.
- Mohammed, T.U. and Hamada, Hidenori. (2003). "Corrosion of Steel Bars in Concrete at Joints under Tidal Environment." *ACI Materials Journal*. V. July-Aug, pp. 265-273.
- Neumann, A.C. (1966). "Observations on Coastal Erosion in Bermuda and Measurements of the Boring Rate of the Sponge, *Cliona lampa*," *Limnology and Oceanography*, V. 11, pp. 92-108.
- Neville, A.M. (1997). *Properties of Concrete*, 4 ed., John Wiley and Sons, New York, NY, pp. 844.
- Nicol, W.L. and Reisman, H.M. (1976). "Ecology of the Boring Sponge (*Cliona celata*) at Gardiner's Island, New York," *Chesapeake Science*, V. 17, pp. 1-7.
- Papadakis, V.G., et. al. (1991). "Fundamental Modeling and Experimental Investigation of Concrete Carbonation." *ACI Materials Journal*, V. 88, pp. 363-373.
- Pedersen, V., and Arntsen, B. (1998). Effect of Early-Age Curing on Penetration of Chloride Ions into Concrete in the Tidal Zone," *Concrete Under Severe Conditions 2: Environment and Loading*, E & FN Spon, pp. 468-477.
- Polder, R.B. (1995) "Chloride Diffusion and Resistivity Testing of Five Concrete Mixes for Marine Environment," *Rilem International Conference*, Paris, France.
- Scott, P.J.B., et. al. (1988). "Bioerosion of Concrete and Limestone by Marine Organisms," *Marine Pollution Bulletin*, V. 19, pp. 219-222.
- Skalny, J., et. al. (2002). *Sulfate Attack on Concrete*, Spon Press, New York, NY, pp. 217.
- Stanish, K.D., et. al. (1997). *Testing the Chloride Penetration Resistance of Concrete: A Literature Review*, FHWA contract report, pp. 33.

Stanish, K.D. and Thomas, Michael. (2003). "The use of bulk diffusion tests to establish time-dependent concrete chloride diffusion coefficients." *Cement and Concrete Research*. V. 33, pp. 55-62.

Thomas, M. and Bamforth, P. (1999). "Modelling chloride diffusion in concrete: Effect of fly ash and slag." *Cement and Concrete Research*. V. 29, pp. 487-495.

Torii, K. and Kawamura, M. (1994). "Effects of fly ash and silica fume on the resistance of mortar to sulfuric acid and sulfate attack." *Cement and Concrete Research*, V. 24, pp. 361-370.

Zea, S. and Weil, E. (2003). "Taxonomy of the Caribbean excavating sponge species complex *Cliona caribbaea* – *C. Aprica* – *C. langae* (Porifera, Hadromerida, Clionaidae)," *Caribbean Journal of Science*, V. 39, pp. 348-370.

4. Background – Interviews

4.1 GDOT Preconstruction and Maintenance Division Interviews

Interviews were performed with staff from the GDOT preconstruction and maintenance divisions to establish observed damage, current design methods and criterion, and research areas of interest. Interviews were later conducted with GDOT field office employees in District 5, Savannah and Brunswick. Mr. Richard Potts of Standard Concrete Products, Savannah, was also interviewed because that company supplies many prestressed concrete piles to GDOT.

4.2 Paul Liles, Assistant State Preconstruction Engineer, and Mike Clements, Bridge Maintenance Engineer

Messrs. Paul Liles and Mike Clements were interviewed on January 25th, 2010 at the Georgia Department of Transportation's One Georgia Center location. Topics discussed in the meeting were the goals that the Georgia Department of Transportation (GDOT) hopes to achieve from this project, observed trends of corrosion induced damage in coastal Georgia bridges, GDOT experience with mitigation techniques, and current design practices.

It was established the desired goals of the project for GDOT are as follows: (1) the development and implementation of corrosion resistant stainless steel strands for prestressed concrete piles in the substructure of coastal bridges; (2) development of service life and damage estimation capabilities based on salinity maps for concrete mix designs; and (3) provide design recommendations to achieve service lives in excess of 100 years.

Corrosion induced damage has been observed primarily in simple pile bent bridges in coastal and marsh regions. The damage is localized primarily in the piles, not in the pile or pier caps. This may partially be due to the fact that most of the bridges have the pile caps directly below the girders and elevated from the water. GDOT prefers to use prestressed concrete piles over steel H-piles and sheet piling in aggressive environments. The damage on the concrete piles is mostly found in the splash zone, extending approximately 18" to either side of the mean water level in most cases. There is also concern that piles may be damaged during driving which may lead to cracking. No testing has been done to verify this, but driving guidelines are given in the GDOT specifications to prevent this damage. The state currently does not have requirements for the jetting of piles for placement except in special soil conditions.

GDOT is currently employing the following design practices to provide corrosion resistance in prestressed concrete piling: (1) Use of high performance concretes that contain supplementary cementitious materials, a low water to cementitious material ratio, and are limited to a maximum of 2000 coulombs charge passed on the rapid chloride permeability test; (2) a minimum cover distance of 2 inches is required for increased durability, and no piling less than 12" in width is used; and (3) the superstructures of bridges are built a minimum of 1 to 2 ft above the 50 year storm water level. Additional information on the standard pile sections is available

through AASHTO and the GDOT website. Currently no service life modeling efforts are used in the design of prestressed concrete piles.

GDOT has attempted to implement several other methods for providing corrosion resistance, but have discontinued the use for various reasons. A bridge in Chatham county was constructed using corrosion inhibitors, epoxy coated rebar, and supplementary cementitious materials on individual piles. A report was written in the 1980's on this project, but no monitoring after construction was completed. Cathodic protection was implemented on the Sidney Lanier Bridge in Brunswick, Georgia. The system proved to have large maintenance issues and GDOT no longer will use electrochemical methods of protection for future projects. Epoxy coated rebar was briefly used in concrete piles, but was discontinued after poor performance was observed by the Florida DOT.

4.3 Mike Clements, Bridge Maintenance Engineer, and Andy Doyle, State Bridge Inspection Engineer

Messrs. Mike Clements and Andy Doyle were interviewed on February 1st, 2010 at the Georgia Department of Transportation's Confederate Avenue office. Topics discussed included inspection techniques used, typical damage to concrete piles observed, and repair techniques for damaged piles.

GDOT performs inspections of prestressed concrete piles using a dive team of inspectors. The submerged regions of piles are inspected by visually scanning the surface of each face of the pile along the length while also running hands along surface for damage. A small hammer is used to tap at the surface if damage is suspected. If cracks are observed, the size is noted and attempt to open them is made. The atmospheric and splash zones of the piles are visually inspected for damage and a hammer is used similarly in the submerged section of the piles.

Typical types of damage that have been observed are as follows: (1) degradation and softening of concrete starting at 1 to 2 ft below the water line and extending to the mudline; (2) longitudinal cracks along the corners of the piles extending from mudline to low tide region of pile; and (3) color change and spalling of concrete along corners of piles in submerged region.

If damage is observed, GDOT does not have standard methods of repair. The repair methods employed vary by district, and are only performed in response to damage. Currently no preventative repair is performed on concrete piles.

4.4 Myron Banks, Concrete Engineer, and Jeff Carroll, Materials and Research Branch

Messrs. Myron Banks and Jeff Carroll were interviewed on February 8th, 2010 at the GDOT Materials and Research Branch facility. Topics discussed included GDOT mix design specifications for prestressed concrete piles, reported damage patterns to concrete piles, and areas of research needed.

GDOT has two mix design specifications for prestressed concrete piles. Any piling in an aggressive environment has been required to follow the high performance concrete (HPC) specifications for the last 2 to 3 years. The HPC guidelines require a maximum of 2,000 coulombs passes on the rapid chloride permeability test, a maximum water to cementitious materials ratio of 0.35, and a 28 day strength of at least 5,000 psi. Fly ash can be used as a cement replacement up to 15%, without any restrictions on whether Type C or F is used. If alkali silica reaction (ASR) is a concern, then Type F is used with a CaO limit of 5%. Silica fume is allowed as a replacement up to 10%. Mix designs meeting these criteria often contain air entraining admixtures and super-plasticizers. For other regions, a Class AAA concrete can be used. The specification for this mix has been in place and unchanged for over 25 years. The mix has a minimum cement requirement of 675 lb/yd³, a maximum water to cementitious materials ratio of 0.44, an air content of 2.5 to 6%, and a minimum strength of 5,000 psi at 28 days of age.

The prestressed concrete piles are typically placed at between 7 to 14 days of age. Standard designs utilize a 3 in. cover distance for strands. No life cycling modeling is currently employed, but is an area of interest. GDOT has not attempted to implement mitigation methods that are available or in use in other states. South Carolina requires the use of a calcium nitrite corrosion inhibitor in its mix designs. GDOT does allow for the use of fibers and slag, but neither is being utilized.

The following types of damage have been reported or observed: (1) transverse cracking with a spacing of 3 to 5 ft, possibly due to over-driving or reflective cracking; (2) spalling of corners of the piles down to the level of the corner strand in the splash zone; (3) surface wear from wave action; and (4) delamination of cover concrete due to corrosion.

Areas of interest for research are the as follows: (1) development of lower permeability concrete mix designs; (2) the effect of micro-cracking during driving practices on the durability of prestressed concrete piles; and (3) feasibility of self-healing concrete for improved durability characteristics.

4.5 Mike Garner, Bridge Liasson, and Slade Cole, Assistant Area Engineer

Messrs. Mike Garner and Slade Cole were interviewed on May 3, 2010 in the Savannah GDOT District 5 office. The damage patterns in piles were discussed, as well as the repair techniques employed. Until recently, overdriving of piles was not considered or heavily monitored. Contractors would continue to attempt to drive the piles without regard to a “refusal” limit, which is approximately 10 blows per ½ in. Overdriving in the coastal region now is typically only a concern when a hard layer of soil or lime rock layer is reached, but the refusal limits are monitored.

The reflective cracking of piles is still an area of concern for GDOT. It most commonly occurs when a soft layer of soil is hit immediately following a hard layer, or when the contractor is not following standard practice (bad pads or oversized hammer). Reflective cracking is identified by “dusting” of the piles where a small amount of powdery material is lost from the cracked region. The cracks are typically very small, and hard to find (hairline) due to prestressing effects. If a reflective crack occurs in the Savannah region, the procedure for repair

varies, depending on the location in the pile. If the crack location is below the mud line, then no repair is made; however, if the crack will be located above the mud line, then it is patched with epoxy. The 18" square piling is the most common to have reflective cracking occur. The hypothesized reasoning for this is that the 18" design has a lower precompression stress than the other sizes and therefore is more susceptible to developing tensile forces during driving.

Once piles begin showing major signs of deterioration, there are two primary methods of repair that are used. The first method is to encase the piling in concrete, by either placing a corrugated steel tube around it and filling with concrete, or by using a plastic jacket and pumping concrete into it. The second method of repair is to epoxy jacket the piles, which is expensive to perform. This technique was employed on the Back River Bridge discussed in Section 5.5. These are not long-term solutions to bridge deterioration, but simply methods to add a short amount of time before the bridge will require replacement.

For future research, construction is about to begin on a project which will have over 1000 piles driven, and the GDOT is willing to help in attempting to determine the effects of driving on permeability due to microcracking. Additionally, GDOT may also be able to provide a boat to aid in future bridge inspections.

4.6 Standard Concrete Products

Messrs. Richard Potts and Alan Pritchard of Standard Concrete Products (SCP) – Savannah were interviewed on May 3, 2010 at the plant. Concrete mix designs were discussed and their variability between requirements of different states. In Georgia, any piling going into "aggressive" coastal environments is required to be cast using a high performance concrete. The HPC mix specifications require a rapid chloride permeability of less than 2000 Coulombs, which is the upper limit for the rating of "Low Chloride Ion Penetrability" according to ASTM C 1202. Fly ash can be used as up to 15% cement replacement and silica fume for up to 10%. Additionally, once cast, the concrete must age at least 18 hours or until the release strength is met, which is between 3,500-4,000 psi depending on the pile size. The piles must meet 5,000 psi design strength requirements before placement and must also be at least 5 days of age.

The mix design that SCP uses contains 15% Class F fly ash replacement, no silica fume, and a high paste content of approximately 900 lb/yd³ of cementitious material. Their mix design has an ultimate strength of 8,000 to 10,000 psi. Silica fume is avoided in their mix designs due to its higher cost and an increased susceptibility to shrinkage cracking. All of their mix designs specify a granite coarse aggregate and a natural sand fine aggregate. The piles are typically delivered and placed at 7-14 days of age.

The normal strength standard mix that is produced for piling in regions other than the "aggressive" environment is a 750 lb/yd³ cement content mix with no supplementary cementitious materials and no requirement on the rapid chloride permeability.

The mix designs for other states vary considerably with those for Georgia. The mix design for Florida employs 18% fly ash replacement and a variable design strength which is typically 6,000 to 8,000 psi. Florida also allows for the use of ultra-fine fly ash. South Carolina utilizes a

calcium nitrite corrosion inhibitor in several of its mixes. Alan Pritchard agreed to email the mix designs and state specifications that are used for these states.

The concrete piles that were forensically investigated from the I-95 at Turtle River Bridge were most likely produced at Gates Precast in Jacksonville, Florida. The mix designs at the time of construction were typically a 0.5 w/c with no SCM addition. Richard Potts will contact the former plant manager there and attempt to find out more specific information.

It was reiterated that overdriving of piles in Georgia was previously not heavily controlled or monitored. Also, Mr. Potts said that the 18" piling is understressed compared to the other size designs in Georgia with an effective prestress of approximately 700 psi after losses compared to most other piling having 800-900 psi, and he believed that such understressing is the cause of increased amount of reflective cracks noticed when using 18" piling.

The use of epoxy coated or stainless steel prestressing strand to increase the corrosion resistance of piles was also discussed. Richard stated that SCP had used epoxy coated strand briefly. Temperature control problems (which influence the properties of the epoxy) were found to be a concern in addition to the sand grit embedded in the epoxy to increase bond. The sand grit causes excessive wear on the beds and grips. SCP expressed interest in the use of stainless steel strand for the construction of "highly" corrosion resistant piling, although they were concerned that the high cost to produce the piles (~40% of cost is steel currently) would limit the economic feasibility of their use in bridge construction.

4.7 Lisa Sikes, Bridge Liasson, and Brian Scarbrough, Area Engineer

Messrs. Lisa Sikes and Brian Scarbrough were interviewed on May 4, 2010 in the GDOT Brunswick office. Damage and construction practices of piling were discussed. It was reiterated again that the 18" piling is problematic with reflective cracking. In contrast to the Savannah office, the Brunswick office personnel will reject piling if "dusting" is seen during driving. The commonplace practice of overdriving in older construction was again discussed. When asked about a few of the bridges of interest, it was noted that there were paper mills present in close proximity and that run-off from them may be partially responsible for some damage seen on the piles. Brian Scarbrough agreed to email pictures of damaged piling on another bridge that was not visited over the South Brunswick River on I-95.

The I-95 at Turtle River piles that were delivered to the Georgia Tech Structures Laboratory were battered piles located on the edge of the bents. The remainder of the piling is still in place, although no longer in a load carrying capacity. Photos are shown in Chapter 5.

5. Georgia Coastal Bridge Inspections

5.1. Overview

Bridges of interest in the coastal counties with reported damage to the concrete piling were inspected from May 2nd through the 4th, 2010. Additionally, interviews were performed with Georgia Department of Transportation (GDOT) personnel at the Savannah and Brunswick offices and with Standard Concrete Products (SCP) engineers in Savannah.

5.2. Bridge Inspections

Eleven bridge sites shown in Figure 5-1 were inspected during the trip. Table 5-1 gives the bridge numbers and names. The sites were selected based on the extent and types of damage noted in inspection reports provided by the GDOT Bridge Maintenance Office, varying proximities to the coast, and distribution throughout the coastal counties of Georgia. All bridges spanned rivers or inlets with fresh or brackish waters. At each site, photos were taken of any visible damage, and water samples were collected for pH, sulfate content, and chloride content testing.

Table 5-1. Bridge ID Numbers and Names for Locations Inspected

Bridge Name	Bridge Number
Harriet's Bluff Road at Deep Creek Bridge	039-0049
Houlihan Bridge	051-0054
US 17 at Back River Bridge	051-0059
US 80 at Lazeratto Creek Bridge	051-0066
Island Expressway at Wilmington River Bridge	051-0132
Oatland Island Research Bridge	051-5013
Long Bridge Road at Ebenezer Creek Bridge	103-0030
I-95 at Turtle River Bridge	127-0052
Torras Causeway at Little River Bridge	127-0063
Ocean Highway at Riceboro Creek Bridge	179-0005
Ocean Highway at Champney's River Bridge	191-0005

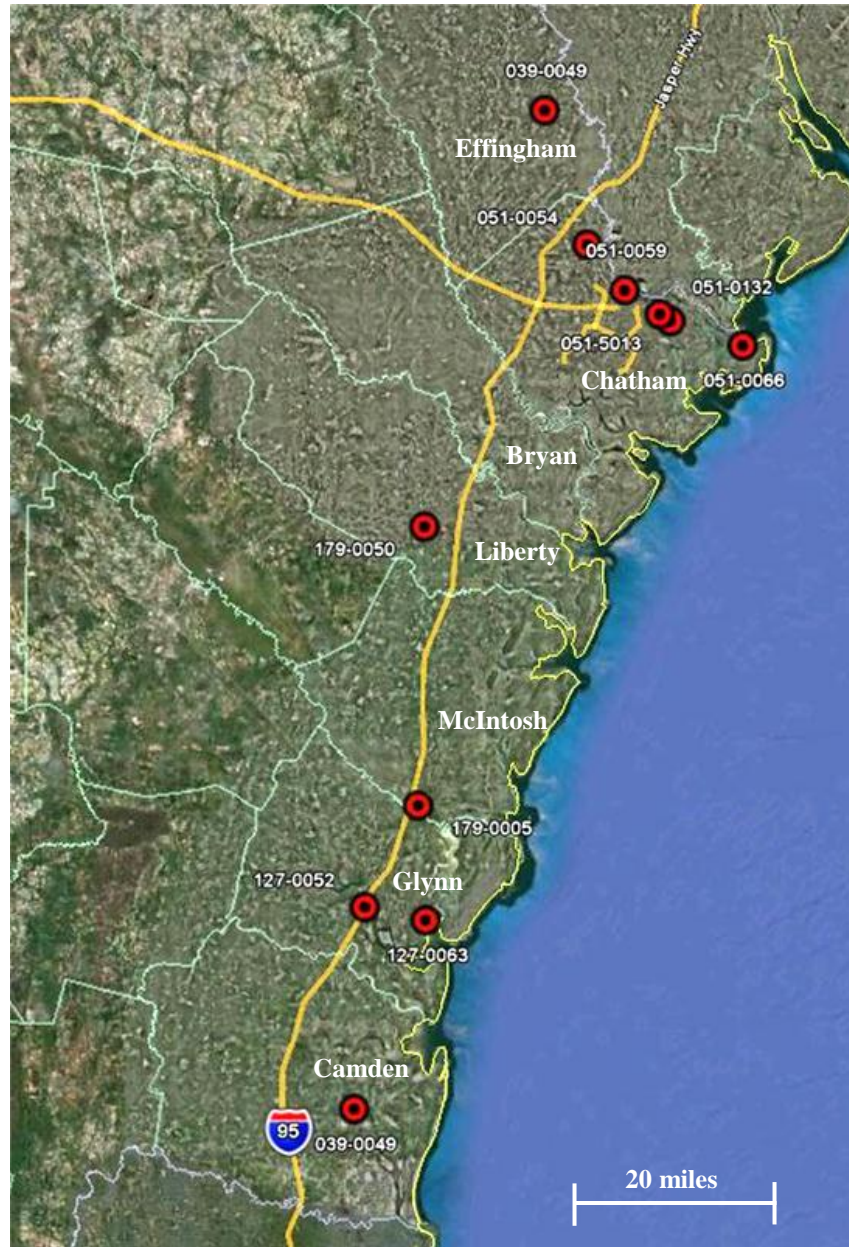


Figure 5-1. Bridges Inspected Along Georgia’s Coastal Counties. Red dots indicate bridge locations.

5.3. Harriett’s Bluff Road at Deep Creek Bridge (Bridge No. 039-0049)

Located approximately 8 miles from the coast in Camden county, the Harriett’s Bluff Road Bridge spanning Deep Creek exhibited significant corrosion-related deterioration, primarily in its superstructure. The bridge was constructed in 1964 with a reinforced concrete superstructure and precast concrete pile-bent substructure system. The substructure looked to be in fairly good condition, with minimal surface abrasion and heavy marine growth and oyster scale in the tidal

region (Figure 5-2). However, given that the inspection coincided with high tide, a detailed assessment of the substructure could not be made.



Figure 5-2. Substructure of Harriett's Bluff Road at Deep Creek Bridge (Bridge No. 039-0049)

The superstructure of the bridge exhibited the most significant deterioration. Cracking and spalling of concrete, especially in the cast-in-place concrete railing/barrier system, was widespread throughout the superstructure. Typical corrosion damage observed in the barrier is shown in Figure 5-3 below.



Figure 5-3. Corrosion Damage in Cast-in-Place Barrier of Harriett's Bluff Road at Deep Creek Bridge (Bridge No. 039-0049)

5.4. Houlihan Bridge (Bridge No. 051-0054)

Constructed in 1953, the Houlihan Bridge is located approximately 17 miles from the coast near Port Wentworth in Chatham county. The bridge consists of a reinforced concrete beam

superstructure, a precast concrete pile-bent substructure, and a central movable steel truss span. An overall view of the bridge is shown in Figure 5-4.



Figure 5-4. Overall View of Houlihan Bridge (Bridge No. 051-0054)

Similar to what had been recorded in GDOT bridge inspection reports, the most significant deterioration observed on the Houlihan Bridge was found in the submerged and tidal zone of the concrete substructure. Significant surface abrasion was ubiquitous, with fully exposed aggregates from the top of the splash zone down. In some cases, abrasion was so aggressive that hourglassing of the piles could be seen even at a distance. Some typical photos of surface abrasion are shown in Figures 5-5 and 5-6. In Figure 5-5, it should be noted that abrasion occurred on both the precast piling and the cast-in-place support for the movable bridge span in the background. Given the bridge's location fairly far inland, little oyster shell was present on the piles.



Figure 5-5. Surface Abrasion of Concrete Substructure on Houlihan Bridge (Bridge No. 051-0054)

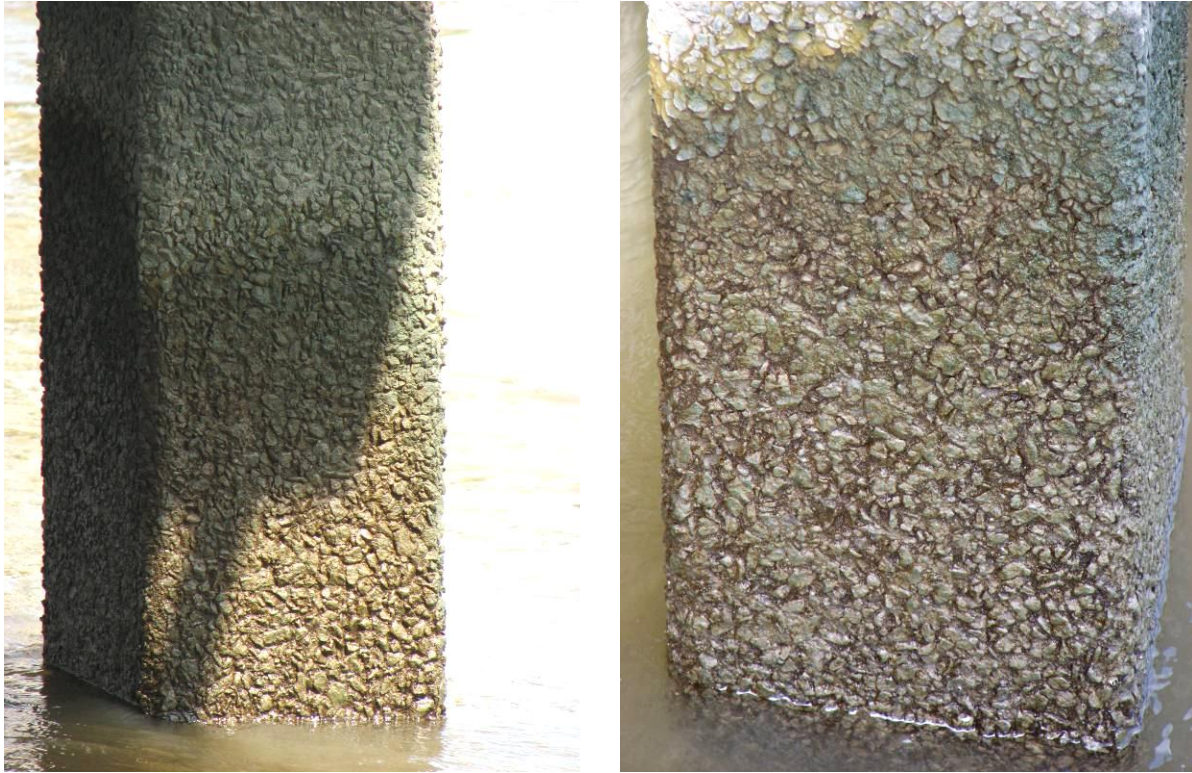


Figure 5-6. Surface Abrasion Observed in Concrete Substructure of Houlihan Bridge (Bridge No. 051-0054)

5.5. US 17 at Back River Bridge (Bridge No. 051-0059)

The Back River Bridge is located at the Georgia – South Carolina border just east from the Talmadge Bridge, approximately 12 miles from the coast in Chatham county. The bridge was constructed in 1954 with a reinforced concrete beam superstructure and a precast pile-bent substructure with a total length of approximately 0.5 miles. The precast pile substructure, which is shown in Figure 5-7, is extensive and has been severely damaged by corrosion.



Figure 5-7. Pile-Bent Substructure of US 17 at Back River Bridge (Bridge No. 051-0059)

Almost all piles have vertical cracks at the corners, extending from the waterline up to 2 to 3 feet above high tide with rust staining present. Many of the cracks appear to be much larger than hairline in width, although measurements were limited due to the marsh surrounding the bridge. Typical damage observed in the piles is shown in Figure 5-8. The substructure had recently undergone a retrofit of the piles conducted by an external contractor. This retrofit consisted of fiber-reinforced polymeric (FRP) jackets being compression fitted onto the most significantly damaged piles in order to provide confinement of the cracked concrete and to limit any subsequent corrosion damage. A typical jacketed pile is shown in Figure 5-9.



Figure 5-8. Vertical Cracking at Corner of Concrete Pile on US 17 at Back River Bridge (Bridge No. 051-0059)



Figure 5-9. Corrosion Damaged Piling with FRP Jacket Retrofit on US 17 at Back River Bridge (Bridge No. 051-0059)

5.6. US 80 at Lazeratto Creek Bridge (Bridge No. 051-0066)

Located adjacent to the coast at the mouth of the Savannah River in Chatham county, the US 80 Bridge spanning Lazeratto Creek was constructed in 1960 with a precast concrete and steel girder superstructure and a precast pile-bent substructure. The overall bridge structure is shown in Figure 5-10 below, with only the central steel spans of the bridge over water.



Figure 5-10. Overall View of US 80 at Lazeratto Creek Bridge (Bridge No. 051-0066)

Due to the marsh adjacent to the bridge and our inspection occurring at high tide, limited access to the substructure in the spans over water was available for photos. In the dry marsh approach spans, a detailed inspection of the precast piles could be made. Grout repairs of what looked to be traverse cracks likely caused during driving were observed in some piles (see Figure 5-11). Poor construction in the cast-in-place pile caps was also evident with honeycombing and exposed reinforcement in some cases (see Figure 5-12).



Figure 5-11. Grout Repair of Traverse Crack in Precast Concrete Pile on US 80 at Lazeratto Creek Bridge (Bridge No. 051-0066)



Figure 5-12. Honeycombing and Exposed Corroding Reinforcement in Pile Cap on US 80 at Lazeratto Creek Bridge (Bridge No. 051-0066)

5.7. Island Expressway at Wilmington River Bridge (Bridge No. 051-0132)

Located approximately 8 miles inland in Chatham County, the Island Expressway Bridge spanning the Wilmington River was constructed in 1963 using a precast concrete girder superstructure and precast pile-bent substructure. A steel moveable span is located in the center of the bridge. An overall view of the bridge as seen from the underside is shown in Figure 5-13. The adjacent bridge shown on the right of Figure 5-13 carrying westbound traffic appears to be much newer and constructed with piers rather than pile bents. No record of the reconstruction of the westbound lanes was found in the inspection reports.



Figure 5-13. Underside of Island Expressway at Wilmington River Bridge (Bridge No. 051-0132)

At low tide a detailed inspection of the submerged regions of the piling was performed. Limestone aggregates showed deterioration and abrasion on all piles (see Figure 5-14). The limestone aggregate were exposed on the surface of the piles due to pop-outs and and showed severe abrasion. Large longitudinal cracks at the corners with rust staining were present in most piles. Severe cases of cracking and spalling, as well as “hour-glassing” in the tidal region, are shown in Figure 5-15.



Figure 5-14. Deterioration of Limestone Aggregates Present at Concrete Surface on Island Expressway at Wilmington River Bridge (Bridge No. 051-0132)



Figure 5-15. Severe Damage to Concrete Piling on Island Expressway at Wilmington River Bridge (Bridge No. 051-0132)

5.8. Oatland Island Research Bridge (Bridge No. 051-5013)

The Oatland Island Research Bridge was constructed in 1987 using precast concrete girders and a precast concrete pile bent substructure. An overall view of the bridge is shown in Figure 5-16. The bridge was constructed using a variety of corrosion mitigation methods. The following methods were used in each bent: epoxy coated strands, calcium nitrite corrosion inhibitors, and high performance concrete with supplementary cementitious materials (SCM's). While access to the substructure for photos was limited due to the surrounding marsh and oyster shell growth on the piling, all of the piles looked to be in excellent condition with no apparent cracking and very limited surface abrasion (Figure 5-17).



Figure 5-16. Oatland Island Research Bridge (Bridge No. 051-5013)



Figure 5-17. Pile-Bent Substructure of Oatland Island Research Bridge (Bridge No. 051-5013)

5.9. Long Bridge Road at Ebenezer Creek Bridge (Bridge No. 103-0030)

Located approximately 30 miles inland in Effingham county, the Long Bridge Road Bridge spanning Ebenezer creek was constructed in 1968 with a reinforced concrete superstructure and precast concrete pile-bent substructure. An overall view of the bridge is shown in Figure 5-18.



Figure 5-18. Long Bridge Road at Ebenezer Creek Bridge (Bridge No. 103-0030)

Bridge 103-0030 was selected for inspection primarily due to the mention of driving cracks in the piles recorded in its inspection report. Transverse cracks which had been repaired with grout were observed on two piles but were not present throughout the bridge. A typical repair is shown in Figure 5-19.



Figure 5-19. Grout Repair of Transverse Cracking Likely Caused by Overdriving on Long Bridge Road at Ebenezer Creek Bridge (Bridge No. 103-0030)

The most predominant deterioration observed on the bridge was degradation of the paste fraction of the concrete piling in regions from the high-water mark down. Above the high-water mark, the concrete was in good condition. Below the high-water mark, the paste was extremely friable and could be scratched easily. This condition was observed on all piles. A typical case of surface abrasion is shown in Figure 5-20.



Figure 5-20. Surface Abrasion of Concrete Below High-Water Mark on Long Bridge Road at Ebenezer Creek Bridge (Bridge No. 103-0030)

5.10. I-95 at Turtle River Bridge (Bridge No. 127-0052)

The Turtle River Bridge is located approximately 10 miles from the coast near Brunswick, GA in Glynn County. The bridge was recently upgraded but was inspected because it was the site where piles were pulled and shipped to the Georgia Tech Structural Engineering and Materials Laboratory for further forensic investigation in February 2010. The piles that used for the forensic investigation showed the following deterioration mechanisms: abrasion and “hour glassing” in the splash zone, longitudinal cracking and spalling in the tidal and submerged regions, rust staining along the corners of the piles, softening of the concrete in the submerged region, and biological attack on the limestone aggregate.

Due to the expense of pulling all the piles, only those which needed to be removed were, with the rest of the piles from the original bridge left in place underneath the new structure. The new structure consists of precast concrete girders and drilled shafts supporting large transfer beams which span to substructure of the old bridge. An overall view of the new Turtle River Bridge is shown in Figure 5-21. Figure 5-22 shows the substructure of the new bridge with the

original piles integrated into the large transfer beam. The bridge was inspected near high-tide and limited access for photos was available under the bridge.



Figure 5-21. Updated I-95 at Turtle River Bridge (Bridge No. 127-0052)



Figure 5-22. Transfer Beam with Original Piles Left In-Place on I-95 at Turtle River Bridge (Bridge No. 127-0052)

5.11. Torras Causeway at Little River Bridge (Bridge No. 127-0063)

The Torras Causeway Bridge was constructed as part of a series of bridges in 1986 close to the coast near Brunswick, GA in Glynn county. The bridge was built to replace an older corrosion damaged bridge using precast concrete girder superstructure and a precast concrete

pile-bent substructure with larger piers in the center spans over the intercoastal waterway. An overall view of the structure is shown in Figure 5-23, taken from the adjacent fishing pier which is actually the remains of the original Torras Causeway Bridge constructed in the 1950s.



Figure 5-23. Torras Causeway at Little River Bridge (Bridge No. 127-0063) on Right and Adjacent Fishing Pier on Left

With the heavy oyster shell growth present in the tidal zone of the piles, it was difficult to see any surface abrasion or damage from a distance. No longitudinal cracking or rust staining could be seen on any of the piles. A typical pile-bent at the waterline is shown in Figure 5-24. Access to the original bridge was also available from the adjacent dry marsh. The piles under the original bridge showed significant deterioration with large longitudinal cracks, rust staining, and spalling of concrete. On many of the piles, concrete repair jackets were present. A typical pile from the older structure is shown in Figure 5-25.



Figure 5-24. Pile-Bent on Torras Causeway at Little River Bridge (Bridge No. 127-0063) Approach Span



Figure 5-25. Corrosion Damage in Original Torras Causeway at Little River Bridge Substructure (Bridge No. 127-0063)

5.12. Ocean Highway at Riceboro Creek Bridge (Bridge No. 179-0005)

Located 20 miles inland over Riceboro Creek in Liberty County, bridge 179-005 was constructed with a reinforced concrete superstructure and precast concrete pile-bent substructure in 1957. An overall view of the bridge is shown in Figure 5-26. All piles showed significant deterioration with surface abrasion of the paste fraction below the high-water mark, longitudinal cracks at the corners, and rust staining from corrosion present on most piles (see Figure 5-27).



Figure 5-26. Ocean Highway at Riceboro Creek Bridge (Bridge No. 179-0005)



Figure 5-27. Deterioration of Precast Concrete Piles in Substructure of Ocean Highway at Riceboro Creek Bridge (Bridge No. 179-0005)

5.13. Ocean Highway at Champney's River Bridge (Bridge No. 191-0005)

The Ocean Highway Bridge is located approximately 10 miles inland spanning Champney's River in McIntosh county. The bridge was constructed in 1981 with a precast concrete girder superstructure and precast concrete pile-bent substructure. An overall view of the structure is shown in Figure 5-28. Hollow square piles, 36"x36", were used in the substructure. Leftover piles from the bridge were placed on the bank forming a seawall at an adjacent boat ramp. Close-up examination of these piles revealed the concrete was manufactured using limestone coarse aggregates (see Figure 5-29).



Figure 5-28. Overall View of Ocean Highway at Champney's River Bridge (Bridge No. 191-0005)



Figure 5-29. Remaining Piles on Bank Adjacent to Ocean Highway at Champney's River Bridge (Bridge No. 191-0005)

A fishing pier attached to the side of the bridge was used to take photos of the substructure. The bridge was inspected at high tide and photos of regions of the piles well below the high water mark could not be taken. Surface abrasion, particularly at the site of limestone aggregates, was present on all of the piles. No significant cracking or rust staining was observed on any of the piles. The typical condition of the piles is illustrated in Figure 5-30.



Figure 5-30. Typical Surface Abrasion of Concrete on Ocean Highway at Champney's River Bridge (Bridge No. 191-0005)

5.14. Water Sample Testing

Water samples were collected at eight of the bridge sites visited. Access to collect samples at the other sites was not possible. The samples were tested for chloride content, sulfate content, and pH. Chloride contents were obtained by diluting 1 mL of the sample with 50 mL of deionized water and titrating using the Metrohm 798 MPT Titrino. A silver / silver chloride standard electrode was used. 0.1 N silver nitrate is added in 0.1 ml steps to the sample until an equivalence point is achieved.

The sulfate content was determined by performing inductively coupled plasma atomic emission spectroscopy (ICP) on a Perkin Elmer Optima 7300 DV Optical Emission Spectrometer. The pH was measured using a Thermo Scientific Orion 3-Star Plus pH Portable Meter. The results of the tests performed on the water samples are given in Table 5-2.

Table 5-2. pH, Chloride, and Sulfate Contents of Water Samples

Bridge Name	Bridge ID	pH	% NaCl (g/g)	Tide	[SO ₄ ²⁻] (mg/L)
Harriet's Bluff Road at Deep Creek Bridge	039-0049	7.41	2.77	High	2070.75
Houlihan Bridge	051-0054	7.04	0.05	Low	52.91
Island Expressway at Wilmington River Bridge	051-0132	7.32	1.38	Low	1058.58
Long Bridge Road at Ebenezer Creek Bridge	103-0030	5.88	0.00	Low	13.65
I-95 at Turtle River Bridge	127-0052	7.47	1.99	High	1527.54
Torras Causeway at Little River Bridge	127-0063	7.41	2.34	Mid	1746.22
Ocean Highway at Riceboro Creek Bridge	179-0005	7.25	0.38	Low	219.95
Ocean Highway at Champney's River Bridge	191-0005	7.18	0.00	High	22.65

The salt content of water is used to differentiate between fresh, brackish, and saline (sea) water. Table 5-3 shows the general ranges of NaCl concentrations as given by the USGS [1]. From Table 5-3, it can be seen that all of the bridges except for the 051-0054, 103-0030, and 191-0005 are in brackish water. The three bridges considered to be in fresh water were located further inland than the rest investigated and no signs of corrosion induced damage were noticed.

Table 5-3. Water Salinity Based on Dissolved Salt (NaCl) Concentration

Fresh water	Brackish water	Ocean Water
<0.1 %	0.1-3.5 %	3.5 %

The pH of water is highly variable. According to the USGS [1], seawater has a pH of between 8 and 9. However, the average field pH is 4.7 for coastal Georgia [1]. The values of pH observed at the inspected bridge sites fell between the two reported values. Only bridge 103-0030 was located in acidic water. The damage observed on the bridge was consistent with the signs of acid attack, including the observations of exposed coarse aggregate on the surface due to the loss of paste, and severe softening of the paste content. The other bridge locations had a near neutral pH, typically measuring in the range of 7.1 to 7.4.

The sulfate contents varied significantly among the water samples. Seawater has an average sulfate content of 2,700 mg/L [2], and a study by Murata [3] suggests that the sulfate content in brackish water is typically in excess of 1,000 mg/L. The measured values of sulfate concentrations at the bridge sites varied by two orders of magnitude. The wide spread of

observed concentrations could be due to both varying distance from the coast, as well as the tide when measured [1]. ACI 201.2 [4] provides design requirements based upon the sulfate content in water, and requires preventative measures to protect against damage to the concrete by sulfate attack for a concentration above 150 mg/L. Additional measures are required for concentrations exceeding 1500 mg/L, which would apply to three of the bridges visited. ACI 201.2 states that for concentrations less than 150 mg/L no special requirements are necessary for sulfate resistance. For concentrations between 150 and 1,500 mg/L the w/c should be no greater than 0.50 and an ASTM C 150 Type II or ASTM C 1174 Class MS cement should be used. For concentrations between 1,500 and 10,000 mg/L the w/c should be no greater than 0.45 and an ASTM C 150 Type V or ASTM C 1174 Class HS cement should be used.

X-ray diffraction was performed on piles from the Turtle River Bridge (127-0052) to examine if sulfate attack was the cause of the softening of the surface concrete. The concentration of sulfates in the water appears to be sufficient to cause significant sulfate attack, but other local sources of sulfates, particularly biological sources, may contribute to the degradation as well.

The concentrations of sulfates and chlorides in the water can vary widely with variations in rainfall and seasonal effects. Regional data will be investigated further to determine the extent of this variation, and how the data collected compares with historical data.

5.15. Summary

The inspections of bridges along the coast suggest that the causes of damage observed during the forensic investigation of piling from the Turtle River Bridge is representative of other bridges located along the coast. The types of damage observed were cracking and staining due to corrosion, abrasion and “hour-glassing” in splash and tidal zones, loss of limestone aggregates, and severe biological growth in tidal zones. The interviews of GDOT field personnel and SCP employees suggest that driving practices for piles have improved over the last several decades; however, when damage is noticed during driving, there is no standard method of repair or rejection criterion.

The current HPC mix design requirements being used by GDOT lead to a significantly more durable concrete than the concrete mixes used in the past. However, GDOT limits the replacement of cement with SCM's to lower levels than currently being employed by Florida, therefore, the benefits of higher replacement levels need to be evaluated. Additionally, GDOT does not require the use of an ASTM C 150 Type II or ASTM C 1174 Class MS cement in coastal concrete piling, but there is evidence that sulfate attack may occur in this environment if preventative measures are not taken.

5.16. References for Chapter 5

[1] *USGS Surface Water Information Pages*, United States Geological Survey, June 3rd, 2010, from <http://water.usgs.gov/osw/>.

[2] Bertolini, L., et. al. (2004). *Corrosion of Steel in Concrete*: Wiley-VCH.

- [3] Murata, K., et. al. (1997), "Determination of sulfate in brackish waters by laser Raman spectroscopy," *Analytica Chimica Acta*, 344, pp 153-157.
- [4] ACI Committee 201, (2008) "ACI 202.2R-08 Guide to Durable Concrete," American Concrete Institute, Farmington Hills, Michigan.

6. Forensic Investigation of Turtle River Bridge Piles

6.1. Introduction

The objective of this research was to characterize the degradation mechanisms present in prestressed concrete piles exposed to marine environments in Georgia. With an in-depth understanding of relevant degradation phenomena, novel methods to increase the durability of coastal bridges can be developed with the goal of increasing bridge service lives to 100+ years. To better identify the pile deterioration mechanisms, piles from the I-95 at Turtle River Bridge in Brunswick, Georgia were investigated.

The deterioration of prestressed concrete piles in marine environments is a growing expense for the Georgia Department of Transportation (GDOT). Bridges are having to be replaced after less than 40 years in service, which is significantly less than the 75 to 100 year service life desired by the Federal Highway Administration (FHWA). For example, the substructure of the I-95 at Turtle River Bridge was replaced after only 32 years in service.

The exposure of structural concrete to the harsh Georgia coastal environment can cause several forms of degradation. The forms of attack vary with the exposure zone on the piling, as shown in Figure 6-1. Corrosion of the prestressing steel typically occurs in the tidal and splash zones, while carbonation and sulfate attack may occur in the submerged regions of the piles (Mehta, 1991). The piles recovered from the Turtle River Bridge upgrade were investigated for these damage mechanisms, in addition to inspection for any other potential degradation hazards. Section 6.2 investigates damage caused by corrosion of the prestressing steel. Section 6.3 examines the degradation of the piles due to sulfate attack. Section 6.4 investigates the biological attack that occurred on the concrete piles. Section 6.5 presents the conclusions and recommendations drawn from this study and suggest future research in certain areas.

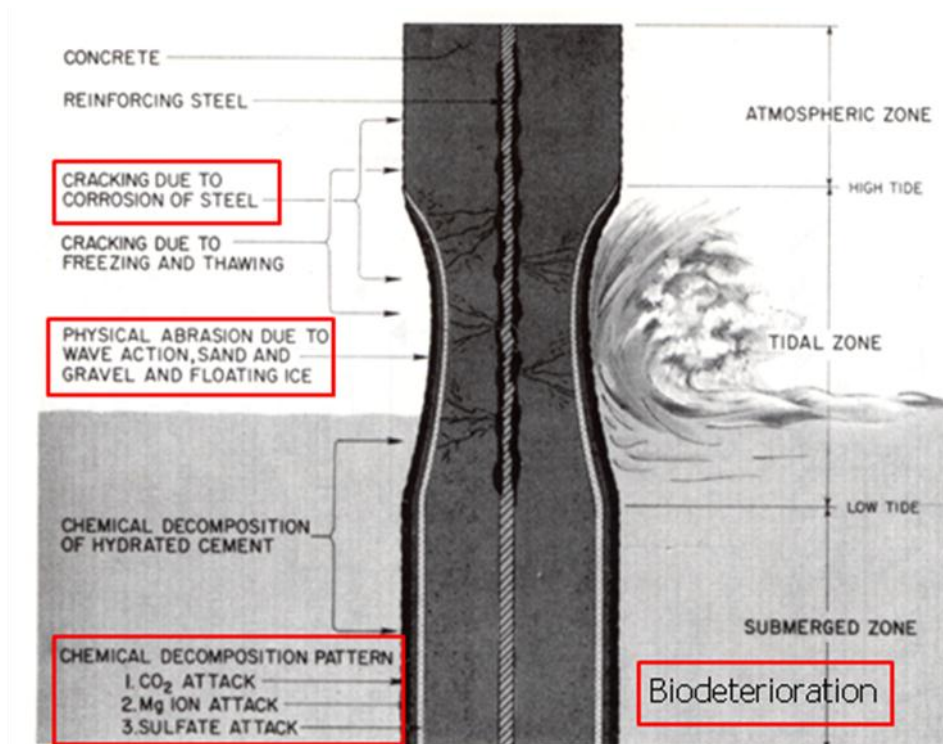


Figure 6-1: Typical degradation mechanisms in coastal concrete piling (Mehta, 1991)

6.1.1 Bridge Description

The I-95 at Turtle River Bridge (Structure ID: 127-0052-1) is located approximately 10 miles from the Atlantic coast, near Brunswick, GA, in Glynn County, as shown in Figures 6-2. The original bridge was constructed in 1977, and upgraded in 2009 by replacing the heavily damaged substructure. The damage observed by inspection teams is presented in section 6.1.2. Figure 6-3 shows the original and upgraded Turtle River Bridge. The bridge has 43 spans and has a total length of 3,488 ft. The bridge has a concrete road deck. The bridge has three primary spans, which are approximately 200 ft in length and are supported by steel I-girders. The remaining 40 spans are supported by prestressed concrete girders. The girders rested on elastomeric bearing pads on pier caps. The substructure consisted of 30"x30" hollow prestressed concrete piles, which supported the pier caps.

The piles were constructed with 9/16" prestressing strands and a 0.50 water-to-cement (w/c) ratio concrete using ASTM C 150 Type I cement. Natural sand was used for the fine aggregate, and a 1" maximum size aggregate (MSA) limestone was used for the coarse aggregate.

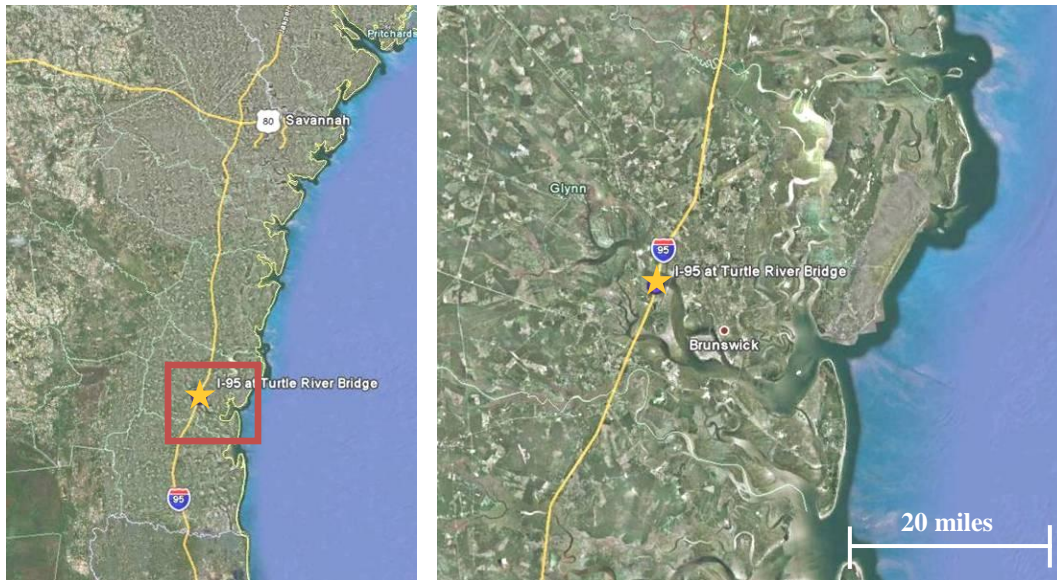


Figure 6-2: Location of I-95 at Turtle River Bridge



(a)



(b)

Figure 6-3: Overall view of bridge (a) before and (b) after upgrade

The substructure on the bridge was replaced using large transfer beams and drilled caissons into the subgrade. Figure 6-4 shows the original and upgraded substructure. The piles used for the forensic investigation were removed during construction so that the new caissons could be built. Only existing piles that interfered with the new substructure were removed. In Figure 6-4 (b), the old piling can be seen in place under the new bridge structure.



(a)



(b)



(c)

Figure 6-4: View of bridge substructure (a) before, (b) transfer girder after upgrade, and (c) drilled caisson support after upgrade

Four piles were delivered to the Georgia Tech in February, 2010. Figure 6-5 shows the piles upon delivery. Three of the piles contained the splash, tidal, and submerged regions, and the fourth was a fully submerged section. Figure 6-6 shows a pile after cleaning the biological growth off of the surface. The splash, tidal, and submerged zones are labeled.



Figure 6-5: Piles from Turtle River Bridge

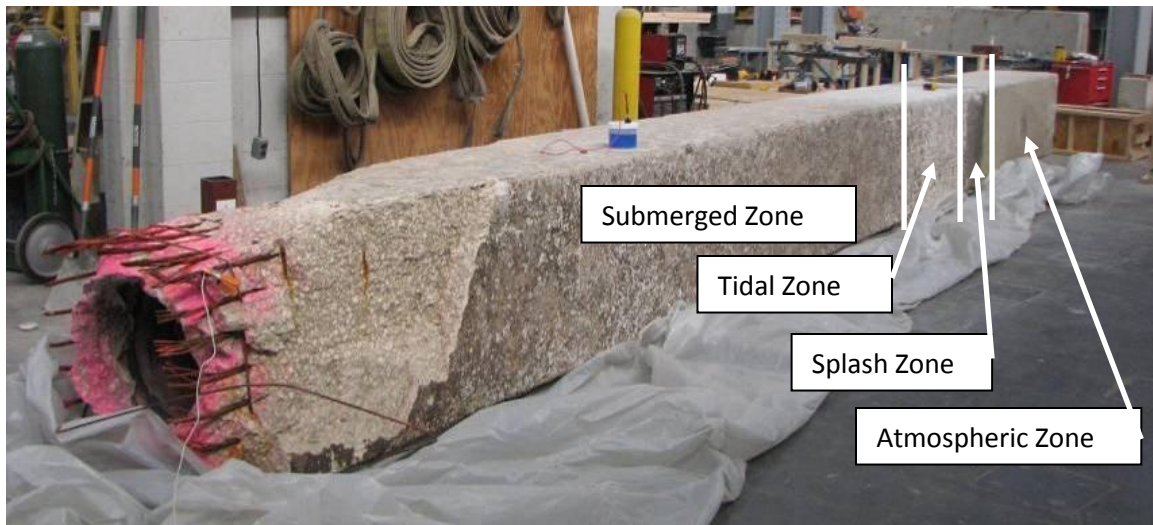


Figure 6-6: Pile after removal of biological growth

6.1.2 Inspection Report Data for Original Substructure

Access to the most recent inspection reports for the Turtle River Bridge was provided by GDOT. The most recent inspection of the substructure before replacement was performed in 2005, along with notes from previous inspections. The bridge inventory listing and bridge inspection reports are given in Appendix A.

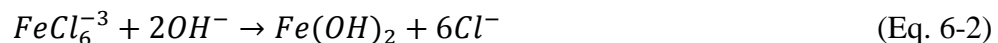
In the splash and tidal zones of piles, visual inspection of the piles showed heavy marine growth, moderate scaling and abrasion, vertical cracking, spalling, exposed prestressing steel, rust staining, and delaminations. The reported vertical cracks varied in width from hairline to 1/4 in. For the submerged region of the piles, it was noted that the concrete piles were “soft” and that the concrete could be easily chiseled off. Also, several piles had vertical cracks in the corners that ran from the mudline up 6 ft to 12 ft, with a width varying from hairline to 1/32 in. (0.030-in.) in width. Additionally, according to the report, multiple piles had been encased in a fiberglass sheath with epoxy as a rehabilitation method.

The inspection reports suggest visual signs of degradation consistent with chloride-induced corrosion of the reinforcement plus chemical attack and potential biological attack of the concrete. The forensic investigation of the recovered piles characterized the deterioration mechanisms present that caused the observed damage.

6.2. Corrosion of Prestressing Steel

Concrete’s highly alkaline environment allows for the formation of a thin oxide layer on the surface of reinforcing steel. The thin passive film protects the steel from corrosion in alkaline environments. If the passive layer is destroyed, active corrosion can occur. The passive film can be broken down by decreasing the pH of the surrounding environment, local attack from aggressive ions, or a concurrence of both (Bertolini, et. al., 2004).

Chlorides from the surrounding marine environment are able to ingress into the concrete over time through various transport mechanisms. The protective oxide film that forms on the surface of the steel in the alkaline concrete environment is broken down locally by the presence of a sufficient local chloride concentration, and pitting corrosion can result. Pitting is a localized form of corrosion which initiates when chlorides attack defect sites in the passive film. Two reactions that occur in breaking down the passive film are given below in Eq. 6-1 and Eq. 6-2 (Bertolini, et. al., 2004).



The reactions do not consume the chlorides, and lower the pH at the pitting site by depleting the OH^{-} ions in the formation of the iron oxides. In concrete, the surrounding regions remain alkaline, and hydroxide ions are available in the pore solution which causes the surrounding regions to act as cathodes for the corrosion reactions. As the pit grows, it gains a net positive charge from the hydrogen and metal ions which attract more chlorides into the pit, causing an

autocatalytic reaction. At the surface, a porous cap can form from the corrosion products that further allows the pit to grow.

The corrosion of the prestressing steels leads to a loss of steel section. Additionally, the corrosion of steel leads to the formation of iron oxides which are less dense than the original steel and occupy more volume. The formation of oxides causes tensile forces in the surrounding concrete and can lead to cracking and delamination of the cover concrete, as well as rust staining on the surface of the piles.

The causes and extent of damage produced by chloride-induced corrosion were investigated by performing a visual assessment of the damage (section 6.2.1), mapping the corrosion potentials (section 6.2.2), and determining the chloride profiles (section 6.2.3). The chloride profiles were used for service life modeling.

6.2.1 Visual Assessment of Damage

A visual inspection of the splash and tidal zones of the piles showed vertical cracks along the corners of the piles as shown in Figure 6-7. The average crack widths were approximately 0.01", but were as large as 0.05". Additionally, delamination of the cover concrete had occurred over the corner strand on one pile. The exposed surface showed extensive corrosion damage to the strand and staining of the surrounding concrete (Figure 6-8). The delamination occurred normal to the surface of the concrete through the corner strand location as illustrated in Figure 6-9.



Figure 6-7: (a,b) Corrosion induced longitudinal cracking of piles



(a)



(b)

Figure 6-8: (a,b) Corrosion induced delamination, loss of steel section, and staining of piles

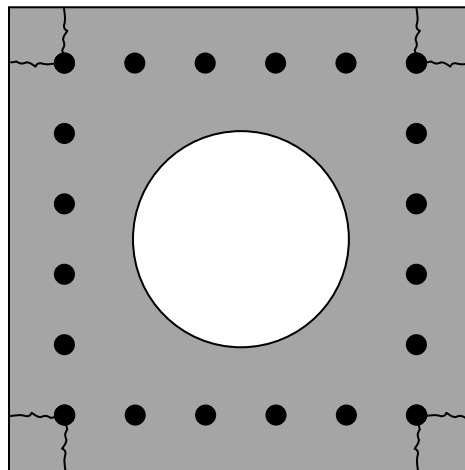


Figure 6-9: Cracking and delamination pattern on the cross-section in splash and tidal zone

Inspection of corroded strands indicated the presence of pits and preferential locations in the crevices between the braided wires of the strand. Figure 6-10 shows a core through a corroded strand and a magnified image of the corrosion products around the strand.

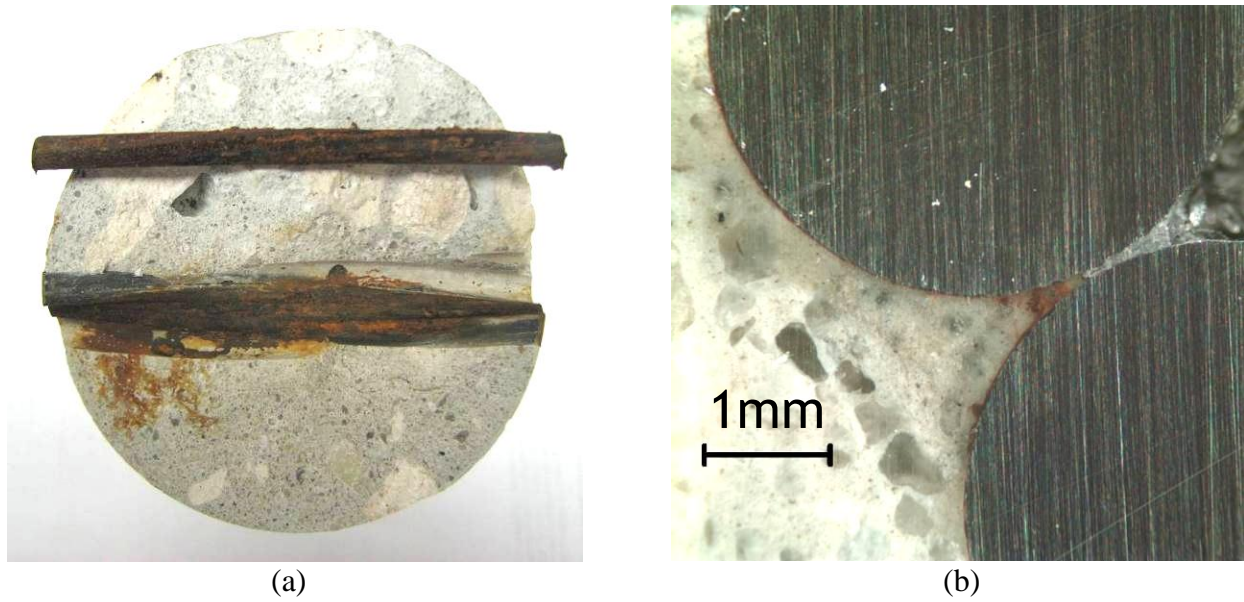


Figure 6-10: Corrosion of prestressing steel in extracted core

The pH of the concrete cover was studied by using a phenolphthalein indicator solution on freshly cut surfaces of the piles. The indicator solution turns pink if the pH is above approximately 9.2, representing uncarbonated concrete. The carbonation front can be seen in Figure 6-11. The carbonation front was found to be approximately 1" beneath the exposed surface of the piling, both in the submerged and tidal regions. This limited depth suggests that it is unlikely that corrosion of the reinforcement was caused by carbonation, but that a combination of decreased pH and ingress of chlorides caused pitting corrosion to occur.

Although carbonation of the concrete did not cause general corrosion of the reinforcement, it may have contributed to degradation of the cover concrete. Carbonation of concrete leads to the depletion of calcium hydroxide, which causes the decrease in pH, and can lead to a loss of calcium silicate hydrate (C-S-H), which is the primary strength giving component of hydrated cement paste (Neville, 1997). Additionally, ettringite is unstable at a pH below 11 (Neville, 1997).

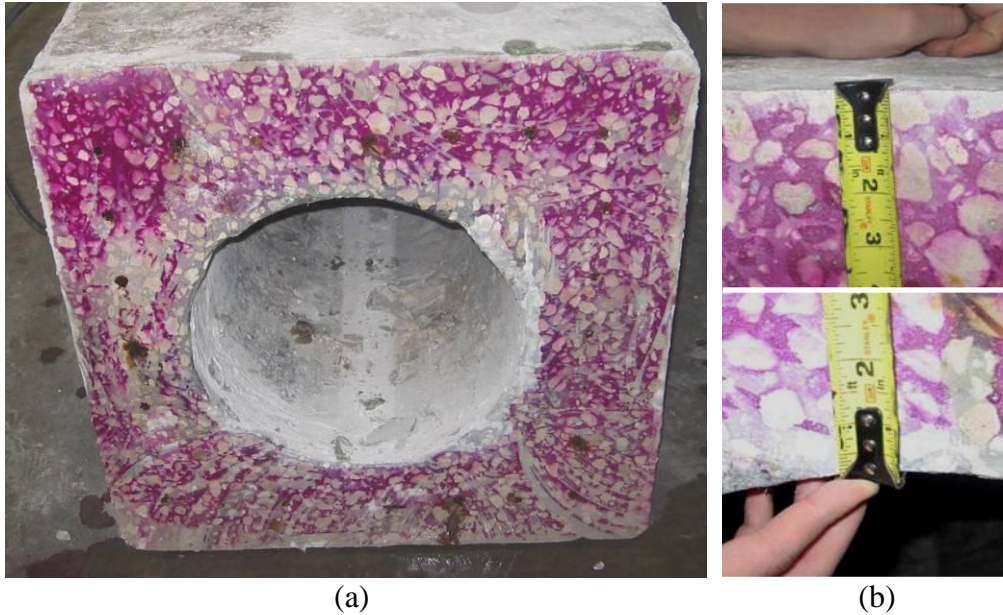


Figure 6-11: (a) Phenolphthalein indicator solution on sawn surface of pile, and (b) measurement of carbonation front

6.2.2 Half-cell Corrosion Potentials

The half-cell potential of the imbedded steel strands was used to identify regions where corrosion was occurring in accordance with ASTM C 879 (2009). The measurements were performed by measuring the half-cell potential of a strand versus a Cu/CuSO₄ electrode (CSE) using a voltmeter and by measuring the potential at one-foot intervals along the length of the pile. An electrical contact solution consisting of liquid dish detergent mixed with water was used to wet the surface for readings. Figure 6-12 shows the experimental set-up used.



Figure 6-12: Half-cell potential measurement set-up

Figure 6-13 shows the half-cell corrosion potentials from all four sides of a pile. According to ACI Committee 222 (2001), a half-cell potential greater than 350 mV indicates a 90% or greater probability of corrosion occurring. A half-cell potential less than 200 mV indicates a 10% or less probability of corrosion occurring. The results suggest that from 2 ft above high tide and below that there is a strong probability that corrosion is occurring. The rate of corrosion cannot be determined using this method. Therefore, a half-cell potential in excess of 350 mV does not indicate that corrosion is occurring at a highly deleterious rate. The corrosion rate is heavily influenced by environmental factors, including adequate presence of moisture and oxygen. If insufficient oxygen is present, then the corrosion rate can be orders of magnitude smaller.

The lack of oxygen in the submerged zones of piles explains why no corrosion induced damage was seen, even though the half-cell potential suggests that corrosion is occurring. The tidal and splash zones of piles have adequate access to moisture and oxygen due to the wetting and drying cycles present. This leads to a significantly faster corrosion rate, which could be the reason for the large amount of damage found.

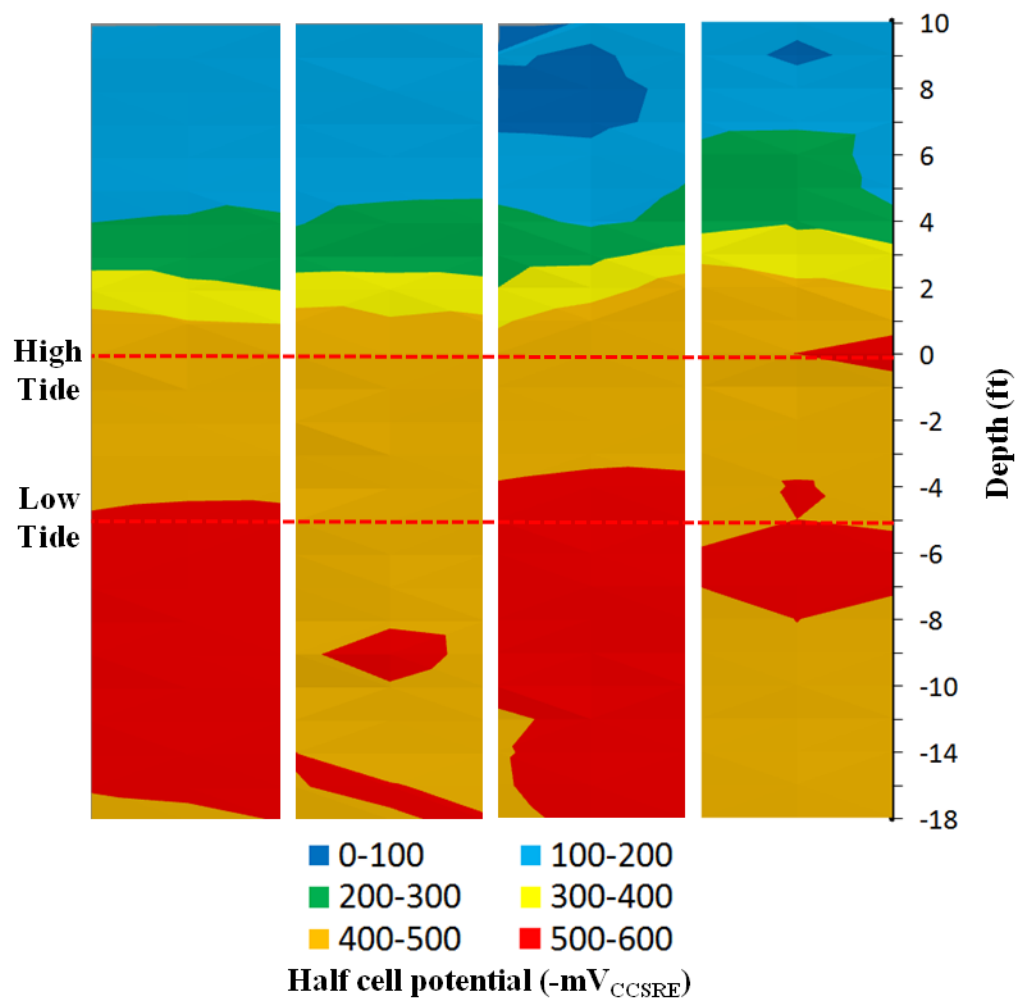


Figure 6-13: Half-cell potential map of the four faces of a Turtle River Bridge pile

6.2.3 Chloride Profiles

The concentration of chloride ions near the reinforcement surface is critical in causing the onset of pitting corrosion and in furthering the corrosion reactions; therefore, it is important to understand the migration of chloride ions through the concrete and to understand the interactions between those ions and the cementitious system. Chlorides ingress into the concrete piles from the surrounding brackish water. Their movement through the concrete is often modeled with Fick's second law of diffusion. However, other transport mechanisms, like capillary action, can affect the transport of chlorides through the cement paste. The apparent diffusion coefficient of a concrete mix exposed to chlorides can be determined experimentally and used for service life estimation in a given environment (Bertolini, et.al., 2004).

Within the concrete, chlorides exist in a free or uncombined form and in bound forms, where they may combine with existing hydration products or unhydrated cementitious phases. In the bound form, the most common product formed is Friedel's salt $[\text{Ca}_2\text{Al}(\text{OH})_6\text{Cl}\cdot 2\text{H}_2\text{O}]$. When the concentration of chlorides reaches a threshold value at the surface of the reinforcing steel, corrosion will initiate when the passive film is broken down. There is considerable debate as to how to define the chloride threshold limit (CTL) and what the value should be (Mohammed and Hamada, 2003). The threshold values are typically reported as the total or free chlorides as a percent mass of concrete (or cement) or by the ratio of the concentration of chloride ions to the concentration of hydroxyl ions ($[\text{Cl}^-]/[\text{OH}^-]$).

In practice, the total chloride content is used more frequently for threshold values, even though it is generally believed that the free chlorides are responsible for the initiation of corrosion (Mohammed and Hamada, 2003). The CTL is typically assumed to be between 0.4% to 1% mass of binder, or approximately 0.05% to 0.2% by mass of concrete, for total chloride content (Bertolini, et. al., 2004). However, reported values for the CTL have varied from 0.04% to 8.34% by mass of binder based upon total chloride content (Angst, et. al., 2009). The CTL is difficult to define since the reported values vary with cement composition, water to cement ratio, exposure temperature, internal pH, and type of steel used (Angst, et. al., 2009).

6.2.3.1 Test Methodology

The total chloride concentration was measured using the ASTM C 1152 (2004) procedure, which was performed by taking 3" diameter cores through the depth of the cross-section, drilling at 1/2" increments using a 3/8" masonry bit, and collecting the powder. The concrete powder was ground using a mortar and pestle and sieved until a minimum of 30 g passed through the 850 mm sieve for each depth increment. The acid soluble chloride testing was performed by measuring 10 g of the powder into a beaker and adding 75 ml of reagent water. Next, 25 ml of dilute (1:1) nitric acid was added to the beaker. The sample was stirred until any lumps were broken up. Next, the sample was rapidly heated to a boil for 10 seconds, then removed from heat. The sample was then filtered using a Buchner funnel and filtration flask with suction through a Grade 41 coarse-textured filter paper. The sample was then allowed to cool to 25 °C. The sample was titrated with Silver nitrate solution (0.1 N) to determine the acid soluble chloride content.

The free chloride concentration was measured using the ASTM C 1218 (1999) procedure, which was performed by taking 3" diameter cores through the depth of the cross-section, drilling at 1/2" increments using a 3/8" masonry bit, and collecting the powder. The concrete powder was ground using a mortar and pestle and sieved until 30 g passed through the 850 mm sieve for each depth increment. The water soluble chloride testing was performed by measuring 10 g of the powder into a beaker and adding 50 ml of reagent water. Next, the sample was covered and brought to a rapid boil for 5 minutes. The sample was allowed to sit for 24 hours. Next, the sample was filtered using a Buchner funnel and filtration flask with suction through a Grade 40 Class G filter paper. After filtering, 3 ml of (1:1) nitric acid and 3 ml of hydrogen peroxide (30% solution) were added to the sample, which was then covered and allowed to stand for 1 minute. The sample was then brought to a boil for 10 seconds while still covered, then removed from heat. The sample was then allowed to cool to 25 °C. The sample was titrated to determine the water soluble chloride content.

Titration was performed using the Metrohm 798 MPT Titrino. A silver/silver chloride standard electrode was used. Silver nitrate solution (0.1 N) was added in 0.1 ml aliquots to the sample until an equivalence point was achieved. Figure 6-14 shows the filtration and titration methods. The chloride content was then determined using Eq. 6-3 to compute the percent chlorides by mass of sample.

$$\text{Cl, \%} = 3.545 * V * N / W \quad (\text{Eq. 6-3})$$

Where,

- V = milliliters of AgNO_3 solution used for titration at equivalence point
- N = exact normality of AgNO_3 solution
- W = mass of sample, g



(a)



(b)

Figure 6-14: (a) Filtration of chloride sample, and (b) titration of sample

6.2.3.2 Results, Chloride Concentrations

Total and free chloride concentrations were determined at various heights along the pile, as shown in Figure 6-15. The locations were chosen to coincide with the atmospheric, splash, high and low tide, and submerged regions of the pile. The notation used for identifying samples was that a positive value indicated a depth below high tide, and a negative value was above high tide. Cores were taken in the center of the pile to avoid the effect of 2-D transport from another surface of the pile.

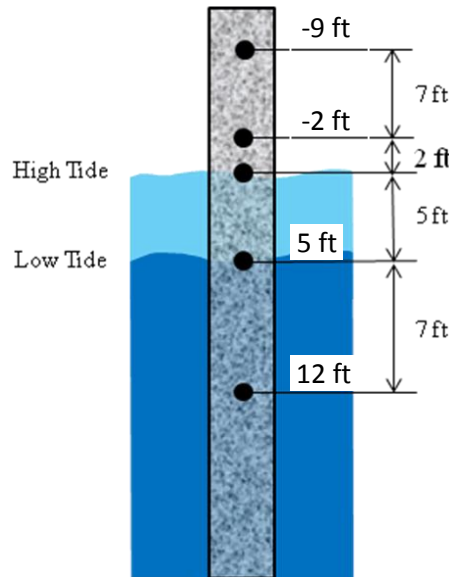


Figure 6-15: Locations of chloride concentration sampling

Figure 6-16 shows the total chloride concentrations from each sampling location with respect to depth into the cross-section. The results suggest that the concentration of total chlorides at the level of the reinforcement is significantly higher than the CTL values given in the literature. The concentrations were in agreement with the half-cell corrosion potentials, which suggested that active corrosion was occurring due to depassivation and destruction of the passive film on the surface of the steel. The chloride profiles for high tide, 5 ft, and 12 ft elevations were very similar. However, the concentration at the surface varied widely between the elevations and may be due to the presence of wetting and drying cycles in the tidal zone compared to the fully saturated condition in the submerged region. The 2 ft above high tide profile had a greatly reduced chloride content compared to submerged regions. Additionally, was observed from the 9 ft above high tide data that the background chloride content in the mix was 0.01% by mass of concrete. The low background content suggested that the mix did not use seawater for mixing, dredged fine aggregate, or large quantities of chloride containing admixtures.

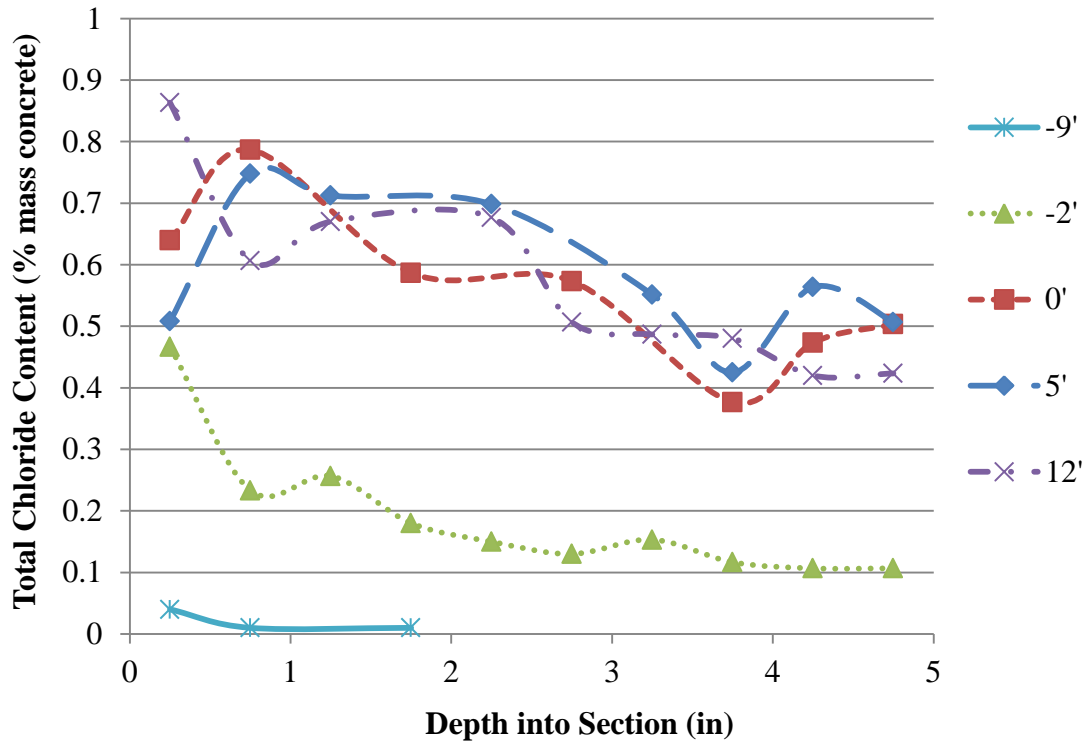


Figure 6-16: Total chloride content of concrete columns at various depths

Figure 6-17 shows the free chloride concentration profile at the selected locations along the length of the pile. The results suggest that the concentration of free chlorides at the level of the reinforcement is significantly higher than the CTL values given in the literature. The free chloride profiles follow a similar trend to the total chloride profile at each depth. The profile for 9 ft above high tide shows that all chlorides present over $\frac{1}{2}$ in. into the section were bound.

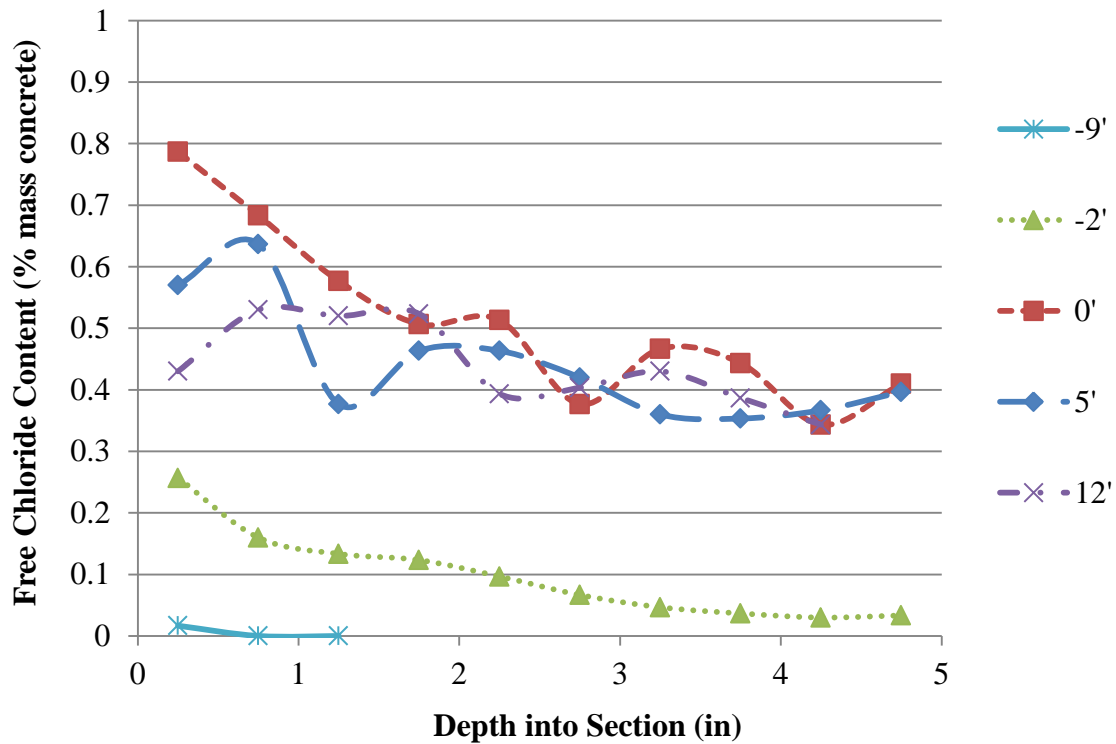


Figure 6-17: Free chloride content of concrete columns at various depths

A comparison of the total to free chloride content measured at each increment from the piles is given in Figure 6-18. From a simple linear regression between the total and free chloride concentrations, it was found that 18.6% of the total chloride content is bound. There is a large scattering of data, but the percent bound chlorides is consistent with the value of 18.7% found by Mohammed and Hamada (2003) from field exposure measurements.

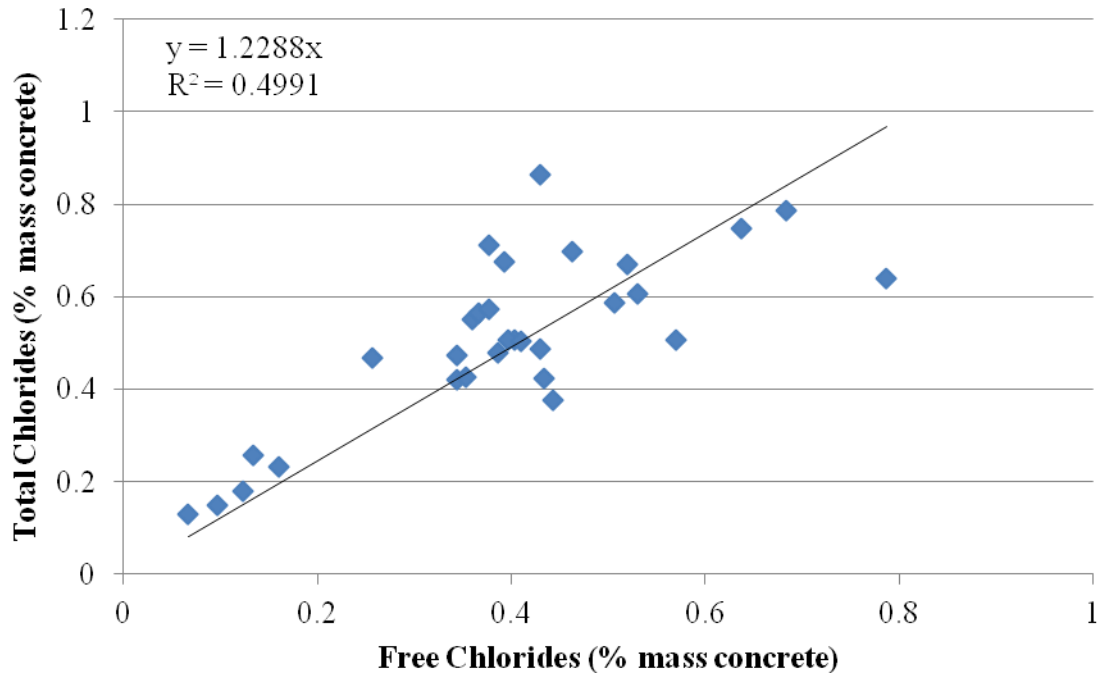
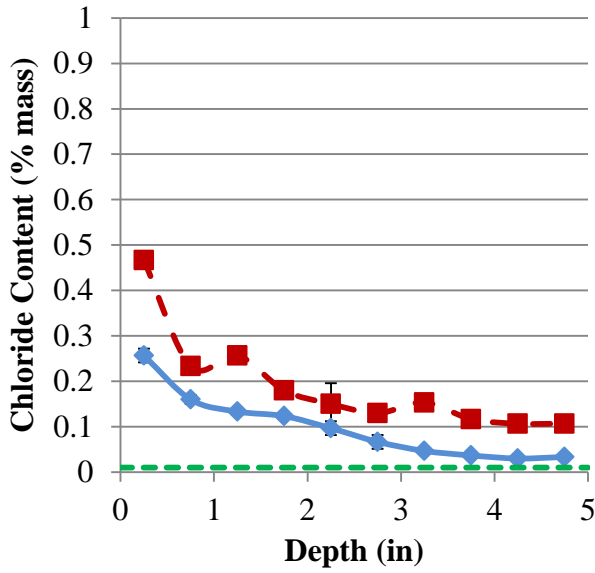
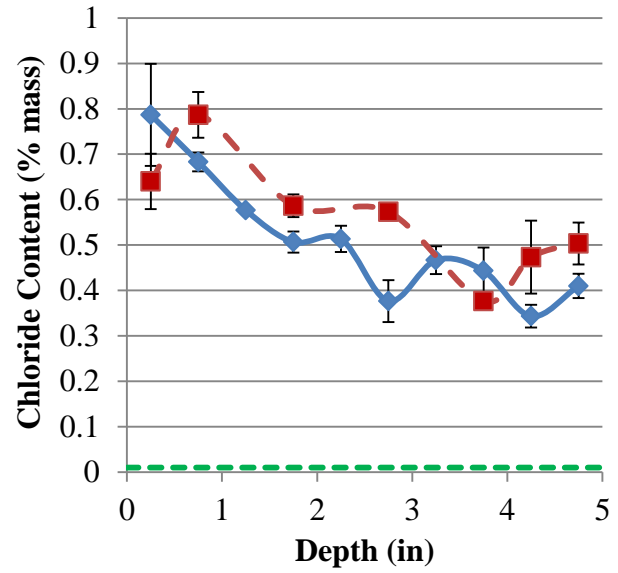


Figure 6-18: Comparison of total to free chloride concentrations

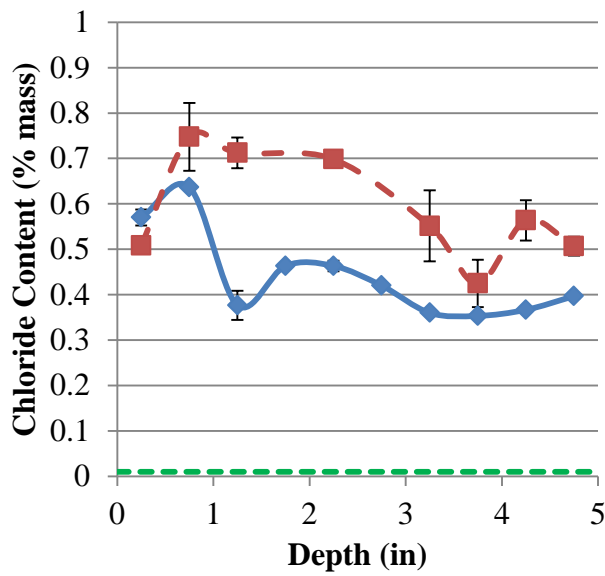
Figure 6-19 shows the free and total chloride concentrations at 12 ft, 5 ft, high tide, and -2 ft. The free chloride content follows a similar profile to the total chlorides, but the value is reduced due to binding of chlorides. The concentrations near the surface were highly variable between acid and water samples for the same depth, and could be due to variable surface conditions of cores due to biological attack and coring induced damage.



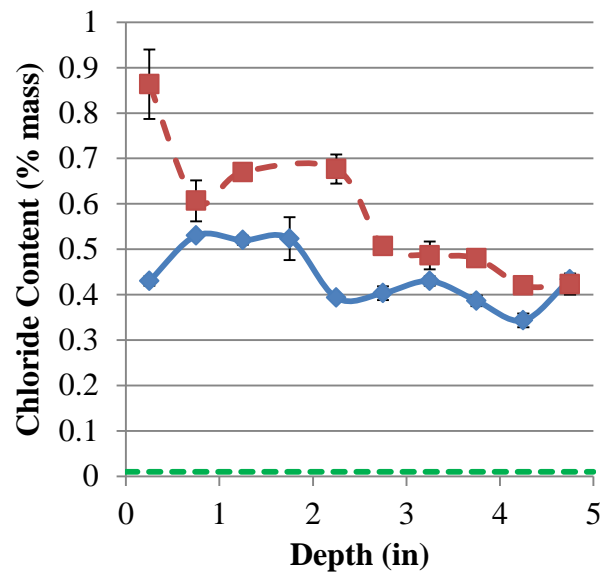
(a)



(b)



(c)



(d)

◆ Free Chlorides
 -■- Total Chlorides
 --- Background Chloride

Figure 6-19: Chloride profiles at (a) 2 ft above high tide, (b) high tide, (c) 5 ft below high tide, and (d) 12 ft below high tide

6.2.3.3 Chloride Ingress Modeling

The ingress of chlorides into a structure is often treated as a diffusion-based transport phenomenon (Bertolini, et. al., 2004). Fick's second law can be used with experimental data to determine the diffusion coefficient that characterizes the diffusion-based transport properties of a concrete mix. Additionally, if the diffusion coefficient and environmental parameters are known, the time necessary for the CTL to be reached can be determined and used for service life modeling.

The chloride profiles were used to determine the apparent chloride diffusion coefficient by performing a non-linear regression analysis, using the method of least squares to fit to the equation given by Eq. 6-4 (ASTM C 1152, 2004).

$$C(x,t) = C_s - (C_s - C_i) * \operatorname{erf}\left(\frac{x}{\sqrt{4*D_a*t}}\right) \quad (\text{Eq. 6-4})$$

Where,

- $C(x,t)$ = chloride concentration, measured at depth x and exposure time t , mass %
- C_s = projected chloride concentration at the interface between the exposure liquid and test specimen that is determined by the regression analysis, mass %
- C_i = initial chloride-ion concentration of the cementitious mixture prior to submersion in the exposure solution, mass %
- x = depth below the exposed surface (to the middle of a layer), m
- D_a = apparent chloride diffusion coefficient, m^2/s
- t = the exposure time, s
- erf = error function
 $= \frac{2}{\sqrt{\pi}} * \int_0^z \exp(-u^2) du$

An approximation developed by Winitzki (2006) for the error function was used to perform the regression analysis. The approximation, given in Eq. 6-5, results in a maximum relative error of less than 1.3%.

$$\operatorname{erf}(x) \approx \left[1 - \exp\left(-x^2 \left(\frac{\frac{4}{\pi} + 0.147x^2}{1 + 0.147x^2}\right)\right) \right]^{\frac{1}{2}} \quad (\text{Eq. 6-5})$$

Life 365 Service Life Prediction Model (Ehlen, 2009) was used to estimate the diffusion coefficient and expected service life of the structure. The primary parameters necessary for using Life 365 are the structure location, exposure type, concrete cover distance to reinforcing steel, and mix design details, including w/cm, percent replacement of cement with supplementary cementitious materials, and use of corrosion inhibitors. The results of the nonlinear regression diffusion coefficient results compared to the Life 365 estimates are shown in Table 6-1. The Life 365 estimates were based upon a marine tidal zone exposure in Savannah, Georgia for a 0.50 w/c mix design using only Portland cement. The experimentally determined data were compared to the Life 365 data for the estimated time to corrosion initiation based upon

a CTL of 0.05% by mass of concrete, which is the default value used by Life 365 (Ehlen, et.al., 2009).

Table 6-1: Comparison of Life 365 estimates to experimental data

	Experimental	Life 365	% Difference
Diffusion Coefficient ($\text{in}^2/\text{s} * 10^{-8}$)	2.56	2.14	16.44
Surface chloride concentration (% mass concrete)	0.797	0.800	0.44
Time to corrosion initiation (years)	3.1	3.7	19.35

Overall, Life 365 gave reasonable predictions of diffusion coefficient, surface chloride concentration and time to corrosion (Table 6-1). Life 365 underestimated the diffusion coefficient that was observed from curve fitting. However, the diffusion coefficient observed could be influenced by other damage mechanisms that were occurring in the piles. The observed biological attack, sulfate attack, and potential cracking from construction practices could all lead to an increased permeability and diffusion coefficient. The discrepancy between diffusion coefficients is responsible for the variation in time to corrosion initiation. Life 365 and the experimental data were in agreement on the surface concentration for this exposure zone. The time to corrosion initiation was significantly less than the 75+ year lifespan desired by GDOT. After corrosion initiates, the time until repair or replacement is required varies heavily on the corrosion rate, which can vary by orders of magnitude. The Life 365 program assumes a 6 year propagation time in their service life calculations (Ehlen, et. al., 2009). However, frequently the failure of a structure due to chloride-induced corrosion is assumed to occur at corrosion initiation for service life modeling (Bertolini, et. al., 2004).

6.2.4 Conclusions, Corrosion of Prestressing Steel

The piles from the Turtle River Bridge showed extensive damage from chloride-induced corrosion. The corrosion half-cell potentials indicated that the prestressing strands were undergoing active corrosion from the tidal zone to mudline. The chloride profiles indicated that the concentration of chlorides at the reinforcement, 0.35% to 0.45% by mass of concrete, was significantly higher than the 0.05% necessary to initiate pitting corrosion. The large amount of concrete cracking and spalling and of steel corrosion damages were limited to the tidal and splash zones on the piles, due to the limited availability of oxygen in the fully submerged regions of the piles.

The diffusion coefficient for chloride transport in the concrete showed that the concentration of chlorides at the level of the steel would exceed the threshold value after only 3.1 years of

service in the marine environment. This suggests that the concrete mix used is not adequate for long-term exposure to this environment. The service life analysis program Life 365 was able to predict the diffusion coefficient to within 16% of the measured value. The measured was higher, likely due to contributions of additional forms of degradation to increased permeability in the concrete piles.

6.3. Sulfate Attack

Concrete piling in seawater and brackish water can be exposed to high concentrations of sulfates. In addition to sulfates present in the water, it is being investigated if additional sulfates may be produced by bacteria on the surface of the piles. The primary forms of sulfates present are NaSO_4 and MgSO_4 (Skalny, et. al., 2002). Damage to the concrete due various reactions between the ingressing sulfate ions and hydration products and anhydrous cement phases in the cement paste is termed “sulfate attack”. Two primary mechanisms are associated with sulfate attack. First, sulfate ions can react with monosulfoaluminate or available tricalcium aluminate to form ettringite. The formation of ettringite can be expansive and lead to cracking and spalling. The calcium consumed in this reaction comes from the dissolution of available portlandite. In addition, sulfate ions may react with available calcium hydroxide to form gypsum. If there is no portlandite present, then the calcium comes from the decomposition of the calcium silicate hydrate phase (C-S-H). The loss of calcium from the C-S-H leads to a reduction in strength (Skalny, et. al., 2002).

In the case of magnesium sulfate attack, additional reaction mechanisms are possible. Magnesium sulfate reacts with portlandite to form brucite, in addition to gypsum. Simultaneously, C-S-H is decomposed and converted to an amorphous hydrous silica or magnesium silicate hydrate phase. The decomposition of C-S-H is significantly faster with exposure to magnesium sulfate compared to sodium sulfate (Skalny, et. al., 2002).

Visible signs of sulfate-induced damage include a whitish appearance of the cement paste in damaged areas, as well as cracking (due to expansion), softening of the paste, delaminations, and spalling, with the damage typically starting at corners and edges. In addition, loss of strength and modulus can be measured (Neville, 1997). The sulfate attack damage to the bridge piles was characterized by performing a visual inspection of the piles, hardness measurements, and TGA (thermo-gravimetric analysis) and XRD (x-ray diffraction) analysis.

6.3.1 Visual Assessment of Damage

A visual assessment of the submerged region was performed. Cracks were found near the corners of the piles that extended from the mudline up to low tide. The width of these crack varied widely, with a maximum of 0.05 in., but most were approximately 0.025 in. in width. Spalling and abrasion was also apparent at the surface. Additionally, marine life had grown along the cracks that growth may have led to increased deterioration. Figure 6-20 shows the measurement of a crack, along with marine growth inside of a crack.



Figure 6-20: (a) Cracking along corner of pile, and (b) marine growth in crack

A core taken through the cross-section revealed a visible whitish discoloration of the cement paste near the surface in the submerged region of the pile as shown in Figure 6-21. The depth of the color change was consistent with the cracking location along the corners of the piles.

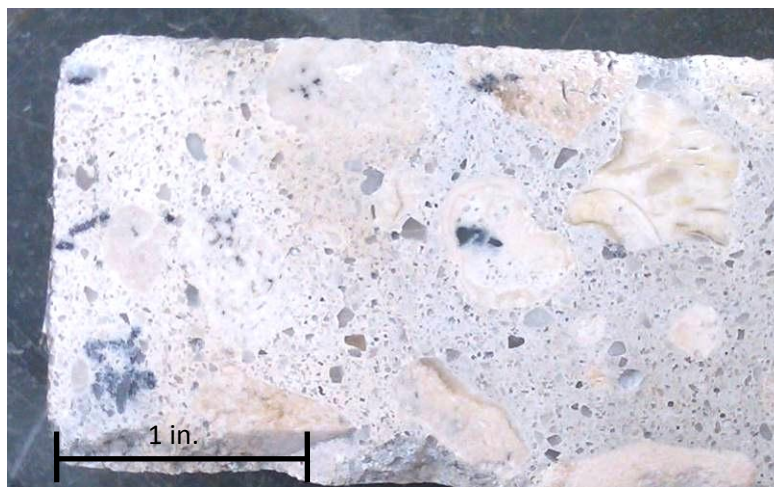


Figure 6-21: Whitish discoloration near surface in submerged region

6.3.2 Hardness Measurements

To determine if a variation existed between the different exposure regions, the hardness of the concrete was measured using two different methods - rebound hammer to measure coarser variations in hardness along the length of the piles and Vickers hardness to measure finer variations in hardness through the depth of the pile. . Rebound hammer testing was performed at 1 ft increments along the length of the pile in accordance with ASTM C 805 (2008). A minimum of 10 readings were taken at each location on a smooth surface. Any reading outside the average by more than 6 units was discarded. The calibration from rebound number to strength (or hardness) is provided by the manufacturer for each orientation of testing. The calibration is affected by moisture condition of the concrete, depth of carbonation, and other environmental factors that make the relationship highly variable. However, the rebound hammer

number was correlated to a strength for interpreting results to correct for the orientation of the hammer during testing, which affects the rebound number. The calibration from rebound number to strength (or hardness) was provided by the manufacturer (Figure 6-22).

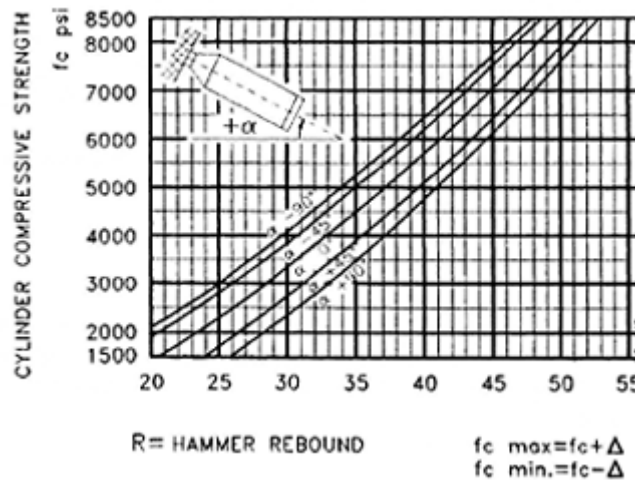


Figure 6-22: Rebound hammer calibration

The results from the rebound hammer testing performed on two piles have been converted into compressive strengths, as previously described, and are shown in Figure 6-23. A negative depth represents above high tide; a positive depth is below high tide. The results suggest a large change in surface hardness, and potentially strength, that occurs in between the splash and low tide region of the piles. The results show an average reduction in strength of approximately 50% from the region of the pile exposed to the atmosphere to the submerged concrete. The reduction in strength occurred rapidly near the high tide region of the piles, and continued to decrease at a gradual rate with increasing depth.

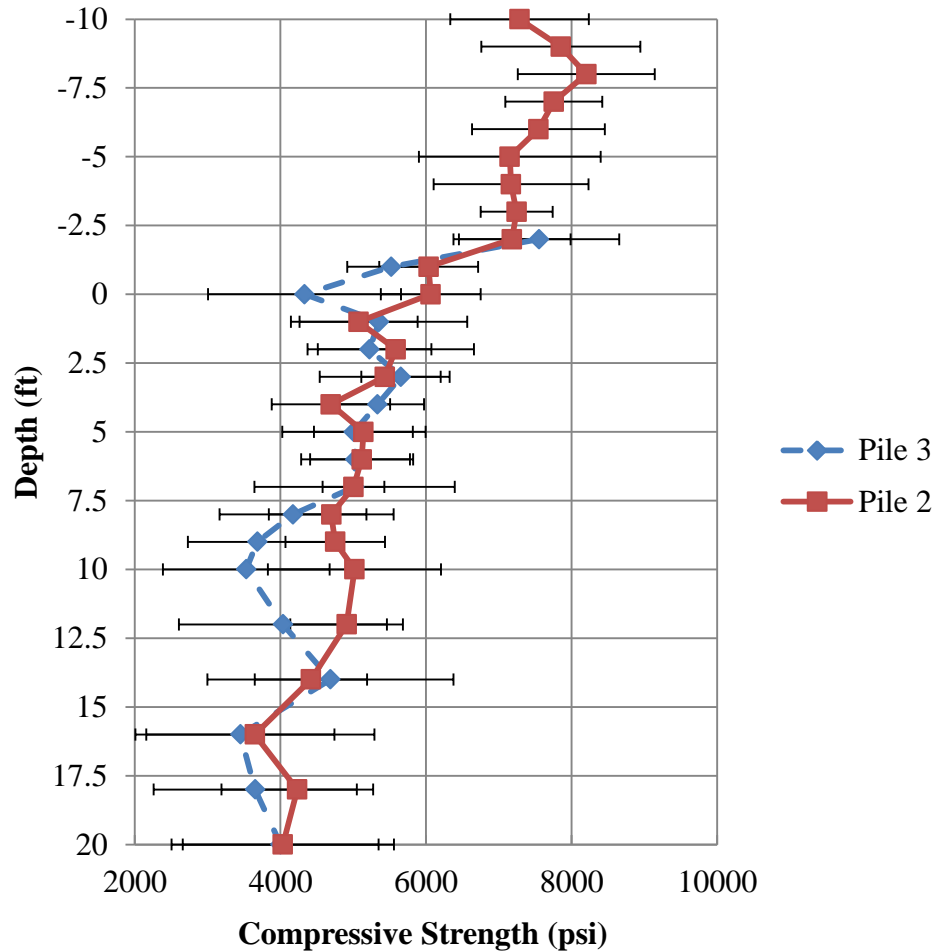


Figure 6-23: Rebound hammer results

Vicker's indentation measurements were performed on polished slices of cores to determine the variation in micro-hardness of the cement paste with depth into the section. Vicker's indentations were performed in accordance with ASTM C 1327 (2008) using 1 kg mass applied for 15 seconds. A minimum of 5 indentations were made at ¼ in. increments into the section on sections polished with 1 micron alumina.

The indentations were measured using a Leica TCS NT confocal microscope. Measurements were made to the nearest micrometer across both diagonals, then the average used for calculating the hardness number. Figure 6-24 shows the results of the measurements for 2 ft above high tide and 12 ft below in the submerged region. The outer 2 in. of the submerged region had a reduced hardness compared to the 2 ft above high tide sample. The depth at which the hardness significantly increased coincided with the location of the whitish color change on the samples.

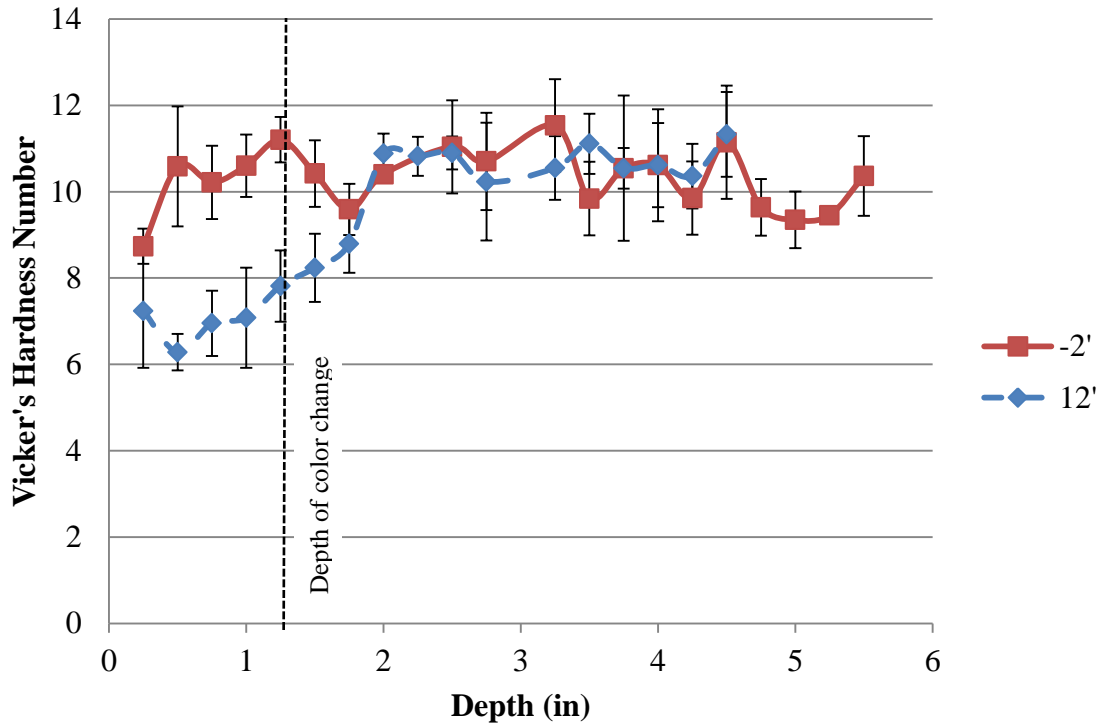


Figure 6-24: Vicker's hardness measurements

6.3.3 Compressive Strength Testing

The compressive strength of the piles was determined in accordance with ACI 214.4R-10 (ACI Committee 214, 2010) and ASTM C 39 (2005). Two sets of tests were performed. First, three 3 in. diameter cores were obtained away from the surface of the pile, as shown in Figure 6-28. Three sets of cores were taken along the length of the pile in the atmospheric, tidal, and submerged zones for comparison of the undamaged concrete along the length of the piles. The specimens were cut to a 6 in. length using a wet cut concrete saw.

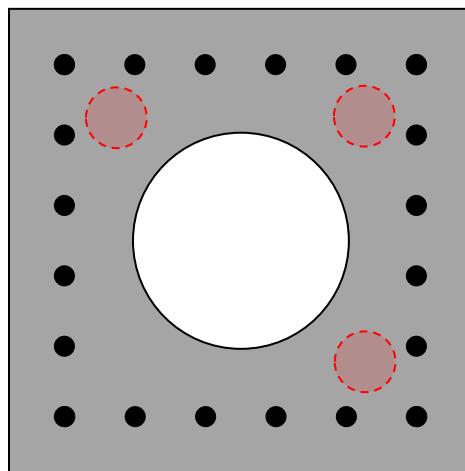


Figure 6-28: Compressive strength core locations

Also, cores were taken through the section to determine if there was a variation between concrete near the surface and the interior undamaged concrete. Cores were taken at -9 ft, high tide, 5 ft, and 12 ft depth. Four 3 in. diameter cores were taken through the section and cut to 3 in. lengths, one at the surface and a section near the center of the pile at each location tested. The location and diagram of the stub specimens are shown in Figure 6-29.

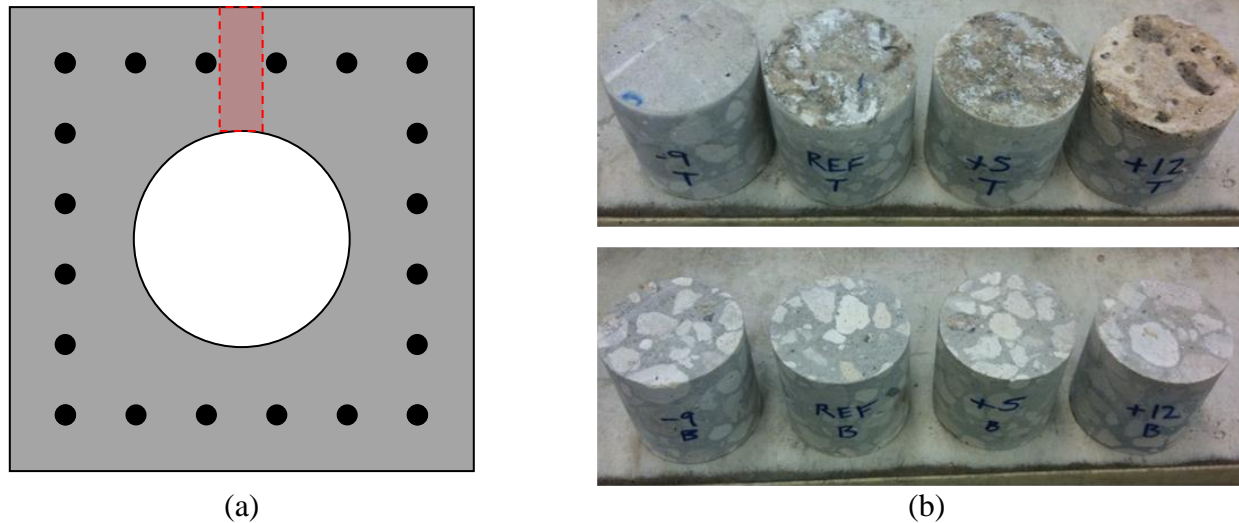


Figure 6-29: (a) Compressive strength core locations, and (b) surface (top) and interior samples (bottom)

The results of the compressive strength testing of undamaged interior concrete along the length of the piles are given in Figure 6-30. The average compressive strength from all three locations was 5.92 ksi, which is above the design strength of 5 ksi. ANOVA testing, using an alpha of 0.1, showed that the concrete from all three locations at the interior of the pile was statistically equivalent. Since the undamaged interior concrete was shown to be the same in the submerged, tidal, and atmospheric zones of the pile, the data suggested that the variation in rebound hammer results was due to a softening of the surface, and not a variation in undamaged concrete properties.

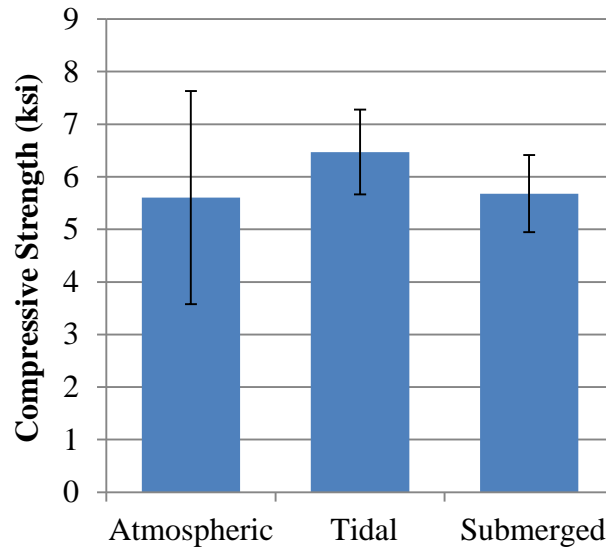


Figure 6-30: Compressive strength of undamaged interior concrete

The results of the stub compression tests comparing the surface to interior concrete are shown in Figure 6-31. The compressive strengths of the interior samples at all depths were determined to be statistically equivalent using ANOVA testing with alpha equal to 0.1. ANOVA analysis between the surface and interior concrete at each depth showed that only the -9 ft and high tide sections were statistically equivalent. The 5 ft and 12 ft samples both had statistical evidence to show the average compressive strengths were not the same. At 5 ft depth, the surface compressive strength was 80% of the interior concrete's strength. In the submerged region, the surface compressive strength was 55% of the interior concrete's strength. The strengths measured were consistent with the strengths determined from the impact hammer measurements.

The large reduction in compressive strength may be explained by a loss of C-S-H from sulfate attack or other forms of degradation, including carbonation. All of the surface samples from 12 ft below high tide failed due to a crushing near the surface and a single large crack through the remainder of the sample. The paste portion in the crushed region was a powdery consistency after failure.

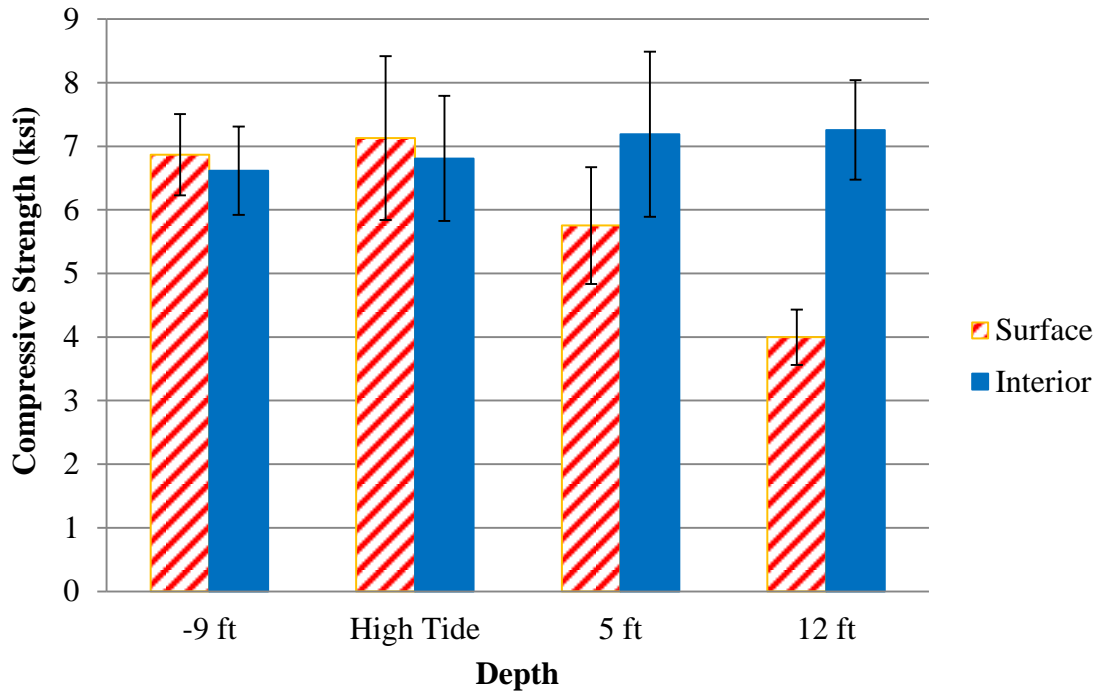


Figure 6-31: Compressive strength of surface versus interior concrete

6.3.4 X-Ray Diffraction

Powder X-ray diffraction (XRD) was performed on ground concrete samples to identify variances in the composition at various heights and depths into the cross section. Samples were taken at -9 ft, -2 ft, high tide, 5 ft, and 12 ft. Powder was obtained by taking a 3 in. diameter core through the section and then drilling at controlled increments using a 3/8 in. masonry bit. Powder was collected from the surface a 1/2 in. increment, then at 1 in. increments into the cross-section. The powder samples were then ground with mortar and pestle and sieved through an 850 μm (No. 20) sieve. Figure 6-32 shows a prepared XRD sample.

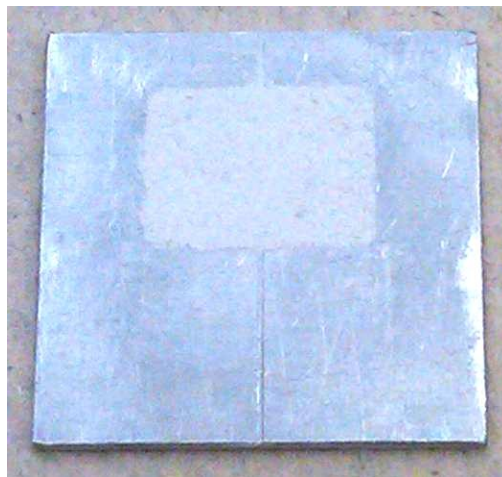


Figure 6-32: XRD sample

XRD analysis was performed using a Philip's X'Pert XRD system. The scan was performed over a 2θ range of 5° to 75° using a scan rate of 0.05° per second under Cu K- α radiation. Table 6-2 gives the notation used in labeling the peaks on the XRD profiles for each sample. In multiple incidences, peak locations for two or more phases overlapped. If other unique peaks for each phase were identified, then the shared peak was labeled for both phases.

The calcium carbonate and calcium magnesium carbonate phases represented the coarse aggregate in the concrete, as well as carbonated cement and calcium hydroxide. The quartz phase represented the fine aggregate used. The calcium hydroxide, ettringite, and gypsum phases occurred in the hydrated cement paste fraction of the sample. Calcium silicate hydrate, the predominant product of portland cement hydration, is largely amorphous, producing a broad peak around 30° on the 2θ scale.

Table 6-2: Chemical Symbols with Correlated Composition for XRD Profiles

Symbol	Composition
CH	Calcium Hydroxide
Ca	Calcium Carbonate (Calcite)
Ca(Mg)	Calcium Manganese Carbonate
Q	Quartz
E	Ettringite
G	Gypsum

6.3.4.1 XRD Results from 9 ft above High Tide

The results at 9 ft above high tide is given in Figures 6-33 and 6-34 for the 0 to 0.5 in. and 0.5 to 1.5 in. increments, respectively. The results from these samples serve as a reference for samples located in the exposure zones of the piles. The 9 ft above high tide samples showed the same compositions at both depth increments. Quartz, calcium carbonate, and calcium magnesium carbonate were all present due to the coarse and fine aggregate. The peaks from the aggregate are more intense than the paste phases due to their increased volume fraction. Calcium hydroxide was detected, but no residual ettringite from hydration or gypsum. Additionally, the amorphous rise is present from a 2θ of approximately 20° to 75° and indicates the presence of non-crystalline phases like calcium silicate hydrate.

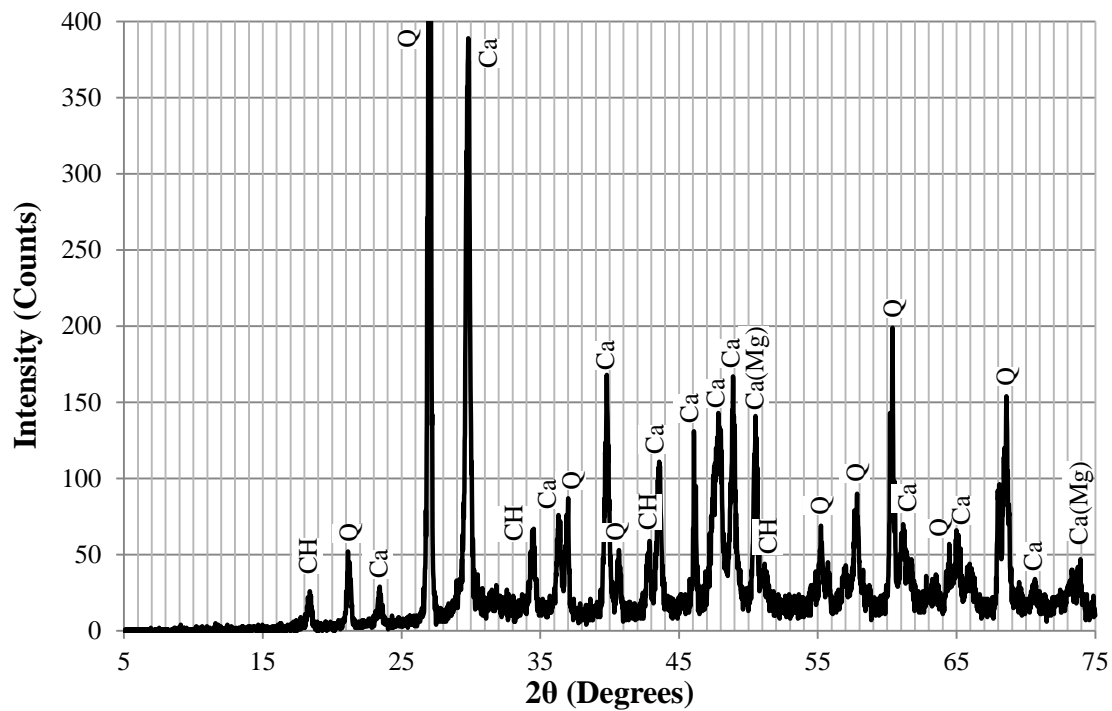


Figure 6-33: XRD profile for 9 ft above high tide at 0 – 0.5 in. increment into section

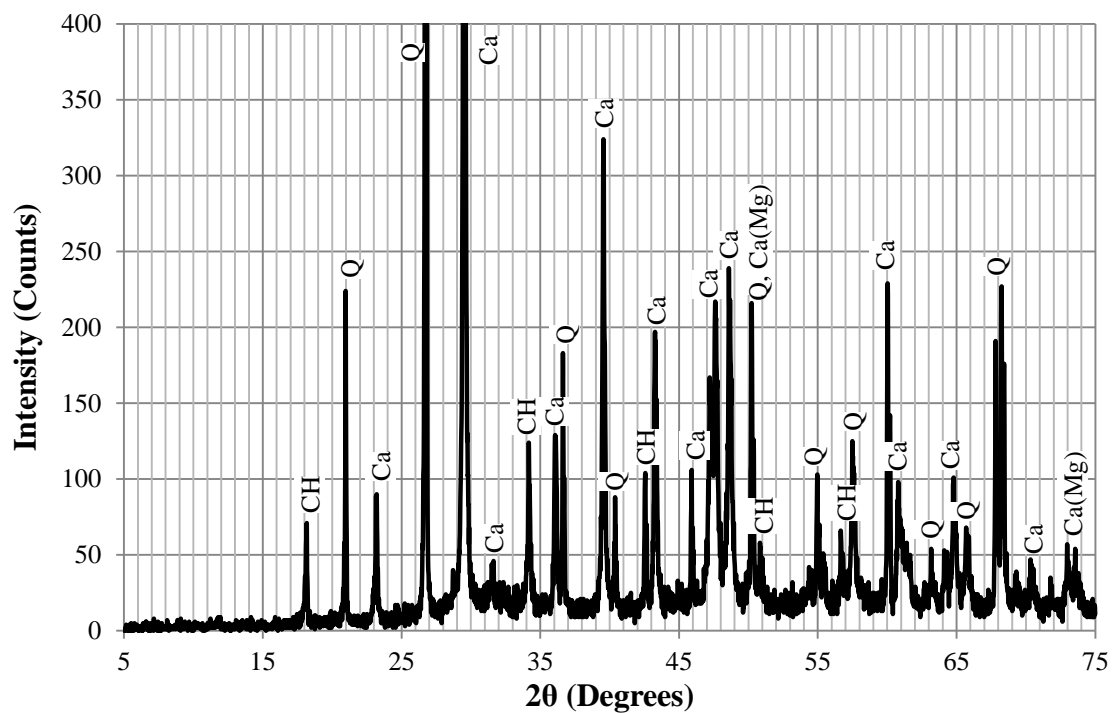


Figure 6-34: XRD profile for 9 ft above high tide at 0.5 – 1.5 in. increment into section

6.3.4.2 XRD Results from 2 ft above High Tide

Samples from 2 ft above high tide were taken to characterize the splash zone of the piles. Table 6-3 provides a summary of the results from all increments tested, where a check-mark represents the phase was present and an x-mark if not found in the increment. Calcium carbonate, calcium manganese carbonate, and quartz were detected in all samples.

Table 6-3: XRD results summary for 2 ft above high tide

	0-0.5"	0.5-1.5"	1.5-2.5"	2.5-3.5"	3.5-4.5"
Calcium Hydroxide	✓				
Ettringite	x				
Gypsum	✓	✓	✓	x	x
Calcite	✓				
Calcium Manganese Carbonate	✓				
Quartz	✓				

The XRD profiles for the 0-0.5 in., 0.5-1.5 in., 1.5-2.5 in., 2.5-3.5 in., and 3.5-4.5 in. increments are given in Figures 6-35, 6-36, 6-37, 6-38, and 6-39, respectively. The results show the presence of gypsum near the surface, but it was not detected deeper than 2.5 in. into the section, and no ettringite was detected. The presence of gypsum may result from prolonged exposure to brackish water, which contains large amounts of sodium sulfate and magnesium sulfate. The sulfate concentration was measured to be 1527 mg/L at the Turtle River Bridge during high tide. Calcium hydroxide was present at all depths sampled, suggesting that an alkaline pH was maintained. The XRD profiles deeper than 2.5 in. into the section are identical to the reference samples from 9 ft above high tide, which suggest that no significant changes to the microstructure have occurred in those increments.

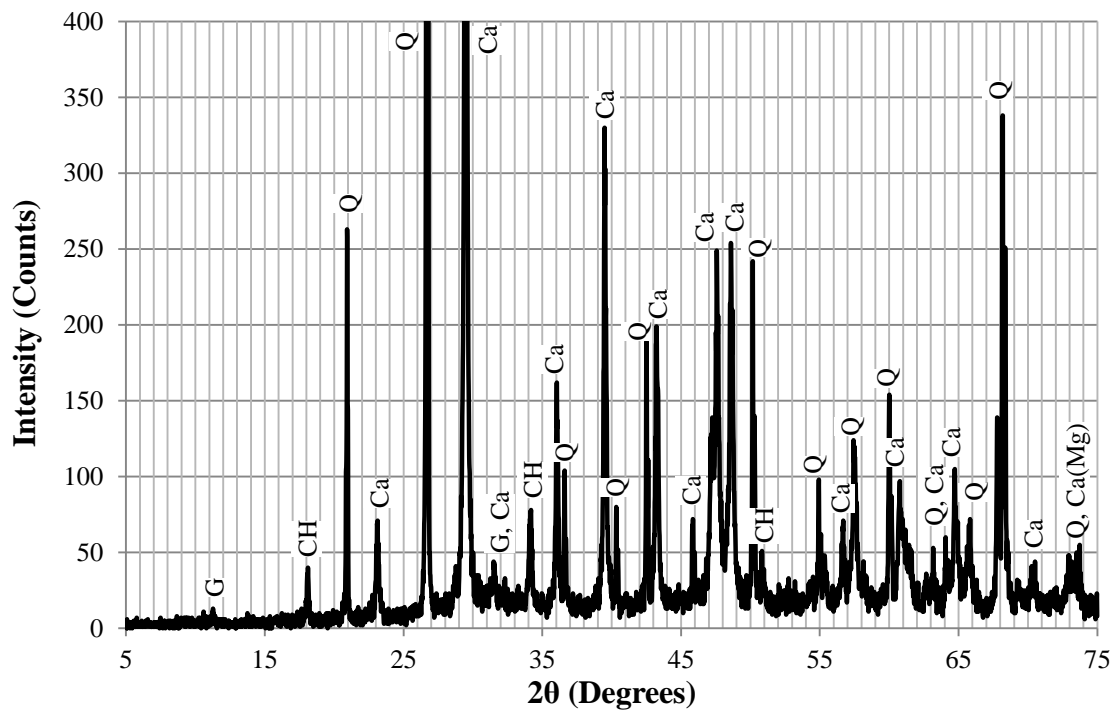


Figure 6-35: XRD profile for 2 ft above high tide at 0 – 0.5 in. increment into section

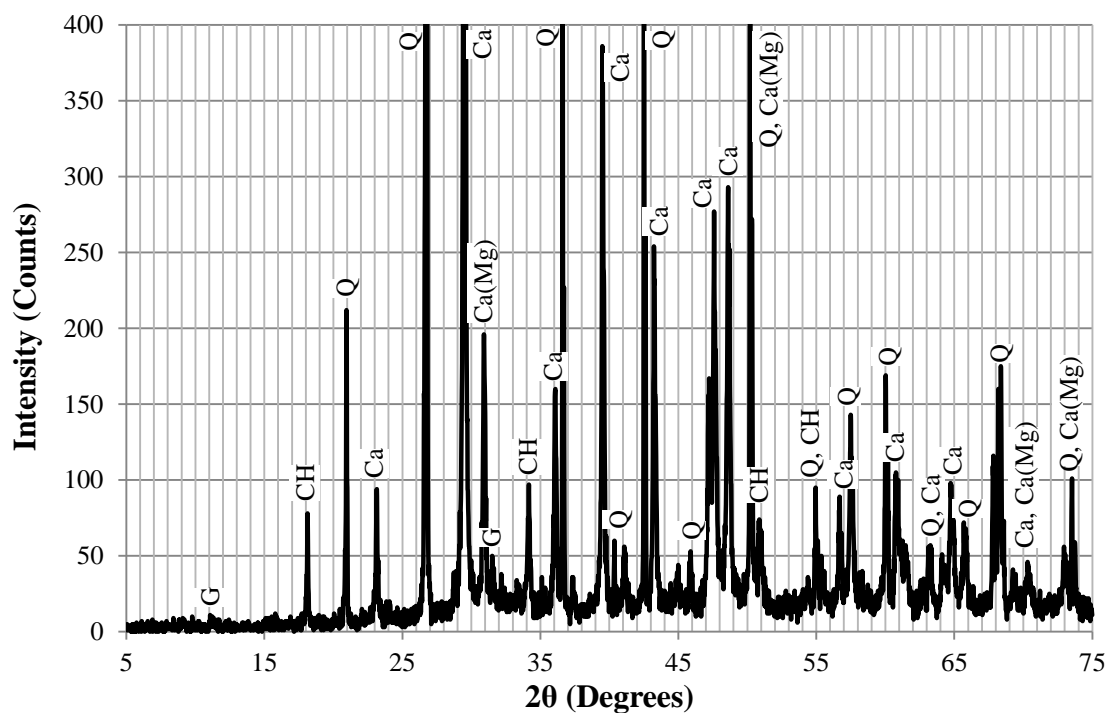


Figure 6-36: XRD profile for 2 ft above high tide at 0.5 – 1.5 in. increment into section

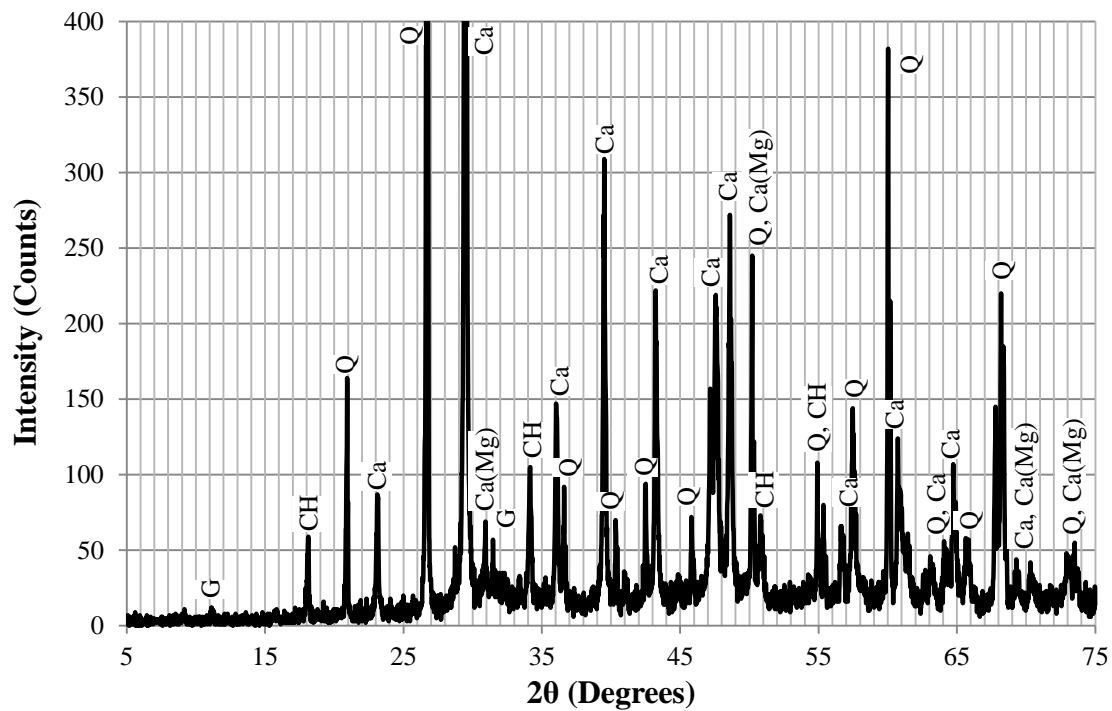


Figure 6-37: XRD profile for 2 ft above high tide at 1.5 – 2.5 in. increment into section

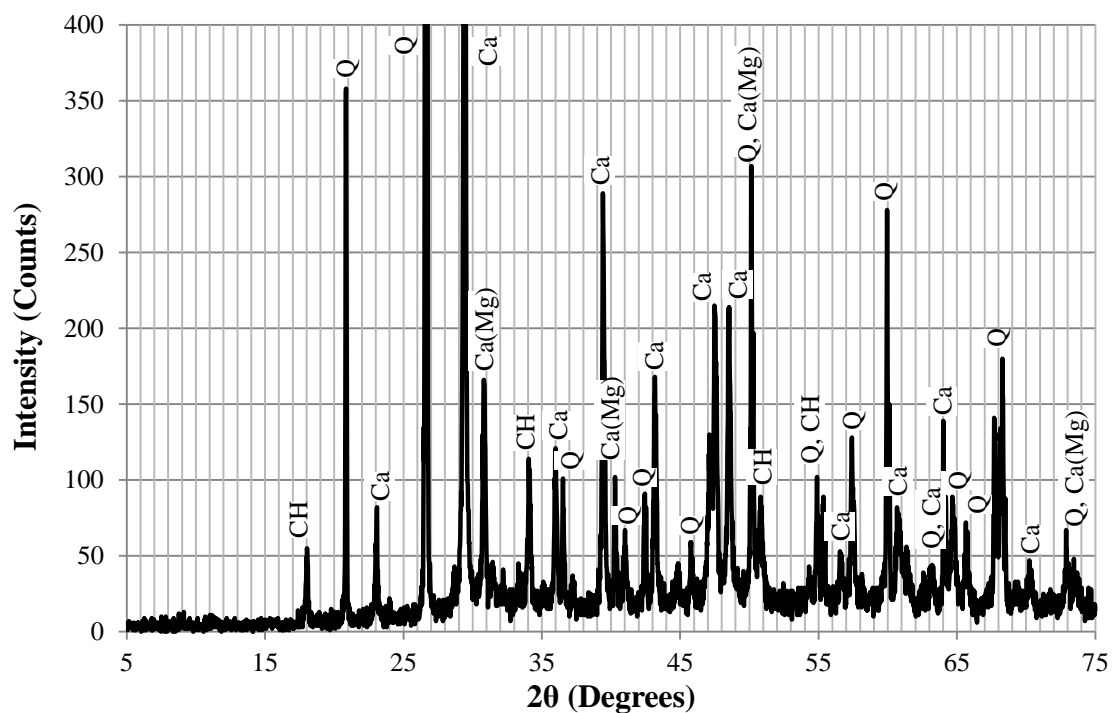


Figure 6-38: XRD profile for 2 ft above high tide at 2.5 – 3.5 in. increment into section

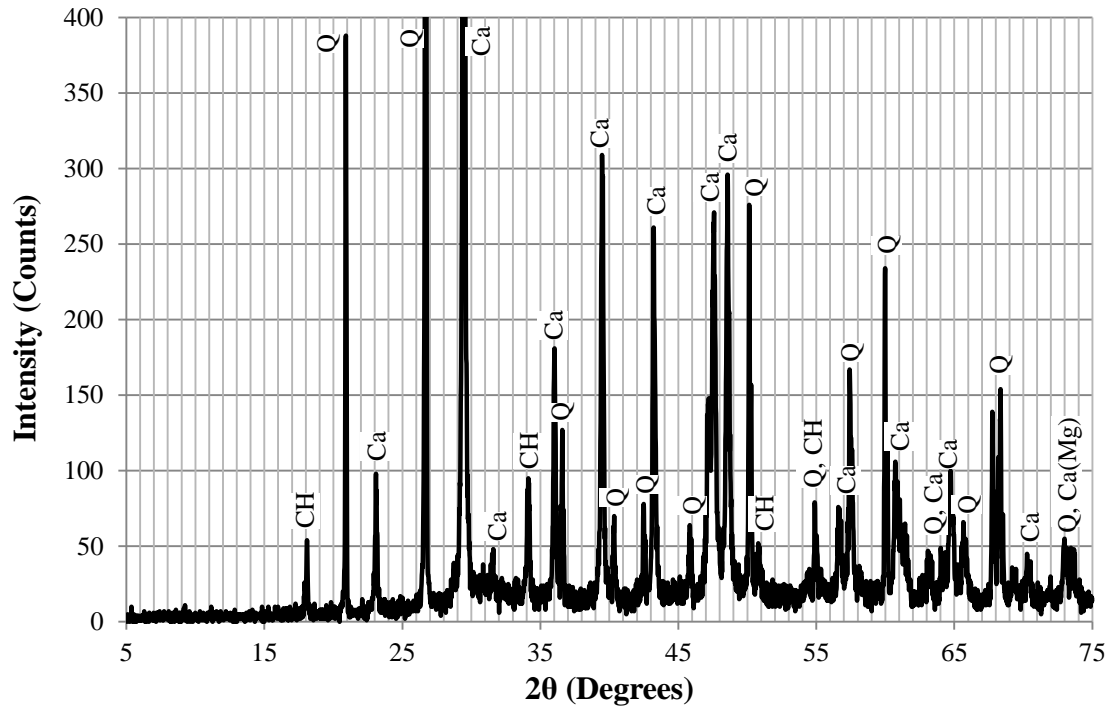


Figure 6-39: XRD profile for 2 ft above high tide at 3.5 – 4.5 in. increment into section

6.3.4.3 XRD Results from High Tide Region

Table 6-4 provides a summary of the results from all increments tested at the high tide region of the pile.

Table 6-4: XRD results summary for high tide

	0-0.5"	0.5-1.5"	1.5-2.5"	2.5-3.5"	3.5-4.5"
Calcium Hydroxide	✓				
Ettringite	✓	✓	✗	✓	✗
Gypsum	✓				
Calcite	✓				
Calcium Manganese Carbonate	✓				
Quartz	✓				

The XRD profiles for the 0-0.5 in., 0.5-1.5 in., 1.5-2.5 in., 2.5-3.5 in., and 3.5-4.5 in. increments can be found in Figures 6-40, 6-41, 6-42, 6-43, and 6-44, respectively. The results show a small presence of ettringite in the surface to 3.5 in. depth increments, and gypsum throughout the depth. Calcium hydroxide was present at all depths, but the intensity near the surface is greatly reduced from the other increments. These results suggest changes in the microstructure from the reference samples that are consistent with sulfate attack. The presence

of ettringite at depths nearer to the surface and gypsum throughout the section depth suggest that sulfate ions were able to penetrate through much of the depth of the pile at the high tide location.

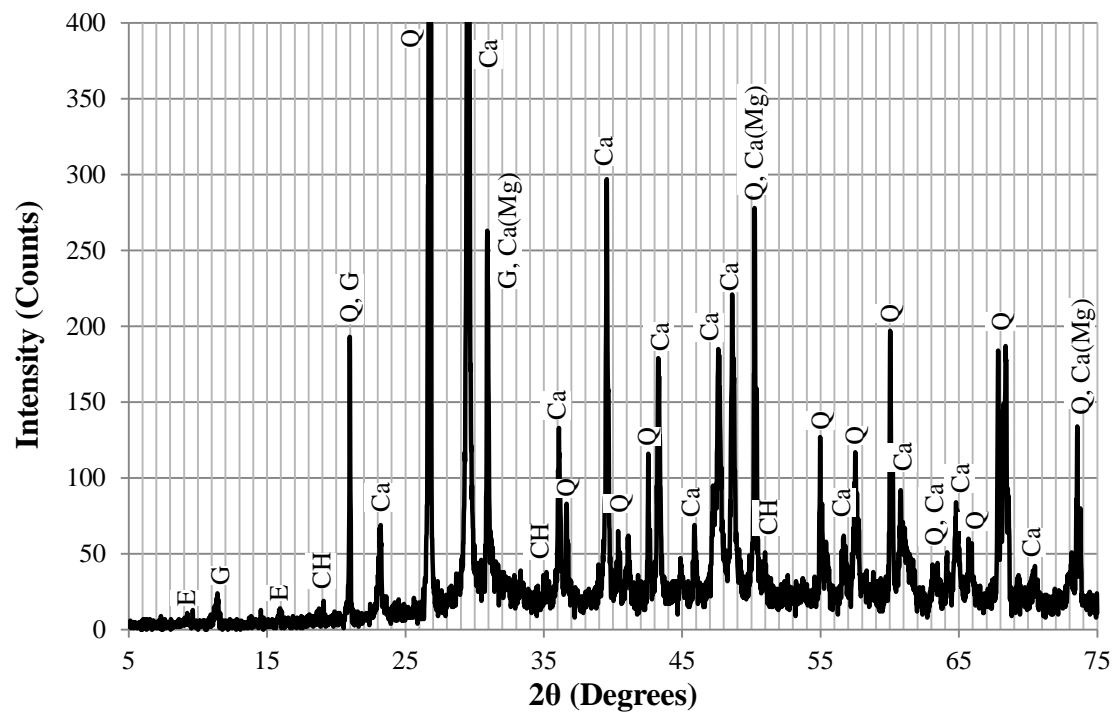


Figure 6-40: XRD profile for high tide region at 0 – 0.5 in. increment into section

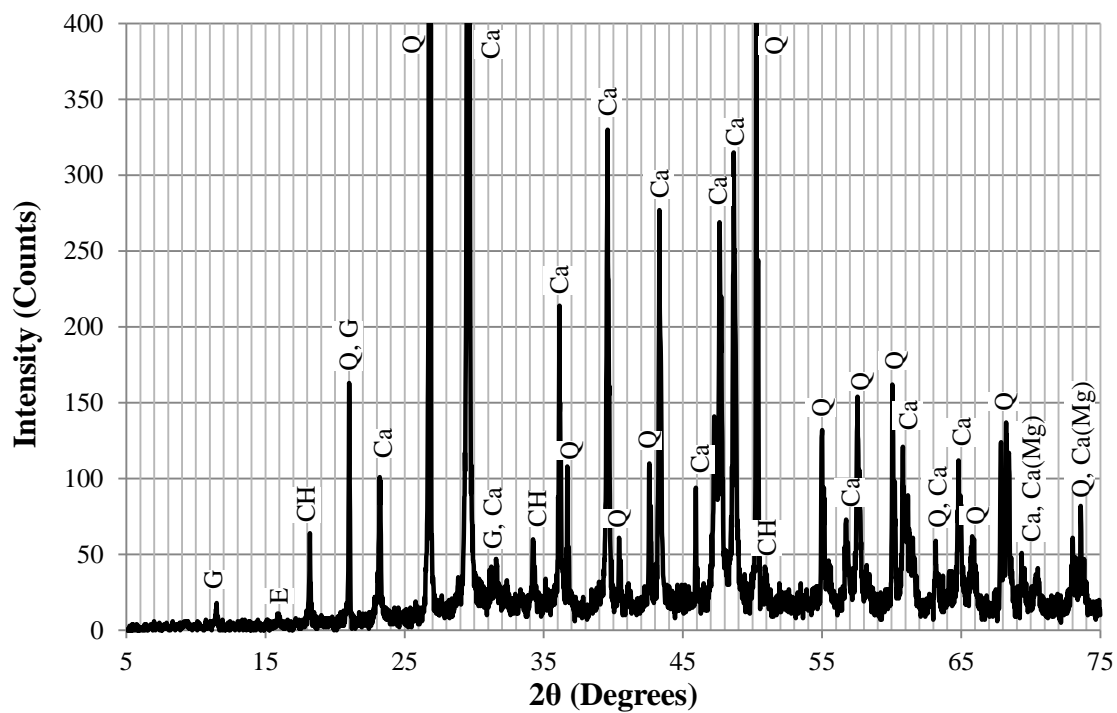


Figure 6-41: XRD profile for high tide region at 0.5 – 1.5 in. increment into section

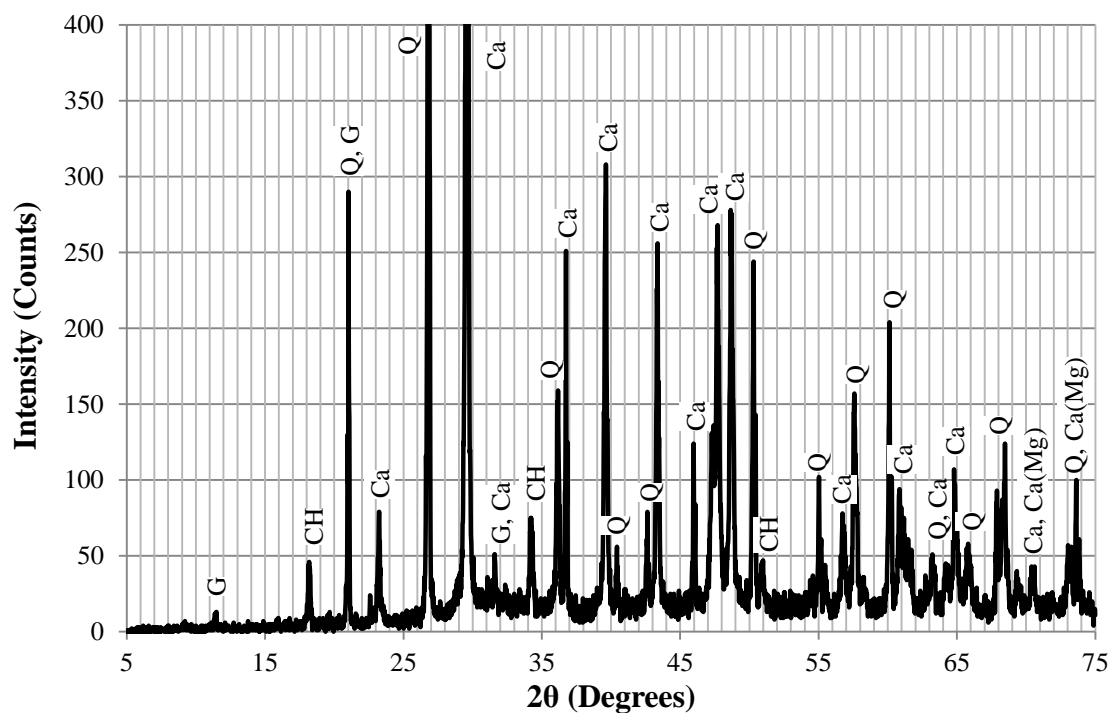


Figure 6-42: XRD profile for high tide region at 1.5 – 2.5 in. increment into section

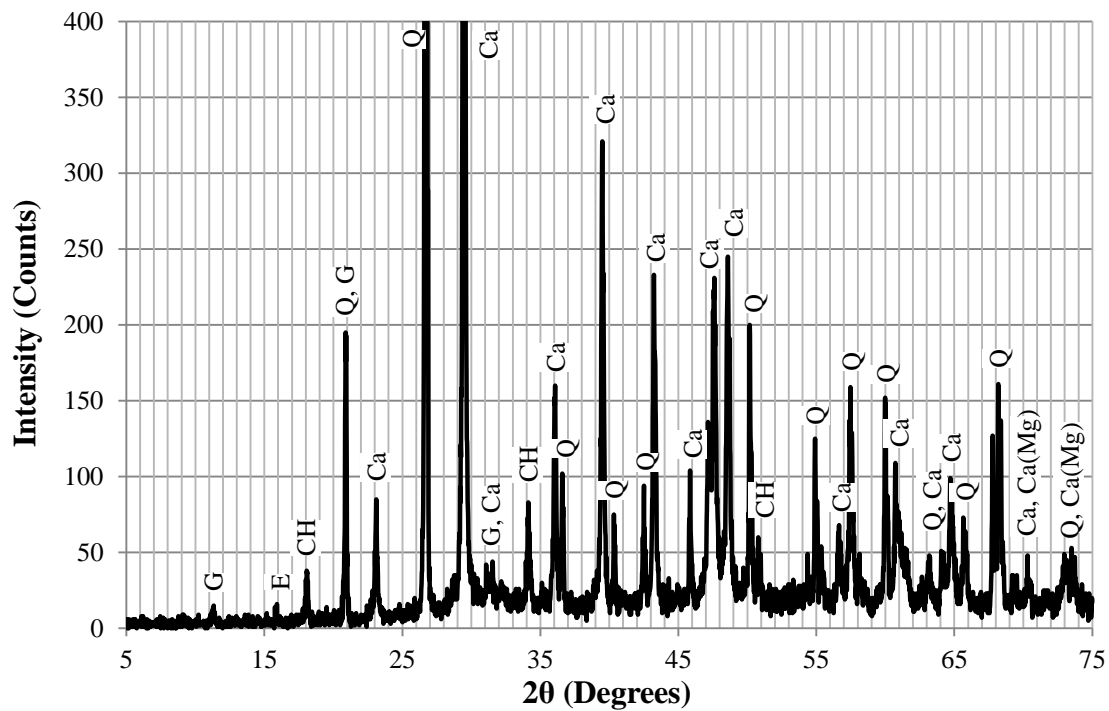


Figure 6-43: XRD profile for high tide region at 2.5 – 3.5 in. increment into section

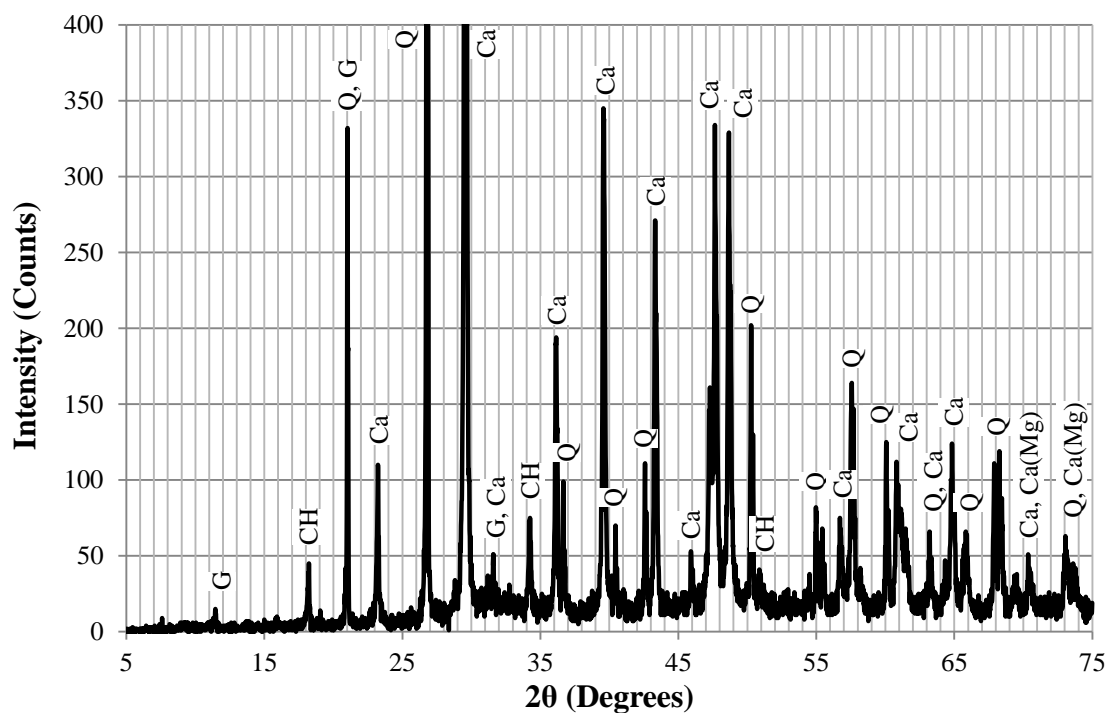


Figure 6-44: XRD profile for high tide region at 3.5 – 4.5 in. increment into section

6.3.4.4 XRD Results from 5 ft below High Tide

Samples from 5 ft below high tide were taken to characterize the low tide region of the piles. Table 6-5 provides a summary of the results from all increments tested.

Table 6-5: XRD results summary for 5 ft below high tide

	0-0.5"	0.5-1.5"	1.5-2.5"	2.5-3.5"	3.5-4.5"
Calcium Hydroxide	✗	✗	✓	✓	✓
Ettringite	✓	✗	✗	✗	✗
Gypsum	✓				
Calcite	✓				
Calcium Manganese Carbonate	✓				
Quartz	✓				

The XRD profiles for the 00-0.5 in., 0.5-1.5 in., 1.5-2.5 in., 2.5-3.5 in., and 3.5-4.5 in. increments can be found in Figures 6-45, 6-46, 6-47, 6-48, and 6-49, respectively. The results show a small presence of ettringite at the surface, and gypsum throughout the depth. Calcium hydroxide was not detected in the outer 1.5 in. of the section, but was present in depth increments farther into the section. These results, like the others presented previously, suggest changes in the microstructure compared to the reference samples that are consistent with sulfate attack and carbonation.

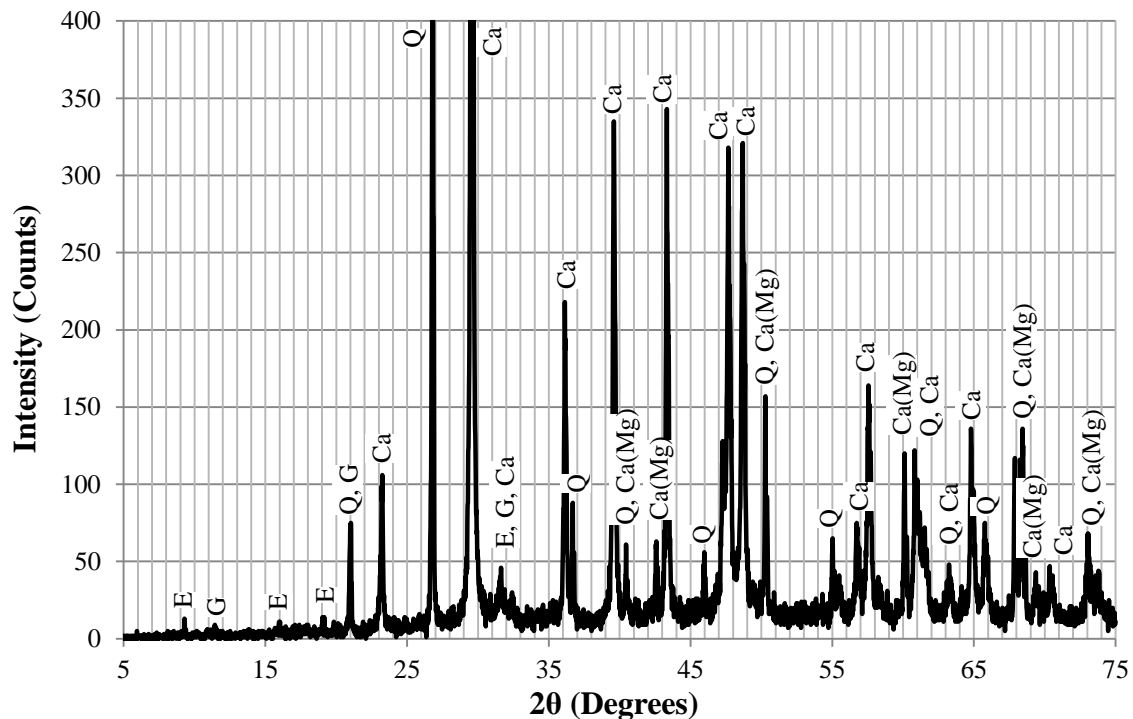


Figure 6-45: XRD profile for 5 ft below high tide at 0 – 0.5 in. increment into section

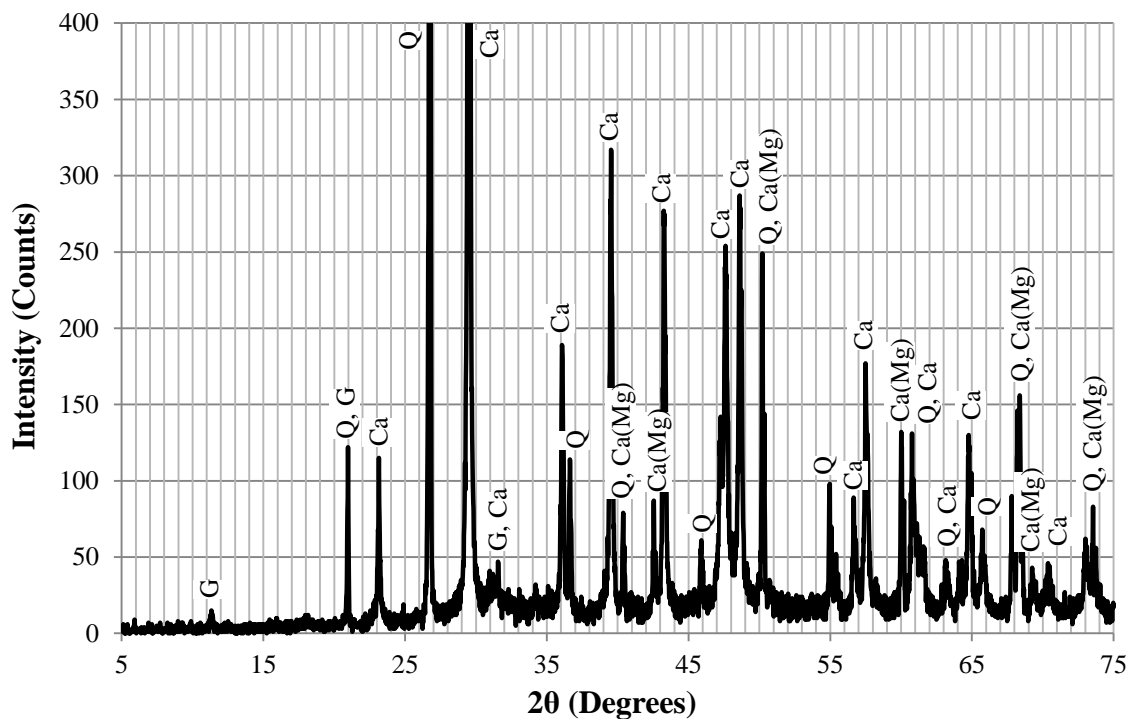


Figure 6-46: XRD profile for 5 ft below high tide at 0.5 – 1.5 in. increment into section

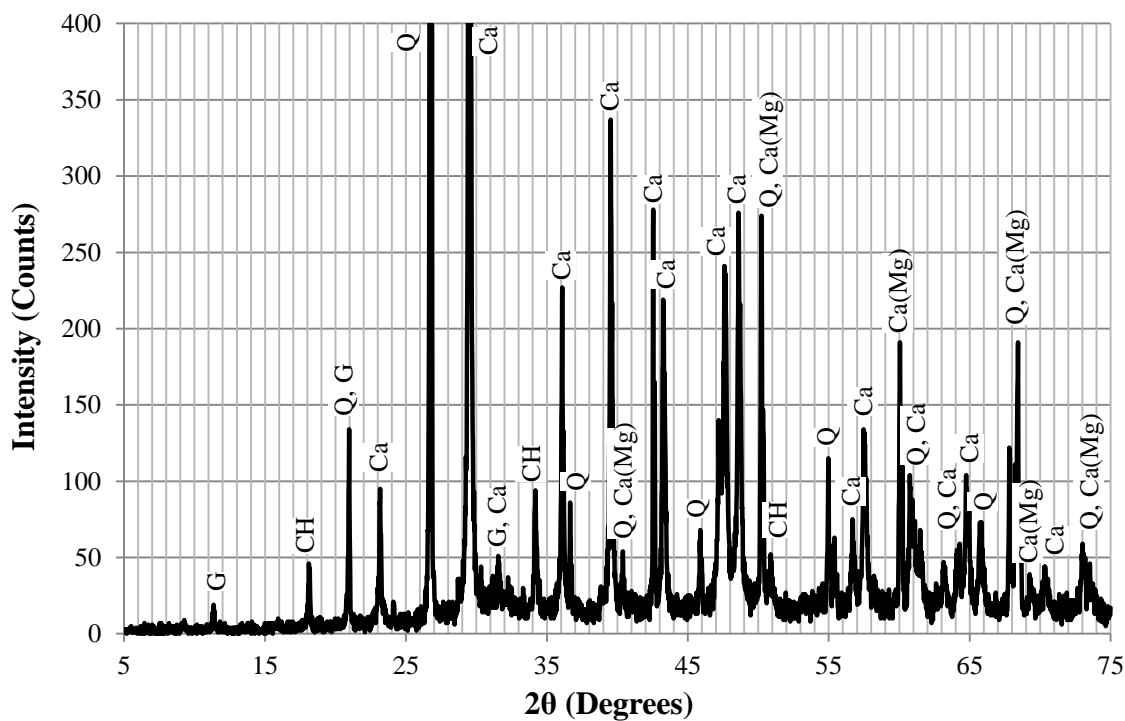


Figure 6-47: XRD profile for 5 ft below high tide at 1.5 – 2.5 in. increment into section

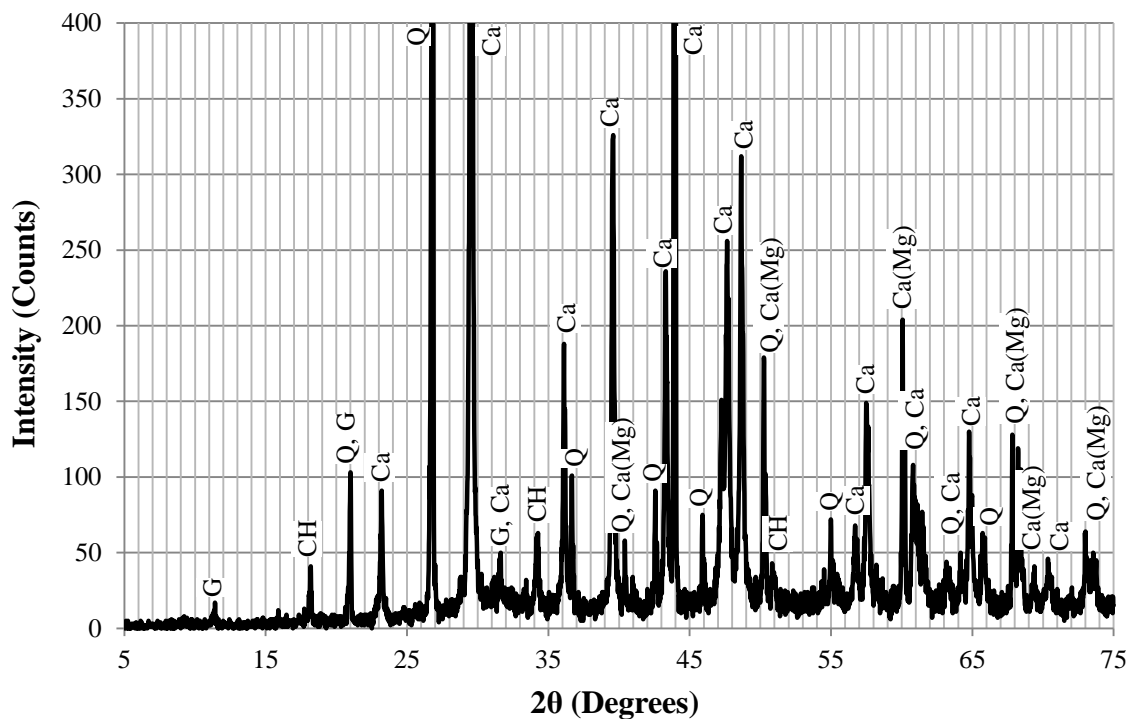


Figure 6-48: XRD profile for 5 ft below high tide at 2.5 – 3.5 in. increment into section

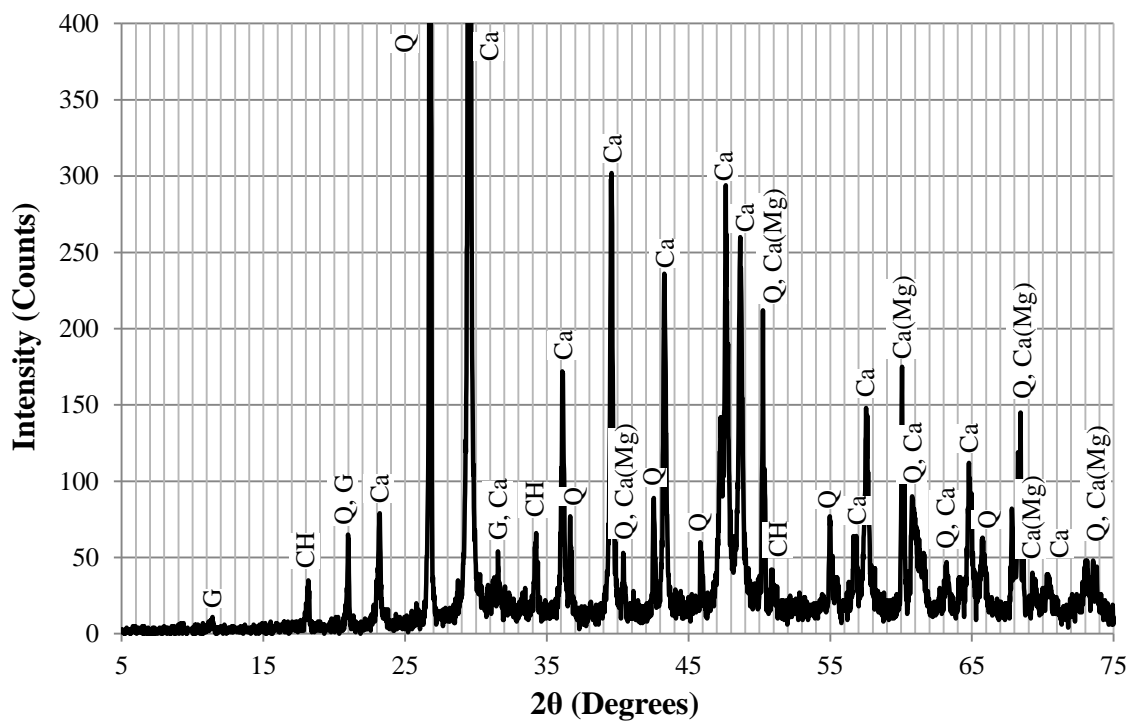


Figure 6-49: XRD profile for 5 ft below high tide at 3.5 – 4.5 in. increment into section

6.3.4.5 XRD Results from 12 ft below High Tide

Samples from 12 ft below high tide were taken to characterize the submerged region of the piles. Table 6-6 provides a summary of the results from all increments tested.

Table 6-6: XRD results summary for 12 ft below high tide

	0-0.5"	0.5-1.5"	1.5-2.5"	2.5-3.5"	3.5-4.5"
Calcium Hydroxide	✗	✗	✓	✓	✓
Ettringite	✓	✓	✗	✗	✗
Gypsum	✓				
Calcite	✓				
Calcium Manganese Carbonate	✓				
Quartz	✓				

The XRD profiles for the 0-0.5 in., 0.5-1.5 in., 1.5-2.5 in., 2.5-3.5 in., and 3.5-4.5 in. increments can be found in Figures 6-50, 6-51, 6-52, 6-53, and 6-54, respectively. The results show a presence of ettringite near the surface, and gypsum throughout the depth. Calcium hydroxide was not detected in the outer 1.5 in. of the section, but was present at deeper depths into the section. These results suggest changes in the microstructure compared to the reference samples that are consistent with sulfate attack. The lack of calcium hydroxide near the surface also suggests carbonation and/or leaching.

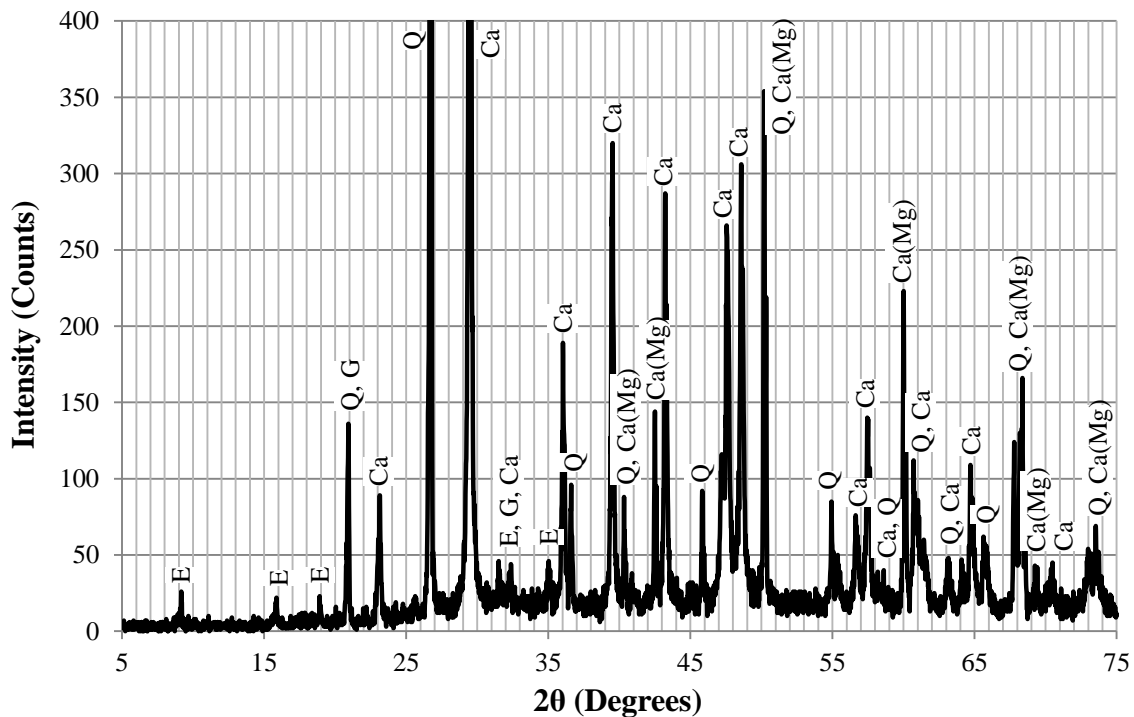


Figure 6-50: XRD profile for 12 ft below high tide at 0 – 0.5 in. increment into section



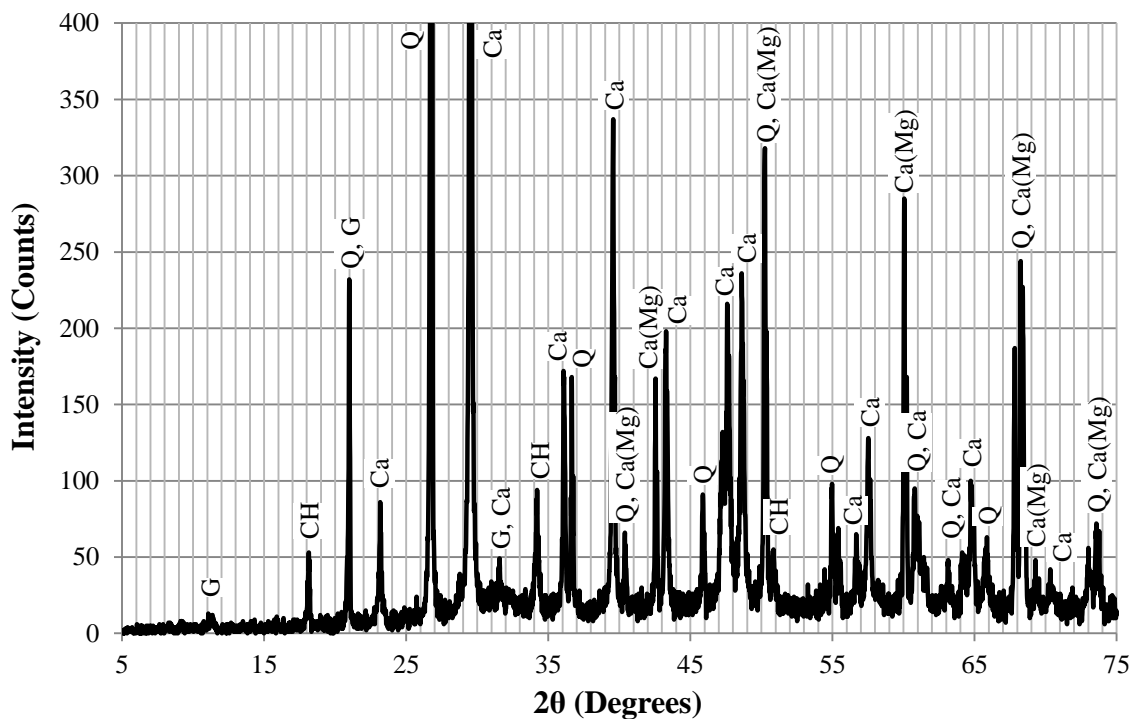


Figure 6-53: XRD profile for 12 ft below high tide at 2.5 – 3.5 in. increment into section

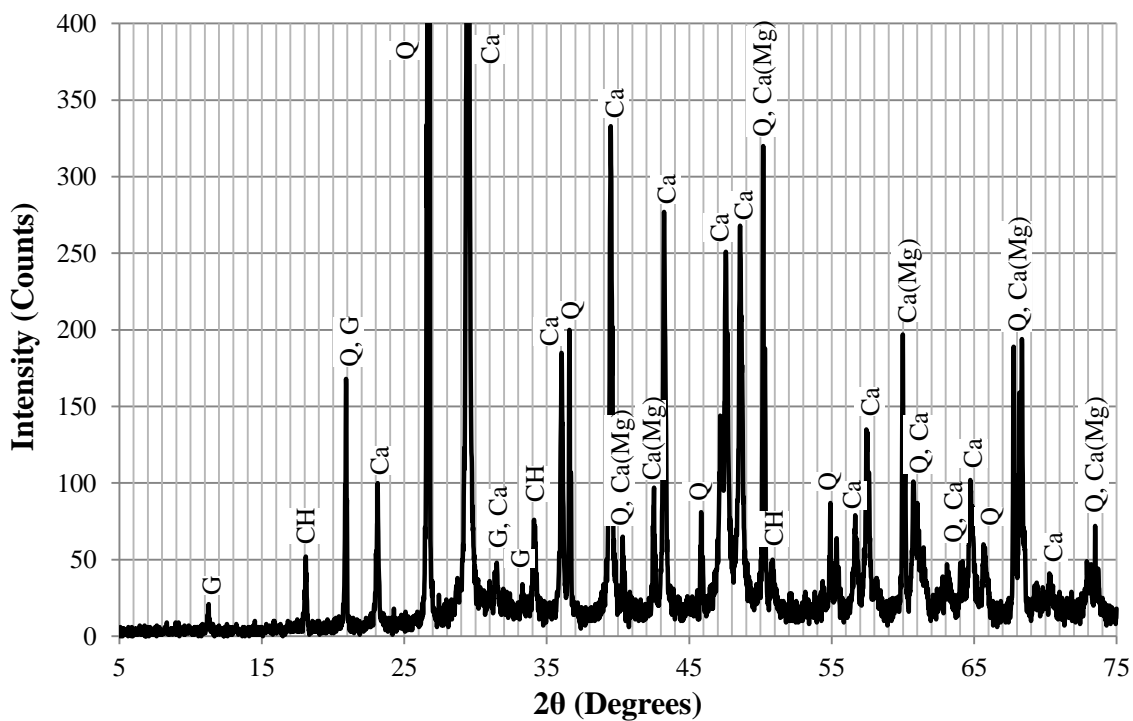


Figure 6-54: XRD profile for 12 ft below high tide at 3.5 – 4.5 in. increment into section

6.3.5 Thermo-Gravimetric Analysis

Thermo-gravimetric analysis (TGA) was performed on ground concrete samples to identify variations in the composition at various heights and depths into the cross section. Samples were taken at -9 ft, -2 ft, high tide, 5 ft, and 12 ft. Powder was obtained by taking a 3 in. diameter core through the section and then drilling at controlled increments using a 3/8 in. masonry bit. Powder was collected from the surface ½ in. increment, then in 1 in. increments into the cross-section. The powder samples were then ground with mortar and pestle and sieved through an 850 µm (No. 20) sieve.

The analysis was performed using a Seiko TG/DTA in accordance with ASTM E 1131 (2008). Approximately 30 mg of sample powder were placed in platinum pans and brought to 100°C and held for one hour to remove any remaining free water from the sample. After the initial hold period, the sample was heated at a rate of 10°C per minute up to a maximum temperature of 950°C, while continually measuring the mass of the sample.

TGA analysis allows for determination of phases present based upon mass loss over their degradation temperatures. Ettringite decomposes at temperatures less than 115°C and is not easily determined using TGA due to degradation temperature coinciding with the evaporation of free water. C-S-H undergoes dehydration between 100°C to 200°C, and a decomposition and change in structure between 200°C and 400°C. Portlandite (Ca(OH)_2) undergoes dehydroxylation between 425°C and 600°C. Above 750°C, calcium carbonate degrades. However, because the coarse aggregate used was primarily calcium carbonate, the mass loss in this temperature range does not represent only a degradation of calcium carbonate in the cement paste.

Figures 6-55 and 6-56 show the TGA mass loss curves for the 9 ft and 2 ft above high tide samples. Both curves show a consistent mass loss in the regions due to alteration of C-S-H and decomposition of portlandite. The mass loss due to alteration of C-S-H is a gradual change over the thermal range. The decomposition of portlandite occurs over a small temperature range near 425°C. A consistent mass loss of 1% occurred in all of the samples at these depths due to the loss of portlandite. The presence of portlandite in all of the depths tested is consistent with the XRD results.

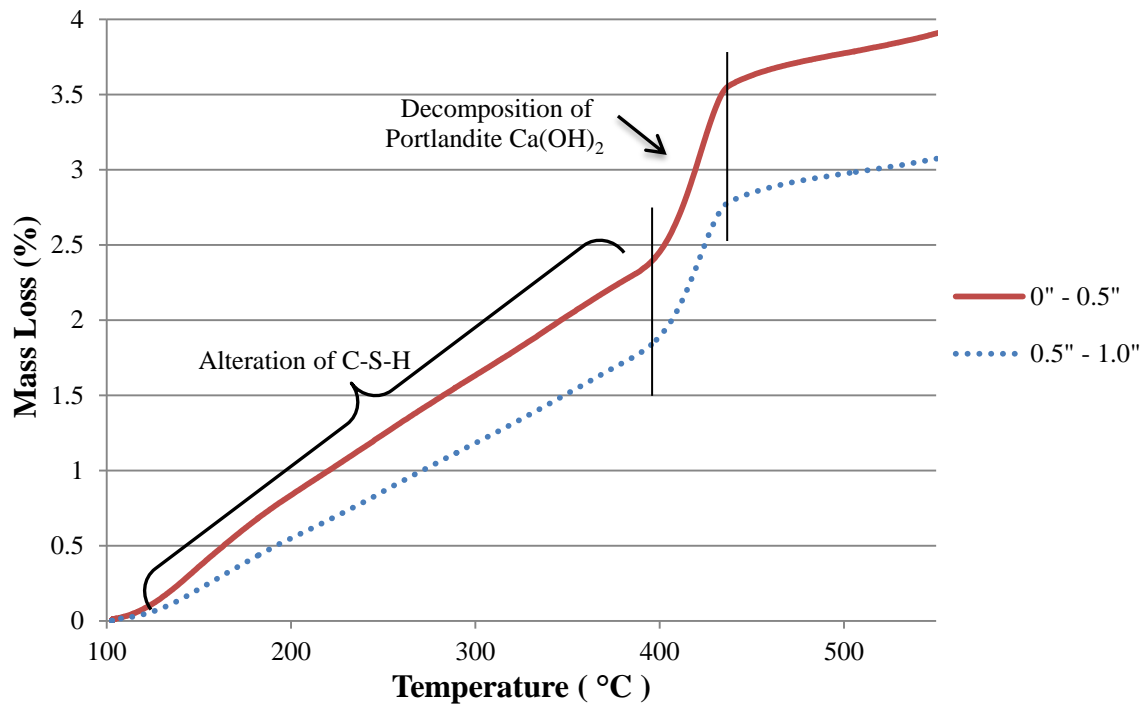


Figure 6-55: TGA for 9 ft above high tide

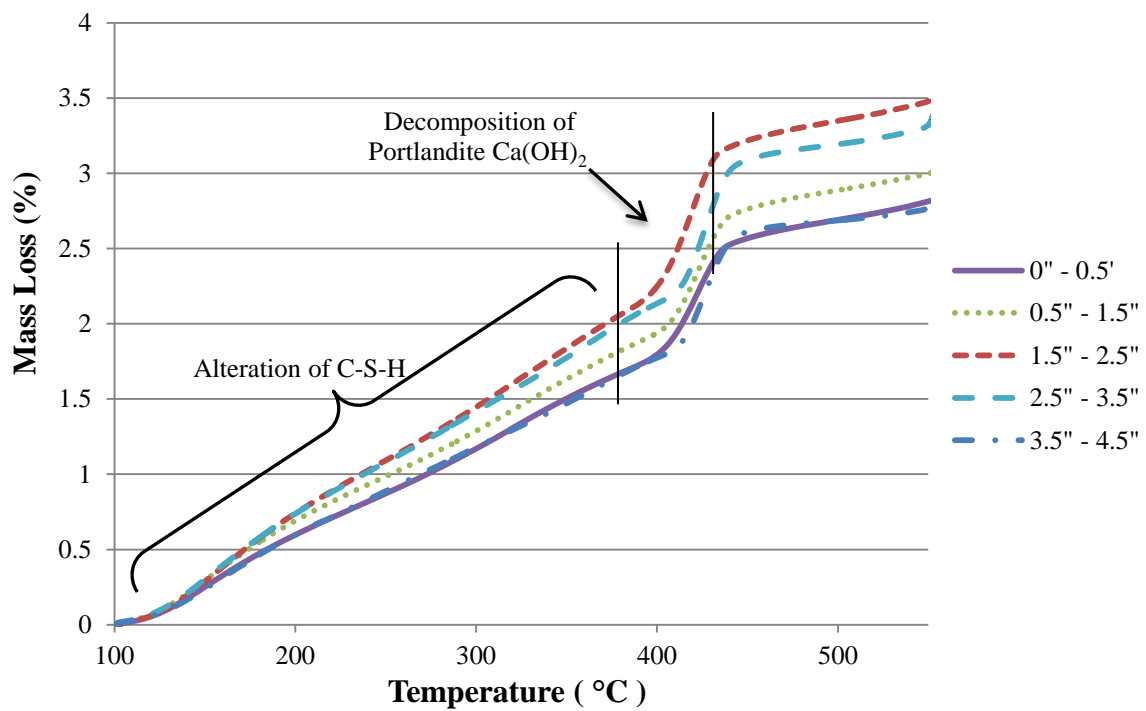


Figure 6-56: TGA for 2 ft above high tide

The results of TGA on the high tide region are shown in Figure 6-57. The samples from 0.5 in. and farther into the section are consistent with the 9 ft and 2 ft above high tide samples. There is a consistent mass loss due to degradation of portlandite present. The surface interval sample does not show an appreciable mass loss due to portlandite degradation. This is not in complete agreement with XRD results, which suggested a small amount of portlandite was present compared to the other increments tested at the depth. The TGA data may be more accurate due to the test giving quantitative characterization of phases present and being more sensitive to small amounts of phases present.

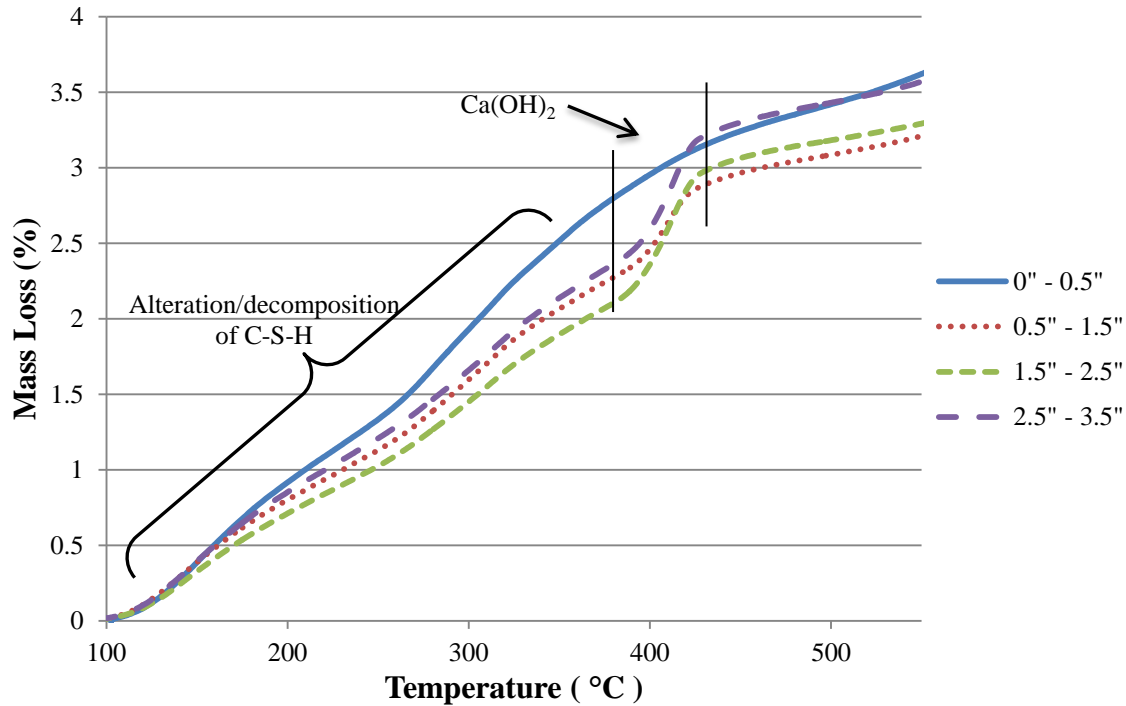


Figure 6-57: TGA for high tide region

The TGA results for 5 ft and 12 ft below high tide are shown in Figure 6-58 and 6-59, respectively. The surface interval on both data sets showed a decreased rate of mass loss between 100°C and 400°C than samples farther into the cross-section and at unsubmerged depths. This suggests that C-S-H was lost on the surface of the piles, most likely due to sulfate attack and carbonation. Additionally, the outer 1.5 in. of both samples showed an absence of portlandite. This is consistent with XRD results for these depths. Additionally, the mass loss during the degradation of portlandite decreased from the loss 9 ft above high tide samples, suggesting a decreased amount present. These results are consistent with the damage patterns that would occur with sulfate attack.

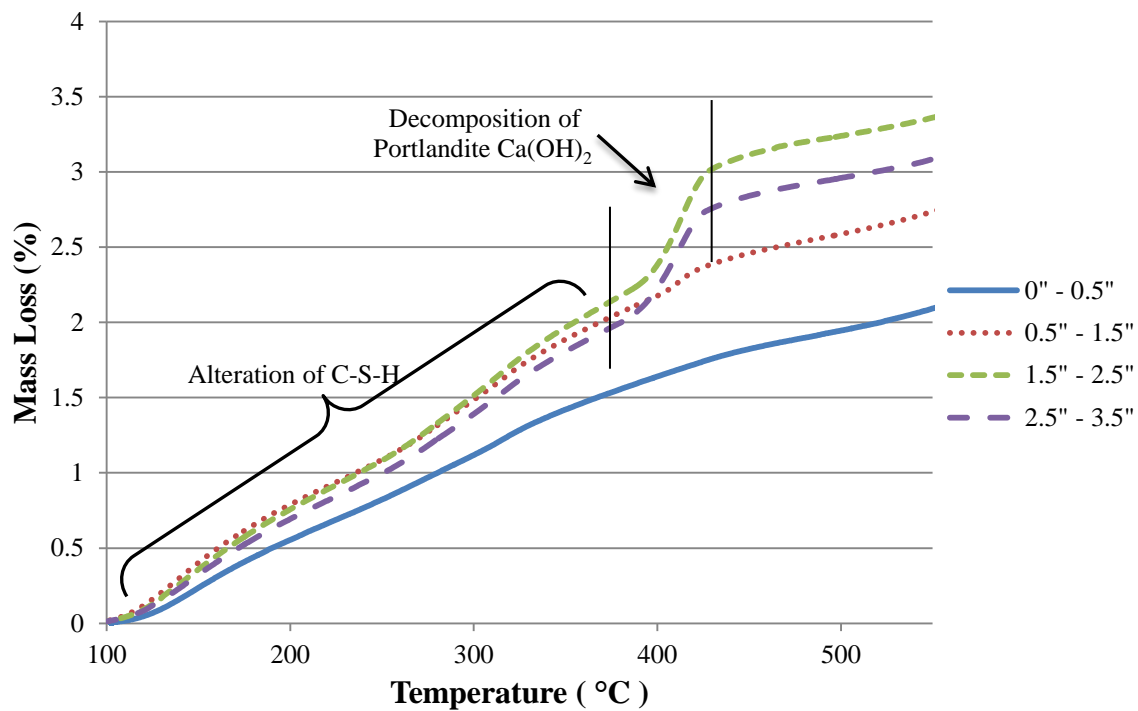


Figure 6-58: TGA for 5 ft below high tide

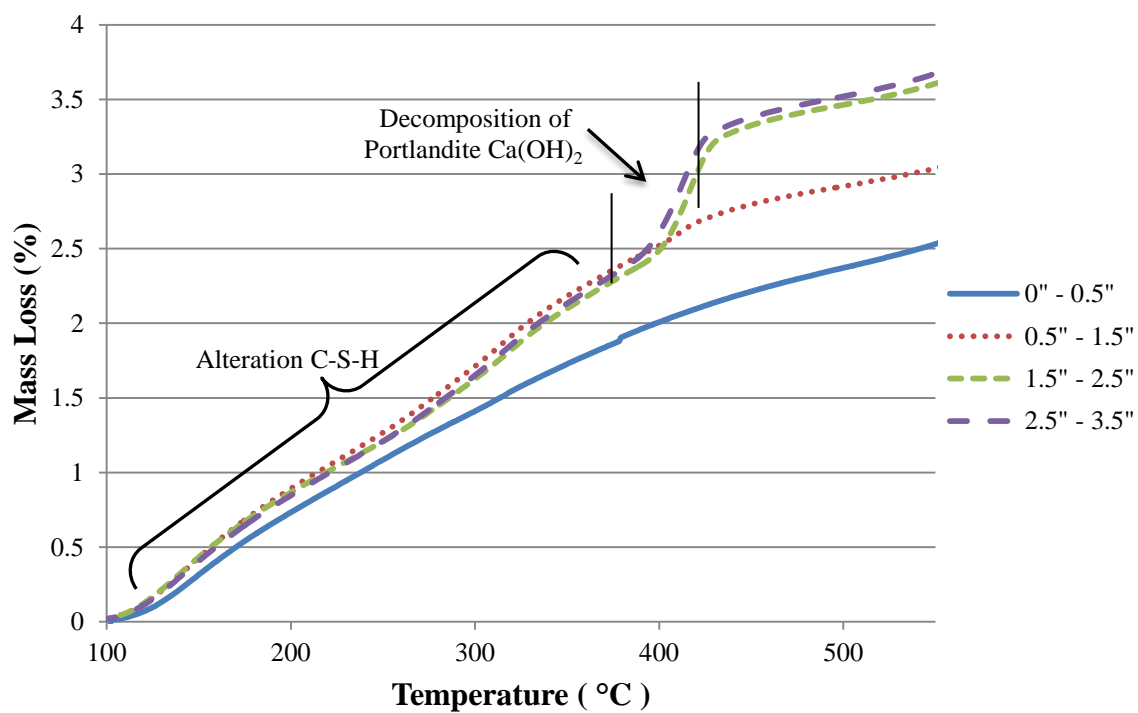


Figure 6-59: TGA for 12 ft below high tide

6.3.6 Conclusions, Sulfate Attack

The piles from the I-95 at Turtle River Bridge exhibited several characteristics of sulfate attack. The submerged regions of the piles showed an absence of calcium hydroxide near the surface, and the presence of gypsum and ettringite. This result is consistent with sulfate attack, which would lead to a decrease in calcium hydroxide near the surface, and the presence of ettringite and gypsum. Additionally, TGA suggested a decrease in C-S-H near the surface that is also consistent with carbonation and which would cause decreased compressive strength. Testing of cores for compressive strength showed a decrease of 45% near the surface of the pile in the submerged regions. The use of a ASTM C 150 (2009) Type I cement, an ordinary rather than sulfate-resisting cement, and a w/c of 0.50 could have allowed the sulfates from the surrounding water to ingress into the section over time and cause the extensive damage found.

6.4. Biodeterioration

There have been few reported cases of biological attack on coastal concrete structures. Here, a visual inspection and microscopic analysis techniques were used to characterize the biological attack on the piles.

6.4.1 Visual Inspection of Damage

A visual inspection was performed on the submerged region of the piles. No significant deterioration was visible until after cleaning the marine growth off of the surface of the piles. After removal of biological growth, large amounts of surface damage were visible. The damage, as seen in Figure 6-60, consisted of large pits on the surface of the piles. The damage was more pronounced along the corners of the piles, where the presence of boreholes and spalling were present. The pits occurred where coarse aggregate had been present on or near the surface of the piles.



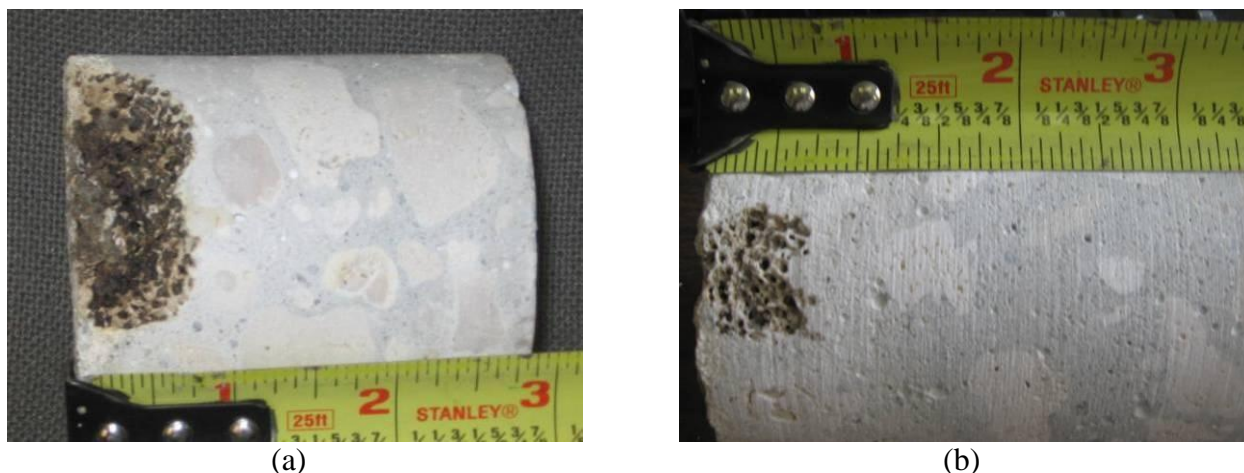
(a)



(b)

Figure 6-60: Surface damage to concrete piling

Cores taken in the submerged region showed extensive damage to aggregate within 1.0 in. of the surface of the piles, as shown in Figure 6-61. Boreholes were present in aggregate near the surface in over 70% of cores taken. Damage was observed at over 1 in. depth into the section.



(a) (b)
Figure 6-61: Boreholes in limestone aggregate of cores

The damage pattern observed visually was consistent with reported descriptions of *Cliona* borings on limestone and coral. A reported case of boring sponge attack was reported in Jamaica due to *Cliona lampa* (Scott, et. al., 1988). The sponges burrowed through the limestone aggregate of concrete masonry blocks. The damage was primarily at the corners, and irregular shaped bore holes occurred in the aggregate. The sponges use etching secretions to penetrate calcium carbonate and form the boreholes (Nicol and Reisman, 1976). The genus *Cliona* sponges leave silicate spicules near the surface of their borings. The length of the spicules varies by species but is typically between 200 μm to 400 μm (Zea and Weil, 2003). Figure 6-62 shows spicules from *Cliona caribbaea*.

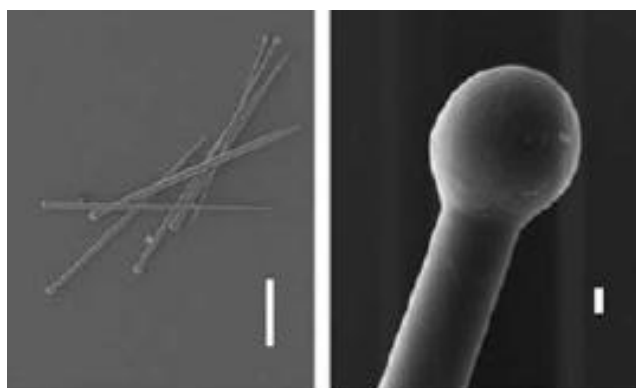


Figure 6-62: Spicules of *Cliona caribbaea* (Zea and Weil, 2003)

There have been reports of *Cliona* sponges at Gardiner's Island, New York (Nicol and Reisman, 1976), along the coast of Virginia (Hopkins, 1962), Corpus Christi, Texas (Miller, et. al., 2010), and off the coast of Jamaica (Scott, et. al., 1988). Studies on the erosion rate of the sponge show that the rate may exceed 1 mm (0.04 in.) per year of ingress in solid limestone (Neumann, 1966). The rate of biological degradation of the limestone aggregate in these piles,

>1 in. in 35 years, is consistent with the rate of attack measured by Neumann (1966) for *Cliona* on solid limestone. The boring sponge is shown in Figure 6-63 on a coral reef.

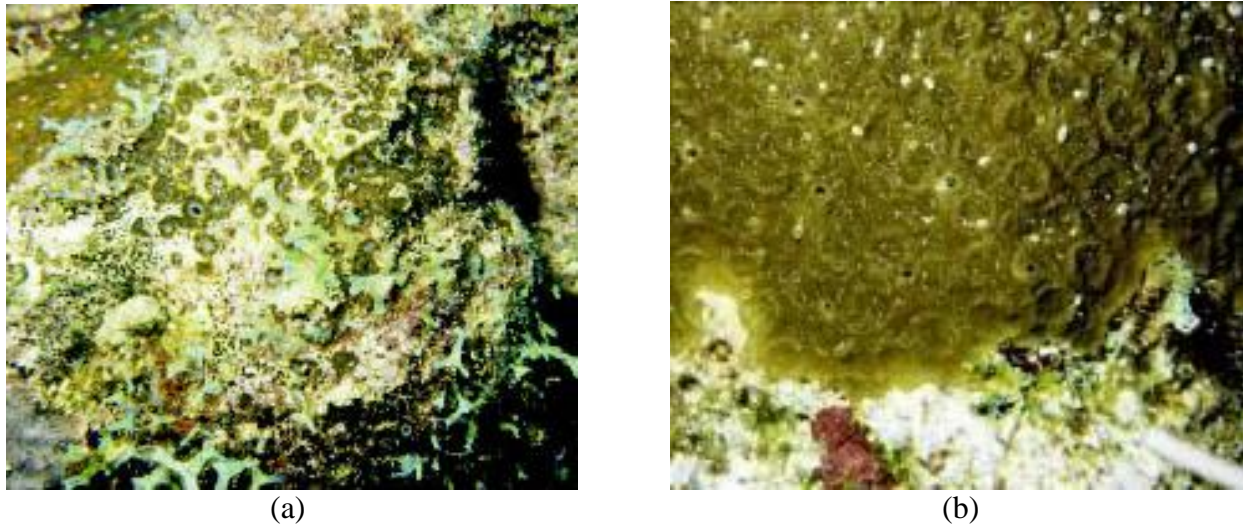


Figure 6-63: *Cliona caribbaea* boring sponge (Zea, 2003)

6.4.2 Microscopy Characterization

Further investigation of the boreholes using environmental scanning electron microscopy (ESEM) revealed the presence of rod-like structures. Energy dispersive x-ray analysis (EDS) of the rod-like structures revealed them to be highly silicate in composition. The rod-like structures inside of a borehole in the aggregate are shown in Figure 6-64, and the corresponding EDS spectrum is shown in Figure 6-65.

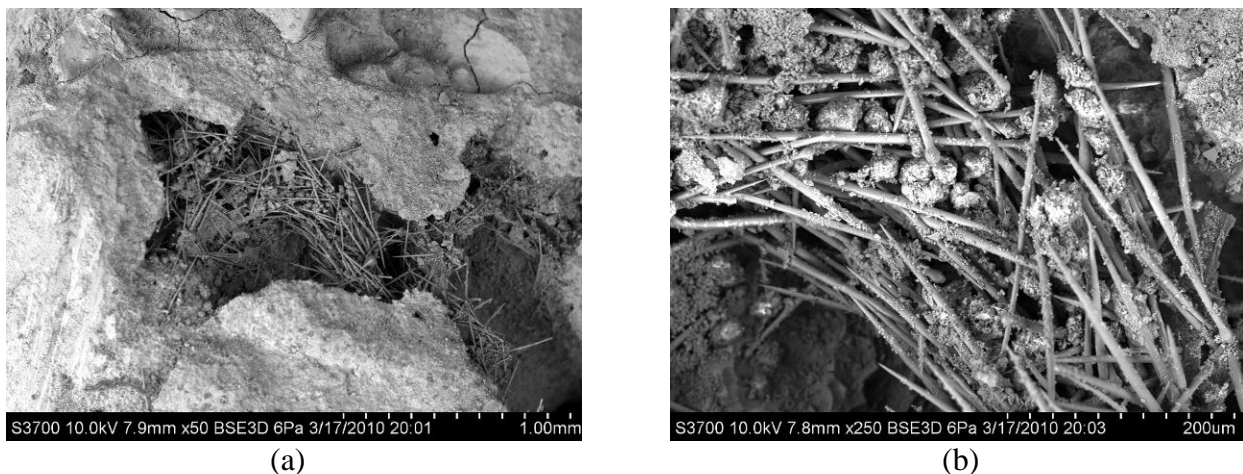


Figure 6-64: (a,b) Silicate rod-like structures inside of boreholes through aggregate (Courtesy of Robert Moser)

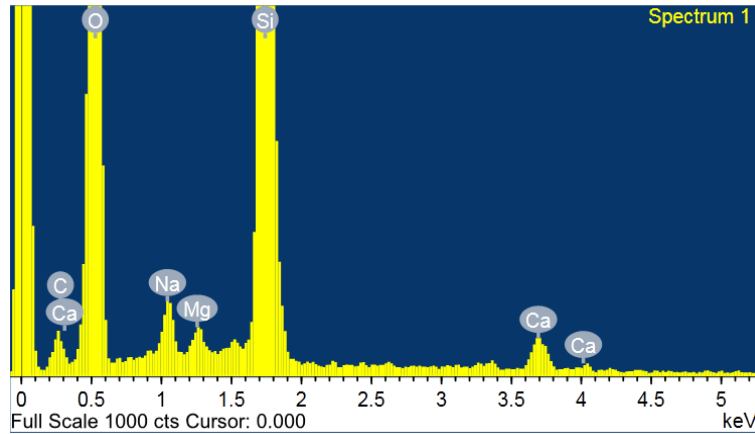


Figure 6-65: EDS spectrum of rod-like structures
(Courtesy of Robert Moser)

Characterization of the limestone aggregate by EDS showed that the aggregate was composed primarily of calcium carbonate, although some aggregates were calcium magnesium carbonate, as expected. The types of calcite present were in agreement with XRD results. The composition of the aggregate suggests it is a Pleistocene limestone that is commonly found in southern Florida and the Bahamas.

Morphological and chemical comparison suggests that the rod-like structures resemble the siliceous spicules of *Cliona* boring sponges. The bioerosion patterns were similar to those reported by Scott (1988) in submerged concrete structures in Jamaica subjected to bioerosion from *Cliona caribbaea*. The patterns suggest that boring sponges are the most likely source of this form of damage to the piles. Further research is needed to better understand how the boring sponge damages the aggregate and to develop mitigation techniques for preventing damage in new construction.

6.5. Characterization of Prestressing Steel

In order to evaluate the prestressing steel used in the Turtle River piling, cores including segment of prestressing strand were extracted and split to expose the strand. The surface condition and corrosion damage of the strand was characterized using SEM. The microstructure of the prestressing steel was examined using SEM and optical microscopy by polishing longitudinal and transverse cross sections of the steel and wet etching in a 2% Nital solution. EDS analysis was conducted in conjunction with SEM imaging in order to determine the elemental composition of features present on the surface of the steel. The composition of the prestressing steel was determined using combustion and ion coupled plasma (ICP) atomic emission techniques conducted by an external laboratory.

6.5.1. Surface Condition of Prestressing Steel

The electron micrograph shown in Figures 6-66 illustrates the typical morphology present on the surface of prestressing steel strands extracted for cores. The surface of the prestressing steel was observed to have an extremely heterogeneous microstructure with some regions of only exposed steel, some regions with the ZnPO_4 coating intact, and other areas largely comprised of corrosion products. Interestingly, the ZnPO_4 coating was found to be in a similar condition to that of as-produced prestressing steel with very little degradation. The presence of this coating at later ages indicates that the effect of surface coating and possible defects in coating should be included when evaluating the long-term corrosion resistance of prestressing steels.

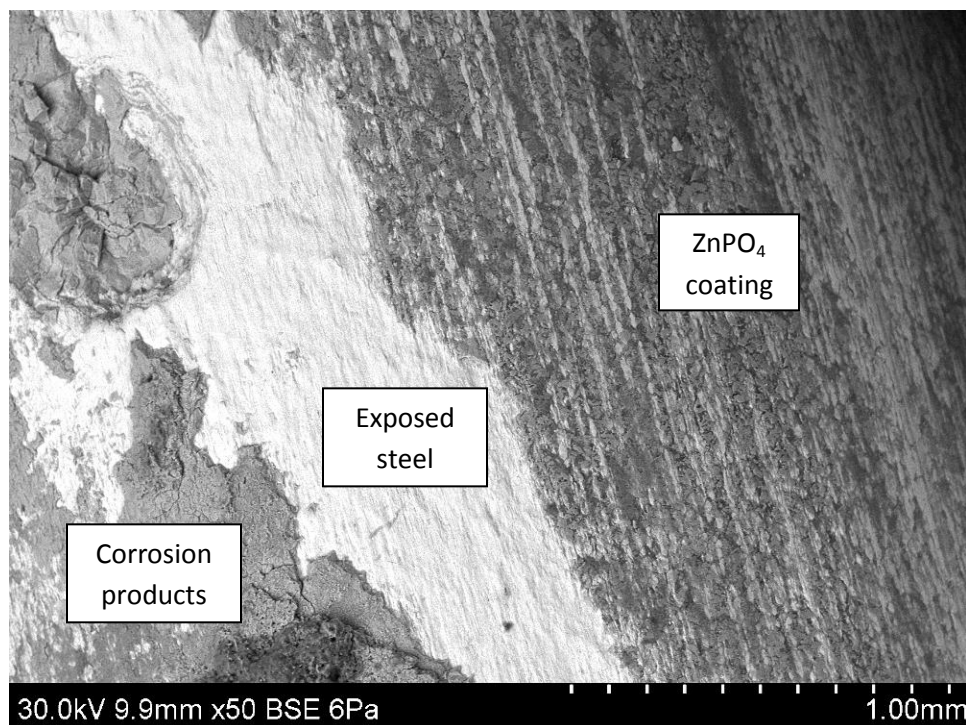


Figure 6-66. Surface morphology of prestressing steel strand

Figure 6-67 depicts a typical region where the ZnPO_4 has been partially retained on the surface of the prestressing steel with damage to the coating aligned with the longitudinal drawing direction of the steel. As observed by backscattered electron SEM imaging coupled with EDS, brighter regions were found to be primarily composed of steel (i.e., Fe) while darker regions were found to be a mixture of Zn, P, Fe, and Ca. The presence of Ca may be due to residual coatings of stearate drawing lubricants not removed during cleaning of the strand following stabilization heat treatments and/or cement hydration products.

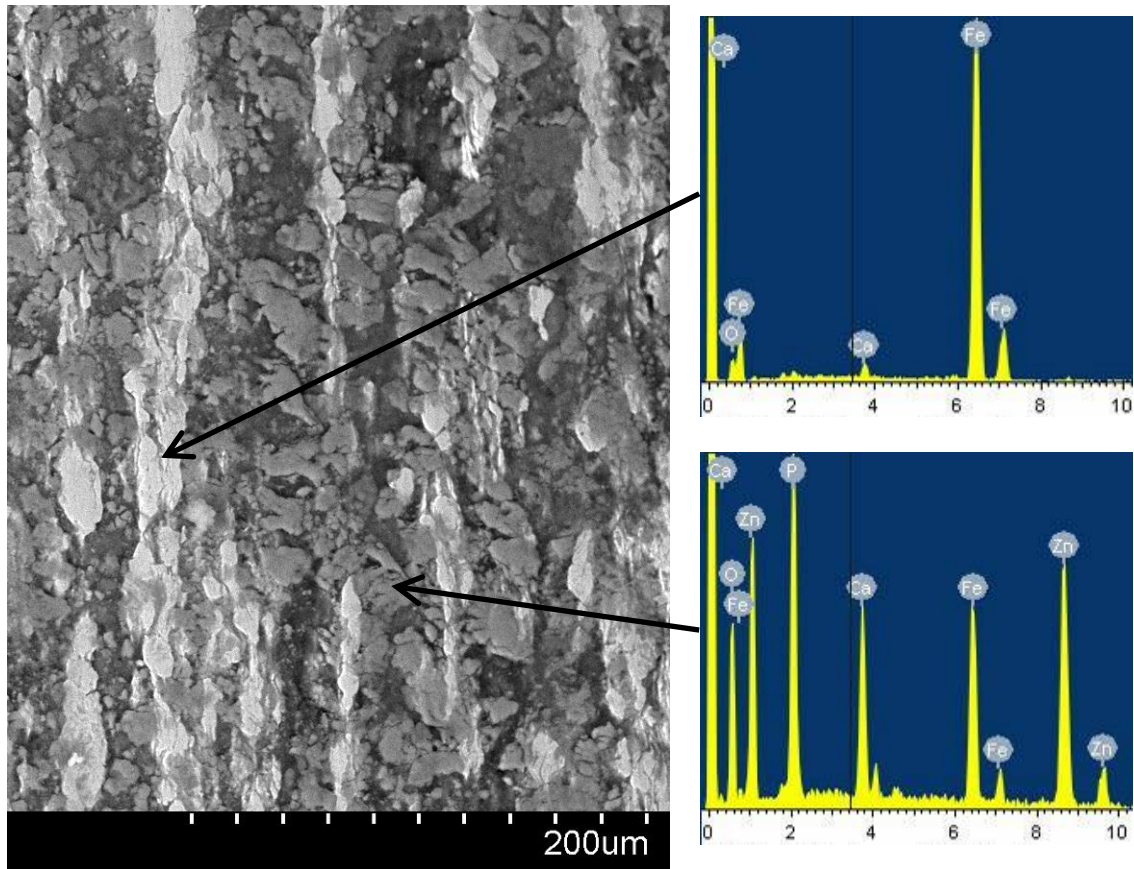


Figure 6-67. Composition of residual surface coating

Prestressing strand segments were also dissected to expose the center “king” wire of the strand. The interstitial regions of the strand were found to be largely void of cement hydration products, being either completely empty or partially filled with corrosion products. Figure 6-68 depicts the typical surface of the center wire. Similar to the surface of the entire prestressing strand, the highly defective ZnPO_4 coating was found to be largely intact with sparsely distributed precipitates of $\text{Ca}(\text{OH})_2$ crystals being bonded to the surface of the steel. At the crevice / impingement sites between prestressing wires adjacent to corrosion product deposits pitting corrosion sites were also observed (see Figure 6-69).

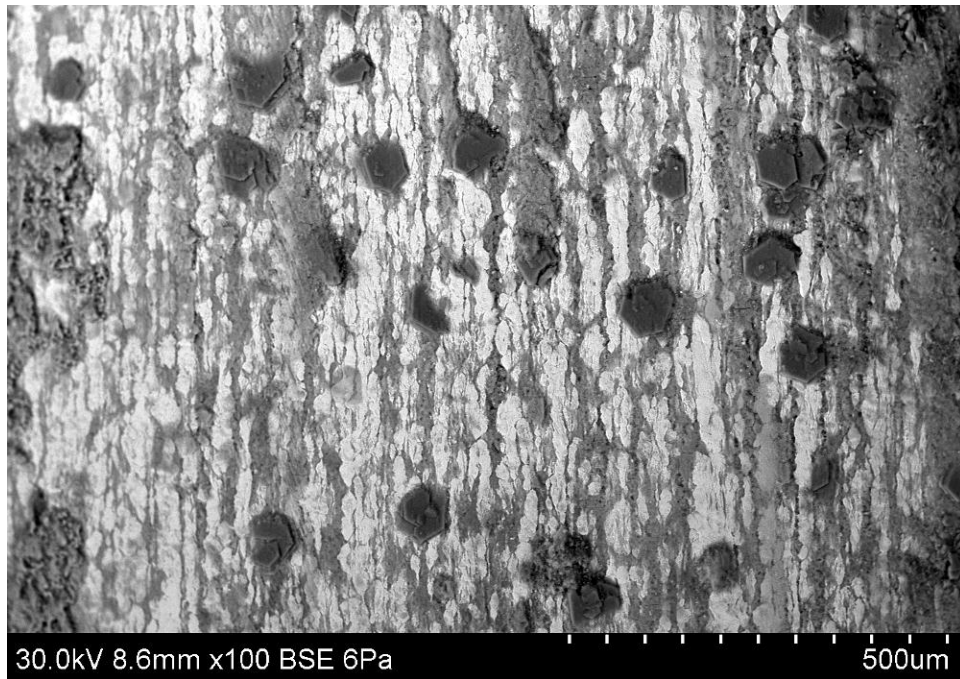


Figure 6-68. Surface of center wire extracted for prestressing strand sample



Figure 6-69. Pitting / crevice corrosion sites present at wire impingement sites

6.5.2. Microstructure of Prestressing Steel

As expected for highly cold drawn eutectoid prestressing steel, a highly oriented anisotropic microstructure was observed with the lamellar pearlitic microstructure preferentially aligned with the direction of cold drawing. The optical micrographs shown in Figures 6-70 and 6-71 illustrate the typical longitudinal and transverse etched microstructures observed, respectively. When compared with modern prestressing steels, the microstructure of the prestressing steel used in the Turtle River piling was found to have a larger grains of ferrite and distributed regions of pearlite (ferrite + cementite). This can be seen in the electron micrograph shown in Figure 6-72 with the brighter regions being primarily ferrite and the distributed pearlitic regions shown by black and white striations.

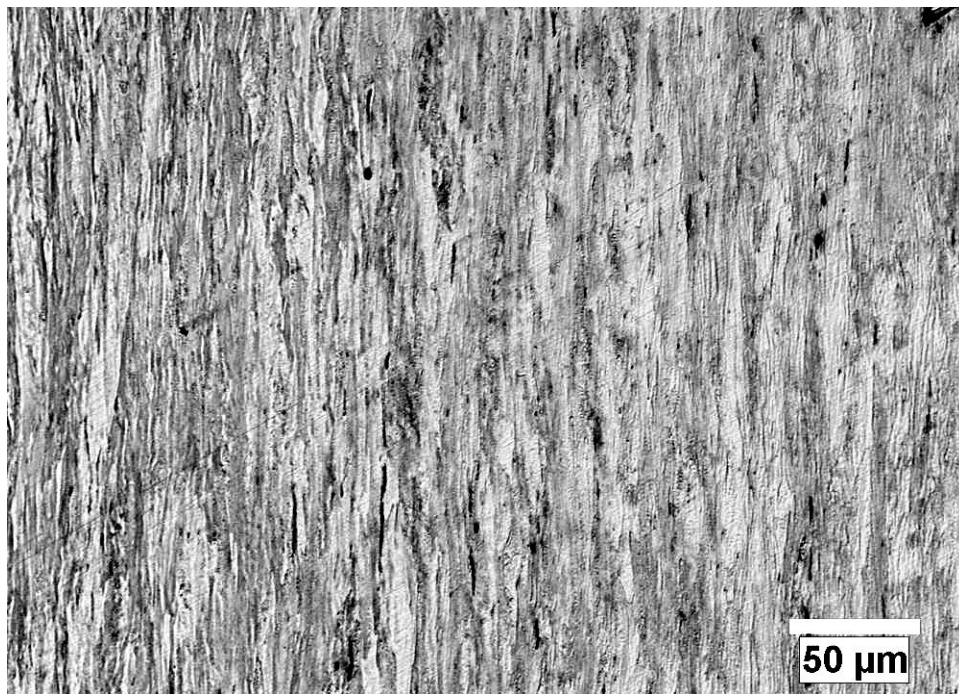


Figure 6-70. Longitudinal microstructure of prestressing steel

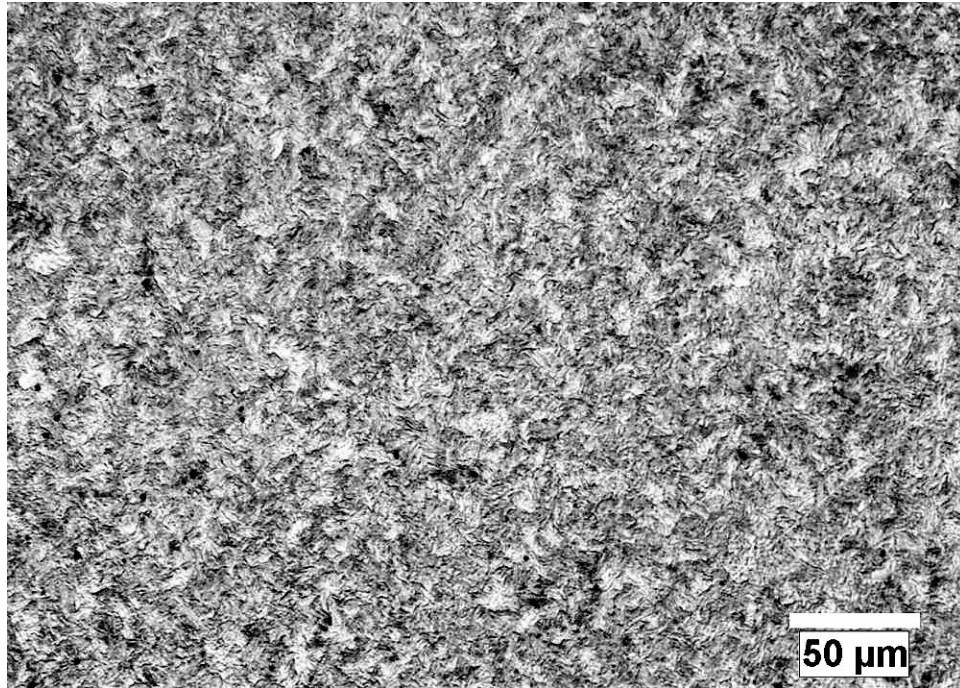


Figure 6-71. Transverse microstructure of prestressing steel

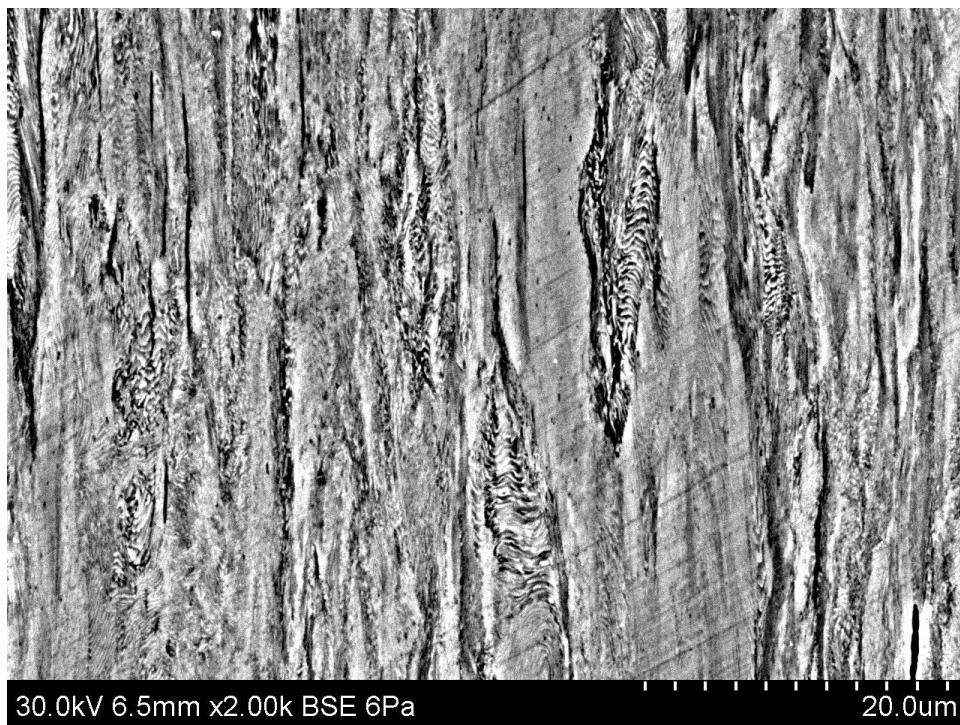


Figure 6-72. SEM image of etched prestressing steel microstructure

6.5.3. Composition of Prestressing Steel

Table 6-7 details the composition of the prestressing steel used in the Turtle River piling. This composition conforms with the currently specified AISI 1080 steel used for the production of A416 prestressing strand. While the C content of 0.78% is slightly lower than the typical 0.81% for modern prestressing steel, this deviation is well within the standard error associated with C content measurements.

Table 6-7. Elemental composition in % of prestressing steel (Fe Balance)

Identification	C	Mn	P	S	Si	Ni	Cr	Mo	Cu	V
AISI 1080 Spec.	0.75-0.88	0.6-0.9	0.04	0.05	-	-	-	-	-	-
Turtle River Steel	0.78	0.69	0.01	0.025	0.26	0.01	0.02	<0.01	0.02	<0.01

6.6. Conclusions

6.6.1 Summary of Results

The forensic investigation of the I-95 at Turtle River Bridge piles revealed extensive damage from multiple deterioration mechanisms. Chloride-induced corrosion of the prestressing strands in the splash and tidal zones of the piling had induced cracking and delamination of the cover concrete as well as a loss of steel cross-section. The level of ingress of chloride ions suggested that the concrete was inadequate to provide 100+ year service life in the marine environment. Additionally, severe deterioration of the concrete due to sulfate attack and carbonation occurred in the submerged regions of the piles. A loss of over 40% of the compressive strength near the surface of the piles occurred due to loss of C-S-H and the formation of ettringite and gypsum. Also, in the submerged regions of the piles, extensive damage to the coarse aggregate had occurred. This damage was likely caused by the presence of *Cliona* boring sponges. The piles exhibited extensive damage that led to the discovery of unexpected threats to bridge substructures in marine environments, and the study emphasized the need for adequate protection from known environmental hazards.

6.6.2 Future Research Topics and Recommendations

The forensic investigation of the damage to the piles from the I-95 at Turtle River Bridge indicated a need for research in several areas as follows: (1) the development of high performance, normal strength concretes capable of withstanding sulfate attack, carbonation and chloride ingress to ensure service lives exceeding 100+ years while also meeting strength and design criteria necessary for precast concrete applications; (2) the development and implementation of corrosion resistant metallurgies possessing the mechanical properties necessary for use as prestressing strand; and (3) the biological attack on piles needs to be investigated, and a foundation of knowledge on the species causing attack, the rate and effects of

their ingress, as well as methods of preventing and mitigating damage to existing piles need to be assessed.

The forensic investigation also demonstrated a need for changes in the construction materials used. First, eliminate the use of calcium carbonate-based (Limestone) aggregate to prevent a large source of nutrients for the biological life that attacked the surface of the piles. The use of limestone powder in cement has not yet been examined, but may also provide a source of nutrients for the biological life. Second, use an ASTM C 150 (2009) Type II or ASTM C 1157 (2004) Class MS cement in place of an ASTM C 150 (2009) Type I or III cement to mitigate the risk of sulfate attack on future concrete structures as recommended by ACI Committee 201 (2008). An ASTM C 150 (2009) Type III Cement can be used in conjunction with supplementary cementitious materials or admixtures if the expansion for the ASTM C 1012 (2009) test meets the limits given by ACI Committee 201 (2008). Future research to be performed will develop draft design recommendations and concrete specifications to mitigate damage from the marine environment and allow for longer service lives.

6.7. References for Chapter 6

ACI Committee 201, (2008). “ACI 202.2R-08 Guide to Durable Concrete,” *ACI Manual of Concrete Practice*, ACI 201.2R-08, American Concrete Institute, Farmington Hills, MI, pp. 53.

ACI Committee 214 (2010). “Guide for Obtaining Cores and Interpreting Compressive Strength Results,” *ACI Manual of Concrete Practice*, ACI 214.4R-10, American Concrete Institute, Farmington Hills, MI, pp. 17.

ACI Committee 222 (2001). “Corrosion of Prestressing Steels,” *ACI Manual of Concrete Practice*, ACI 222.2R-01, American Concrete Institute, Farmington Hills, MI, pp. 43.

Angst, U., et. al. (2009). “Critical chloride content in reinforced concrete – A review,” *Cement and Concrete Research*, V. 39, pp. 1122-1138.

ASTM C 39 (2005). “Standard Test Method for Compressive Strength of Cylindrical Concrete Specimens,” American Society for Testing and Materials, West Conshohocken, PA, pp. 7.

ASTM C 150 (2009). “Standard Specification for Portland Cement,” American Society for Testing and Materials, West Conshohocken, PA, pp. 10.

ASTM C 805 (2008). “Standard Test Method for Rebound Number of Hardened Concrete,” American Society for Testing and Materials, West Conshohocken, PA, pp. 3.

ASTM C 876 (2009). “Standard Test Method for Corrosion Potentials of Uncoated Reinforcing Steel in Concrete,” American Society for Testing and Materials, West Conshohocken, PA, pp. 7.

ASTM C 1012 (2009). “Standard Test Method for Length Change of Hydraulic-Cement Mortar Bars Exposed to a Sulfate Solution,” American Society for Testing and Materials, West Conshohocken, PA, pp. 6.

ASTM C 1152 (2004). “Standard Test Method for Acid-Soluble Chloride in Mortar and Concrete,” American Society for Testing and Materials, West Conshohocken, PA, pp. 4.

ASTM C 1157 (2004). “Standard Performance Specification for Hydraulic Cement,” American Society for Testing and Materials, West Conshohocken, PA, pp. 5.

ASTM C 1218 (1999). “Standard Test Method for Water-Soluble Chloride in Mortar and Concrete,” American Society for Testing and Materials, West Conshohocken, PA, pp. 3.

ASTM C 1327 (2008). “Standard Test Method for Vickers Indentation Hardness of Advanced Ceramics,” American Society for Testing and Materials, West Conshohocken, PA, pp. 8.

ASTM E 1131 (2008). “Standard Test Method for Compositional Analysis by Thermogravimetry,” American Society for Testing and Materials, West Conshohocken, PA, pp. 5.

Bertolini, L., et. al. (2004). *Corrosion of Steel in Concrete: Prevention Diagnosis, Repair*, Wiley-VCH, pp. 392.

Ehlen, M.A. (2009). *Life 365* (Version 2.0.1) [Software]. Available from <http://www.life-365.org>

Ehlen, M.A., et. al. (2009). “Life 365 Service Life Prediction Model Version 2.0,” *Concrete International*, V. 31, pp. 41-46.

Hopkins, S.E. (1962). “Distribution of the species of *Cliona* (boring sponge) on the eastern shore of Virginia in relation to salinity,” *Chesapeake Science*, V. 3, pp. 121-125.

Mohammed, T.U., and Hamada, H. (2003). “Relationship between free chloride and total chloride contents in concrete,” *Cement and Concrete Research*, V. 33, pp. 1487-1490.

Mehta, P.K. (1991). *Concrete in the Marine Environment*, Elsevier Science Publishers, New York, NY, pp. 214.

Miller, A.N., et. al. (2010). “Effects of Heat and Salinity Stress on the Sponge *Cliona celata*,” *International Journal of Biology*, V. 2, pp. 3-16.

Neumann, A.C. (1966). “Observations on Coastal Erosion in Bermuda and Measurements of the Boring Rate of the Sponge, *Cliona lampa*,” *Limnology and Oceanography*, V. 11, pp. 92-108.

Neville, A.M. (1997). *Properties of Concrete*, 4 ed., John Wiley and Sons, New York, NY, pp. 844.

Nicol, W.L. and Reisman, H.M. (1976). "Ecology of the Boring Sponge (*Cliona celata*) at Gardiner's Island, New York," *Chesapeake Science*, V. 17, pp. 1-7.

Scott, P.J.B., et. al. (1988). "Bioerosion of Concrete and Limestone by Marine Organisms," *Marine Pollution Bulletin*, V. 19, pp. 219-222.

Skalny, J., et. al. (2002). *Sulfate Attack on Concrete*, Spon Press, New York, NY, pp. 217.

Winitzki, S. (2006). "A handy approximation for the error function and its inverse," Lecture note, Ludwig-Maximilians University, Munich, Germany.

Zea, S. and Weil, E. (2003). "Taxonomy of the Caribbean excavating sponge species complex *Cliona carribaea* – *C. Aprica* – *C. langae* (Porifera, Hadromerida, Clionaidae)," *Caribbean Journal of Science*, V. 39, pp. 348-370.

7. Preliminary Experiments: Corrosion of A416 Prestressing Steel

7.1. Introduction

Decades of research conducted on the corrosion of reinforcing steels in concrete has provided many insights into the fundamental mechanisms of corrosion initiation and propagation. It is known that in a typical reinforced concrete system, the alkaline solution present in the pore space of the hydrated cement paste with pH of 12.5-13.7 infers exceptional corrosion resistance via passive film formation on the surface of the steel (Ahmad, 2003, Poursaei, et al., 2007). It is only when chlorides reach a sufficient concentration (i.e., the chloride threshold level (CTL)) or with carbonation of concrete and its associated reductions in pH to the depth of the reinforcing steel that corrosion may initiate (Angst, et al., 2009). Reinforced concrete structures exposed to marine environments or heavy doses of deicing salts are typically most prone to premature deterioration caused by the initiation of corrosion (NACE, 2008).

Numerous studies examining CTLs, the passivity of steel in concrete, models for service life estimation, and novel corrosion mitigation / rehabilitation strategies have been conducted in the laboratory and the field; yet, the problems associated with corrosion continue to plague concrete structures around the globe (Virmani, et al., 1998). Further, a vast majority of prior research has focused on the corrosion of mild steel reinforced concrete structures, with relatively less research effort devoted to prestressed concrete (PSC). With the advent of PSC structural systems, engineers have been able to overcome the weak tensile strength of concrete by applying “precompressive” stress; allowing for longer spans, more complex structural systems, and in many cases decreased cost (Nawy, 2000). Precompressive stresses are typically applied by the tensioning of high-strength prestressing steels embedded in concrete as shown in Figure 7-1. Through design, prestressing forces can be tailored to negate tensile stresses induced by self weight and external loadings, thus limiting deleterious tensile cracking and increasing durability. In corrosive environments, bridges utilizing PSC elements (e.g., girders, piles) have seen increasing use in the last two decades as PSC bridges are generally considered to have superior durability compared with other bridge systems along with the other benefits discussed above (West, et al., 1999).

High-strength prestressing steels used in the construction of PSC elements are typically highly cold drawn, eutectoid (100 % pearlitic) steels with an ultimate strength of approximately 1860 MPa and ductility of 5-8 % (Nawy, 2000). A coating (typically rich in ZnPO_4) is applied to the surface of the steel to aid in drawing and in preventing atmospheric corrosion prior to embedding in concrete (Diaz, et al., 2009). Following drawing, thermomechanical stress relief treatments are performed to minimize stress relaxation and increase stress vs. strain linearity. For most applications, the resulting cold drawn wire with diameter of approximately 4 mm is produced in a stranded geometry as shown in Figure 7-2, allowing it to be shipped as a coil for use in subsequent construction processes. Most importantly, in a stranded geometry, crevices are formed at the impingement sites between adjacent wires (see Figure 7-2), leading to concerns for crevice corrosion mechanisms which may influence resistance to corrosion initiation (Talbot, et

al., 1998). Thus, when compared with low-carbon ferritic mild steels used in reinforced concrete structures, high-strength prestressing steels are fundamentally different in composition, surface condition, and geometric configuration – all of which likely play a synergistic role in their corrosion behavior in concrete. Consequently, the vast amount of knowledge gained from research conducted on the corrosion of mild steel reinforcement in concrete is not directly applicable to PSC systems when considering the underlying mechanisms of corrosion initiation in prestressing steels.

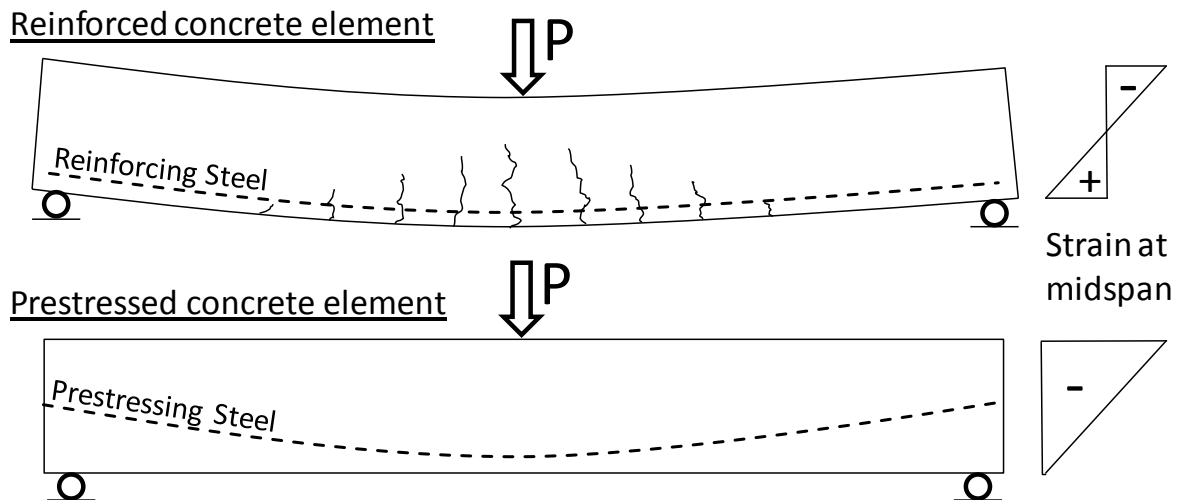


Figure 7- 1. Influence of prestressing reinforcement on the behavior of a concrete element

Previous research evaluating the corrosion resistance of prestressing steels can generally be divided into two categories: (1) small-scale electrochemical studies conducted in simulated concrete pore solutions using prestressing wires (Diaz, et al., 2009, Hartt, et al., 1993), and (2) large-scale studies using prestressing strand embedded in concrete and exposed to chloride containing solutions (Ahern, 2005, Kalina, 2009, Lean, 2008). Relatively few studies have considered the crevice effects associated with stranded geometries or the influence of as-received surface coatings (i.e., most used polished samples) on the electrochemical behavior of prestressing steels (Brooks, 2003, Proverbio, et al., 2002). Of these, only qualitative relationships between the presence of crevices between wires in a stranded geometry and alterations in corrosion resistance were examined (Proverbio, et al., 2002). In order to properly evaluate the corrosion resistance of prestressing steels with the goal of calculating CTLs and predicting service lives, these effects must be considered in order to reliably predict the field performance of PSC structures exposed to corrosive environments.

This chapter presents the results of a study examining the corrosion behavior of prestressing steels considering crevice effects and surface imperfections. Single wire and stranded prestressing steel specimens were produced with their as-received surface coatings left intact. Specimens were exposed to a simulated concrete pore solution with additions of NaCl and evaluated using cyclic potentiodynamic polarization (CPP) techniques. Following testing,

samples were characterized using optical and scanning electron microscopy (SEM) coupled with elemental analysis by energy dispersive X-ray spectroscopy (EDX). Select additional electrochemical experiments were performed to validate proposed corrosion damage mechanisms based on the results of polarization experiments. The primary objectives of this study were: (1) to quantitatively determine the impact of crevices caused by stranding on the chloride-induced corrosion resistance of prestressing steels, (2) to determine if the presence of imperfections in as-received surface coatings influences corrosion behavior, (3) to develop a model describing corrosion initiation processes in prestressing strands in concrete, and (4) to determine the influence of stranding on the service lives of PSC structures.

7.2. Experimental Program

7.2.1. Materials

Prestressing steel used for all experiments was produced by MMIStrandCo, LLC. (Newnan, GA) with a diameter of 15.2 mm in the 7-wire geometry shown in Figure 7-2. The chemical composition of the steel used is recorded in Table 7-1. As is typical for most highly cold drawn prestressing steels, a highly anisotropic pearlitic microstructure was observed with alternating lamellae of ferrite (white) and cementite (black) oriented longitudinally in the direction of cold drawing as illustrated in the electron micrographs shown in Figure 7-3 by wet etching in a 2 % Nital solution. The electron micrograph shown in Figure 7-4 depicts the disordered morphology of the as-received ZnPO_4 surface coating on the prestressing steel. Both the morphology and composition of the as-received surface coating are evidence of flaws generated during cold drawing and subsequent thermomechanical processing during strand production (Osborn, et al., 2008).

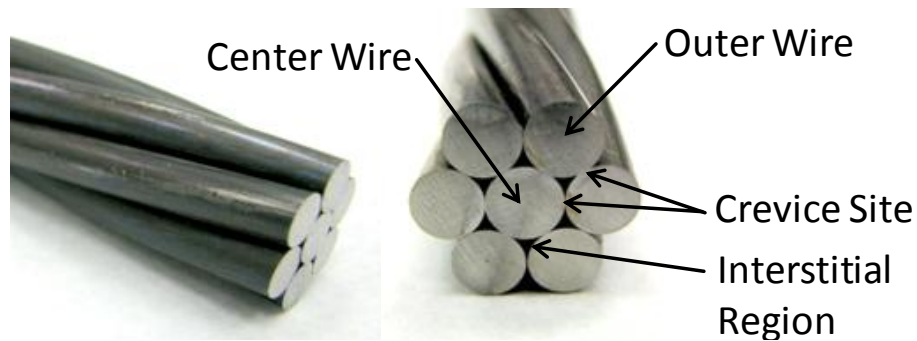


Figure 7-2. Stranded prestressing steel configuration

Table 7-1. Elemental composition of prestressing steel

Element	C	Mn	P	S	Si	Cr	Ni	Mo	Cu	V
Weight %	0.81	0.73	0.009	0.005	0.24	0.04	0.06	0.01	0.11	0.08

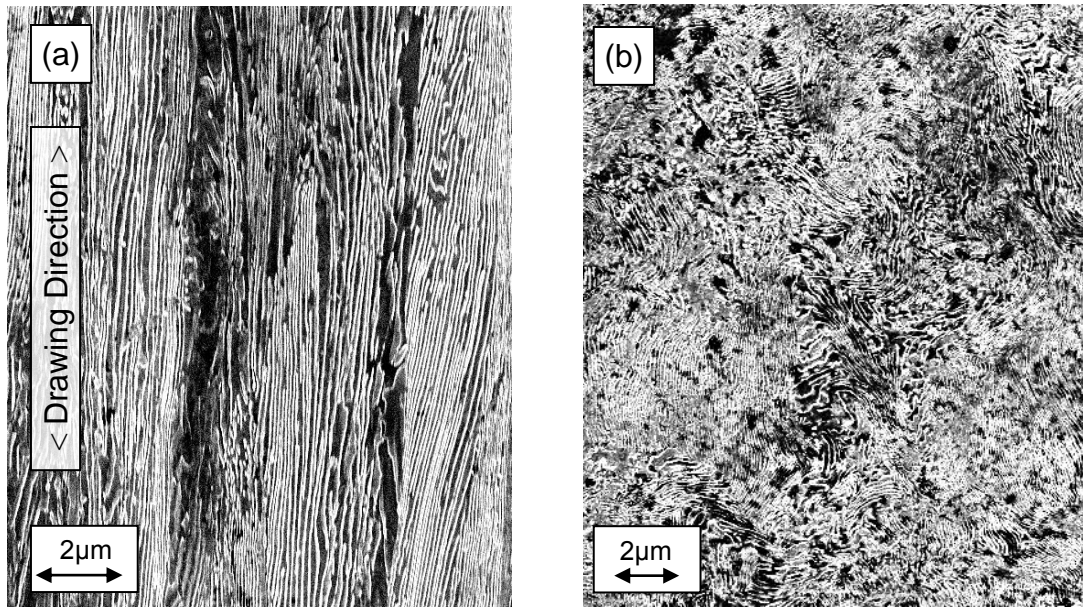


Figure 7- 3. Pearlitic microstructure of prestressing steel in (a) longitudinal and (b) transverse orientations

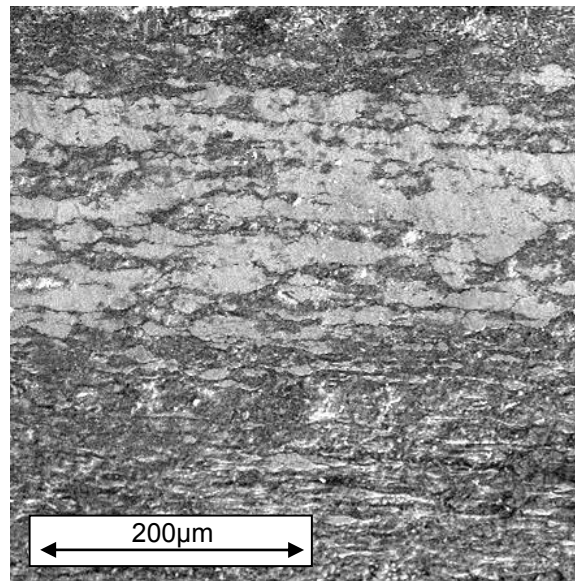


Figure 7- 4. As-received ZnPO_4 surface coating on prestressing steel

7.2.2. Fabrication of Test Specimens

Two specimen geometries were developed through numerous trials to simulate a single prestressing wire and a 7-wire prestressing strand. Details on the fabrication techniques used for each specimen geometry are described below.

7.2.2.1. Wire Specimen Geometry

Figure 7-5 (a) depicts a typical completed wire specimen. The center wire of a 7-wire prestressing strand was extracted and used to fabricate prestressing wire corrosion test specimens. A slow-speed diamond wafering saw was used to cut 63.5 mm long segments of the center wire. Polyolefin heat-shrink tubing was applied to the upper portion of the specimen to eliminate any air / solution interface effects. A polytetrafluoroethylene (PTFE) plug was affixed with epoxy to the end of the specimen to be immersed in the solution to isolate only the ZnPO_4 coated surface to the testing solution. Silicon adhesive sealant was applied circumferentially around the top and bottom of the area to be exposed to the testing solution as to prevent crevice corrosion from occurring under the heat shrink tubing or the PTFE plug. The resulting wire specimen had an exposed area of 3.5 cm^2 .

7.2.2.2. Strand Specimen Geometry

Figure 7-5 (b) depicts a typical completed strand specimen. All strand specimens were fabricated using as-received 7-wire prestressing strand. A slow-speed diamond wafering saw was used to cut 37 mm long segments of the prestressing strand. In order to preserve the original geometry of the strand (helical twist and impingement locations between wires), plastic cable ties were secured along the segment prior to prevent movement of the wires during cutting. Following cutting, the segments were ultrasonicated in ethanol to remove any oils, metal shavings, or debris lodged in the interstices of the strand. The seven wires of the strand were then soldered together and to an electrical lead to be connected to the potentiostat. To ensure that only the ZnPO_4 coated surface would be exposed to the testing solution and to seal off the soldered connections, both ends of the specimens were potted in epoxy (Sikadur 32 Hi-Mod) which had a viscosity that allowed it to properly encapsulate the strand without wicking up into the interstices. Once the epoxy had cured, the cable ties were removed and the specimen could be tested. The resulting strand specimen had an exposed area of 24.5 cm^2 .

7.2.3. Testing Procedures

All experiments were performed at 25°C in a solution based on a composition present in the pore space (i.e., a pore solution) of the hydrated cement paste of a typical concrete (Page, et al., 1983, Poursaee, et al., 2007) with composition shown in Table 7-2. The resulting solution possessed a pH of approximately 13.6. Chlorides (Cl^-) were added to solutions with NaCl up to 1.0 M concentration in steps of 0.1 M (i.e., 0.0 M, 0.1 M, 0.2 M, and so on). All CPP experiments were conducted in a basic three-electrode electrochemical cell shown diagrammatically in Figure 7-6 with a platinum foil counter electrode with surface area of 4 cm^2 , a saturated calomel reference electrode (SCE), and the working electrode being either the wire (as shown in Figure 7-6) or strand specimen. Wire specimens were tested in a solution volume of 250 ml while strand specimens were tested in a solution volume of 700 ml. These solution volumes were used in order to meet minimum solution volume-to-specimen surface area requirements of 0.2 ml/mm^2 outlined in ASTM G 31 (ASTM, 2004).

Table 7-2. Composition of simulated concrete pore solution

Compound	KOH	NaOH	CaSO ₄ ·2H ₂ O	Ca(OH) ₂	NaCl
Conc. (g/L)	17.94	5.24	0.55	2.40*	Varies

*Mostly precipitated out of solution

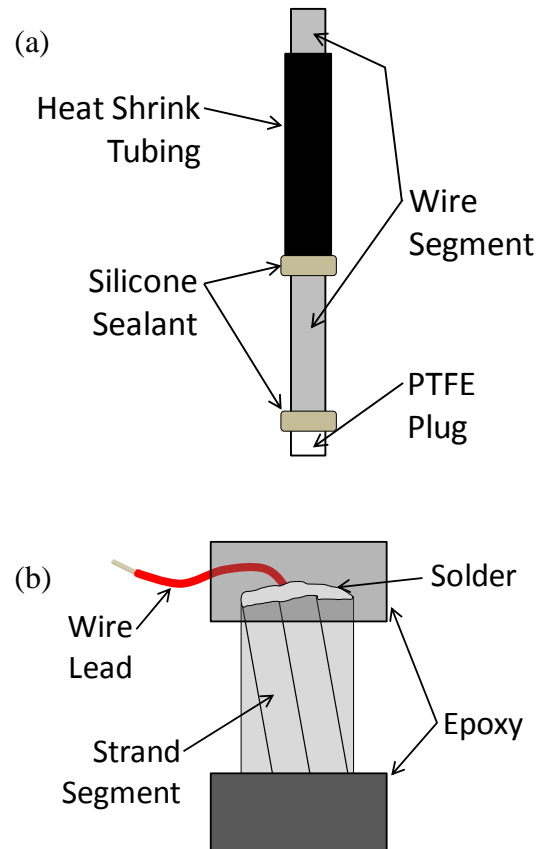


Figure 7-5. Overview of prestressing (a) wire specimen and (b) strand specimen configuration

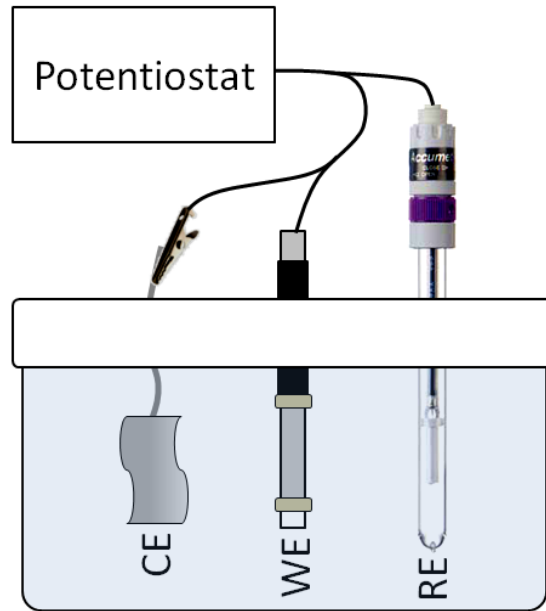


Figure 7- 6. Three electrode electrochemical cell used for CPP experiments

Prior to CPP testing, a two-step sample conditioning procedure was used for each sample tested. First, specimens were exposed to the simulate pore solution without Cl^- for 90 min in order to stabilize the passive film as it would be in the field prior to any Cl^- exposure. Following the 90 min passivation period, specimens were transferred into a pore solution containing the Cl^- concentration to be tested and allowed to acclimate for an additional 30 min, yielding total sample conditioning time of 120 min prior to testing. Time periods selected for sample conditioning were based on open circuit potential (OCP) vs. time studies which showed that after approximately 90 min the OCP began to stabilize as shown in Figure 7-7.

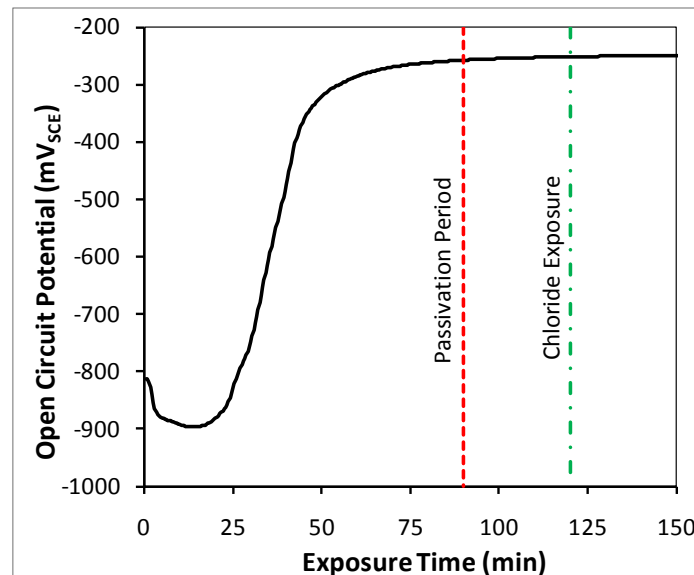


Figure 7- 7. Open circuit potential vs. time for prestressing wire immersed in simulated concrete pore solution without chlorides

Following the 120 min sample conditioning period, CPP was used to evaluate each specimen's resistance to corrosion initiation when exposed to a given Cl^- concentration. It is important to note that each experiment utilized a new sample that underwent its own sample conditioning procedure. CPP experiments were performed using GAMRY PC3/300, PC4/750, and Reference 600 potentiostats and an EG&G-PAR 263A potentiostat. A scan rate of 0.1 mV/s was used for all tests. Scans began at -25 mV vs. OCP (to limit cathodic film removal) and were run until reaching a current density of 0.25 mA/cm², at which point the scan rate was reversed and the potential was brought back down to -25 mV vs. the original OCP. The maximum current density 0.25 mA/cm² generally corresponded to an increase in current of approximately two decades due to either O₂ evolution or the initiation of localized corrosion. Following each experiment, tested samples were forensically thoroughly examined to ensure that no unintended crevice corrosion had initiated due to poor sample preparation techniques. If, for example, unintended corrosion was found under heat shrink tubing in one of the wire specimen, the data was disregarded and a new test was performed with a new specimen.

Using CPP techniques, corrosion initiation was clearly indicated by a sudden increase in current density during the anodic scan occurring at the breakdown potential ($E_{\text{breakdown}}$), with the current density remaining high even as the potential is reduced during the reversed scan (Alonso, et al., 2002, Bertolini, et al., 2009, Li, et al., 2002). An example of this is shown in Figure 7-8 for a prestressing wire specimen, where no corrosion initiation occurs under a 0.0 M Cl^- exposure whereas when exposed to a 0.9 M Cl^- solution localized corrosion clearly initiates at an $E_{\text{breakdown}}$ of 175 mV_{SCE} with the current density remaining high through the remainder of the test.

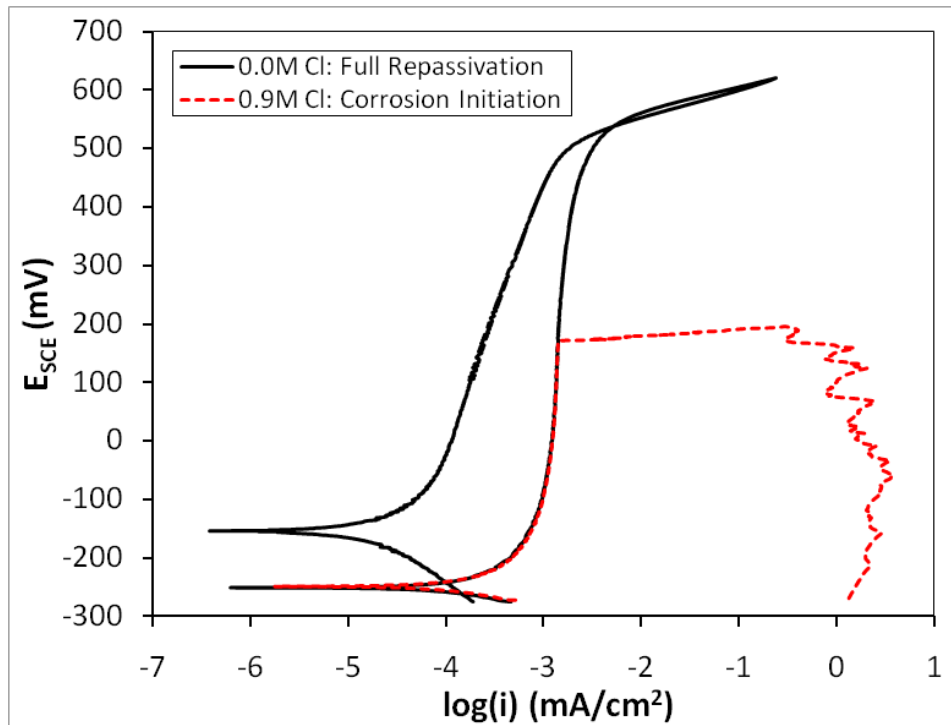


Figure 7- 8. Comparison between polarization behavior under 0.0M and 0.9M Cl^- exposures

One important factor to consider in any electrochemical experiment (particularly CPP studies) is the inherent variability in corrosion initiation and the $E_{\text{breakdown}}$ at which it may occur (Li, et al., 2002). These effects become especially important when evaluating systems where localized corrosion which is highly dependent on the random presence of surface defects to provide initiation sites. An example of the typical variability in CPP results obtained for triplicate specimens in the present study is shown in Figure 7-9. When no Cl^- is present (Figure 7-9 (a)), polarization behavior is easily replicated as the electrochemical reactions occur uniformly across the surface of the steel (e.g., uniform passive film formation or the evolution of O_2). However, when Cl^- is added to the solution (Figure 7-9 (b)), while corrosion does initiate in all cases, the $E_{\text{breakdown}}$ at which it occurs varies over a range of approximately 200 mV. In order to account for these effects, triplicate tests were performed at all Cl^- concentrations studied. Additionally, five to six replicate tests were performed near Cl^- concentrations that resulted in corrosion initiation (i.e., CTLs) to capture any stochastic variability in observed polarization behavior.

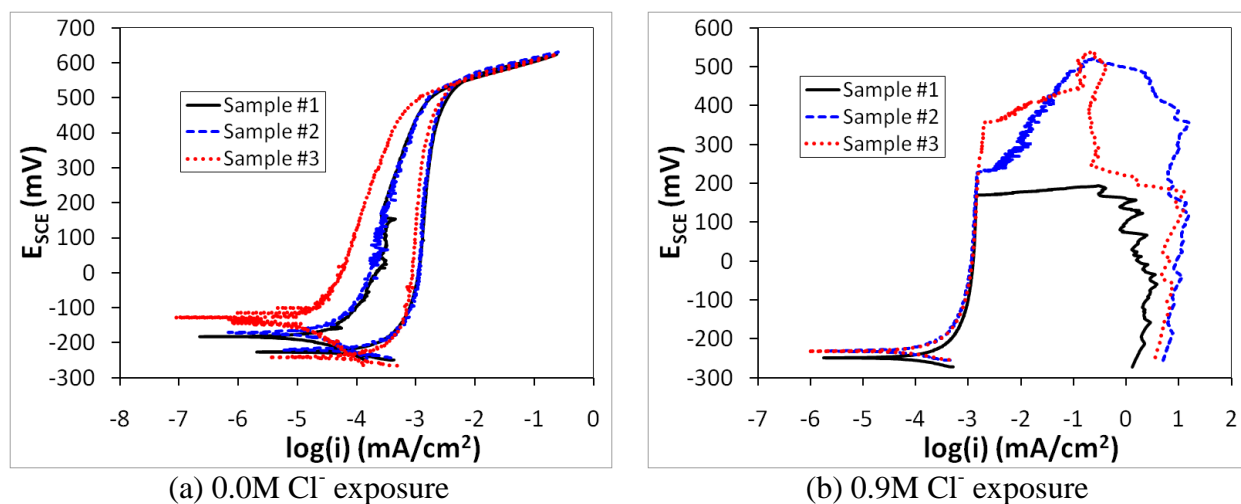


Figure 7- 9. Polarization behavior of triplicate specimens under different exposure conditions

7.2.4. Materials Characterization

Following testing, corrosion damage was characterized using either a LEO 1530 thermally-assisted field emission SEM or a Hitachi S-3700N variable pressure SEM. All images were acquired using backscattered electron detectors. Both systems are equipped with Oxford INCA EDX detectors for performing elemental analysis in conjunction with imaging. The Hitachi S-3700N is capable of imaging non-conductive samples at low vacuum. Samples analyzed using the LEO 1530 required sputter coating with Au for imaging. Samples with extensive buildup of corrosion products were imaged using the Hitachi S-3700N as it does not require the products be removed or sputter coated for imaging. A Leica MZ6 stereomicroscope was also used to characterize corrosion damage at low magnifications after testing.

7.3. Experimental Results and Discussion

7.3.1. Chloride-Induced Corrosion

7.3.1.1. Prestressing Wire

Figure 7-10 shows the polarization curves obtained from CPP experiments conducted on prestressing wire specimens in 0.0, 0.7, 0.8, 0.9, and 1.0 M Cl^- exposures. Cl^- concentrations which showed little effect (i.e., no corrosion initiation) have not been included in Figure 7-10 for brevity. Following the 120 min sample conditioning period, an open circuit corrosion potential (E_{corr}) of approximately $-240 \text{ mV}_{\text{SCE}}$ was measured for all wire specimens regardless of Cl^- concentration.

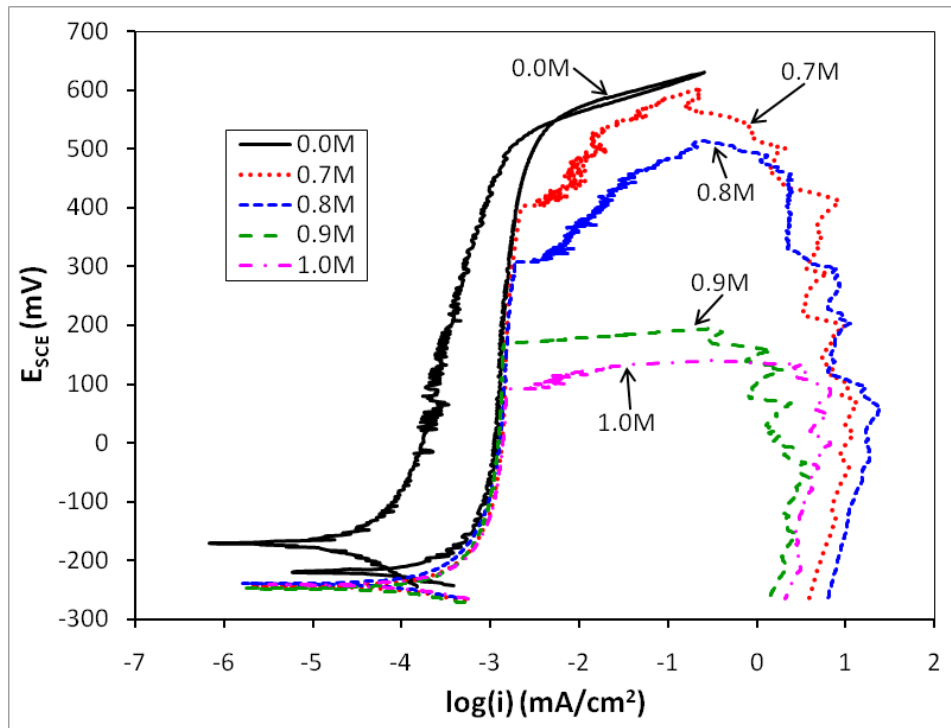


Figure 7- 10. Polarization curves for prestressing wire specimens at various Cl^- concentrations

When no Cl^- was present in solution, full repassivation was observed during the reverse potential scan following polarization into the O_2 evolution region (E above approximately $500 \text{ mV}_{\text{SCE}}$). Little influence of Cl^- was detectable until reaching a concentration of 0.6 M , at which point localized corrosion initiated during the anodic scan with the formation of an $E_{\text{breakdown}}$ prior to entering the O_2 evolution region. Based on the simulated concrete pore solution used for all experiments with pH of 13.6 (an $[\text{OH}^-]$ of 0.4 M), this Cl^- concentration (0.6 M) would correspond to a $[\text{Cl}^-]/[\text{OH}^-]$ ratio of approximately 1.5, a value which is comparable to CTLs determined using similar experiments on mild steel reinforcing bars in simulated concrete pore solutions (Alonso, et al., 2009, Angst, et al., 2009). As expected, Figure 7-10 also shows that as

Cl^- concentration increased, the barriers to corrosion initiation decreased as evidenced by the continual decrease in $E_{\text{breakdown}}$.

One other key result shown in Figure 7-10 is that no protection potential (E_{prot}) was formed during the reverse potential scan portion of the CPP scan above the original E_{corr} ; that is, once corrosion initiated, anodic dissolution continued to occur even without the application of an overpotential by the potentiostat. These effects become particularly apparent as shown in Figure 7-11 when comparing values of E_{corr} before and after conducting CPP experiments for the Cl^- concentrations studied. Prior to the CPP scan, the influence of Cl^- concentration on E_{corr} was negligible even up to 1.0 M exposure for 30 min during the second portion of the sample condition procedure. Following the CPP scan, as Cl^- concentrations increased from 0.0 M to 0.6 M a slight decrease of 60 mV in E_{corr} was measured, indicating a weak interaction between Cl^- and the passive film that did not result in corrosion initiation. However, above 0.6 M Cl^- , on the reverse scan E_{corr} shifted drastically to near -900 mV_{SCE}. This result is critically important because it suggests that the Cl^- concentration at which irreversible corrosion initiation occurs in CPP experiments (above 0.6 M in the case of prestressing wire) should be considered as the CTL for the prestressing wire specimen geometry and solution composition tested.

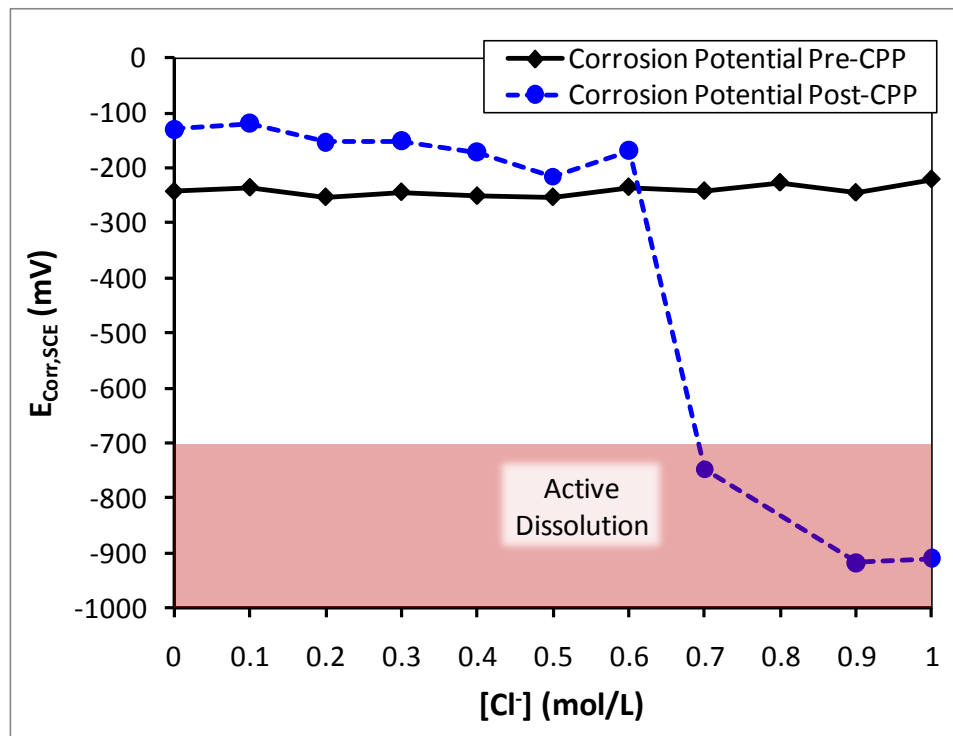


Figure 7- 11. E_{corr} vs. $[\text{Cl}^-]$ for prestressing wire specimens before and after CPP testing

7.3.1.2. Prestressing Strand

Figure 7-12 shows the polarization curves obtained from CPP experiments conducted on prestressing strand specimens in pore solutions with 0.0, 0.2, 0.3, 0.4, and 1.0 M Cl^- . Results for

other Cl^- concentrations have not been included in Figure 7-12 for brevity. Following the 120 min sample conditioning period, E_{corr} was approximately $-330 \text{ mV}_{\text{SCE}}$; 90 mV less than the E_{corr} of prestressing wire specimens. This shift in E_{corr} relative to prestressing wires is likely an indication of the formation of concentration / aeration cells between the outer portion and inner (mass transport limited) portion of the prestressing strand resulting in a measured cathodic polarization of E_{corr} (Jones, 1996, Landolt, 2007).

At Cl^- concentrations of 0.0 and 0.1 M, no corrosion initiation occurred with full repassivation after polarization into the O_2 evolution region. Corrosion initiation in prestressing strands occurred at a Cl^- concentration of 0.2 M (a $[\text{Cl}^-]/[\text{OH}^-]$ of 0.5) and higher – significantly less than that of prestressing wire specimens and clear evidence that stranding geometry does have a significant influence on the prestressing steel's resistance to chloride-induced corrosion. Similar to the behavior observed for prestressing wires, as Cl^- concentration increased $E_{\text{breakdown}}$ continued to shift negatively until reaching $-100 \text{ mV}_{\text{SCE}}$ at 1.0 M Cl^- .

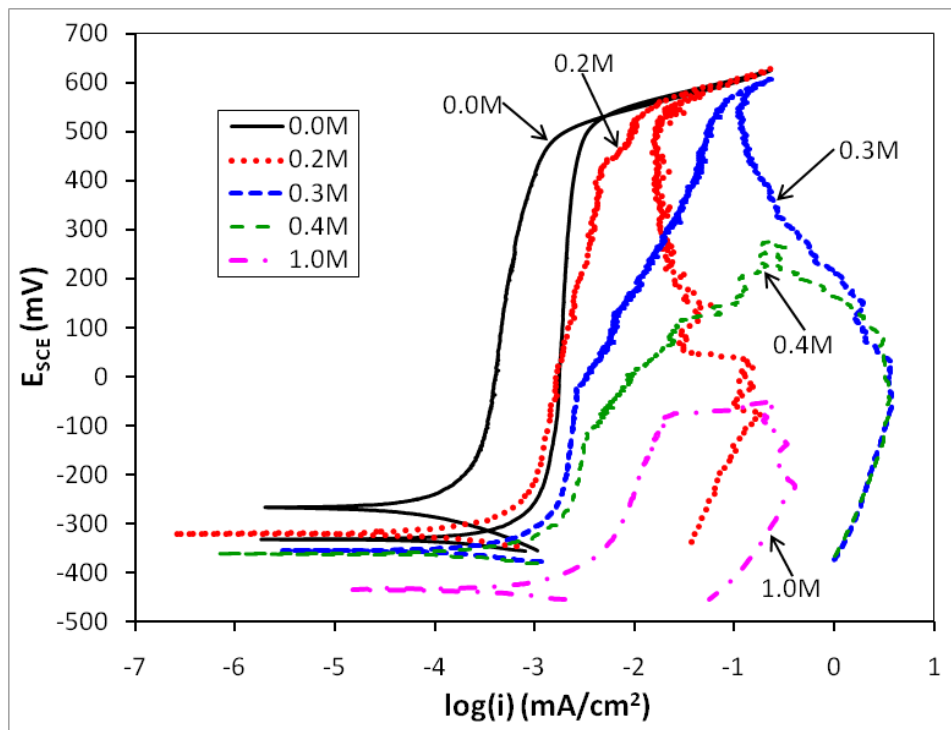


Figure 7- 12. Polarization curves for prestressing strand specimens at various Cl^- concentrations

Measurements of E_{corr} made before and after CPP testing of prestressing strand samples are shown in Figure 7-13. At Cl^- concentrations below 0.5 M, E_{corr} values were fairly stable near $-330 \text{ mV}_{\text{SCE}}$, while at higher concentrations, values of E_{corr} varied significantly between -300 and $-450 \text{ mV}_{\text{SCE}}$ and generally began to shift negatively immediately after being transferred from the non- Cl^- pore solution to Cl^- containing pore solution during sample conditioning – an indication that Cl^- were beginning to interact with the specimen prior to polarization. Analogous to the results obtained for prestressing wires, once corrosion initiated (at $[\text{Cl}^-]$ greater than 0.2 M)

repassivation with the formation of an E_{prot} did not occur and E_{corr} continued to decrease to less than $-900 \text{ mV}_{\text{SCE}}$ following CPP testing. Therefore, in prestressing strands, the Cl^- concentration at which corrosion initiates may also be considered as the CTL for the prestressing strand specimen geometry and solution composition tested.

7.3.1.3. Prestressing Strand vs. Wire

Figure 7-14 presents a comparison between the mean $E_{\text{breakdown}}$ determined for all replicate prestressing wire and strand specimens at each Cl^- concentration tested. The limiting $E_{\text{breakdown}}$ of $500 \text{ mV}_{\text{SCE}}$ shown for both prestressing wire and strand specimens represents the potential above which O_2 evolves. As discussed previously, for prestressing wires, $E_{\text{breakdown}}$ began to decrease above Cl^- concentration of 0.6 M , while for prestressing strands corrosion initiated at Cl^- concentrations as low as 0.2 M . For prestressing strands, at Cl^- concentrations above 0.4 M , $E_{\text{breakdown}}$ reached a limiting potential of approximately $-100 \text{ mV}_{\text{SCE}}$. This limit was not observed for prestressing wires, although perhaps if wires had been tested at higher Cl^- concentrations a limiting in $E_{\text{breakdown}}$ may have occurred. Nonetheless, when compared with prestressing wires, stranding was found to have a significant impact on resistance to chloride-induced corrosion initiation, resulting in a 67 % reduction in the CTL. The most important ramification of reductions in the CTL of prestressing strands is its impact on the accuracy of service life models that typically utilize CTLs based on mild steel reinforcement to predict the field performance of PSC structures exposed to corrosive environments.

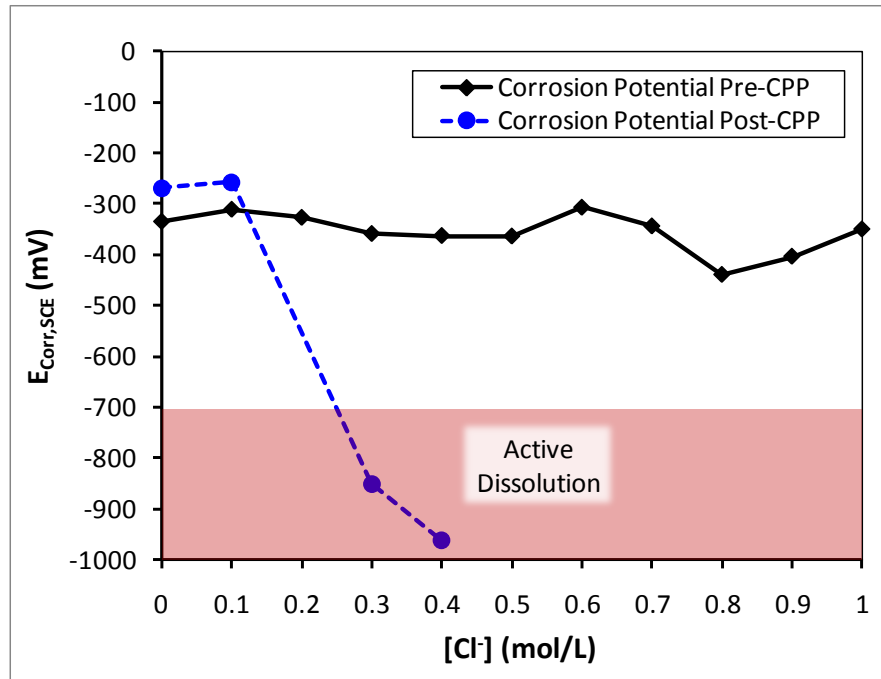


Figure 7-13. E_{corr} vs. $[\text{Cl}^-]$ for prestressing strand specimens before and after CPP testing

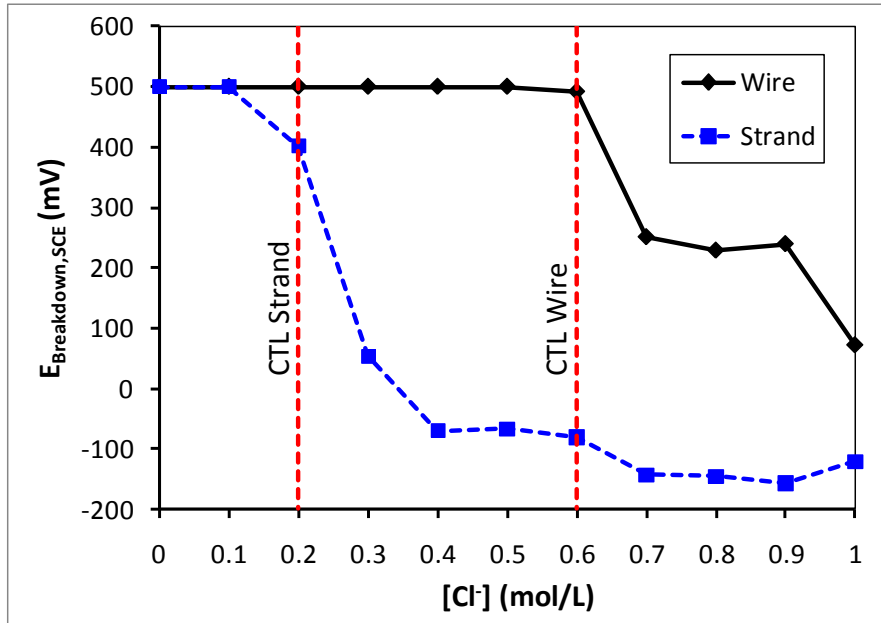
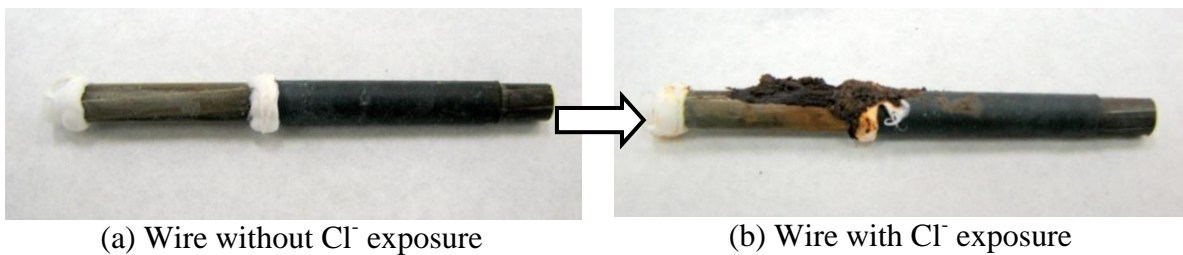


Figure 7-14. Breakdown potential vs. Cl^- concentration for prestressing wire and strand specimens

7.3.2. Morphology of Corrosion Damage

Following all CPP experiments, each specimen was examined to characterize the morphology of corrosion damage. Once corrosion initiated at Cl^- concentrations above the CTL for each specimen geometry, the damage observed and products formed were similar for both prestressing wires and strands. Figure 7-15 depicts the typical damage observed before and after testing at Cl^- concentrations above the CTL. Observed corrosion damage on prestressing wires and strands could generally be divided into two types: (1) localized pitting or crevice corrosion associated with corrosion initiation, and (2) uniform surface attack associated with corrosion propagation following initiation.



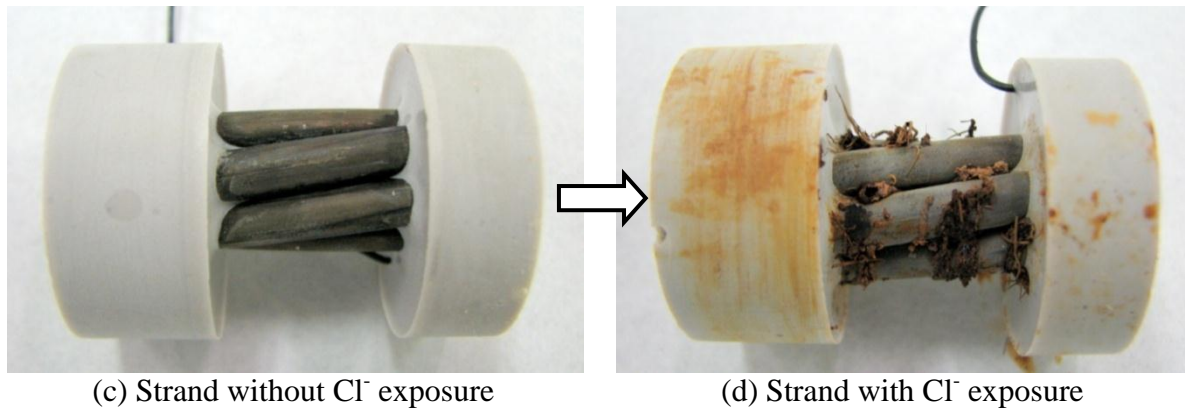


Figure 7- 15. Specimens before and after corrosion initiation by CPP experiments

In prestressing wires (Figure 7-15 (a) and (b)), corrosion was observed to initiate at surface imperfections with the formation of localized pitting type of corrosion attack, followed by uniform attack of the surface. Additional details on the influence of surface imperfections on corrosion initiation are provided in Section 7.3.3. In prestressing strands (Figure 7-15 (c) and (d)), corrosion was observed to initiate first in the crevice regions of the strand with products forming between wires, followed by more uniform attack spreading onto the outer portions of the strand. Cross sections of strands imaged using optical microscopy before and after testing (see Figure 7-16) showed that attack was also occurring in the interstices of the strand, with the formation of corrosion products adjacent to the impingement sites between wires.

Interestingly, at sites of localized corrosion (i.e., surface pitting or crevice corrosion) products formed as hollow “whiskers” with a morphology similar to that reported by Cherry and Price (Cherry, et al., 1980). In many cases whiskers were up to 1 cm long suspended in solution. X-ray diffractions patterns generated from whisker formations ground into a powder showed that the whiskers were primarily goethite (FeOOH). Extensive pitting was observed at the base of the whisker formations when removed. Figure 7-17 depicts a typical pit observed at the base of a whisker formation using SEM. Pits ranged in diameter from 5 to 20 μm and typically exhibited concentric circular deposits of corrosion products on the pit walls as shown in Figure 7-17. With corrosion products removed in regions of uniform surface attack, corrosion damage was found to be preferentially aligned in the drawing direction of the steel as shown in Figure 7-18. This type of damage mechanism was first described by Trejo et. al,(Trejo, et al., 2000) who proposed that given the dual phase microstructure of pearlitic steel, microgalvanic cells may form on the surface of the steel with ferrite acting as the anode and cementite acting as the cathode.

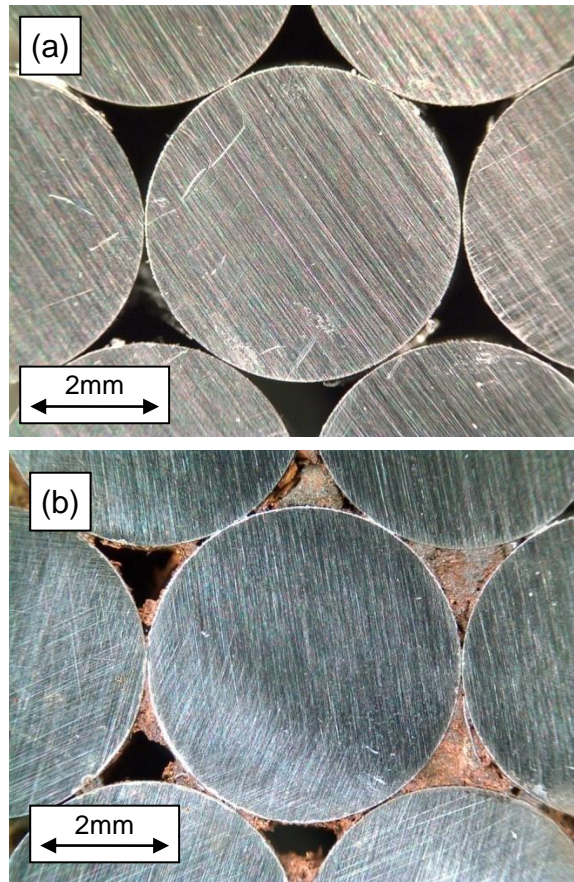


Figure 7-16. Cross section of prestressing strand (a) without exposure to Cl^- and (b) after corrosion initiation above the CTL

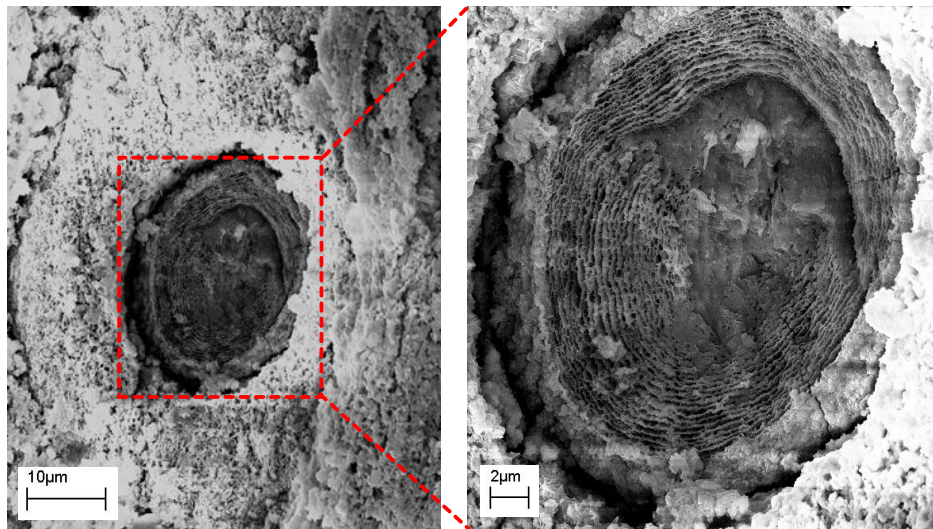


Figure 7-17. Typical pitting site on surface of prestressing steel with concentric circular deposits of corrosion product on the pit wall

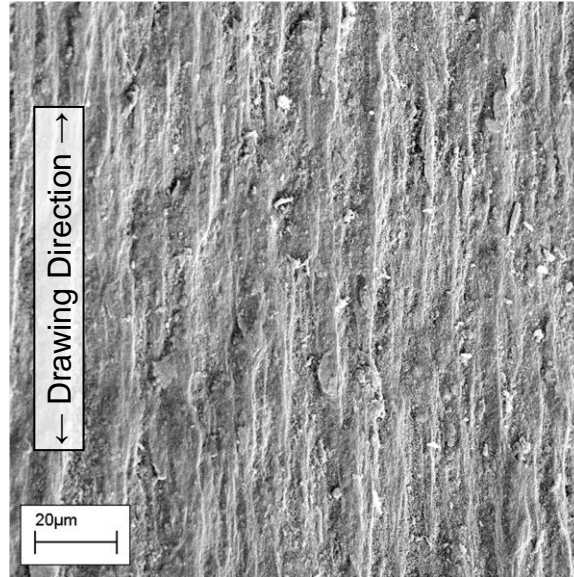


Figure 7-18. Uniform surface corrosion damage preferentially aligned in the drawing direction of the prestressing steel

Based on this investigation of corrosion damage, it was concluded that corrosion initiation in prestressing strands is controlled primarily by the presence of crevices at the impingement sites between wires along with imperfections in surface coatings, while in prestressing wires corrosion is influenced by the presence of surface imperfections which provide initiation sites. Once corrosion has initiated, its propagation occurs in a similar manner in both prestressing wires and strands, spreading from sites of localized corrosion into a more uniform attack of the surface.

7.3.3. Influence of Surface Imperfections

Through the characterization of corrosion damage discussed in Section 7.3.2, it became apparent that imperfections in the surface coating of the prestressing steel (along with crevices in prestressing strands) were typically the sites where corrosion would initiate. Imperfections in the ZnPO_4 surface coating can be divided into two categories: (1) scratches and blemishes in the coating due to cold-drawing prior to stranding operations, and (2) abrasion of the coating due to relative displacement between the wires which can occur during stranding and tensioning. Type 1 imperfections are typically present as either carbon rich (from wearing of the drawing die) or bare metal “streaks” aligned in the drawing direction of the wire. Type 2 imperfections are typically present as bare metal “streaks” running helically with the twist of the strand and can only be seen if the strand is dissected.

In-depth SEM and EDX analyses were performed on prestressing steel samples to characterize imperfections in their as-received surface coatings. Figure 7-19 details the heterogeneity present in a 1 mm^2 area of the coating at a Type 2 imperfection site (i.e., at the impingement site between two wires in a strand). EDX analyses performed at three sites are also shown. In the center of the backscattered image shown in Figure 7-19, a bright diagonal Type 2

imperfection band (marked by dashed lines) is evident making a helical twist at the impingement site between an outer wire and center wire of the prestressing strand. EDX analysis of this region indicates that most of the ZnPO_4 coating has been abraded off, leaving only Fe exposed. Adjacent to this imperfection, the surface coating remains intact with EDX analyses showing the presence of both Zn and P. In many cases trace amounts of Ca were also detected in the surface coating. These Ca deposits are likely residual coatings of stearate-type drawing lubricants which were not completely removed during post-processing stress relief and cleaning treatments (Osborn, et al., 2008).

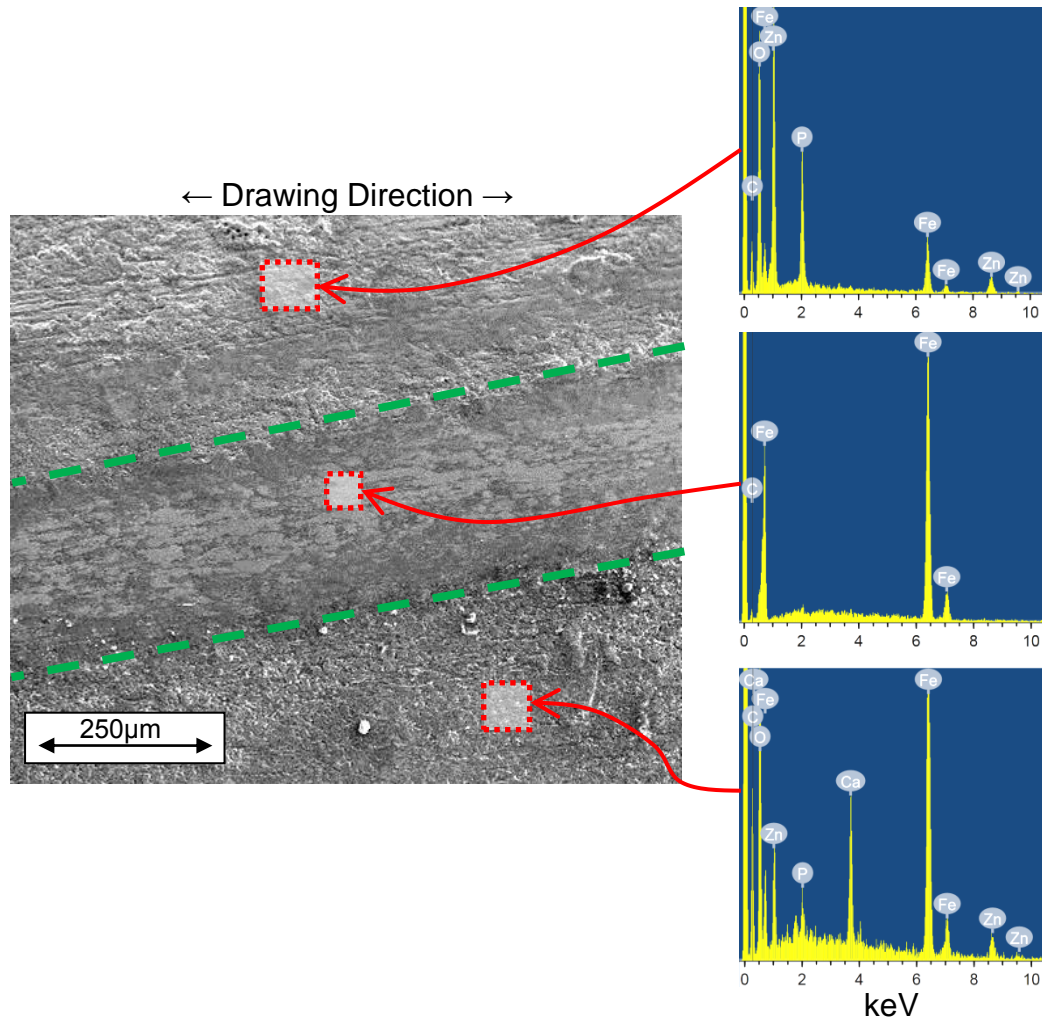


Figure 7-19. Typical Type 2 imperfection in ZnPO_4 surface coating of prestressing steel

In order to elucidate the effects of surface imperfections, additional CPP experiments were conducted on prestressing wire specimens. These tests were conducted using similar procedures to those presented in Section 7.2.3; however, when corrosion initiated at $E_{\text{breakdown}}$ the test was halted and the sample was removed and flushed with acetone. Using this technique, sites of corrosion initiation could be identified prior to the extensive formation of corrosion products

like those shown in Figure 7-15. Figure 7-20 depicts two samples tested using this procedure to determine preferential surface sites for corrosion initiation. Initiation was found to occur at Type 1 and Type 2 imperfections prior to general attack of the ZnPO_4 coated steel surface. Type 1 attack is clearly shown in Figure 7-20 on sample #2 with corrosion products forming on the carbon rich black streaks aligned in the drawing direction. Corrosion initiation at Type 2 imperfections is also shown in Figure 7-20, with corrosion products aligned with the helical twist of outer prestressing wires around the central prestressing wire. These results suggest that the presence of, and more importantly imperfections in, as-received surface coatings play an integral role in providing sites for corrosion to initiate. Such effects would not be detected by experiments conducted on polished samples. Moreover, considering that Type 2 imperfections occur at the same location as crevices in prestressing strands (impingement sites between wires), surface imperfections may act synergistically with crevice mechanisms to reduce the barriers to corrosion initiation in prestressing strands.

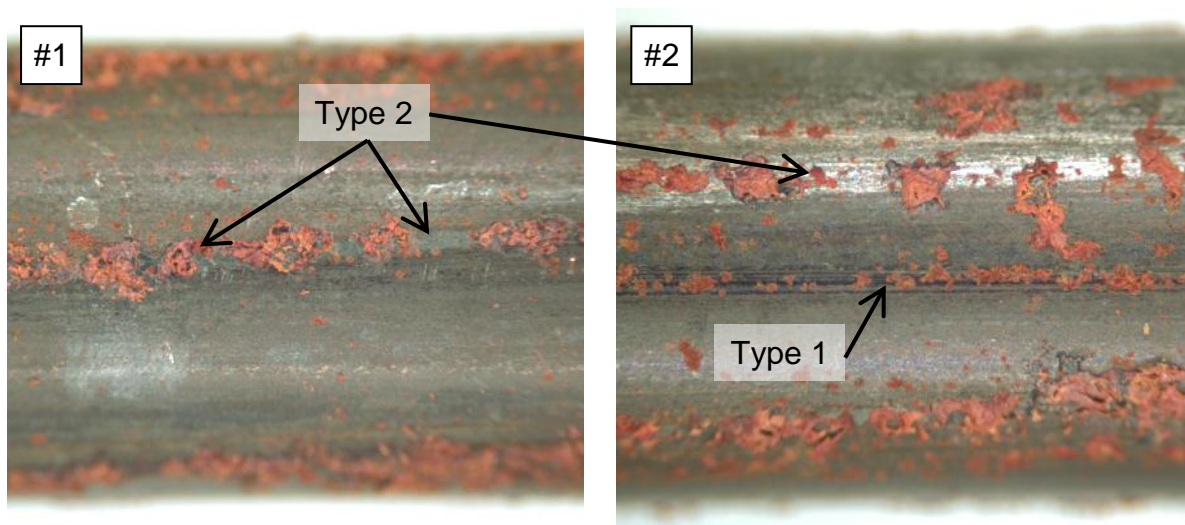


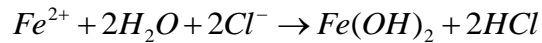
Figure 7- 20. Attack of surface imperfections during CPP corrosion initiation experiments

7.3.4. A Model for Corrosion Initiation in Prestressing Strands

Based on these data, many insights into the fundamental mechanisms of corrosion initiation in prestressing strands can be made. The results presented in Sections 7.3.1 and 7.3.2 have shown that both the electrochemical behavior and morphology of damage observed in prestressing strands is fundamentally different than that of prestressing wires. Crevice corrosion phenomena have been studied extensively in other fields of corrosion science but have only recently been noted as a possible mechanism for corrosion initiation in prestressing strands. Crevice mechanisms which may occur in the Cl^- containing pore solution system include:

- O_2 deficiencies in crevice regions due to mass transport limitations causing impaired passivity (Sharland, 1992). Lack of O_2 within the crevice may also result in the attraction of higher mobility Cl^- into the crevice in order to preserve charge neutrality (Jones, 1996).

- Acidification of the crevice region due to the hydrolysis of water in the presence of Cl^- leading to the formation of HCl and corrosion products (Jones, 1996) according to the reaction:



In addition to crevice mechanisms, results presented in Section 7.3.3 showed that imperfections in as-received coatings also play a role in corrosion initiation. Key in the case of prestressing strands is the fact that the location of Type 2 surface imperfections coincides with the location of crevices formed at the impingement site between adjacent prestressing wires. Another factor to consider is that prestressing strand is embedded into concrete wherein the outer surface of the strand is in direct contact with cement hydration products (including $\text{Ca}(\text{OH})_2$) while the interstitial space of the strand is not. Once corrosion initiates within crevices and acidification occurs in the interstitial region of the strand, the outer surface of the strand will be continuously buffered by solid $\text{Ca}(\text{OH})_2$ while the inner portion likely continues to acidify, thus amplifying concentration cell effects between the inner and outer portions of the strand.

Building on these mechanisms and the results presented herein, a three-step “thought” model has been proposed to describe the corrosion initiation and propagation process in prestressing strands. An overview of the model is shown diagrammatically in Figures 7-21 (a) to (c) and is described as follows:

- Step 1 – Figure 7-21 (a): Crevice corrosion initiates at the impingement sites between adjacent prestressing wires once Cl^- concentration exceeds the CTL.
- Step 2 – Figure 7-21 (b): Following initiation, localized corrosion continues to occur at crevice sites accompanied by acidification of the interstitial region of the prestressing strand as indicated by change in color from black to white.
- Step 3 – Figure 7-21 (c): Once corrosion products have built up to a sufficient amount such that the mass transport of reactants to crevice sites is limited, corrosion attack spreads to the surface of the strand resulting in damage similar to what was observed on prestressing wires.

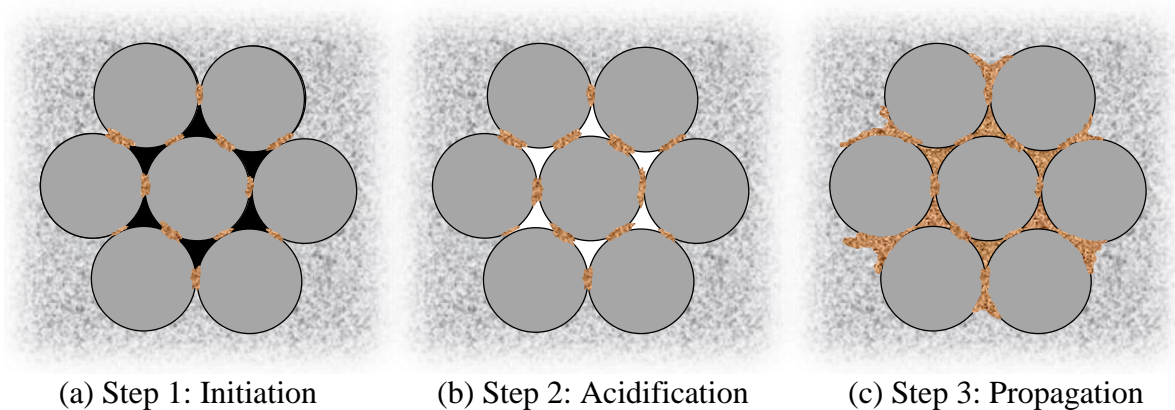


Figure 7- 21. Model for corrosion initiation in prestressing strands

7.3.5. Potential Impact on Service Lives

A final point warranting further discussion is the impact of this study on the field performance of PSC structures exposed to corrosive environments and the techniques used to predict their service lives. For any service life model to reliably predict field performance of PSC structures, an accurate value for the CTL is necessary. These data show that in the case of prestressing steel produced in a stranded geometry, using CTLs based on the results of studies evaluating the corrosion resistance of mild steel reinforcement and prestressing wires may not be entirely accurate. Based on the results of the present study, reductions in the CTL due to stranding would likely decrease the time required for corrosion to initiate but have little effect on its propagation. Using a basic Collepardi type non-steady state Fickian diffusion model (Nilsson, 2009) like that shown in Figure 7-22, it is clear that reducing the CTL from that of a prestressing wire (same as mild steel reinforcement) to that of a prestressing strand can result in premature corrosion initiation provided that Cl^- has reached a sufficient concentration at the cover depth.

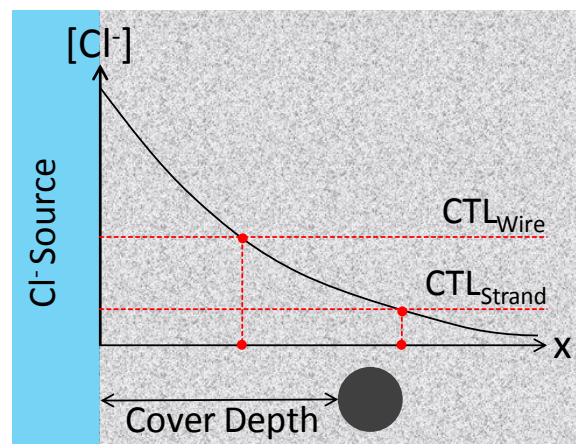


Figure 7-22. Influence of reductions in CTL on corrosion initiation based on 2nd-order Fickian diffusion

In order to investigate the influence of reductions in the CTL due to stranding on predicted service lives, a series of virtual experiments were conducted on model concrete systems using the service life and life-cycle cost estimation tool Life 365 (Thomas, et al., 2009). One-dimensional Cl^- diffusion experiments were conducted using a cover depth of 50 mm and surface Cl^- concentration of 18.8 kg/m^3 . The CTLs for prestressing wires and strands were assumed to be 1.0 and 0.33 kg/m^3 , respectively based on the results of the present study. For simplicity, the influence of Cl^- binding, reductions in diffusivity with time, and corrosion propagation time prior to repair/replacement were neglected. Virtual experiments were conducted using diffusion coefficients ranging from $1 \cdot 10^{-12} \text{ m}^2/\text{s}$ representing a concrete with w_{cm} below 0.4 containing supplementary cementitious materials such as fly ash or silica fume to $100 \cdot 10^{-12} \text{ m}^2/\text{s}$ representing an ordinary portland cement concrete with w_{cm} near 0.7 (Thomas, et al., 1999).

Results of virtual time-to-corrosion experiments are shown in Figure 7-23 for prestressing wires and strands. Reductions in the CTL to account for stranding did lead to a decrease in the time-to-corrosion. However, this decrease was not linearly related to the change in the CTL. For a 67 % reduction in the CTL from 1 kg/m³ (based on mild steel reinforcement) to 0.33 kg/m³ to account for stranding, the time to corrosion was reduced by approximately 34 %. While the authors accept that additional research is required to validate laboratory-based electrochemical studies and virtual service life experiments presented herein, these results clearly demonstrate that stranding and its associated reduction in the CTL should be considered in any service life model used for predicting the field performance of PSC structures exposed to corrosive environments.

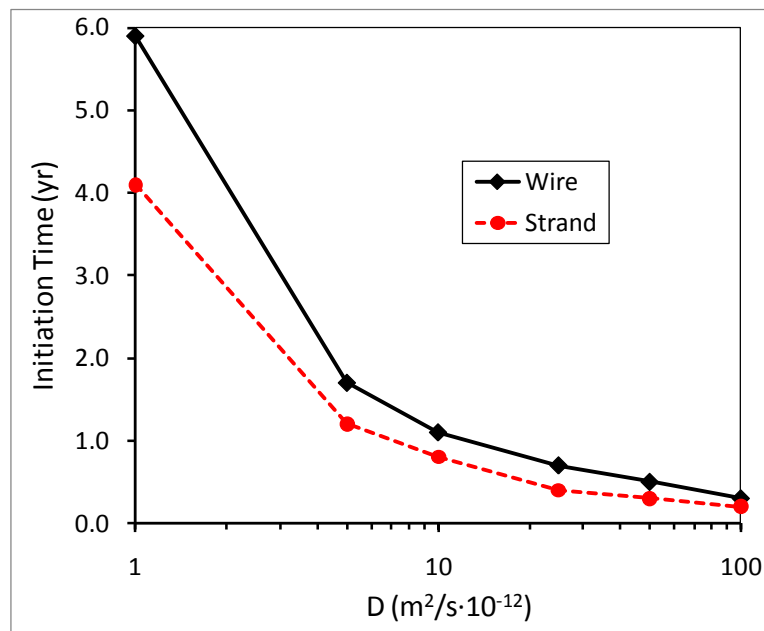


Figure 7-23. Influence of reductions in CTL on corrosion initiation times using Life 365

7.4. Conclusions of Preliminary Experiments on A416 Prestressing Strands

The influence of crevices present in stranded geometries and as-received surface coatings on the corrosion resistance of prestressing steels was evaluated using CPP techniques. Prestressing wire and strand specimens were exposed to a simulated concrete pore solution with Cl⁻ added as NaCl up to 1.0 M.

- 1) CPP experiments conducted on prestressing strand samples showed a 67 % reduction in values of the CTL when compared with prestressing wires. Once above a Cl⁻ concentration at which corrosion would initiate, repassivation did not occur and samples continued to undergo anodic dissolution at an E_{corr} of approximately -900 mV_{SCE} without any perturbation by the potentiostat.

- 2) Corrosion initiation in prestressing wires occurred primarily at the imperfections in the as-received ZnPO_4 coated steel surface. Corrosion initiation in prestressing strands was found to occur initially in crevices located at the impingement sites between adjacent wires. The morphology of corrosion propagation following initiation was observed to be similar in both wires and strands, transitioning from localized corrosion into more uniform surface attack.
- 3) Additional CPP corrosion initiation experiments indicate that imperfections in the as-received ZnPO_4 surface coating provide preferential sites for localized corrosion to initiate. These effects would not be detected by experiments conducted on polished prestressing steel specimens.
- 4) Based on the results of CPP studies and characterization of corrosion damaged samples, a “thought” model was developed to describe the mechanisms of corrosion initiation in prestressing strands. Traditional crevice corrosion mechanisms likely interact with surface imperfections, resulting in the significant reduction in CTLs found for prestressing strand.
- 5) Virtual CI ingress experiments conducted on model concrete systems showed that a reduction in the CTL due to stranding of 67 % resulted in a decrease in the time-to-corrosion initiation of 34 %. In order to accurately predict the field performance of PSC structures exposed to corrosive environments, service life models must take into account the influence of stranding on reductions in the CTL.

7.5 References for Chapter 7

- Ahern, M. E. (2005). "Design and Fabrication of a Compact Specimen for Evaluation of Corrosion Resistance of New Post-Tensioning Systems." MS, University of Texas at Austin, Austin, TX.
- Ahmad, S. (2003). "Reinforcement Corrosion in Concrete Structures, its Monitoring and Service Life Prediction - A Review." *Cement & Concrete Composites*, V. 25, pp. 459-471.
- Alonso, C., Castellote, M., and Andrade, C. (2002). "Chloride threshold dependence of pitting potential of reinforcements." *Electrochimica Acta*, V. 47 (21), pp. 3469-3481.
- Alonso, M. C., and Sanchez, M. (2009). "Analysis of the variability of chloride threshold values in the literature." *Materials & Corrosion*, V. 60 (8), pp. 631-637.
- Angst, U., Elsener, B., Larsen, C. K., and Vennesland, Ø. (2009). "Critical chloride content in reinforced concrete -- A review." *Cement & Concrete Research*, V. 39 (12), pp. 1122-1138.
- ASTM (2004). "G31 - Standard Practice for Laboratory Immersion Corrosion Testing of Metals." American Society of Testing and Materials, West Conshohocken, PA.

Bertolini, L., and Redaelli, E. (2009). "Depassivation of steel reinforcement in case of pitting corrosion: detection techniques for laboratory studies." *Materials & Corrosion*, V. 60 (8), pp. 608-616.

Brooks, M. A. (2003). "Influence of interstitial crevice corrosion in accelerated corrosion testing." BS, Penn State University, State College, PA.

Cherry, B. W., and Price, S. M. (1980). "Pitting, Crevice and Stress-Corrosion Crackign Studies of Cold Drawn Eutectoid Steels ." *Corrosion Science*, V. 20 (11-12), pp. 1163.

Diaz, B., Freire, L., Novoa, X. R., and Perez, M. C. (2009). "Electrochemical behaviour of high strength steel wires in the presence of chlorides." *Electrochimica Acta*, V. 54 (22), pp. 5190-5198.

Hartt, W. H., Kumria, C. C., and Kessler, R. J. (1993). "Influence of Potential, Chlorides, pH, and Precharging Time on Embrittlement of Cathodically Polarized Prestressing Steel." *CORROSION*, V. 49 (5), pp. 377-385.

Jones, D. A. (1996). *Principles and Prevention of Corrosion*, Prentice Hall, Upper Saddle River, NJ.

Kalina, R. D. (2009). "Comparitive Study of the Corrosion Resistance of Different Prestressing Strand Types for use in Post-Tensioning of Bridges." MS, University of Texas at Austin, Austin, TX.

Landolt, D. (2007). *Corrosion and Surface Chemistry of Metals*, EPFL Press, Lausanne, Switzerland.

Lean, S. M. (2008). "Comparison of the Corrosion Resistance of New and Innovative Prestressing Strand Types used in the Post Tensioning of Bridges." MS, University of Texas at Austin, Austin, TX.

Li, L., and Sagues, A. A. (2002). "Chloride corrosion threshold of reinforcing steel in alkaline solutions - Cyclic polarization behavior." *CORROSION*, V. 58 (4), pp. 305-316.

NACE (2008). "How Much Can a Bridge Take?", NACE, Houston, TX.

Nawy, E. G. (2000). *Prestressed Concrete - A Fundamental Approach*, Prentice Hall, Upper Saddle River, NJ.

Nilsson, L.-O. (2009). "Models for chloride ingress into concrete - from Collepardi to today." *International Journal of Modeling, Indentification, and Control*, V. 7 (2), pp. 129-134.

Osborn, A. E. N., Lawler, J. S., and Connolly, J. D. (2008). "Acceptance Tests for Surface Characteristics of Steel Strand in Prestressed Concrete." NCHRP.

Page, C., and Vennesland, Ø. (1983). "Pore solution composition and chloride binding capacity of silica-fume cement pastes." *Materials & Structures*, V. 16 (1), pp. 19-25.

- Poursaee, A., and Hansson, C. M. (2007). "Reinforcing steel passivation in mortar and pore solution." *Cement & Concrete Research*, V. 37 (7), pp. 1127-1133.
- Proverbio, E., and Bonaccorsi, L. M. (2002). "Failure of Prestressing Steel Induced By Crevice Corrosion in Prestressed Concrete Structures." *9th International Conference on Durability of Materials and Components* Brisbane, Australia.
- Sharland, S. M. (1992). "A Mathematical-Model of the Initiation of Crevice Corrosion in Metals." *Corrosion Science*, V. 33 (2), pp. 183-201.
- Talbot, D., and Talbot, J. (1998). *Corrosion Science and Technology*, CRC Press LLC, Boca Raton, FL.
- Thomas, M. D. A., Bamforth, P. B., and Banerjee, M. K. (1999). "Modelling chloride diffusion in concrete effect of fly ash and slag." *Cement & Concrete Research*, V. (29), pp. 487-495.
- Thomas, M. D. A., Bentz, E. C., and Ehlen, M. A. (2009). "Life-365 v. 2.0.1." Life-365 Consortium.
- Trejo, D., Monteiro, P. J. M., Ben C. Gerwick, J., and Thomas, G. (2000). "Microstructural Design of Concrete Reinforcing Bars for Improved Corrosion Performance." *ACI Materials Journal*, V. 97 (1), pp. 78-84.
- Virmani, Y. P., and Clemena, G. G. (1998). "Corrosion Protection: Concrete Bridges." Turner-Fairbank Highway Research Center.
- West, J. S., Larosche, C. J., Koester, B. D., J. E. Breen, and Kreger, M. E. (1999). "State-of-the-Art Report about Durability of Post-Tensions Bridge Substructures." University of Texas at Austin, Austin, TX.

8. Stainless Steels for Prestressing Strand

8.1. Introduction

Corrosion of reinforcing and prestressing steels in concrete structures exposed to corrosive environments is the predominant deterioration mechanism that reduces service life. While significant research on corrosion mitigation in concrete has been conducted over the last few decades, the challenges associated with the corrosion of steel reinforcement in concrete remain. Recent studies indicate that 15 % of structural deficiencies in U.S. bridges are the result of corrosion, with direct annual costs of \$3.5 billion for the replacement of bridges damaged by corrosion and \$4 billion to maintain and replace corroded concrete bridge decks and substructures (Koch, et al., 2008).

Recent initiatives such as the Bridge Life Extension Act and FHWA's 100+ year bridge service life goal have provided a new impetus for the implementation of corrosion mitigation technologies in new concrete structures (Koch, et al., 2008, NACE, 2008). A majority of developed corrosion mitigation technologies have focused on concrete structures reinforced with mild ferritic steels, including high performance / low permeability concretes (Hansson, 2005, Hope, et al., 2001), epoxy coated and galvanized reinforcing steels (Darwin, et al., 2007, Sagüés, et al., 1994, Zemajtis, et al., 1999), electrochemical methods of protection (Bertolini, et al., 1993, Cramer, et al., 2002, Sharp, et al., 2006), corrosion inhibitors (Zemajtis, et al., 1999), and surface coatings and sealers (Broomfield, 2007).

One of the most effective methods of corrosion mitigation in reinforced concrete is the use of corrosion resistant reinforcing (CRR) materials, typically austenitic and/or duplex (austenite + ferrite) stainless steel reinforcing bars (Bautista, et al., 2006, Garcia-Alonso, et al., 2007, Hartt, et al., 2004, Nürnberger, et al., 2008). Stainless steels possess chloride (Cl⁻) threshold levels (CTLs) typically more than one order of magnitude greater than normal mild reinforcing steels (Hartt, et al., 2004). However, the extension of CRRs from reinforced to prestressed concrete (PSC) is a topic which has received limited attention in the literature, but is one which looks to provide many of the same durability benefits witnessed in reinforced concrete structures. The growing use of PSC elements, especially in bridge structures (e.g., piles and girders) is a cause for increased awareness of the corrosion issues and mitigation techniques; especially because prestressing steels differ in composition, surface treatment, and geometry when compared with mild reinforcing steels.

The goals of this chapter are: (1) to provide a basic understanding of PSC structural systems and their degradation by corrosion, (2) to briefly examine the corrosion resistance of stainless steels in reinforced concrete, (3) to critically review research performed on high-strength stainless steels (HSSs) for use in prestressed concrete, and (4) to present a synopsis of research on HSSs conducted in other industries which may be applicable for corrosion mitigation in PSC.

8.2. Characteristics and Degradation of Prestressed Concrete Structural Systems

Concrete structures utilizing prestressing reinforcement (either pre-tensioned or post-tensioned) instead of mild steel reinforcement allow for longer spans with smaller cross sections, more complex structural systems, and less tendency for deleterious tensile cracking of the concrete which can accelerate corrosion by Cl^- ingress and/or carbonation of the cover concrete. Prestressing steel is typically stressed between 60 to 80 % ultimate tensile capacity (σ_{ult}) to apply a “precompression” force to the concrete element as shown in Figure 8-1 (Nawy, 2000). These stresses are much higher than the 40 to 50 % σ_{ult} typically used for tendons in suspension and cable-stayed bridge structures.

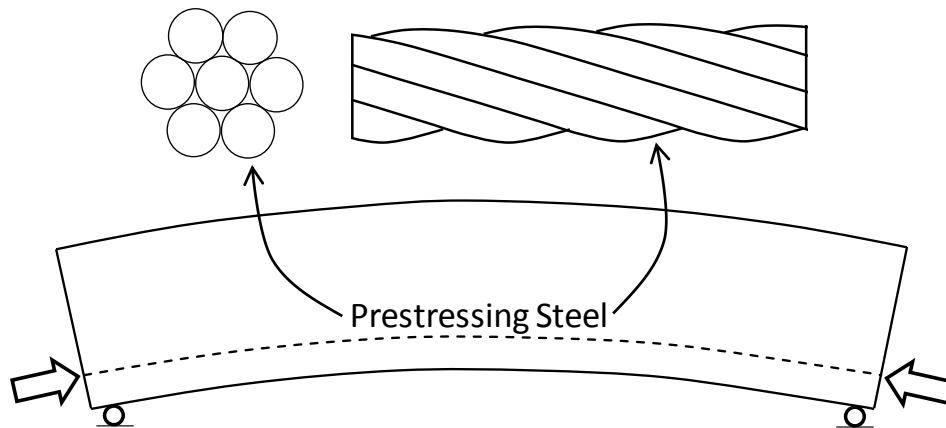


Figure 8-1: Behavior of simply-supported prestressed concrete beam

Typical prestressing systems utilize fully pearlitic (δ -ferrite + Fe_3C -cementite) eutectoid steels (0.8 % C, 0.75 % Mn, 0.25 % Si, and other trace elements) which when cold drawn significantly increase their tensile strength. Low-relaxation thermomechanical processing is performed using an inline induction furnace at approximately 370 °C and 40 % σ_{ult} (Atienza, et al., 2007). The resulting “stabilized” product possesses a yield strength (σ_y) of approximately 1720 MPa, σ_{ult} of 1860 MPa, ductility (ϵ_{ult}) of 7 %, and stress relaxation ($\Delta\sigma_r$) less than 2 to 3 % (2006, Hope, et al., 2001). As illustrated in Figure 8-2, these mechanical properties place prestressing steels among the highest strength steels used in engineering practice. Prestressing steels are typically manufactured as 12.7 to 15.2 mm seven-wire (“1x7”) strand (see Figure 8-1), allowing the material to be shipped in a coiled form for use in subsequent construction processes.

Due to the small 3 to 5 mm diameter of wires used in prestressing strands, small cross section losses caused by corrosion can quickly lead to significant structural deficiencies (Nürnberg, 2002). Some researchers have noted that the interstitial regions and wire impingement sites in a stranded geometry are inherent crevice sites where localized corrosion may be preferentially initiated (Ahern, 2005, Brooks, 2003, Proverbio, et al., 2002). Recent studies conducted by the authors have shown that prestressing steels produced in a stranded geometry resulted in a 67 % reduction in measured CTLs compared with single prestressing

wires (Moser, et al., 2010). In addition to traditional corrosion mechanisms, susceptibility to environmentally assisted cracking (EAC) is also a concern due to the prestressing steel's inherent metallurgical properties when combined with high tensile stress (Mietz, 2000, Nürnberger, 2009, Schroeder, et al., 2003). The following section reviews corrosion and EAC mechanisms relevant to the degradation of prestressing steels.

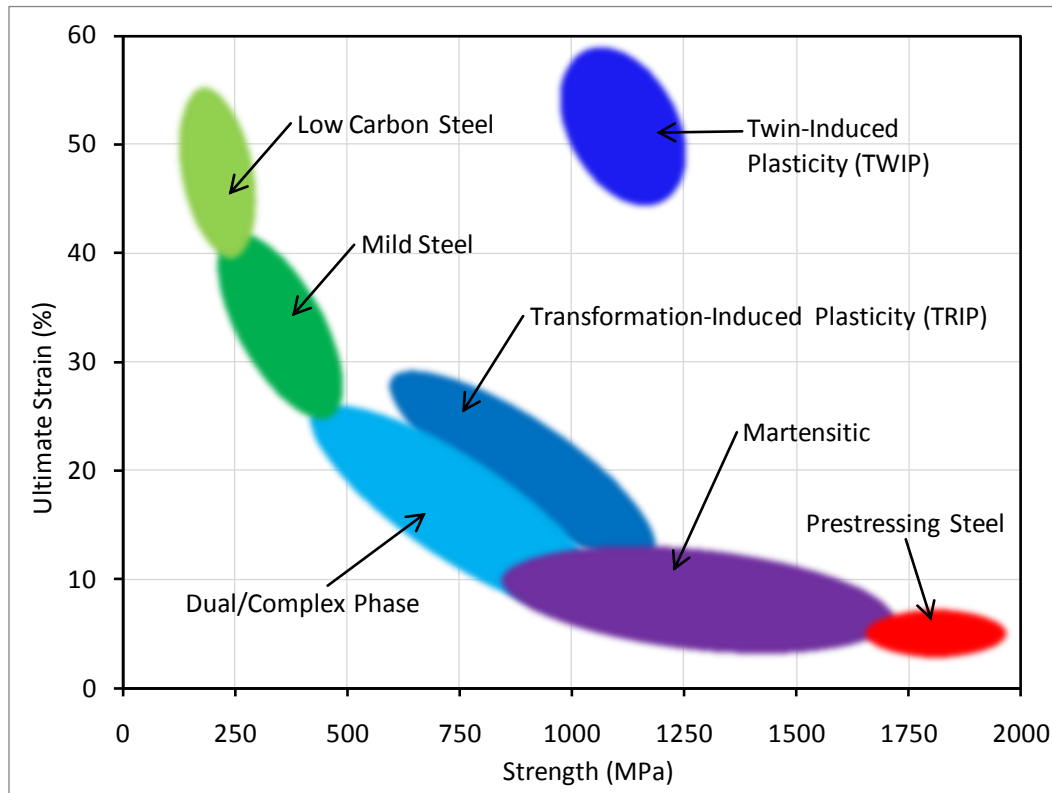


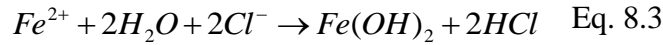
Figure 8-2: Strength vs. ultimate strain formability chart for a variety of engineering steels

8.2.1. Mechanisms of Prestressing Steel Degradation

Similar to the behavior of mild steel reinforcement, prestressing steels are typically highly resistant to corrosion when embedded in concrete. The alkaline solution with pH 12.5 to 13.5 (Mehta, et al., 2006) present in the capillary pore space of the hydrated cement paste infers exceptional corrosion resistance by the formation of a stable passive film on the surface of the steel (Poursaee, et al., 2007). This film, consisting primarily of Fe oxides and oxy-hydroxides (Addari, et al., 2008, Rossi, et al., 2001), has been shown to decrease anodic dissolution rates by multiple orders of magnitude by limiting corrosion reactions on the metal surface (Schmuki, 2002). It is only when this film is degraded by the ingress of aggressive agents from the environment or when conditions for EAC are present that damage can occur.

8.2.1.1. Corrosion Initiation by Chloride Ingress

In modern PSC structures, the ingress of Cl^- from the external environment by marine and/or deicing chemical exposure is the predominant mechanism that can initiate corrosion of prestressing steels (Andrade, et al., 2001, Hansson, et al., 2006). Cl^- will ingress into concrete, generally according to non-steady state Fickian diffusion, eventually building up to a sufficient concentration at the depth of the reinforcing steel that results in the initiation of corrosion (i.e., at the CTL) (Nilsson, 2009). Cl^- at the passive film – electrolyte interface will preferentially attack defect sites in the film such as inclusions or film grain boundaries (A. Rossi, 2001, Schmuki, 2002), resulting in anodic dissolution of Fe and the formation of corrosion products according to equations 8.1 to 8.3 (Kurtis, et al., 1997).



It should be noted that the reaction shown in Eq. 8.3 involves the formation of $\text{Fe}(\text{OH})_2$ corrosion product and, most importantly, the release of the HCl. Thus, the breakdown of the passive film is an autocatalytic reaction, with the Cl^- reactant not being bound into the corrosion products and acidification of the local environment near the initiation site (Jones, 1996). Once pits become numerous, they eventually coalesce and lead to cracking, spalling, and strength and stiffness degradation of the concrete structure.

8.2.1.2. Environmentally Assisted Cracking

In prestressing steels, EAC typically falls into three categories: SCC, HE, and a combination of SCC and HE, hydrogen-induced stress corrosion cracking (H-SCC) (Hope, et al., 2001, Mietz, 2000, Nürnberger, 2002). In most cases, a specific environment in conjunction with a susceptible alloy and tensile stress may result in EAC and a loss in strength and ductility. SCC is typically caused by localized electrochemical dissolution (e.g., pitting corrosion caused by Cl^-) which follows the path of galvanic microcells present in the steels microstructure, such as grain boundaries (Hope, et al., 2001, Mietz, et al., 2002). These deep, localized attacks when combined with external tensile stress can result in stress concentrations, leading to mechanical fracture by SCC.

In the case of HE and H-SCC, the absorption of atomic hydrogen (H_{ab}) into the metal lattice initiates damage. Atomic hydrogen is typically present in corrosion pits acidified by hydrolysis of Fe^{2+} or in cathodic reaction regions (Nürnberger, 2002, Nürnberger, 2009). In most cases, H^+ produced by cathodic reactions will combine with electrons at the cathodic site to form H , followed by the reaction $2\text{H} \rightarrow \text{H}_2$ to form molecular hydrogen (Mietz, 2000). However, in many cases such reactions may be slowed by the presence of compounds (such as As, S, and thiocyanates) which may poison the formation of H_2 and promote the absorption of H_{ab} (Mietz, et al., 2002). Once absorbed, H_{ab} will reside in microvoids, dislocation sites, and interstices present in the lattice structure, leading to HE by limiting ductile slip mechanisms (Hope, et al., 2001). When combined with tensile stress, HE can result in the initiation and propagation of cracks as

H-SCC (Hope, et al., 2001, Nürnberger, 2002). The author notes that many other theories have been developed to explain the mechanisms driving damage by EAC. The reader is referred to the following seminal texts and papers for further information (Jones, 1996, Landolt, 2007, Mietz, et al., 2002, Nürnberger, 2002, Nürnberger, 2009, Schroeder, et al., 2003, Skorchelletti, 1976).

8.2.2. Historical Corrosion Damage of Prestressed Concrete Structures

Corrosion-induced structural failures of PSC structures are rare; in fact, most would agree that PSC provides much higher durability than normal reinforced concrete. This is, in part, due to the relatively young age of PSC infrastructure when compared to normal reinforced concrete structures along with the generally higher quality of construction present in PSC structures. In general, corrosion initiation is likely caused by poor construction practices, insufficient design details, improper materials (e.g., concrete of poor quality and susceptible prestressing steels), and excessively severe environmental exposures (Hope, et al., 2001, Nürnberger, 2002). Yet corrosion of PSC has caused many structural elements to be repaired or replaced with resulting significant economic impact (Griggs, 1987, Hamilton III, 2007, Thaessler, et al., 2005).

The occurrence of brittle failures initiated by environmentally assisted cracking (EAC) (i.e., anodic stress corrosion cracking (SCC) and hydrogen embrittlement (HE)) is rare as currently used cold drawn and stabilized eutectoid prestressing steels have shown exceptional resistance to EAC (Lewis, 1969, Mietz, 2000). In a study performed by Schupack and Suarez in 1982, 10 of the 50 structures investigated exhibited damage likely caused by EAC (Schupack, et al., 1982). A majority of these failures were caused by improper construction and exposure to extremely severe environments (e.g., sewage digesters).

8.2.3. Corrosion Mitigation Methods in Prestressed Concrete

Many technologies have been investigated to mitigate corrosion in reinforced concrete. Of those, high performance concretes and large cover thicknesses along with proper design (i.e., limiting cracking) have found the greatest use in PSC structures exposed to corrosive environments. Galvanized coatings and cathodic protection methods have fallen out of favor (and in fact are not allowed in many localities) due to concerns of HE and H-SCC resulting from the excessive generation of hydrogen by unintentional “overprotection” of the steel substrate (Hartt, et al., 1993, Raharinaivo, 2005, Virmani, et al., 1998). Epoxy coated strands have been used but suffer the same concerns as epoxy coated rebar: reduced bond, potential breakdown of bond, and coating defects caused by handling and construction (Salas, et al., 2008). Fiber reinforced polymers have been investigated for use in prestressing systems, but the high cost of manufacturing, limited applied research, shear lag deficiencies, lack of ductility, creep and stress relaxation, and concerns related to high temperature and high strain rate behavior have limited their employment in prestressed concrete structures (Salas, et al., 2004).

8.3. Applications of Stainless Steel Reinforcement in Concrete

The use of stainless steels as concrete reinforcement can greatly extend the usable service lives of reinforced concrete structures exposed to even the most severe of environments (Hartt, et

al., 2004). Such alloys provide exceptional corrosion resistance by the formation of a highly stable passive film which maintains its integrity over a much wider range of pH and Cl^- concentration and which is mainly composed of Cr oxides and oxy-hydroxides (with contributions by Ni and Mo if present) (A. Rossi, 2001, Addari, et al., 2008, Schmuki, 2002). As shown in the Schaeffler constitution diagram in Figure 8-3, stainless steels can be divided into four different families: austenitic, ferritic, martensitic, and duplex (a mixture of γ -austenite and δ -ferrite). In Figure 8-3, the Ni equivalent has been shown including the DeLong correction to account for the effect of N on austenite stability (DeLong, et al., 1956). The stable phase depends primarily on composition, with Ni, C, Mn, and N acting as austenite stabilizers and Cr, Mo, and Si acting as ferrite stabilizers.

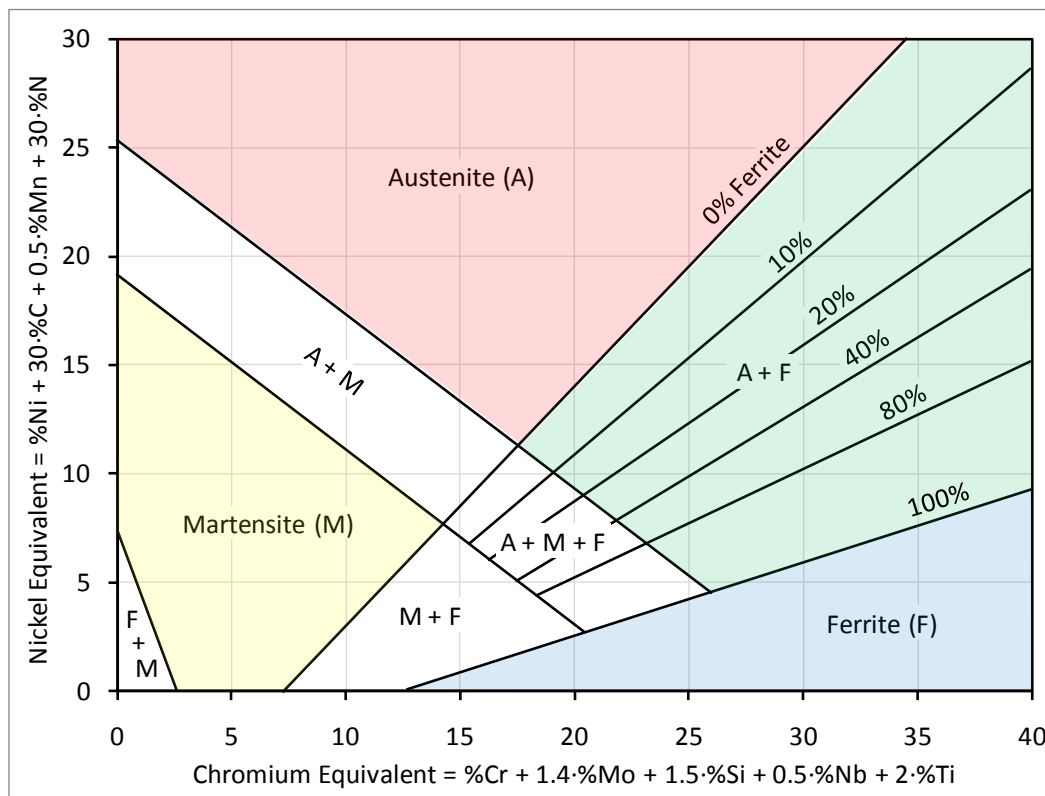


Figure 8-3: Schaeffler – DeLong constitution diagram for stainless steels (adapted from (DeLong, et al., 1956, Schaeffler, 1949))

In the U.S., Canada, and Europe, stainless steels have been increasingly used in bridge decks and coastal bridge substructures to mitigate corrosion. Austenitic grades SAE 304 and 316 and duplex Type 2205 have seen the largest use as reinforcement in concrete, primarily owed to their high availability and the extensive amount of research conducted on their corrosion resistance in concrete (Hart, 2005). Ferritic grades such as SAE 430 have also been investigated for use as reinforcement in concrete but have seen limited application due to the superior corrosion resistance of readily available austenitic grades (Hart, et al., 2004). Lower cost lean duplex alloys such as 2101 and 2304 have also been investigated for used as reinforcement in

concrete and generally exhibit exceptional mechanical properties and corrosion resistance comparable with SAE 304 and 316 (Clemen, 2003, Dupoiron, et al., 1996, Hartt, 2005, Hurley, 2006). Specialty alloys such as low-Ni, N-charged or Mn rich stainless steels (e.g., ASTM XM-29 / Nitronic® 33) and lean Cr microcomposite steels (e.g., MMFX-IITM) have seen increasing interest recently due to their lower cost (decreased Ni and Mo content) when compared with traditional austenitic grades such as SAE 316 (García-Alonso, et al., 2007, Presuel-Moreno, et al., 2010). Typical elemental compositions for these alloys are shown in Table 8-1. The relative resistance of these stainless steels to chloride-induced pitting corrosion has also been recorded in Table 8-1 as the pitting resistance equivalency number (PREN) calculated according to Eq. 8-4 (Markeset, et al., 2006).

$$PREN = \%Cr + 3.3 \times \%Mo + \beta \times N \quad \text{Eq. 8-4}$$

Where: $\beta = 30$ for duplex grades
 $\beta = 16$ for other grades

Table 8-1: Elemental composition and PREN for common stainless steel grades investigated for use as reinforcing steel in concrete

Grade	Type	Composition (wt.%) – Fe Balance						PREN
		C	N	Cr	Ni	Mo	Other	
304	Austenitic	0.04	0.06	18.2	8.1	-	-	19.2
316	Austenitic	0.04	0.06	17	11	2.8	-	27.2
XM-29	Austenitic	0.08	0.30	18	3	-	13Mn	22.8
430	Ferritic	0.04	-	16.5	-	-	-	16.5
MMFX-II	Microcomposite	0.15	0.05	9	-	-	1.5Mn, 0.5Si	9.8
2101	Duplex	0.03	0.22	21.5	1.5	0.3	5Mn	29.1
2205	Duplex	0.02	0.17	22	5.5	3	-	37.0
2304	Duplex	0.02	0.10	23	4.8	0.3	-	27.0

The use of stainless steels to replace normal mild steel reinforcement has been shown to provide decreases in maintenance costs of greater than 50% while extending the structure's service life to far greater than 100 years in most applications with only modest increases in initial expenditures (Cramer, et al., 2002). One of the best examples of the performance of stainless steel reinforcement is the Progreso Pier located on Mexico's Yucatan Peninsula, constructed using SAE 304 reinforcing in an extremely corrosive environment. The pier, built in 1939 with poor quality concrete and a cover thickness of 25 mm, is now over 70 years old and shows no signs of corrosion, while a companion pier built in 1979 with normal ferritic mild steel reinforcement has had to be demolished due to corrosion damage after two decades of service (Knudson, et al., 1999).

With the success of stainless steels when utilized in reinforced concrete structures, their use in PSC structures may provide a means to corrosion mitigation which warrants further

investigation. As presented by Schupack (Schupack, 2001) and as discussed below, limited research (particularly applied research) has been conducted on the use of stainless steels as prestressing reinforcement for concrete structures. The challenges associated with optimizing mechanical properties, materials production and processing techniques, resistance to corrosion and EAC, and economic considerations have made research on HSSs for PSC a difficult task which few have pursued.

8.4. High-Strength Stainless Steels

8.4.1. Austenitic Stainless Steel Grades SAE 304 and 316 for PSC

The most significant investigations of austenitic HSSs for PSC applications stem from research conducted as a part of COST Action 534 – New Materials and Systems in PSC Structures, an effort supported by the European Union (Alonso, 2007, Alonso, et al., 2007, Alonso, et al., 2008, Nürnberger, 2003, Nürnberger, et al., 2005, Nürnberger, et al., 2008, Wu, et al., 2009). HSSs of grades SAE 304, 316, and 316LN (a low C, N-charged grade) were cold drawn until achieving ultimate strengths in the range of 1400 to 1850 MPa. Stress relaxation of these HSSs was found to be approximately 7 % (much higher than the 2-3 % typical for prestressing steels). Higher strengths were achieved with SAE 304 when compared with SAE 316. This result is expected given the low stacking fault energy (SFE) of meta-stable austenitic SAE 304 which will readily undergo transformation-induced plasticity (TRIP) during cold drawing – transforming from face centered cubic (FCC) γ -austenite to body centered cubic (BCC) α' -martensite (Dash, et al., 1963). Given the large cold reductions used to achieve these high strengths, α' -martensite volume contents exceeding 50 % can be expected in SAE 304 (Milad, et al., 2008). The presence of α' -martensite was confirmed in SAE 304 through metallographic observations along with magnetic permeability measurements. Magnetic permeabilities of 17.7, 1.2, and 1.0 were measured for SAE 304, 316, and 316LN, respectively. In the case of SAE 316 and 316LN, the increasing Ni content (and N addition in 316LN) increases austenite stability, resulting in strengthening primarily through dislocation pinning and Hall-Petch effects with little contribution by TRIP mechanisms present in SAE 304.

Corrosion susceptibility of these alloys was evaluated using potentiodynamic polarization techniques on samples exposed to simulated concrete pore solutions with Cl^- added up to 2.5 M concentration (Alonso, 2007) or embedded into alkaline or carbonated mortar cylinders with 5 wt.% Cl^- by weight of cement. Using this technique, corrosion susceptibility is clearly indicated by the formation of a breakdown potential prior to entering the O_2 evolution region (Hurley, 2006) indicating that the threshold resistance for chloride-induced corrosion has been exceeded. The results of these studies suggest that SAE 304, 316, and 316LN are resistant to corrosion initiation up to Cl^- concentrations of 1.5 M, above which SAE 304 becomes susceptible while 316 and 316LN remain resistant. It should be noted that even though SAE 304 was found to be susceptible to corrosion initiation above Cl^- concentrations of 1.5 M, the typical Cl^- concentration of seawater does not exceed 0.5 M. Therefore, as long as alkalinity of the pore solution is preserved, corrosion initiation will likely not occur even for SAE 304.

Similar performance of SAE 304 was also observed in tests conducted in Cl^- -containing mortars (Wu, et al., 2009). Figure 8-4 summarizes the results of testing conducted in alkaline and

carbonated mortars for samples with and without cold drawing. The researchers state that the poor performance of SAE 304 was most likely due to the presence of α' -martensite which initiated pitting by galvanic microcells occurring between martensite inclusions (which function as anodic sites) and the surrounding austenite phases. In the carbonated mortars, pitting potentials with and without cold drawing decreased approximately 200 mV universally. In all cases, SAE 316LN provided the highest resistance to pitting corrosion, with little to no degradation even in the case of a carbonated Cl^- containing mortar embedments. Thus, the researchers concluded that SAE 316 grades tested should provide acceptable corrosion resistance, while corrosion of SAE 304 may be a concern.

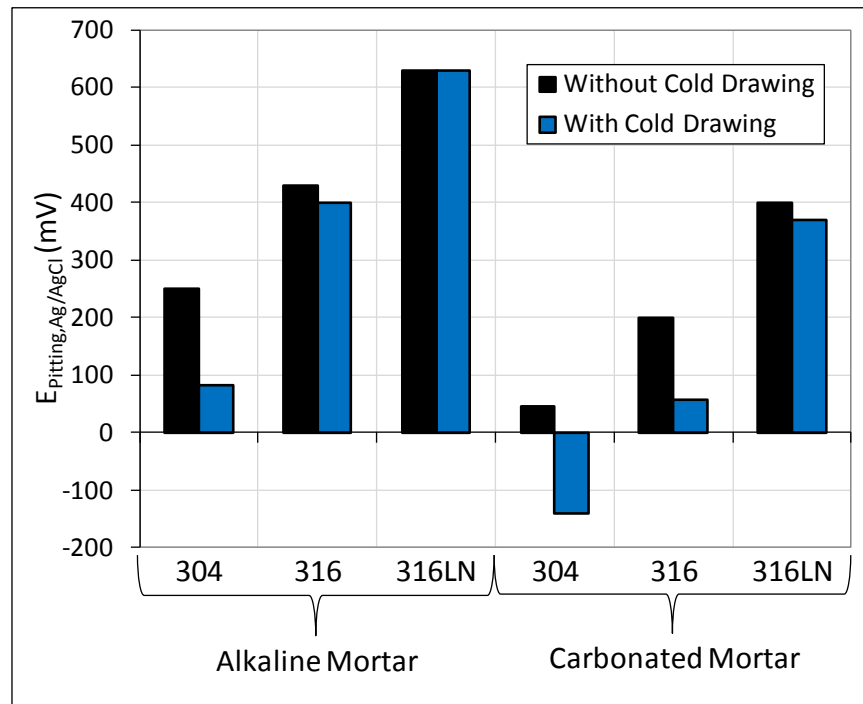


Figure 8-4: Pitting potential of HSSS embedded in alkaline and carbonated Cl^- -containing mortars (adapted from (Wu, et al., 2009))

Chloride-assisted SCC was evaluated using U-bend specimens placed in Cl^- -containing solutions with pH of 4.5 (such as in an ungrouted post-tensioning duct), 8.5 (typical of carbonated concrete), and 12.1 (alkaline concrete) at temperature between 30 and 80 °C. It was accepted by the researchers that a HSSS is sufficiently resistant against Cl^- -assisted SCC in the respective medium if it does not fracture up to a threshold temperature of 40 °C after 20,000 hours of exposure. Only SAE 304 was found to be susceptible to SCC in pH 4.5 and 8.5 environments and thus may not be acceptable for use if such exposure is anticipated. The researchers again attributed the reduced stress corrosion performance of SAE 304 to inclusions of α' -martensite. SAE 316 maintained resistance to Cl^- -induced SCC in all ranges of pH.

Additional testing for H-SCC susceptibility was performed using the standard International Federation of Prestressed Concrete (FIP) time-to-failure method. The FIP test utilizes an ammonium thiocyanate solution exposure maintained at 50 °C which promotes the uptake of H_{ab} while recording the time-to-failure of a wire stressed to 80 % σ_{ult} . It is generally considered that times-to-failure greater than 5 hours indicate acceptable resistance to H-SCC. Times-to-failure of 131, 2820, and 5000+ (no fracture) were recorded for SAE 304, 316, and 316LN, respectively, indicating that these alloys are highly resistant to H-SCC when compared with typical prestressing steels.

8.4.2. Nitronic® 33 Nitrogen-Strengthened Austenitic Stainless Steel for PSC

One of the first studies investigating the use of HSSS for PSC applications was lead by the Naval Facilities Engineering Command (Jenkins, 1987). The primary goal of this study was to develop a high-strength non-magnetic prestressing steel for use in concrete piling to be placed in a military deperming facility where ships and submarines are serviced to reduce their magnetic signature to camouflage them from magnetic detection techniques. Consequently, an austenitic stainless steel with high resistance to the formation of ferromagnetic α' -martensite was desired in order to preserve paramagnetic properties even under excessive cold drawing. A nitrogen-strengthened high Mn proprietary alloy known as Nitronic® 33 (ASTM XM-29) was cold drawn and produced as 7-wire prestressing strand. The resulting strand exhibited σ_y of 800MPa, σ_{ult} of 938MPa, and ϵ_{ult} of 33.3%. No stress relaxation values were reported. These mechanical properties are far below those required for most prestressing systems, although strengths as high as 1650 MPa have been achieved using the same alloy in more recent unpublished studies (Insteel Industries, 2002).

Durability testing of the Nitronic® 33 HSSS focused on chloride-induced corrosion, with no investigation of SCC and H-SCC. Preliminary testing conducted in mortar extracts with the addition of Cl^- at pH values between 10.0 and 12.1 found that normal carbon prestressing steel suffered significant corrosion at a pH of 11.6 with a small addition of 200ppm Cl^- , while Nitronic 33 suffered no damage even at a pH of 10.0 and 6000ppm Cl^- . Further testing performed in cracked concrete specimens exposed to seawater solutions showed that corrosion initiated on carbon prestressing steels, while Nitronic 33 remained passive in all cases. Full-scale PSC piles constructed using Nitronic 33 prestressing strands were also included in the study. Nondestructive potential measurements indicated that corrosion may have initiated on the Nitronic 33 HSSS. Upon forensic autopsy of the piles, corrosion was only found to be occurring on carbon steel wire ties used to secure the Nitronic 33 HSSS prestressing strands with no damage found on the strands themselves. Subsequent investigation of piles using Nitronic 33 HSSS placed in the Port of Tacoma Washington has indicated no signs of corrosion initiation (Jenkins, 1987).

8.4.3. Duplex Stainless Steel Type 2205 for PSC

The only documented research which has examined a duplex grade HSSS for PSC was performed by the Shinko Wire Company in collaboration with Kyoto University (Shirahama, et al., 1999). The duplex HSSS investigated was similar in composition to Type 2205 with σ_{ult} of 1636 MPa and ϵ_{ult} of 4.0 % following cold drawing and stranding. Stress relaxation of 0.5 % for

the duplex HSSS was also similar to normal prestressing steel when tested by an accelerated 10 hour method. These results indicate that the mechanical behavior of 2205 duplex HSSS may be far superior to the austenitic HSSSs discussed in Section 8.4.1.

In addition to mechanical testing, durability tests examined the susceptibility to damage by chloride-induced corrosion, exposure nitrate containing solutions, and H-SCC. Pitting corrosion time-to-failure tests were performed on duplex HSSS stressed to 80 % σ_{ult} while immersed in a 3 % NaCl solution maintained at 90 °C. The tests were stopped after 350 hours when failure had not occurred. A similar test was used to test for damage caused by nitrates, a problem encountered in industrial and agricultural environments. Strands were stressed to 70 % σ_{ult} while immersed in ammonium nitrate (NH_4NO_3) solutions maintained at 100 °C. Once again, the tests were stopped after 350 hours when failure had not occurred. For comparison, normal eutectoid prestressing steel which also was included in the study failed these tests after 100 hours of exposure. H-SCC resistance was evaluated using the FIP test method presented in Section 8.4.1. The developed duplex HSSS did not fracture even after 350 hours of exposure, while the eutectoid prestressing steel failed after 8 hours. No testing to evaluate resistance to Cl^- induced SCC was performed. These results, when combined with mechanical behavior, indicate that the developed duplex HSSS with composition similar to Type 2205 provides the better balance between mechanical performance and corrosion resistance, particularly when compared to austenitic HSSSs.

8.4.4. Developments in Other Industries

While the aforementioned studies have provided many useful insights into the use of HSSSs for corrosion mitigation in PSC systems, developments from other industries also warrant investigation. A majority of research on HSSSs has been conducted in the aerospace and spring wire industries. In the case of spring wire, it is not high tensile strength which is desired, but rather a high range of elasticity. HSSS research in these industries has mainly focused on techniques to strengthen readily available grades such as SAE 304 and 316. The replacement of C with N, or the addition of N along with C has been shown to be an extremely effective means of strengthening austenitic grades in conjunction with cold drawing (Shanina, et al., 2002). N has been shown to be an effective solid-solution strengthener, has a much higher solubility than C (0.4 wt.% and up to 1 wt.% if high pressure melting techniques are employed), and N also acts as an austenite stabilizer (i.e., prevents the formation of α' -martensite) (Simmons, 1996). N addition along with cold drawing has been successfully used to increase the strength of austenitic stainless steels to levels similar to those used in prestressing applications (i.e., 1500 to 1900 MPa) (Stein, et al., 1990).

Precipitation hardenable (PH) stainless steels such as 15-5, 17-4, and 17-7 have long been used in the aerospace industry for their moderate corrosion resistance and high tensile strengths (approximately 1000 MPa in the annealed condition) which can be increased through cold drawing. PH stainless steels have received little attention as reinforcement in concrete as even their annealed strengths far exceed the typically required tensile strengths of reinforcing steels of approximately 500 MPa. However, given the high desired tensile strengths of prestressing reinforcement, PH stainless steels may make an ideal candidate. Semiaustenitic PH grade 17-7 is one of the most used HSSS in the spring wire industry as it readily work hardens by a

transformation from an austenitic to fully martensitic microstructure, resulting in strengths of up to 1800 MPa in the range of wire diameters typically used in prestressing strands (Izumida, et al., 2005). The composition of PH grade 17-7 and its PREN value is recorded in Table 8-2.

Table 8-2: Elemental composition and PREN of 17-7PH stainless steel

Grade	Type	Composition (wt.%) – Fe Balance						PREN
		C	N	Cr	Ni	Mo	Other	
17-7	Semiaustenitic PH	0.09	-	17	7.1	-	1Mn, 1Si, 1Al	16

As discussed in Section 8.3, duplex stainless steels exhibit exceptional mechanical properties and corrosion resistance along with economically “leaner” compositions. More recent work in the spring wire industry has resulted in the development of high- and super-high-strength duplex stainless steels with tensile strengths exceeding 2000 MPa (Chai, et al., 2007). While limited research has been conducted on the corrosion resistance of these newly developed duplex HSSs, based on the results presented in Section 8.4.3, further investigation of common duplex grades such as 2205 as well as new lean grades such as 2003, 2101, and 2304 for PSC applications is certainly warranted.

8.5 Conclusion Regarding Stainless Steel Reinforcement

Service life limiting deterioration resulting from corrosion of reinforced and PSC structures is a problem of critical concern which, even with extensive research, continues to plague civil infrastructure. Recent efforts to increase the durability and sustainability of civil infrastructure have provided a new impetus for the development of novel and innovative corrosion mitigation technologies. Research and field studies on stainless steels used in reinforced concrete applications have shown the potential for significant increases in service lives with decreased maintenance costs. The use of HSSs as prestressing reinforcement to mitigate corrosion has the potential to play an integral role in the construction of durable and sustainable PSC structures in the future.

The research contributions reviewed in Section 8.4 have provided many useful insights into the behavior of HSSs for use in prestressing systems and in other applications. However, the limitations associated with optimizing mechanical performance in conjunction with corrosion resistance are vast. Furthermore, prior research has been limited to a select few alloys, namely austenitic SAE 304 and 316, and duplex Type 2205. Future studies will be required to investigate other alloys (e.g., Types 2003, 2101, and 2304 duplex, PH, and low-Ni grades) and new proprietary microcomposite alloys (e.g., MMFX-IITM) which may provide many of the same benefits at a lower cost. Significant basic and applied research on these alloys will be required to develop a catalog of data as robust as that available for currently used eutectoid prestressing steels. Future studies should also focus on critical mechanical parameters (e.g., fatigue resistance and stress relaxation) and production considerations which have received limited attention compared to corrosion resistance in previous studies. HSS prestressing reinforcements developed under such guidelines will be more readily implementable in civil engineering practice.

8.6 References

ASTM A416 / A416M - 06 Standard Specification for Steel Strand, Uncoated Seven-Wire for Prestressed Concrete." American Society of Testing and Materials, West Conshohocken, PA.

A. Rossi, R. T. B. E. (2001). "Surface analytical and electrochemical study on the role of adsorbed chloride ions in corrosion of stainless steels." *Materials and Corrosion / Werkstoffe und Korrosion*, V. 52 (3), pp. 175-180.

Addari, D., Elsener, B., and Rossi, A. (2008). "Electrochemistry and surface chemistry of stainless steels in alkaline media simulating concrete pore solutions." *Electrochimica Acta*, V. 53 (27), pp. 8078-8086.

Ahern, M. E. (2005). "Design and Fabrication of a Compact Specimen for Evaluation of Corrosion Resistance of New Post-Tensioning Systems." MS, University of Texas at Austin, Austin, TX.

Alonso, M. C. "Corrosion Performance of High Strength Stainless Steel for Tendon Applications." *Proc., Final Conference of COST Action 534*.

Alonso, M. C., and Recio, F. J. "Aceros Inoxidables De Alta Resistencia Mecanica En Medios Alcalinos con Cloruros." *Proc., XXIV Encuentro del Grupo Nacional de Fractura*.

Alonso, M. C., Recio, F. J., and Sanchez, M. "High Strength Stainless Steels for Prestressed Concrete Structures in Marine Environment." *Proc., 1st International Conference. Construction Heritage in Coastal and Marine Environments. Damage, Diganosis, Maintenance and Rehabilitation*.

Andrade, C., Keddarn, M., Nóvoa, X. R., Pérez, M. C., Rangel, C. M., and Takenouti, H. (2001). "Electrochemical Behaviour of Steel Rebars in Concrete: Influence of Environmental Factors and Cement Chemistry." *Electrochimica Acta*, V. 46, pp. 3905-3912.

Atienza, J. M., and Elices, M. (2007). "Role of Residual Stresses in Stress Relaxation of Prestressed Concrete Wires." *Journal of Materials in Civil Engineering*, V. 19 (8), pp. 703-708.

Bautista, A., Blanco, G., and Velasco, F. (2006). "Corrosion Behaviour of Low-Nickel Austenitic Stainless Steel Reinforcements: A Comparative Study in Simulated Pore Solutions." *Cement & Concrete Research*, V. 36, pp. 1922-1930.

Bertolini, L., Bolzoni, F., Cigada, A., Pastore, T., and Pedferri, P. (1993). "Cathodic Protection of New and Old Reinforced Concrete Structures." *Corrosion Science*, V. 35 (5-8), pp. 1633-1639.

Brooks, M. A. (2003). "Influence of interstitial crevice corrosion in accelerated corrosion testing." BS, Penn State University, State College, PA.

Broomfield, J. P. (2007). *Corrosion of Steel in Concrete*, Taylor and Francis Group.

- Chai, G., Soderman, A., and Etheridge, P. (2007). "High and Super-High-Strength Duplex Stainless Steels for Wire Applications." Sandvick Materials Technology, Sweden.
- Clemena, G. G. (2003). "Investigation of the Resistance of Several New Metallic Reinforcing Bars to Chloride-Induced Corrosion in Concrete." Virginia Transportation Research Council.
- Cramer, S. D., Jr., B. S. C., Bullard, S. J., Holcomb, G. R., Russell, J. H., Nelson, F. J., Laylor, H. M., and Soltesz, S. M. (2002). "Corrosion Prevention and Remediation Strategies for Reinforced Concrete Coastal Bridges." *Cement & Concrete Composites*, V. 24, pp. 101-117.
- Darwin, D., Browning, J., Jr., C. E. L., and Nguyen, T. V. (2007). "Multiple Corrosion Protection Systems for Reinforced Concrete Bridge Components." University of Kansas, 95.
- Dash, J., and Otte, H. M. (1963). "Martensite Transformation in Stainless Steel." *Acta Metallurgica*, V. 11 (10), pp. 1169-&.
- DeLong, W. T., Ostrom, G. A., and Szumachowski, E. R. (1956). "Measurement and calculation of ferrite in stainless steel weld metal." *Journal of Welding*, V. 35 (11), pp. 521-528.
- Dupoiron, F., and Audouard, J. P. (1996). "Duplex stainless steels: a high mechanical properties stainless steel family." *Scandinavian Journal of Metallurgy*, V. (25), pp. 95-102.
- Garcia-Alonso, M. C., Escudero, M. L., Miranda, J. M., Vega, M. I., Capilla, F., Correia, M. J., Salta, M., Bennani, A., and Gonzalez, J. A. (2007). "Corrosion behaviour of new stainless steels reinforcing bars embedded in concrete." *Cement & Concrete Research*, V. 37 (10), pp. 1463-1471.
- Griggs, R. D. (1987). "Structural Concrete in the Georgia Coastal Environment." GDOT, Atlanta, GA.
- Hamilton III, H. R. (2007). "St. George Island Bridge Pile Testing." FDOT.
- Hansson, C. M. (2005). "Effects of High Performance Concrete on Corrosion of Reinforcement." P. C. Association, Skokie, IL.
- Hansson, C. M., Poursaee, A., and Laurent, A. (2006). "Macrocell and Microcell Corrosion of Steel in Ordinary Portland Cement and High Performance Concretes." *Cement & Concrete Research*, V. 36, pp. 2098-2102.
- Hartt, W. H. (2005). "Jobsite Evaluation of Corrosion Resistant Alloys for use as Reinforcement in Concrete." Florida Atlantic University, 82.
- Hartt, W. H., Kumria, C. C., and Kessler, R. J. (1993). "Influence of Potential, Chlorides, pH, and Precharging Time on Embrittlement of Cathodically Polarized Prestressing Steel." *CORROSION*, V. 49 (5), pp. 377-385.

- Hartt, W. H., Powers, R. G., Leroux, V., and Lysogorski, D. K. (2004). "Critical Literature Review of High-Performance Corrosion Reinforcements in Concrete Bridge Applications." Florida Atlantic University, 53.
- Hope, B. B., and Nmai, C. K. (2001). "Corrosion of Prestressing Steels." American Concrete Institute Committee 222, 43.
- Hope, B. B., and Nmai, C. K. (2001). "Protection of Metals in Concrete Against Corrosion." American Concrete Institute Committee 222, 41.
- Hurley, M. F. (2006). "Threshold Chloride Concentrations of Selected Corrosion-Resistant Rebar Materials Compared to Carbon Steel." *CORROSION*, V. 62 (10), pp. 892-904.
- Insteel Industries, I. (2002). "1/2" 240K Stainless Steel Strand." Sanderson, FL.
- Izumida, H., Kawabe, N., Takamura, S., Morita, H., and Murai, T. (2005). "Development of High-tensile-strength Stainless Steel Wire." *Sumitomo (SEI) Steel Wire Corp. Technical Review*, V. 60.
- Jenkins, J. F. (1987). "Validation of Nitronic 33 in Reinforced and Prestressed Concrete." Naval Facilities Engineering Command.
- Jones, D. A. (1996). *Principles and Prevention of Corrosion*, Prentice Hall.
- Knudson, A., and Skovsgaard, T. (1999). "The Optimal Use of Stainless Steel Reinforcement in Concrete Structures." Ramboll Arminox, 8.
- Koch, G. H., Brongers, M. P. H., Thompson, N. G., Virmani, Y. P., and Payer, J. H. (2008). "Corrosion Costs and Preventive Strategies in the United States." NACE, Houston, TX, 12.
- Kurtis, K. E., and Mehta, K. "A Critical Review of Deterioration of Concrete Due to Corrosion of Reinforcing Steel." *Proc., Durability of Concrete*, ACI, 535-554.
- Landolt, D. (2007). *Corrosion and Surface Chemistry of Metals*, EPFL Press, Lausanne, Switzerland.
- Lewis, A. F. G. (1969). *Steel for Prestressing*, Lowe & Brydone Limited, London, UK.
- Markeset, G., Rostam, S., and Klinghoffer, O. (2006). "Guide for the use of stainless steel reinforcement in concrete structures." Norwegian Building Research Institute.
- Mehta, P. K., and Monteiro, P. J. M. (2006). *Concrete: Microstructure, Properties, and Materials*, McGraw-Hill Companies Ltd.
- Mietz, J. (2000). "Investigations on Hydrogen-Induced Embrittlement of Quench and Tempered Prestressing Steels." *Materials and Corrosion*, V. 51, pp. 80-90.
- Mietz, J., and Isecke, B. (2002). "Assessment of test methods for evaluation stress corrosion cracking susceptibility of prestressing steels." *Materials and Corrosion*, V. 53 (6), pp. 373-384.

- Milad, M., Zreiba, V., Elhalouani, F., and Baradai, C. (2008). "The effect of cold work on structure and properties of AISI 304 stainless steel." *Journal of Materials Processing Technology*, V. 203 (1-3), pp. 80-85.
- Moser, R. D., Singh, P. M., Kahn, L. F., and Kurtis, K. E. (2010). "Chloride-Induced Corrosion of Prestressing Steels Considering Crevice Effects and Surface Imperfections." *CORROSION*, In Review.
- NACE (2008). "How Much Can a Bridge Take?", National Association of Corrosion Engineers.
- Nawy, E. G. (2000). *Prestressed Concrete - A Fundamental Approach*, Prentice Hall, Upper Saddle River, NJ.
- Nilsson, L.-O. (2009). "Models for chloride ingress into concrete - from Collepardi to today." *International Journal of Modeling, Identification, and Control*, V. 7 (2), pp. 129-134.
- Nürnberg, U. (2002). "Corrosion induced failure mechanisms of prestressing steel." *Materials and Corrosion*, V. 53 (8), pp. 591-601.
- Nürnberg, U. (2003). "High Strength Stainless Steel - Alternative Materials for Tension Members in Civil Engineering." *Otto-Graf-Journal*, V. 14, pp. 45-66.
- Nürnberg, U. "Hydrogen Induced Cracking of Prestressing Steel in Concrete Constructions." *Proc., EUROCORR*.
- Nürnberg, U., and Wu, Y. "High-Strength Stainless Steel in Prestressed Concrete." *Proc., Workshop of COST on NTD Assessment and New Systems in Prestressed Concrete Structures*, Institute for Terotechnology, 33-38.
- Nürnberg, U., and Wu, Y. (2008). "Stainless steel in concrete structures and in the fastening technique." *Materials and Corrosion*, V. 59 (2), pp. 144-158.
- Poursaei, A., and Hansson, C. M. (2007). "Reinforcing steel passivation in mortar and pore solution." *Cement & Concrete Research*, V. 37 (7), pp. 1127-1133.
- Presuel-Moreno, F., Scully, J. R., and Sharp, S. R. (2010). "Literature Review of Commercially Available Alloys That Have Potential as Low-Cost Corrosion-Resistant Concrete Reinforcement." *CORROSION*, V. 68 (8), pp. 1-13.
- Proverbio, E., and Bonaccorsi, L. M. (2002). "Failure of Prestressing Steel Induced By Crevice Corrosion in Prestressed Concrete Structures." *9th International Conference on Durability of Materials and Components* Brisbane, Australia.
- Raharinaivo, A. "Galvanised Carbon Steel Tendons." *Proc., Workshop of COST on NTD Assessment and New Systems in Prestressed Concrete Structures*, Institute for Terotechnology, 41-48.

Rossi, A., Tulifero, R., and Elsener, B. (2001). "Surface analytical and electrochemical study on the role of adsorbed chloride ions in corrosion of stainless steels." *Materials and Corrosion*, V. 52 (3), pp. 175-180.

Sagüés, A. A., Lee, J. B., Chang, X., Pickering, H., Nystrom, E., Carpenter, W., Kranc, S. C., Simmons, T., Boucher, B., and Hierholzer, S. (1994). "Corrosion of Epoxy Coated Rebar in Florida Bridges." University of South Florida, 135.

Salas, R. M., Schokker, A. J., West, J. S., Breen, J. E., and Kreger, M. E. (2004). "Conclusions, Recommendations and Design Guidelines for Corrosion Protection of Post-Tensioned Bridges ", Center for Transportation Research Austin, TX, 85.

Salas, R. M., Schokker, A. J., West, J. S., Breen, J. E., and Kreger, M. E. (2008). "Corrosion risk of bonded, post-tensioned concrete." *PCI Journal*, V. 53 (1), pp. 89-107.

Schaeffler, A. L. (1949). "Constitution diagram for stainless steel weld metal." *Metals Progress*, V. 56 (11), pp. 680.

Schmuki, P. (2002). "From Bacon to barriers: a review on the passivity of metals and alloys." *Journal of Solid State Electrochemistry*, V. 6 (3), pp. 145-164.

Schroeder, R. M., and Müller, I. L. (2003). "Stress Corrosion Cracking and Hydrogen Embrittlement Susceptibility of an Eutectoid Steel Employed in Prestressed Concrete." *Corrosion Science*, V. 45, pp. 1969-1983.

Schupack, M. (2001). "Prestressing Reinforcement in the New Millennium." *Concrete International*, V. 23 (12), pp. 38-45.

Schupack, M., and Suarez, M. G. (1982). "Some Recent Corrosion Embrittlement Failures of Prestressing Systems in the United States." *PCI Journal*, V. March-April, pp. 38-55.

Shanina, B. D., Gavriljuk, V. G., Berns, H., and Schmalt, F. (2002). "Concept of a new high-strength austenitic stainless steel." *Steel Research International*, V. 73 (3), pp. 105-113.

Sharp, S. R., and Virmani, Y. P. (2006). "Factors That Influence the Efficiency of Electrochemical Chloride Extraction During Corrosion Mitigation in Reinforced Concrete Structures." Virginia Transportation Research Council, 30.

Shirahama, S., Fang, S., Kobayashi, T., and Miyagawa, T. (1999). "Basic Properties of Duplex Stainless Prestressing Steel and Flexural Behaviors of Prestressed Concrete Beams Using the Tendon." *Journal of the Society of Materials Science of Japan*, V. 48 (10), pp. 1199-1206.

Simmons, J. W. (1996). "Overview: High-nitrogen alloying of stainless steels." *Mater. Sci. Eng. A-Struct. Mater. Prop. Microstruct. Process.*, V. 207 (2), pp. 159-169.

Skorchelletti, V. V. (1976). *Theory of Metal Corrosion*, Israel Program for Scientific Translations, Jerusalem, Israel.

Stein, G., and Witulski, H. (1990). *High Nitrogen Steels*, Verlag Stahleisen GmbH, Aachen, Germany.

Thaesler, P., Kahn, L., Oberle, R., and Demers, C. E. (2005). "Durable Repairs on Marine Bridge Piles." *Journal of Performance of Constructed Facilities*, V. 19 (1), pp. 88-92.

Virmani, Y. P., and Clemena, G. G. (1998). "Corrosion Protection: Concrete Bridges." Turner-Fairbank Highway Research Center.

Wu, Y., and Nürnberger, U. (2009). "Corrosion-technical properties of high-strength stainless steels for the application in prestressed concrete structures." *Materials and Corrosion*, V. 60 (10), pp. 771-780.

Zemajtis, J., Weyers, R. E., and Sprinkel, M. M. (1999). "Performance Evaluation of Corrosion Inhibitors and Galvanized Steel in Concrete Exposure Specimens." Virginia Transportation Research Council, 74.

9. Future Studies Planned for Part 2

Part 2 of the project will continue to address the durability concerns for prestressed concrete piles exposed to marine environments. A series of experiments will be performed to evaluate the durability characteristics of concrete mix designs exposed to this environment. Corrosion studies of stainless steel prestressed and nonprestressed reinforcement will continue as discussed in Section 9.2.

9.1 Concrete Studies

9.1.1 Concrete Mix Design

The mix designs to be characterized are chosen to represent the current high performance concretes being used and modifications of those to improve durability requirements. Using ACI 211.4R-08 (2008), a base mix design (T2) can be determined for the given chloride exposure and sulfate exposure found in coastal Georgia, which is given in Table 9-1. Table 9-2 gives the mix design (SCP-HP) currently being used for piles in the state of Georgia. SCP-HP contains both an air entraining admixture and a super plasticizer.

Table 9-1: ACI durability criterion mix design (T2)

Material	Weight (lb/yd ³)
Water	305
Type I/II cement	763
Natural Sand	1096
#67 Stone	1905
w/cm	0.4

Table 9-2: Current HPC mix design (SCP-HP)

Material	Weight (lb/yd ³)
Water	307
Type I/II cement	789
Type F Fly Ash	140
Natural Sand	1003
#67 Stone	1606
w/cm	0.33

In order to achieve the desired service lives, further refinements to the mix designs in use are required. The first method of improving durability is decreasing the water to cementitious materials ratio (w/cm) to 0.3. Next, modifications were made to improve durability properties

for chloride exposure, carbonation, and sulfate attack. Table 9-3 shows the base mix design to be investigated. The binder compositions to be investigated are given in Table 9-4. The dosages of air-entraining and high-range water reducers will be determined during mixing to attain desired workability and air content values. Four of the mix designs will also be investigated for the effect of self-healing capabilities on the ingress of chlorides. These mix designs are designated with a check mark by their binder compositions.

Table 9-3: Base experimental mix design

Material	Weight (lb/yd ³)
Water	285
Binder	950
Natural Sand	866
#67 Stone	1905
w/cm	0.30

Table 9-4: Binder compositions for experimental mix designs

Mix ID	Cement (%)	Cement Type	Fly Ash (%)	Slag (%)	Silica Fume (%)	Metakaolin (%)	w/cm	Self-Healing
T2	100	II	0	0	0	0	0.4	-
SCP-HP	85	III	15	0	0	0	0.33	✓
F25	75	II	25	0	0	0	0.3	✓
F25-SF5	70	II	25	0	5	0	0.3	-
F25-MK5	70	II	25	0	0	5	0.3	-
F25-SF10	65	II	25	0	10	0	0.3	-
F25-MK10	65	II	25	0	0	10	0.3	-
S35-MK5	60	II	0	35	0	5	0.3	✓
S50-MK5	45	II	0	50	0	5	0.3	✓
S35-SF5	60	II	0	35	5	0	0.3	-
S50-SF5	45	II	0	50	5	0	0.3	-

9.1.2 Mechanical Property Characterization

The compressive strength and elastic modulus of each mix design will be investigated. The compressive strength will be measured in accordance with ASTM C 99 (2005) on 4" x 8" cylinders. Three cylinders will be tested at 3, 28, and 56 days of age to determine the strength characteristics of each mix for precast use. The elastic modulus will be measured in accordance with ASTM C 469 (2002) on 4" x 8" cylinders. Three cylinders will be tested at 56 days of age.

9.1.3 Carbonation Resistance Properties

The carbonation resistance properties of each mix will be characterized by using an accelerated exposure test. The test will be performed on 3 in. x 3 in. x 11.25 in. concrete prisms. The samples will be removed from the form after 24 hours cured in limewater until 21 days of age. The samples will then be environmentally conditioned at 25° C and 50% relative humidity for 7 days. Next, the samples will be exposed to a 20% carbon dioxide environment, at 55% relative humidity and 40° C in a Nuair US Autoflow NU-4850 Incubator. After exposure periods of 1, 3, 7, 14, 21, and 28 days, samples will be tested by dry cutting three slices through the cross-section at least 3" from each end of the sample. Next, a phenolphthalein indicator solution (1% phenolphthalein, 20% water, 79% ethanol w/v), as used by Kurth (2008), will be applied to the cut surfaces and the distance to the carbonation front, as defined by color change at pH of 9.2. The location of the carbonation front will be measured to the nearest 1/32" at 3 locations along each face of the specimen, except for the face in contact with the racks in the incubator.

The results will be compared with estimator equations developed by Papadakis (2000) and Steffens (2002). Additionally, modeling of the carbonation depth versus time will be performed to aid in service life prediction calculations. The depth of carbonation, in conjunction with modeling of chloride ingress will be used to predict the onset of corrosion in reinforced concrete sections.

9.1.4 Sulfate Attack Resistance Properties

Sulfate resistance of each mix design will be investigated using two accelerated test methods. Accelerated expansion tests will be performed in accordance with ASTM C 1012 (2009) on mortar samples. The mortar samples will be cast using the same relative binder compositions as the concrete mix designs being investigated. For each mix, 6 bars (1 in. x 1 in. x 11.25 in.) and 12 cubes (2 in. x 2 in. x 2 in.) will be cast. Two cubes will be broken at 24 hours after casting, and two more every 24 hours until the samples have reached a minimum of 2850 psi. All samples will be cured in saturated limewater at 23° C until the strength surpasses 2850 psi. After the strength is met, an initial length reading will be performed and the mortar bars will be placed in a sulfate solution (0.5% Na₂SO₄ by mass) and sealed. Readings will be taken at 1, 2, 3, 4, 8, 13, and 15 weeks of exposure. Additional readings will be performed at 6, 9, and 12 months of exposure. At each reading, the sulfate solution will be replaced.

Compressive strength testing will be performed on paste cube samples by the method used by Kurtis, et. al. (2001). Samples will be cast simultaneously with ASTM C 1012 (2009)

samples. For each mix, the compressive strength of 8 samples (0.5 in. cubes) will be tested at the time of exposure, as well as, 28, 90, and 180 days after exposure. The compression testing will be performed at a load rate of 600 lb/min. The samples will be made with the same relative quantities of binder components as the concrete mix designs, using a 0.5 w/c. Samples will be cured in the molds for 24 h followed by moist curing at 50°C until time of exposure. Samples will be exposed to a 4% Na₂SO₄ solution with a controlled pH of 7.2 after the ASTM C 1012 mortar cube samples reach 2850 psi. X-ray diffraction (XRD) will be performed on powder samples from specimens to determine microstructure changes in samples after prolonged exposure to high sulfate concentrations.

9.1.5 Chloride Ion Penetration Resistance

The chloride transport properties of each mix will be evaluated using a rapid migration test and with a long-term exposure test. The rapid chloride permeability of each mix design will be determined using ASTM C 1202 (2007) at 56 days of age. The bulk diffusion test (ASTM C 1556, 2004) will be used to determine long-term exposure properties of the concrete mix designs.

9.1.5.1 Rapid Chloride Permeability

The rapid chloride permeability tests will be performed using the Proove-It test set-up, as shown below in Figure 9-1. The results will be compared between mix designs and with literature for their performance. The current GDOT limit for high performance concrete for bridge piles is 2000 coulombs. Table 9-5 gives the chloride penetrability rating according to ASTM C 1202 (2007).

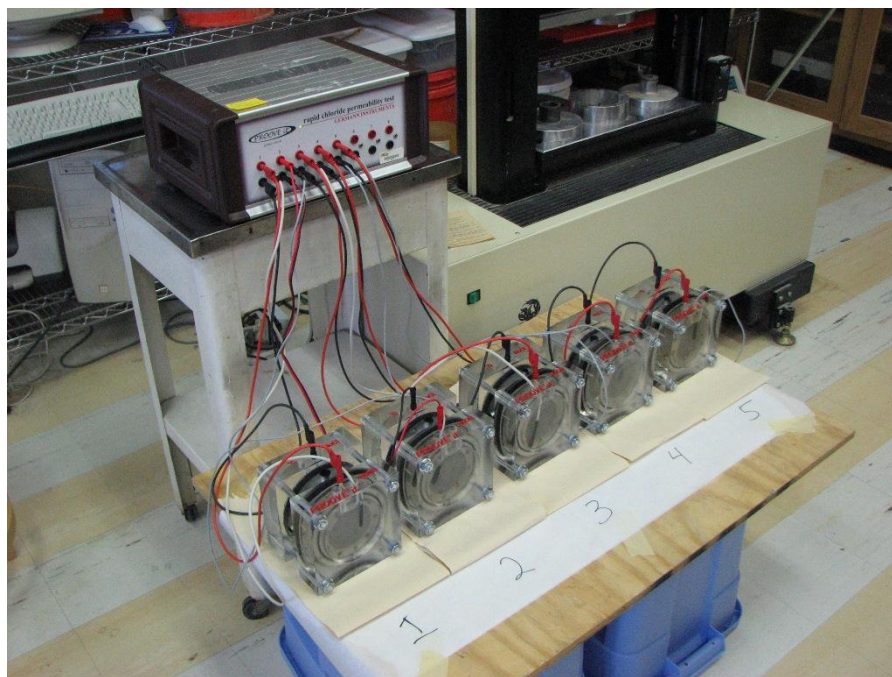


Figure 9-1: Test set up for rapid chloride permeability test

Table 9-5: Chloride ion penetrability based on charge passed (ASTM C 1202, 2007)

Charge Passed (coulombs)	Chloride Ion Penetrability
> 4,000	High
2,000-4,000	Moderate
1,000-2,000	Low
100-1,000	Very Low
<100	Negligible

9.1.5.2 Bulk Diffusion Testing

The bulk diffusion test (ASTM C 1556, 2004) will be performed on slices of 4 in. x 8 in. cylinders. Bulk diffusion samples will be moist cured for 28 days, and then the samples will be prepared and exposed to a chloride solution (165 g/L) for 180 days. After removing from the exposure solution, samples will be rinsed with tap water and allowed to dry for 24 hours. Profile grinding will be performed on the samples using an adapted coring bit in a milling machine that will be donated by Dr. Thomas. Samples will be ground at 0.04 in. increments (1 mm) and the acid soluble chloride content will be determined using ASTM C 1152 (2004).

The chloride profiles will be used to determine the apparent chloride diffusion coefficient by performing a non-linear regression analysis, using the method of least squares to fit to the equation given by Eq. 9.1 (ASTM C 1152, 2004).

$$C(x,t) = C_s - (C_s - C_i) * \operatorname{erf}\left(\frac{x}{\sqrt{4*D_a*t}}\right) \quad (\text{Eq. 9.1})$$

Where,

- $C(x,t)$ = chloride concentration, measured at depth x and exposure time t , mass %
- C_s = projected chloride concentration at the interface between the exposure liquid and test specimen that is determined by the regression analysis, mass %
- C_i = initial chloride-ion concentration of the cementitious mixture prior to submersion in the exposure solution, mass %
- x = depth below the exposed surface (to the middle of a layer), m
- D_a = apparent chloride diffusion coefficient, m^2/s
- t = the exposure time, s
- erf = error function
- $= \frac{2}{\sqrt{\pi}} * \int_0^z \exp(-u^2) du$

An approximation developed by Winitzki (2006) for the error function will be used to perform the regression analysis. The approximation, given in Eq. 9.2, results in a maximum relative error of less than 1.3%.

$$\operatorname{erf}(x) \approx \left[1 - \exp\left(-x^2 \left(\frac{\frac{4}{\pi} + 0.147x^2}{1 + 0.147x^2}\right)\right)\right]^{\frac{1}{2}} \quad (\text{Eq. 9.2})$$

In addition to the traditional ASTM C 1556 (2004) test, a modified version will be run on the SCP-HP mix design. The exposure solution will be modified to contain two concentrations of Na_2SO_4 (0.5% and 4% by mass). These tests will help to show if there is a coupled effect between sulfate attack and chloride ingress, as well as the effect of varying concentrations of sulfates. Mix design SCP-HP was chosen due to its use of an ASTM C 150 (2009) Type III cement, which should be more vulnerable to sulfate attack due to its higher C_3A content.

9.1.6 Self-Healing Characterization

The self-healing capabilities of four mix designs will be evaluated. The mix designs were selected based upon the binder compositions potential for autogenous self-healing to occur. Table 9-6 shows the four selected binder compositions.

Table 9-6: Self-healing mix design binder compositions

Mix ID	Cement (%)	Cement Type	Fly Ash (%)	Slag (%)	Silica Fume (%)	Metakaolin (%)
SCP-HP	85	III	15	0	0	0
F25	75	II	25	0	0	0
S35-MK5	60	II	0	35	0	5
S50-MK5	45	II	0	50	0	5

The self-healing specimen dimensions are shown below in Figure 9-2. These dimensions were selected to ensure that flexure controlled cracking and not shear. Specimens will be cast with a 1-1/2 in. PVC conduit in the center to allow for unbonded post-tensioning of the samples using 1 in. diameter Dywidag post-tensioning bars.

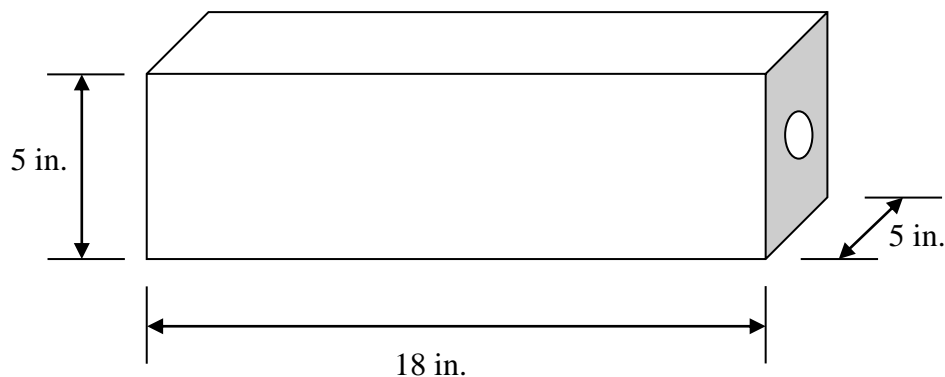


Figure 9-2: Self-healing specimen dimensions

Specimens will be cast with two per mold, separated by a thin 18 gage divider plate, as shown in Figure 9-3. The specimens will remain in this geometry throughout testing to allow for lower losses of prestressing force due to slipping of the nut after jacking. Cast samples are shown in Figure 9-4, and Figure 9-5 shows the conduit at the end of a sample where the post-tensioning bar would be placed.



Figure 9-3: Self-healing specimen formwork



Figure 9-4: Self-healing specimens



Figure 9-5: Post-tensioning bar conduit in self-healing specimen

The specimens will be pre-cracked with a through-specimen crack and flexural crack at 14 days of age, as shown in Figure 9-6. The crack orientations were chosen to represent the possible cracking patterns observed in piles due to reflective tension cracking and flexural cracking during handling. Through cracks will be created using knife edge bearings and flexural cracks will be created using a three point bending test. Specimens will be reinforced, but not prestressed at time of cracking.

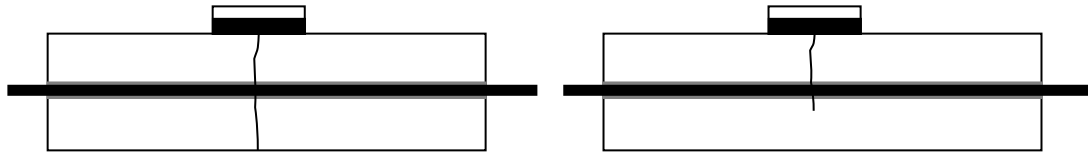


Figure 9-6: (a) Through crack specimen, and (b) flexure crack specimen

After cracking the specimens, 900 psi of prestressing will be applied to the specimens to simulate the current level of prestressing used in the state of Georgia. The set-up for post-tensioning of specimens is shown below in Figure 9-7. After post-tensioning, the crack size will be measured, the sides of the specimen sealed with Sikadur 32 Hi-Mod epoxy, and the ponding container attached to the top of the specimen. Samples will be ponded with a chloride solution (165g/L NaCl). Specimens will be tested at 28 days and 180 days of exposure by grinding powder from the crack location at 0.04 in. increments using a 3/8 in. diameter masonry drill bit. The total chloride concentration will be determined. Profiles will also be determined away from the crack to determine the effect of 2-D ingress from the crack location in addition to the ponding surface.

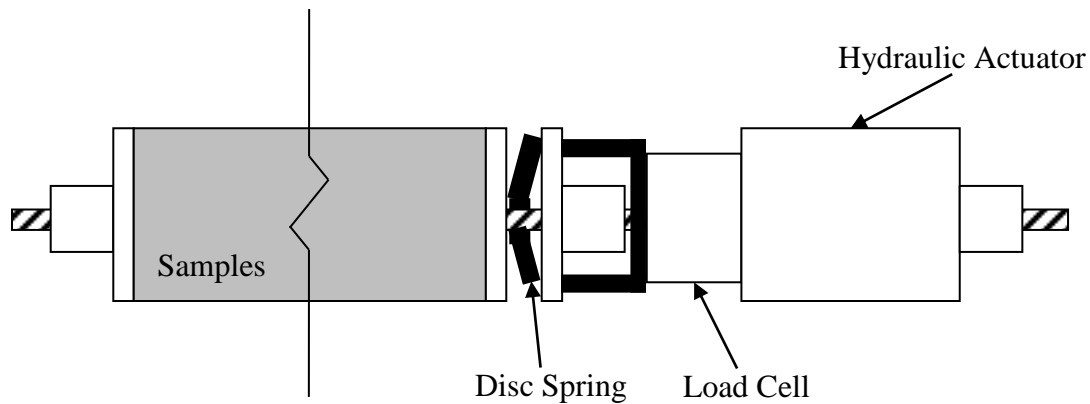


Figure 9-7: Post-tensioning set-up

9.1.7 Service Life Modeling

The results of the bulk-diffusion, self-healing, and carbonation tests will be used to perform service life modeling of the mix designs tested. The results of these tests will be used in conjunction with the Life 365 (Ehlen, 2009) and Femern (Frederiksen and Geiker, 2008) models to predict service lives from chloride ingress. Additionally, using a chloride threshold defined by the chloride to hydroxide concentration will be used to predict service lives due to combined chloride ingress and carbonation of samples.

9.1.8 Concrete Research Activities

The proposed concrete research will be broken into a series of tasks to be completed. The various tasks are listed below.

- 1) Design experimental test specimens
 - a) Construct formwork for self-healing specimens
 - b) Attain raw materials for mix designs
- 2) Perform sulfate attack resistance tests
 - a) Cast ASTM C 1012 (1012) samples
 - b) Perform length change readings on samples
 - c) Cast accelerated sulfate exposure samples
 - d) Perform compressive strength evaluation of samples after exposure periods
 - e) Perform XRD on samples for microstructure changes
- 3) Perform mix design durability characterization
 - a) Cast concrete samples
 - b) Perform mechanical property testing
 - c) Perform carbonation resistance characterization
 - d) Perform rapid chloride permeability testing
 - e) Perform bulk diffusion testing

- 4) Perform self-healing characterization
 - a) Pre-crack specimens
 - b) Apply post-tensioning load
 - c) Begin ponding of salt-solution on surface
 - d) Determine effect of self-healing of crack on chloride ingress
- 5) Create service life estimates for mix designs
 - a) Compare methodologies for service life estimation
 - b) Estimate service life for structures in marine environments
- 6) Create recommendations for longer service lives of prestressed concrete piles
 - a) Propose draft mix design specifications
 - b) Recommend design methods and techniques

9.2 Prestressing Steel Corrosion and Mechanical Characteristics

Our research approach for investigating stainless steel prestressing reinforcement will include three stages of development and testing: (1) production of candidate materials, (2) testing, and (3) identification of an optimal prestressing alloy. An overview of the proposed experimental program is shown diagrammatically below in Figure 9-8.

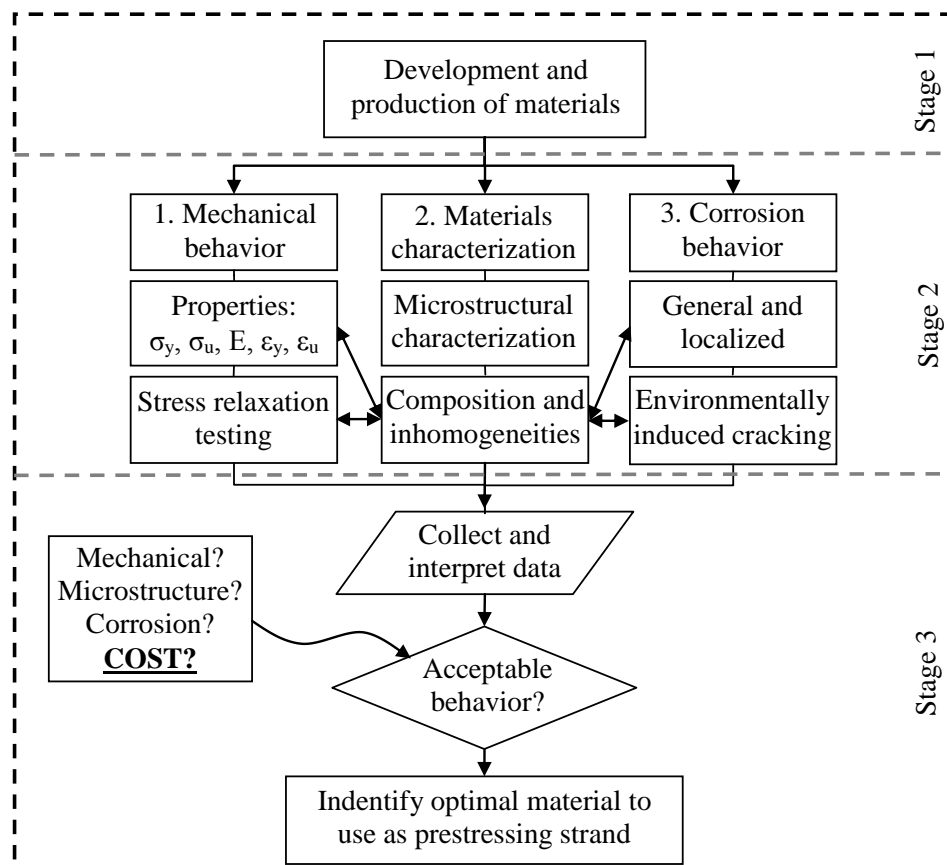


Figure 9-8: Proposed stainless steel experimental program

Stage 1 includes the development and manufacturing of high-strength (greater than 200ksi/1380MPa) stainless steels (HSSs) to be used for testing performed in Stage 2. Alloys consistent with conventional ASTM A416 prestressing steels and currently available stainless steels (austenitic, martensitic, and duplex) will be obtained and processed in a manner similar to those used for prestressing steels (heavy cold drawing). Task 1 will determine the mechanical properties of each alloy, including stress relaxation (a critical parameter in prestressing applications). Task 2 will characterize the microstructure of each alloy, including expected vs. actual compositions, and examination for structural defects and local compositional inhomogeneities. Task 3 will test the corrosion behavior of each alloy. Possible forms of corrosion investigated will include general and localized (pitting) corrosion in addition to more critical hydrogen embrittlement (HE) and stress corrosion cracking (SCC). Stage 3 will evaluate all of the results obtained during Stage 2 with the goal of identifying an optimal alloy for the production of HSSS prestressing strand.

9.2.1 Stage 1 – Production of HSSs

Materials included in our study are shown in Table 9-7 below along with their key alloying elements and PREN values. Two typical austenitic grades (304 and 316) were selected based on their high availability and high corrosion resistance in reinforced concrete. Three duplex grades (2101, 2205, and 2304) were selected for their improved mechanical properties when compared with the austenitic grades and high corrosion resistance. Duplex grades 2101 and 2304 are also referred to as “lean duplex” due to their lower Ni and Mo contents, leading to lower initial raw material cost. One precipitation hardenable (PH) martensitic grade 17-7 will also be included in the study for its high strength. These stainless steel grades were selected based on their availability, potential corrosion resistance, potential for achieving high strengths, and cost. In addition, typical A416 prestressing steel will be included in all testing as a control.

Table 9-7: Candidate HSSs to be produced during Stage 1

Alloy	Structure	Composition (%) – Balance Fe				PREN
		Cr	Ni	Mo	Other	
302/304	Austenitic	18.2	8.1	-	-	19.2
316	Austenitic	17	11	2.8	-	27.2
2101	Duplex	21.5	1.5	-	5Mn, 0.22N	29.1
2205	Duplex	22	5.5	3	0.17N	37.0
2304	Duplex	23	4.8	0.3	0.10N	27.0
17-7PH	Martensitic	17	7	-	1Al, 1Si	17.0

Stainless steels of said compositions will be acquired as raw rod coil material and will be strengthened by cold drawing to form HSSS wires. No strands will be produced during the initial multi-alloy investigation as the production of strands is very costly for this preliminary research. Wires will be cold drawn to achieve desired tensile strengths with a wire diameter of 3.5-6mm (the range typical for a prestressing strand). Wire will be cold drawn at stainless steel spring wire production facilities utilizing equipment similar to that shown in Figure 9-9, wherein stainless

rod coil is drawn at sequential levels of cross section reduction, resulting in a final product exhibiting the desired wire diameter.



Figure 9-9: Stainless steel spring wire cold drawing equipment, typical wire drawing facility

9.2.2 Stage 2 – Testing and Characterization

9.2.2.1 Task 1 – Mechanical Behavior

Testing performed during Task 1 will characterize the mechanical behavior of HSSs produced during Stage 1. For optimized prestressing systems, it is critical to achieve $\sigma_y:\sigma_{uts}$ approaching 1.0 and ductility of approximately 5 %. Stress vs. strain behavior and elastic modulus (E) will be determined for each material by uniaxial tension testing. Tests will also be performed to determine the % stress relaxation which occurs during 200 hr constant strain tests conducted at 70% of the ultimate tensile capacity of the HSSs being examined. Stress relaxation tests will be conducted on tensile creep frames adapted as shown in Figure 9-10.

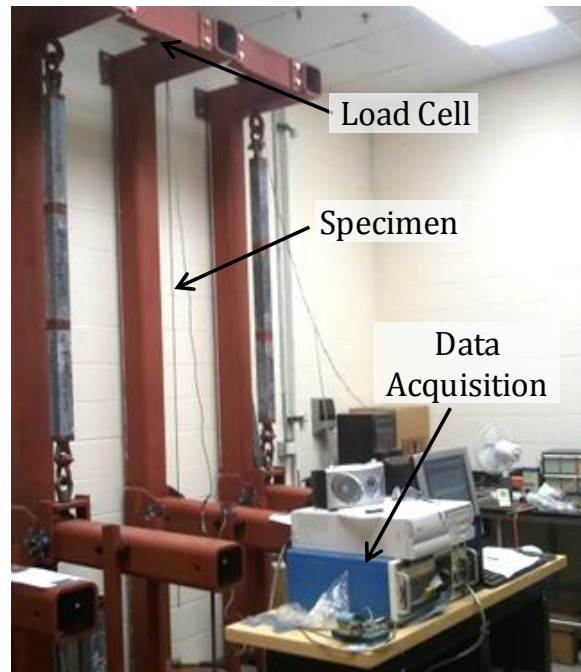


Figure 9-10: Tensile stress relaxation experimental setup

9.2.2.2 Task 2 – Materials Characterization

Each material (including the control) produced during Stage 1 will be tested to determine its exact composition (i.e., Fe, Cr, Ni, C, etc. contents) during Task 2 – occurring concurrently with Task 3. Metallographic techniques will be used to characterize the morphology of each alloy, including grain size and orientation and the presence of deleterious microstructures such as strain-induced martensite inclusions. X-ray diffraction and magnetic permeability techniques will also be used to identify microstructural features which may not be evident using traditional metallography. Following corrosion testing performed during Task 3, each alloy will be inspected using scanning electron microscopy (SEM) for intergranular and/or transgranular cracking induced by HE/SCC and to correlate corrosion damage with microstructural features. Energy dispersive X-ray spectroscopy (EDX) will be used to locally investigate alloy composition at bulk and grain boundary regions where deleterious phase precipitation (such as S, P, and Cr_3C_2) may lead to HE/SCC susceptibility.

9.2.2.3 Task 3 – Corrosion Behavior

Of critical importance to the proposed research is testing of corrosion behavior which will occur during Task 3. First, alloys developed during Stage 1 and the control will be tested using long-term in-solution and cyclic potentiodynamic polarization techniques with and without stress to determine susceptibility to general and localized forms of corrosion (i.e. pitting). The techniques employed and sample types used will be similar to those presented in Chapter 7. Two simulated concrete exposure conditions will be used for all corrosion testing: (1) an alkaline solution of saturated $\text{Ca}(\text{OH})_2$ with pH of 12.5, and (2) a carbonated solution of 0.3M NaHCO_3 and 0.1M Na_2CO_3 with pH of 9. Solution 1 represents a concrete at later ages which has not yet

carbonated, thus leading to a pH of 12.5 corresponding to the maximum solubility of $\text{Ca}(\text{OH})_2$. Solution 2 represents a concrete which has fully carbonated. In order to simulate a marine exposure, Cl^- will be added to these solution as NaCl in concentrations of 0.0M (no Cl^-), 0.25M (brackish water), 0.5M (open ocean water), and 1.0M (worst case). These Cl^- concentrations were conservatively selected considering that at 100+ years of service Cl^- concentrations at the cover depth may begin to approach that present at the surface of the concrete.

Second, each candidate alloy will be tested for susceptibility to EAC mechanisms such as Cl^- assisted SCC and HE. Slow strain rate testing will be conducted using dogbone specimens exposed to simulated concrete pore solutions discussed above. Chlorides will be added to the solution to determine SCC susceptibility and excessive cathodic polarization will be used to determine HE susceptibility. As discussed in Section 9.2.2.2 – Task 2, each alloy tested for HE/SCC will be inspected for cracking and fracture induced during the test as illustrated in Figure 9-11.

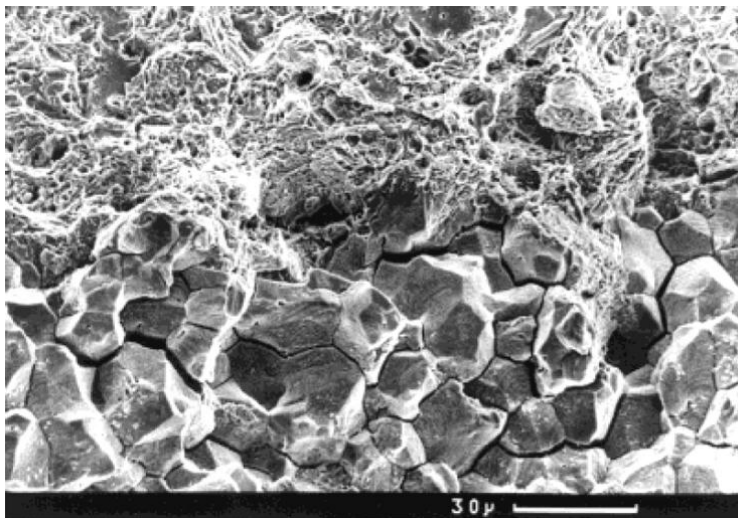


Figure 9-11: Intergranular SCC in a Prestressing Steel (Mietz, 2000)

9.2.3 Stage 3 – Identification of Optimal Prestressing Material

At the completion of Stage 2, all results will be thoroughly examined to determine which alloy presents acceptable mechanical properties and adequate corrosion resistance while also considering factors such as cost and availability. This most optimal material will then be investigated for production as prestressing strand. Larger quantities of rod coil will be predrawn to the correct diameter for prestressing strand, with more attention played to the cold drawing process itself with the goal of achieving higher strengths than were obtained in the initial alloy screen phase discussed in section 9.2.1. Since the microstructure of this material may be different than that originally tested (due to high degree of cold drawing), additional studies similar to those presented in section 9.2.2 will be used to verify that corrosion resistance has not been jeopardized. In addition, tests applicable to prestressed concrete such as pullout strength, transfer length, stress relaxation (of strands), and stress vs. strain behavior of the developed stainless steel prestressing strand will also be performed. Thus, the goal of Stage 3 is to fully characterize the

developed stainless steel prestressing strand such that it can be used in the construction of prestressed concrete elements.

9.3 References

ACI Committee 211, (2008). “ACI 211.4R-08 Guide for Selecting Proportions for High-Strength Concrete Using Portland Cement and Other Cementitious Materials,” *ACI Manual of Concrete Practice*, ACI 211.4R-08, American Concrete Institute, Farmington Hills, MI, pp. 25.

ASTM C 39 (2005). “Standard Test Method for Compressive Strength of Cylindrical Concrete Specimens,” American Society for Testing and Materials, West Conshohocken, PA, pp. 7.

ASTM C 150 (2009). “Standard Specification for Portland Cement,” American Society for Testing and Materials, West Conshohocken, PA, pp. 10.

ASTM C 469 (2002). “Standard Test Method for Static Modulus of Elasticity and Poisson’s Ratio of Concrete in Compression,” American Society for Testing and Materials, West Conshohocken, PA, pp. 5.

ASTM C 1012 (2009). “Standard Test Method for Length Change of Hydraulic-Cement Mortar Bars Exposed to a Sulfate Solution,” American Society for Testing and Materials, West Conshohocken, PA, pp. 6.

ASTM C 1152 (2004). “Standard Test Method for Acid-Soluble Chloride in Mortar and Concrete,” American Society for Testing and Materials, West Conshohocken, PA, pp. 4.

ASTM C 1202 (2007). “Standard Test Method for Electrical Indication of Concrete’s Ability to Resist Chloride Ion Penetration,” American Society for Testing and Materials, West Conshohocken, PA, pp. 6.

ASTM C 1556 (2004). “Standard Test Method for Determining the Apparent Chloride Diffusion Coefficient of Cementitious Mixtures by Bulk Diffusion,” American Society for Testing and Materials, West Conshohocken, PA, pp. 7.

Ehlen, M.A. (2009). *Life 365* (Version 2.0.1) [Software]. Available from <http://www.life-365.org>

Frederiksen, J. M. and Geiker, M.R. (2008). “Chloride ingress prediction: Part 1: Analytical model for time dependent diffusion coefficient and surface concentration,” CONMOD 08, Delft, the Netherlands.

Kurth, J.C. (2008). *Mitigating Biofilm Growth through the Modification of Concrete Design and Practice*. Master’s Thesis. Georgia Institute of Technology. pp. 234.

Kurtis, K.E., et. al. (2001). “Accelerated Test for Measuring Sulfate Resistance of Calcium Sulfoaluminate, Calcium Aluminate, and Portland Cements,” *Journal of Materials in Civil Engineering*, May/June Edition, pp. 216-221.

Mietz, J. (2000). “Investigations on Hydrogen-Induced Embrittlement of Quench and Tempered Prestressing Steels.” *Materials and Corrosion*, V. 51, pp. 80-90.

Papadakis, V.G. (2000). “Effect of supplementary cementing materials on concrete resistance against carbonation and chloride ingress.” *Cement and Concrete Research*, V. 30, pp. 291-299.

Steffens, A., et. al. (2002). “Modeling carbonation for corrosion risk prediction of concrete structures.” *Cement and Concrete Research* V. 32, pp. 935–941.

Winitzki, S. (2006). “A handy approximation for the error function and its inverse,” Lecture note, Ludwig-Maximilians University, Munich, Germany.

10. Conclusions

The interviews with GDOT personnel, the forensic analysis of the piles from the Turtle River Bridge, the preliminary corrosion tests of normal A416 prestressing wire and strands, plus literature reviews of concrete materials and of reinforcement corrosion has led to the following conclusions:

- 1) Marine piles in Georgia are subject to chloride intrusion, cracking due to pile driving, biological attack and sulfate attack. Normal quality concrete is not sufficient to resist these actions. It is unknown if the now-required high performance concrete will provide 100-year performance.
- 2) Sulfate attack on the concrete piles was unknown as a deterioration mechanism in Georgia. Research in Part 2 of this project should include a focus on sulfate attack and on concrete mix designs that resist such attack.
- 3) Biological attack of limestone aggregate and limestone-cement was unknown in Georgia waters. While Georgia now specifies the use of granite aggregates for marine piles, older piles were made using limestone aggregate. New maintenance techniques for those older piles need to be researched and developed to eliminate the biological deterioration and to assure that new limestone cements are resistant to that attack.
- 4) Cracking during pile driving may be limited to piles which have a pre-compressive stress less than 1000 psi. Georgia's prestressed concrete pile design should be reviewed with respect to required pre-compressive stress.
- 5) Typical A416 carbon steel prestressing wire and strand is very susceptible to chloride induced corrosion. Part 1 preliminary studies showed that the crevices created in prestressing strands dramatically increased the onset of corrosion compared to prestressing wires alone. It is noted that the literature is dominated by corrosion studies of wire alone which data lead to non-conservative estimates of durability.
- 6) For typical concrete covers, it is expected that the cover concrete will carbonate between 30 to 40 years after which time the concrete alkalinity will not be sufficient to passivate typical prestressing steel. That prestressing will then corrode rapidly. Therefore, either the concrete cover must be made to have very low permeability to prevent chloride intrusion, or the prestressing steel must be non-corroding, or both.
- 7) The preliminary study of stainless steel prestressing strands investigated common stainless steels like 304 and 316 plus duplex stainless steels like 2101, 2205, and 2304. It also investigated grade 17-7, a nitronic stainless steel which was similar to the grade 33 used previously by the U.S. Navy for marine piles in degaussing facilities. Based on material properties and corrosion resistance, the 2205 and 2304 grades appear most promising for prestressing applications. Other stainless alloys do not develop sufficiently high yield stress for prestressing applications, or they have high stress relaxation which

prevents their use. Of these two alloys, the 2304 appears most economical. It is proposed that both 2205 and 2304 alloys be chosen as the alloys used for further research in Part 2 of the research.

- 8) To assure a 100-life for prestressed concrete piles in Georgia's marine environment, the preliminary conclusion is that a special high-performance, high-durability concrete needs to be developed and that non-corrosive prestressing strand and non-prestressed reinforcing steel should be used. Further research in Part 2 will clarify this preliminary conclusion.

Appendix A: I-95 at Turtle River Bridge Inspection Reports

BRIDGE INVENTORY DATA LISTING GEORGIA DEPARTMENT OF TRANSPORTATION

Structure ID:	127-0052-0	Glynn	SUFF. RATING	81.85
Location & Geography				
* Structure I.D.No:	127-0052-0	* 104 Highway System:	1	
* 200 Bridge Information	91	* 26 Functional Classification:	11	
* 6A Feature Int:	TURTLE RIVER	* 204 Federal Route Type:	1	No.: 00951
* 6B Critical Bridge:	0	* 105 Federal Lands Highway:	0	
* 7A Route Number Carried:	SR00405	* 110 Truck Route:	1	
* 7B Facility Carried:	I-95 SBL	* 206 School Bus Route:	0	
* 9 Location:	2 MIS INT I-95 & SR 27	* 217 Benchmark Elevation:	0000.00	
* 2 DOT District:	5	* 218 Datum:	0	
* 207 Year Photo:	2008	* 19 Bypass Length:	01	
* 91 Inspection Frequency:	24 Date: 12/16/2008	* 20 Toll:	3	
* 92A Fract Crit Insp Freq:	00 Date: 02/01/1901	* 21 Maintenance:	01	
* 92B Underwater Insp Freq:	60 Date: 08/10/2005	* 22 Owner:	01	
* 92C Other Spec. Insp Freq:	00 Date: 02/01/1901	* 31 Design Load:	6	
* 4 Place Code:	00000	* 37 Historical Significance:	5	
* 5 Inventory Route (O/U):	1	* 205 Congressional District:	01	
Type:	1	* 27 Year Constructed:	1977	
Designation:	1	* 106 Year Reconstructed:	0000	
Number:	00095	* 33 Bridge Median:	1	
Direction:	0	* 34 Skew:	00	
* 16 Latitude:	31-11.2770 MMS Prefix: SR	* 35 Structure Flared:	0	
* 17 Longitude:	81-32.5180 MMS Suffix: 00 MP: 33.22	* 38 Navigation Control:	1	
* 98 Border Bridge:	000 %Shared: 00	* 213 Special Steel Design:	0	
* 99 ID Number:	0000000000000000	* 267 Type of Paint:	1	
* 100 STRAHNET:	1	* 42 Type of Service on:	1	
* 12 Base Highway Network:	1	Under:	5	
* 13A LRS Inventory Route:	1271040500	* 214 Movable Bridge:	0	
* 13B Sub Inventory Route:	0	* 203 Type Bridge:	D-O-N-O	
* 101 Parallel Structure:	L	* 259 Pile Encasement:	3	
* 102 Direction of Traffic:	1	* 43 Structure Type Main:	4	02
* 264 Road Inventory Mile Post:	005.54	* 45 No. Spans Main:	003	
* 208 Inspection Area:	05 Initials: WEG	* 44 Structure Type Appr:	5	02
Engineer's Initial:	sgm	* 46 No. Spans Appr:	0040	
* Location I.D. No.:	127-00405D-033.22N	* 226 Bridge Curve Horiz:	0	Vert: 1
		* 111 Pier Protection:	2	
		* 107 Deck Structure Type:	1	
		* 108 Wearing Surface Type:	1	
		Membrane:	8	
		Protection:	8	
Signs & Attachments				
		* 225 Expansion Joint Type:	05	
		* 242 Deck Drains:	1	
		* 243 Parapet Location:	0	
		Height:	0.00	
		Width:	0.00	
		* 238 Curb:	0.00	0
		* 239 Handrail:	9	9
		* 240 Median Barrier Rail:	0	
		* 241 Bridge Median Height:	0.00	
		Width:	0.00	
		* 230 Guardrail Loc Dir Rear:	6	
		Fwd:	0	
		Oppo Dir Rear:	0	
		Fwd:	0	
		* 244 Approach Slab:	3	
		* 224 Retaining Wall:	0	
		* 233 Posted Speed Limit:	55	
		* 236 Warning Sign:	0	
		* 234 Delineator:	1	
		* 235 Hazard Boards:	0	
		* 237 Utilities Gas:	00	
		Water:	00	
		Electric:	00	
		Telephone:	00	
		Sewer:	00	
		* 247 Lighting Street:	0	
		Navigation:	1	
		Aerial:	0	
		* 248 County Continuity No.:	00	

BRIDGE INVENTORY DATA LISTING GEORGIA DEPARTMENT OF TRANSPORTATION

Structure ID: 127-0052-0

Glynn

SUFF. RATING

81.85

Programming Data

201 Project No.: I-95-1 (34) 30 CT.3
 202 Plans Available: 4
 249 Prop. Proj. No. NH-IM-95-1 (154)
 250 Approval Status: 0000
 251 P.I. No.: 511092-
 252 Contract Date: 02/18/2005
 260 Seismic No.: 00000
 75 Type Work: 00 1
 94 Bridge Imp. Cost: \$ 0
 95 Roadway Imp. Cost: \$ 0
 96 Total Imp Cost: \$ 0
 76 Imp. Length: 000000
 97 Imp. Year: 072180 Year: 2027
 114 Future ADT:

Measurements

* 29 ADT: 048120 Year: 2007
 109 % Trucks: 0
 * 28 Lanes On: 02 Under: 00
 210 No. Tracks On: 00 Under: 00
 * 48 Max. Span Length: 0200
 * 49 Structure Length: 3,488
 51 Br. Rwdy. Width: 40.30
 52 Deck Width: 43.50
 * 47 Tot. Horz. Cl: 40.30
 50 Curb/Sdewlk Width: 0.00/0.00
 32 Approach Rdwy Width: 036
 * 229 Shoulder Width:
 Rear Lt: 4.00 Type: 2 Rt: 10.00
 Fwd Lt: 3.00 Type: 2 Rt: 10.60
 Pavement Width:
 Rear: 23.10 Type: 2
 Fwd: 22.70 Type: 2
 Intersection Rear: 0 Fwd: 0
 36 Safety Features Br. Rail: 1
 Transition:
 App. G. Rail: 1
 App. Rail End: 2
 53 Minimum CLOver:
 Under: N
 * 228 Min. Vertical Cl
 Act. OdM Dir: 99 ' 99 "
 Oppo. Dir: 99 ' 99 "
 Posted OdM. Dir: 00 ' 00 "
 Oppo. Dir: 00 ' 00 "
 55 Lateral Undercl. Rt: N 0.00
 56 Lateral Undercl. Lt: 0.00
 * 10 Max Min Vert Cl: 99 ' 99 " Dir: 0
 39 Nav Vert Cl: 035 Horz: 0080
 116 Nav Vert Cl Closed: 000
 245 Deck Thickness Main: 8.00
 Deck Thick Approach: 8.00
 246 Overlay Thickness: 0.00
 212 Year Last Painted: Sup: 1977 Sub: 0000

Ratings

65 Inventory Rating Method: 1
 63 Inventory Rating Method: 1
 66 Inventory Type: 2 Rating: 44
 64 Operating Type: 2 Rating: 73
 231 Calculated Loads
 H-Modified: 20 0
 HS-Modified: 25 0
 Type 3: 28 0
 Type 3s2: 40 0
 Timber: 36 0
 Piggyback: 40 0
 261 H Inventory Rating: 23
 262 H Operating Rating: 46
 67 Structural Evaluation: 5
 58 Deck Condition: 7
 59 Superstructure Condition: 7
 * 227 Collision Damage: 0
 60A Substructure Condition: 5
 60B Scour Condition: 7
 60C Underwater Condition: 5
 71 Waterway Adequacy: 9
 61 Channel Protection a Condi: 8
 68 Deck Geometry: 7
 69 UnderClr. Horz/Vert: N
 72 Appr. Alignment: 8
 62 Culvert: N

Posting Data

70 Bridge Posting Required: 5
 41 Struct Open, Posted, Cl: A
 * 103 Temporary Structure: 0
 232 Posted Loads H-Modified: 00
 HS-Modified: 00
 Type 3: 00
 Type 3s2: 00
 Timber: 00
 Piggyback: 00
 253 Notification Date 02/01/1901
 253 Fed Notify Date: 02/01/1901 0

Hydraulic Data

215 Waterway Data
 Highway Elev.: 0006.0 Year: 1900
 Avg. Streambed Elev.: 0000.0 Freq.: 00
 Drainage Area: 00000
 Area Of Opening: 000000
 113 Scour Critical: 5
 216 Water Depth: 32.0 Br. Height: 40.5
 222 Slope Protection: 1
 221 Spur Dikes Rear: 0 Fwd: 0
 219 Fender System: 1
 220 Dolphin: 0
 223 Culvert Cover: 000
 Type: 0
 No. Barrels: 0
 Width: 0.00 Height: 0.00
 Length: 0 Apron: 0
 * 265 U/W Insp. Area: 2 Diver: RM
 * Location ID, No.: 127-00405D-033.22N

Report Date: 2/4/2010

S/A-2

GEORGIA DEPARTMENT OF TRANSPORTATION

Bridge Inspection Report

District:	5	Inspection Date:	12/16/2008	Inspection Area:	05
Bridge Inspector:	Gene Palmer	Over:	TURTLE RIVER	Bridge Status:	91
Location ID:	127-00405D-033.22N	County:	Glynn		
Structure ID:	127-0052-0	Road Name:	I-95 SBL		
EVALUATION & DEFICIENCIES					

SubStructure:

Year Painted: 0000

Report Date: 2/4/2010

B.I. - 1

GEORGIA DEPARTMENT OF TRANSPORTATION

Bridge Inspection Report

District:	5	Inspection Date:	12/16/2008	Inspection Area:	05
Bridge Inspector:	Gene Palmer	Over:	TURTLE RIVER	Bridge Status:	91
Location ID:	127-00405D-033.22N	County:	Glynn		
Structure ID:	127-0052-0	Road Name:	I-95 SBL		

EVALUATION & DEFICIENCIES

12/16/2008: This structure is being widened and the construction is ongoing. The substructure could not be looked at, due to not being able to be under the structure (with boat or snooper). After talking with the contractor on-site, all previous deficiencies are to be repaired during the widening project. A new inspection should be scheduled after the construction is complete.

The following deficiencies were left in for future inspection:

10/23/2006:

44 Concrete caps. Abutment foundation is unknown. Bents #11 through #20 have 2 concrete columns per bent. All other bents have concrete piles at each bent.

NOTE--Numerous piles have been encased to correct vertical cracking.

Previous deficiencies noted:

- 1) Abutment 1 & 44 caps minor cracking.
- 2) Bents 14 & 18 footers have cracks.
- 3) Bents 32 Pile 1 Bent 33 Pile 5 have cracks.
- 4) Piles with cracks at Piles 2-3, 2-6, 4-1, 3-5, 17-4, 28-2, 28-7, 33-7, 38-2, 38-3, 38-8, 40-1, 40-5 & 41-1.
- 5) Caps cracked at bents 15, 18, and 19.
- 6) Bent 7 Piles 5 & 6 have bar showing.

Dive report

11/98 Tidal area, bents covered with heavy marine growth. B.3 p.5 has vertical crack, 1/8" wide, from 1' above oyster shell down. B.7 p.5 has small spall with rebar exposed. B.8 p.8 has small spall just above shell. Bents 11 - 20 each consist of two concrete columns on a footing which sits on concrete piles. These bents, except b.16, have vertical cracks in the web wall up to 1/8" wide. The footings, except for b.16 & b.20, have vertical cracks on the ends up to 1/8" wide. Those cracks on b.13 & b.18 are up to 1/4" wide. B.22 p.6 has small spall just above shell. Some piles on bents 34 - 41 have been encased to repair severe cracking. Localized scour around bents. Fender system has heavy rot and limnora damage in the splash zone.

03/22/01 Same as noted above. The fender has several boards missing.

8/10/05 and 09/27/05 RMO, JWO

General: Concrete has moderate scale/abrasion from 1' above the encrusting shell down. All piles are encrusted with oyster shell and other marine growth from 1' below the high water mark to the ground line. Most piles under the pile caps have vertical cracks in the corners that range from hairline up to 1/32" running from the midline up 6' to 12'. The concrete on these piles is soft (easily chiseled off where the cracks are). The fender has all walers in place, the steel piles have heavy blistering with moderate section loss above the shell.

Specifics:

Bent 2: Vertical cracks (VC) up to 1/32" on piles 2, 3 and 5.

Bent 3: Piles 5 and 6 have vertical hairline cracks (VHLC) on the left face. Pile 5 has VC up to 1/4" on the front right corner (precursor spall).

Bent 4: VHLC on pile 1 left back corner, precursor spalling at shell. VHLC in Pile 5 left face and Pile 6 back face.

Bent 5: No cracks found.

Bent 6: Pile 1 has precursor spalling with rust stains and VHLC on left back corner.

Bent 7: VHLCs on pile 1 left front corner and pile 2 left back corner and right back corner. Pile 5 has 3 spalls with rebar exposed 3' above the shell on the front face. Pile 6 has VCs up to 1/4" precursor spalling on the right front corner; the front face is delaminating above the shell.

Bent 8: VHLCs precursor spalling on pile 4 left back corner. VHLCs precursor spalling on pile 7 left right corner.

Bent 9: VHLCs precursor spalling on pile 6 left front corner. Pile 7 left front corner is precursor spalling at shell.

Bent 10: VCs up to 1/16" precursor spalling on pile 1 left back corner and right front corner. Pile 1 also has VHLC on all faces. VHLCs on pile 3 left face from the shell up 6'. VHLCs precursor spalling with rust stains on pile 7 left back corner.

Bent 11: VHLCs in web wall. Pile cap has cracks with rust stains on the left back corner and left front corner.

Bent 12: VHLCs in web wall. No cracks found in pile cap.

Bent 13: Vertical and horizontal cracks up to 1/4" on all faces of pile cap with rust stains. The edges of some of the cracks have spalled off

Report Date: 2/4/2010

B.I. - 2

GEORGIA DEPARTMENT OF TRANSPORTATION

Bridge Inspection Report

District:	5	Inspection Date:	12/16/2008	Inspection Area:	05
Bridge Inspector:	Gene Palmer	Over:	TURTLE RIVER	Bridge Status:	91
Location ID:	127-00405D-033.22N	County:	Glynn		
Structure ID:	127-0052-0	Road Name:	I-95 SBL		

EVALUATION & DEFICIENCIES

making the crack larger at the outer edge. VHLCs in web wall.

Bent 14: Vertical and horizontal cracks up to 1/4" on all faces of pile cap with rust stains. Cracks on the left back corner are up to 3/8" with rust stains.

Bent 15: Vertical and horizontal cracks up to 1/32" on the left front and left back corners and on the back face of pile cap. The right and front faces have vertical and horizontal cracks that are up to 1/16".

Bent 16: VHLCs in web wall. No cracks found in the pile cap.

Bent 17: Horizontal hairline cracks (HHLC) with rust stains on the left face of the pile cap. VHLCs in web wall.

Bent 18: Horizontal cracks (HC) up to 1/32" with rust stains on the left face of the pile cap. The front and back faces have HCs that are up to 1/4" and have been patched with epoxy. The patches have cracked through. VHLCs in web wall.

Bent 19: VHLCs in back face of pile cap and web wall.

Bent 20: VCs up to 1/32" in the right back and right front corners of the pile cap. VHLCs in web wall.

Bent 21: VHLCs in piles 2 and 3 left back corner.

Bent 22: VHLCs in pile 1 right back corner from shell going up 1'.

Bent 23: No cracks.

Bent 24: VC up to 1/32" on pile 3 left back corner from shell up 2'.

Bent 25: VC up to 1/16" precursor spalling on pile 1 at left back corner 1' above the shell. VC up to 1/32" precursor spalling on pile 5 right front corner 1' above the shell.

Bents 26 and 27: No cracks.

Bent 28: VC up to 1/4" on pile 2 left front corner. VC up to 1/32" precursor spalling on pile 3 right front corner. VC up to 5/16" on pile 4 left front corner. VC up to 1/4" precursor spalling on piles 7 and 8 left back corner.

Bent 29: VHLC precursor spalling on pile 1 left front corner.

Bent 30: VHLCs in pile 1.

Bent 31: VC up to 1/16" precursor spalling on pile 3 right back corner.

Bent 32: No cracks.

Bent 33: Pile 7 is precursor spalling on the left back and back right corners with VCs up to 1/32".

Bent 34: Pile 1 is encased in fiberglass sheath with epoxy.

Bent 35: No cracks.

Bent 36: VC up to 1/32" precursor spalling on pile 6 right front corner.

Bent 37: Piles 1 and 6 are encased in fiberglass sheath with epoxy.

Bent 38: Piles 1, 3, 4, 5, 6 and 8 are encased in wood forms filled with concrete. Pile 8 is the only one with the wood still in place.

Bent 39: VHLC with rust stain on pile 5 right back corner.

Bent 40: Piles 1, 2, 3 and 5 are encased in fiberglass sheaths with epoxy. Pile 1 has rust stains above the encasements.

Bent 41: Piles 2 through 6 are encased in wood forms filled with concrete. VHLC up to 1/32" from the cap to the shell on pile 1 right back corner.

SuperStructure: **Year Painted:** 1977

12/16/2008: This structure is being widened and the construction is ongoing. The superstructure could not be looked at, due to not being able to be under the structure (with boat or snooper). After talking with the contractor on-site, all previous deficiencies are to be repaired during the widening project. A new inspection should be scheduled after the construction is complete.

The following deficiencies were left in for future inspection:

10/23/2006:

43 Spans. Main spans: 3 Continuous unit steel spans with 5 steel beams per span. Spans 1-4 and 23-43 have 6 PSC Type III beams. Spans 5-14 and 18-22 have 7 PSC Type IV beams.

Previous deficiencies noted:

- 1) Structure corrosion on steel beams.
- 2) Exposed cable or bar in Beams 4-1, 11-6, 19-1, 25-1 & 30-1.

Report Date: 2/4/2010

B.I. - 3

GEORGIA DEPARTMENT OF TRANSPORTATION

Bridge Inspection Report

District:	5	Inspection Date:	12/16/2008	Inspection Area:	05
Bridge Inspector:	Gene Palmer	Over:	TURTLE RIVER	Bridge Status:	91
Location ID:	127-00405D-033.22N	County:	Glynn		
Structure ID:	127-0052-0	Road Name:	I-95 SBL		

EVALUATION & DEFICIENCIES

Deck:

12/16/2008: This structure is being widened and the construction is ongoing. The deck underside could not be looked at, due to not being able to be under the structure (with boat or snooper). After talking with the contractor on-site, all previous deficiencies are to be repaired during the widening project. A new inspection should be scheduled after the construction is complete.

8" Concrete deck. (2 Finger joints)

Deck Top:

The deck top has minor transverse cracks up to 1/32" wide and minor to moderate scale/abrasion.
The deck top has minor spalls up to 5" x 3" x 1" with no exposed steel along the finger joints.

Joints:

The sealant in the joints is deteriorated.

The following deficiencies were left in for future inspection:

10/23/2006:

Deck Underside:

No deficiencies noted.

General:

12/16/2008: This structure is being widened and the construction is ongoing. No channel measurements could be taken. After talking with the contractor on-site, all previous deficiencies are to be repaired during the widening project. A new inspection should be scheduled after the construction is complete. No information on the SI&A was changed. Refer to photos 1 thru 5.

Inspected By Kisinger Campo and Associates

Team Leader: Wm. Earl Greer

Team Member: Gonzalo Silva

The following deficiencies were left in for future inspection:

10/23/2006:

Built in 1977

Design load = HS-20 + M

2 Approach slabs both asphalt overlaid.

This bridge is over a river.

Divers fill out waterway data.

TIDAL ZONE. Used big boat to complete inspection.

NOTE-- Jersey walls has several cracks.

Bridge is elevated on right side.

Spans 2 thru 42 is under contract for snooper inspection.

NOTE--All pile have heavy barnacles.

USED BIG BOAT

Repairs:

1) Seal deck joints.

2) Paint steel beams.

3) Bents 14 & 18 footers have cracks.

4) Bent 32 Pile 1, Bent 33 Pile 5 have cracks,

5) Repair exposed cable or bar in Beams 4-1, 11-6, 19-1, 25-1 & 30-1.

6) Repair piles with cracks at Piles 2-3, 2-6, 4-1, 3-5, 17-4, 28-2, 28-7, 33-7, 38-2, 38-3, 38-8, 40-1, 40-5 & 41-1.

7) Repair cracked caps at Bents 15, 18, and 19.

8) Repair piles with bar showing at Bent 7 Piles 5 & 6.

Report Date: 2/4/2010

B.I. - 4

GEORGIA DEPARTMENT OF TRANSPORTATION

Bridge Inspection Report

District: 5
Bridge Inspector: Gene Palmer
Location ID: 127-00405D-033.22N
Structure ID: 127-0052-0

Inspection Date: 12/16/2008
Over: TURTLE RIVER
County: Glynn
Road Name: I-95 SBL

Inspection Area: 05
Bridge Status: 91

EVALUATION & DEFICIENCIES

Condition Rating

Component	Material	Rating
Substructure	Concrete	5
Superstructure	Steel-Concrete	7
Deck	Concrete	7

Temp Shored: No

Truck Type	Gross/H-Mod	HSMOD	Tand	3-S-2	Log	Piggy
Calculated Posting	20	25	28	40	36	40
Posting Required	No	No	No	No	No	No
Existing Posting	00	00	00	00	00	00

Not a School Bus Route.

Structure Does Not Require Posting

GEORGIA DEPARTMENT OF TRANSPORTATION

Deficiency Report

District: 5	Inspection Date: 12/16/2008	Inspection Area: 05
Bridge Inspector: Gene Palmer	Over: TURTLE RIVER	
Location ID: 127-00405D-033.22N	County: Glynn	
Structure ID: 127-0052-0	Asst. District Engineer: Chad Hartley	

EVALUATION & DEFICIENCIES

I-95 SBL Over TURTLE RIVER—2 MI S INT I-95 & SR 27

Item	Units	Work	P	Date Reported	Location	Date Completed	Complete
520	HOURS	24	B	10/25/2000	See comment 520-1	3/16/2007	2,333.00
830	HOURS	140	B	10/25/2000	See comment 830-1-2.	3/16/2007	2,333.00
800	LIN. FT.	1,720	B	10/8/2002	800-1	3/16/2007	1,620.00
825	PILES	18	B	10/8/2002	825-1	3/16/2007	1,620.00
835	GALLONS	40	B	10/8/2002	835-1	3/16/2007	1,620.00

Comments:

520-1 Cut and remove trees from bridge ends.

800-1 Seal deck joints.

830-1 Exposed cable or bar at these locations, 4-1,11-6, 19-1, 25-1,30-1 . Caps cracked at bents 15, 18, and 19.

830-2 Bents 32 pile 1,bent 33 pile 5 have cracks.

835-1 Paint mains

825-1 Bents 14,&18 footers have cracks. Bents 32 pile 1,bent 33 pile 5 have cracks, Piles with cracks at these locations, 2-3, 2-6, 4-1, 3-5, 17-4,28-2, 28-7, 33-7,38-2, 38-3, 38-8, 40-1,40-5, 41-1. Bent 7 piles 5&6 have bar showing.

Report Date: 2/4/2010

Def-

1

Combined References

ACI Committee 201, (2008) "ACI 202.2R-08 Guide to Durable Concrete," American Concrete Institute, Farmington Hills, Michigan.

ACI Committee 201, (2008). "ACI 202.2R-08 Guide to Durable Concrete," *ACI Manual of Concrete Practice*, ACI 201.2R-08, American Concrete Institute, Farmington Hills, MI, pp. 53.

ACI Committee 211, (2008). "ACI 211.4R-08 Guide for Selecting Proportions for High-Strength Concrete Using Portland Cement and Other Cementitious Materials," *ACI Manual of Concrete Practice*, ACI 211.4R-08, American Concrete Institute, Farmington Hills, MI, pp. 25.

ACI Committee 214 (2010). "Guide for Obtaining Cores and Interpreting Compressive Strength Results," *ACI Manual of Concrete Practice*, ACI 214.4R-10, American Concrete Institute, Farmington Hills, MI, pp. 17.

ACI Committee 222 (2001). "Corrosion of Prestressing Steels," *ACI Manual of Concrete Practice*, ACI 222.2R-01, American Concrete Institute, Farmington Hills, MI, pp. 43.

Addari, D., Elsener, B., and Rossi, A. (2008). "Electrochemistry and surface chemistry of stainless steels in alkaline media simulating concrete pore solutions." *Electrochimica Acta*, V. 53 (27), pp. 8078-8086.

Ahern, M. E. (2005). "Design and Fabrication of a Compact Specimen for Evaluation of Corrosion Resistance of New Post-Tensioning Systems." MS Thesis, University of Texas at Austin, Austin, TX.

Ahmad, S. (2003). "Reinforcement Corrosion in Concrete Structures, its Monitoring and Service Life Prediction - A Review." *Cement & Concrete Composites*, V. 25, pp. 459-471.

Alonso, C., Castellote, M., and Andrade, C. (2002). "Chloride threshold dependence of pitting potential of reinforcements." *Electrochimica Acta*, V. 47 (21), pp. 3469-3481.

Alonso, M. C. "Corrosion Performance of High Strength Stainless Steel for Tendon Applications." *Proc., Final Conference of COST Action 534*.

Alonso, M. C., and Recio, F. J. "Aceros Inoxidables De Alta Resistencia Mecanica En Medios Alcalinos con Cloruros." *Proc., XXIV Encuentro del Grupo Nacional de Fractura*.

Alonso, M. C., and Sanchez, M. (2009). "Analysis of the variability of chloride threshold values in the literature." *Materials & Corrosion*, V. 60 (8), pp. 631-637.

Alonso, M. C., Recio, F. J., and Sanchez, M. "High Strength Stainless Steels for Prestressed Concrete Structures in Marine Environment." *Proc., 1st International Conference. Construction*

Heritage in Coastal and Marine Environments. Damage, Diganosis, Maintenance and Rehabilitation.

Andrade, C., Keddarn, M., Nóvoa, X. R., Pérez, M. C., Rangel, C. M., and Takenouti, H. (2001). "Electrochemical Behaviour of Steel Rebars in Concrete: Influence of Environmental Factors and Cement Chemistry." *Electrochimica Acta*, V. 46, pp. 3905-3912.

Angst, U., Elsener, B., Larsen, C. K., and Vennesland, Ø. (2009). "Critical chloride content in reinforced concrete -- A review." *Cement & Concrete Research*, V. 39 (12), pp. 1122-1138.

Angst, U., et. al. (2009). "Critical chloride content in reinforced concrete – A review," *Cement and Concrete Research*, V. 39, pp. 1122-1138.

Ann, K. Y., and Song, H.-W. (2007). "Chloride Threshold Level for Corrosion of Steel in Concrete." *Corrosion Science*, V. 49 (11), pp. 4113-4133.

ASTM C 39 (2005). "Standard Test Method for Compressive Strength of Cylindrical Concrete Specimens," American Society for Testing and Materials, West Conshohocken, PA, pp. 7.

ASTM C 150 (2009). "Standard Specification for Portland Cement," American Society for Testing and Materials, West Conshohocken, PA, pp. 10.

ASTM A416 / A416M - 06 Standard Specification for Steel Strand, Uncoated Seven-Wire for Prestressed Concrete. American Society of Testing and Materials, West Conshohocken, PA.

ASTM C 469 (2002). "Standard Test Method for Static Modulus of Elasticity and Poisson's Ratio of Concrete in Compression," American Society for Testing and Materials, West Conshohocken, PA, pp. 5.

ASTM C 805 (2008). "Standard Test Method for Rebound Number of Hardened Concrete," American Society for Testing and Materials, West Conshohocken, PA, pp. 3.

ASTM C 876 (2009). "Standard Test Method for Corrosion Potentials of Uncoated Reinforcing Steel in Concrete," American Society for Testing and Materials, West Conshohocken, PA, pp. 7.

ASTM C 1012 (2009). "Standard Test Method for Length Change of Hydraulic-Cement Mortar Bars Exposed to a Sulfate Solution," American Society for Testing and Materials, West Conshohocken, PA, pp. 6.

ASTM E 1131 (2008). "Standard Test Method for Compositional Analysis by Thermogravimetry," American Society for Testing and Materials, West Conshohocken, PA, pp. 5.

ASTM C 1152 (2004). "Standard Test Method for Acid-Soluble Chloride in Mortar and Concrete," American Society for Testing and Materials, West Conshohocken, PA, pp. 4.

ASTM C 1157 (2004). "Standard Performance Specification for Hydraulic Cement," American Society for Testing and Materials, West Conshohocken, PA, pp. 5.

ASTM C 1202 (2007). "Standard Test Method for Electrical Indication of Concrete's Ability to Resist Chloride Ion Penetration," American Society for Testing and Materials, West Conshohocken, PA, pp. 6.

ASTM C 1218 (1999). "Standard Test Method for Water-Soluble Chloride in Mortar and Concrete," American Society for Testing and Materials, West Conshohocken, PA, pp. 3.

ASTM C 1327 (2008). "Standard Test Method for Vickers Indentation Hardness of Advanced Ceramics," American Society for Testing and Materials, West Conshohocken, PA, pp. 8.

ASTM C 1556 (2004). "Standard Test Method for Determining the Apparent Chloride Diffusion Coefficient of Cementitious Mixtures by Bulk Diffusion," American Society for Testing and Materials, West Conshohocken, PA, pp. 7.

ASTM G31 (2004). "Standard Practice for Laboratory Immersion Corrosion Testing of Metals." American Society of Testing and Materials, West Conshohocken, PA.

Atienza, J. M., and Elices, M. (2007). "Role of Residual Stresses in Stress Relaxation of Prestressed Concrete Wires." *Journal of Materials in Civil Engineering*, V. 19 (8), pp. 703-708.

Bamforth, P. (1993). "Concrete Classification for R.C. Structures Exposed to Marine and Other Salt-Laden Environments," *Structural Faults and Repair Conference*, Edinburgh, UK.

Basheer, L., et. al. (2001). "Assessment of the durability of concrete from its permeation properties: a review." *Construction and Building Materials*. V. 15, pp. 93-103.

Basheer, L., Kroppb, J., and Clelandc, D. J. (2001). "Assessment of the durability of concrete from its permeation properties: a review." *Construction and Building Materials*, V. (15), pp. 93-103.

Bautista, A., Blanco, G., and Velasco, F. (2006). "Corrosion Behaviour of Low-Nickel Austenitic Stainless Steel Reinforcements: A Comparative Study in Simulated Pore Solutions." *Cement & Concrete Research*, V. 36, pp. 1922-1930.

Bentz, D.P. (2000). "Influence of Silica Fume on Diffusivity in Cement-Based Materials II. Multi-Scale Modeling of Concrete Diffusivity," *Cement and Concrete Research*, V. 30, pp. 1121-1129.

Bertolini, L., and Redaelli, E. (2009). "Depassivation of steel reinforcement in case of pitting corrosion: detection techniques for laboratory studies." *Materials & Corrosion*, V. 60 (8), pp. 608-616.

Bertolini, L., Bolzoni, F., Cigada, A., Pastore, T., and Pedferri, P. (1993). "Cathodic Protection of New and Old Reinforced Concrete Structures." *Corrosion Science*, V. 35 (5-8), pp. 1633-1639.

Bertolini, L., Elsener, B., Pedferri, P., and Polder, R. (2004). *Corrosion of Steel in Concrete*, Wiley-VCH.

Bertolini, L., et. al. (2004). *Corrosion of Steel in Concrete: Prevention Diagnosis, Repair*, Wiley-VCH, pp. 392.

Bertolini, L., et. al. (2004). *Corrosion of Steel in Concrete*: Wiley-VCH.

Boddy, A., Bentz, E., Thomas, M. D. A., and Hooton, R. D. (1999). "An overview and sensitivity study of a multimechanistic chloride transport model." *Cement & Concrete Research*, V. (29), pp. 827-837.

Bohni, H. (2005). *Corrosion in Reinforced Concrete Structures*, Woodhead Publishing Ltd.

Brooks, M. A. (2003). "Influence of interstitial crevice corrosion in accelerated corrosion testing." BS, Penn State University, State College, PA.

Broomfield, J. P. (2007). *Corrosion of Steel in Concrete*, Taylor and Francis Group.

Chai, G., Soderman, A., and Etheridge, P. (2007). "High and Super-High-Strength Duplex Stainless Steels for Wire Applications." Sandvick Materials Technology, Sweden.

Chandler, K. A. (1984). *Marine and Offshore Corrosion*, Butterworth & Company Ltd.

Cherry, B. W., and Price, S. M. (1980). "Pitting, Crevice and Stress-Corrosion Crackign Studies of Cold Drawn Eutectoid Steels ." *Corrosion Science*, V. 20 (11-12), pp. 1163.

Clemena, G. G. (2003). "Investigation of the Resistance of Several New Metallic Reinforcing Bars to Chloride-Induced Corrosion in Concrete." Virginia Transportation Research Council.

Colleparidi, M., et. al. (1972). "Penetration of Chloride Ions into Cement Pastes and Concrete," *Journal of the American Ceramic Society*, V. 55, pp.534-535.

Cramer, S. D., Jr., B. S. C., Bullard, S. J., Holcomb, G. R., Russell, J. H., Nelson, F. J., Laylor, H. M., and Soltesz, S. M. (2002). "Corrosion Prevention and Remediation Strategies for Reinforced Concrete Coastal Bridges." *Cement & Concrete Composites*, V. 24, pp. 101-117.

Darwin, D., Browning, J., Jr., C. E. L., and Nguyen, T. V. (2007). "Multiple Corrosion Protection Systems for Reinforced Concrete Bridge Components." University of Kansas, 95.

Dash, J., and Otte, H. M. (1963). "Martensite Transformation in Stainless Steel." *Acta Metallurgica*, V. 11 (10), pp. 1169-&.

DeLong, W. T., Ostrom, G. A., and Szumachowski, E. R. (1956). "Measurement and calculation of ferrite in stainless steel weld metal." *Journal of Welding*, V. 35 (11), pp. 521-528.

Devine, T. M. (1997). "Corrosion Science." University of California Berkeley.

- Dhir, R.K., et. al. (1990). "Rapid Estimation of Chloride Diffusion Coefficient in Concrete," *Magazine of Concrete Research*, V. 42, pp. 177-185.
- Diab, H., et. al. (1988). "The Diffusion of Cl⁻ Ions Through Portland Cement and Portland Cement-Polymer Pastes," *Cement and Concrete Research*, V. 18, pp. 715-722.
- Diaz, B., Freire, L., Novoa, X. R., and Perez, M. C. (2009). "Electrochemical behaviour of high strength steel wires in the presence of chlorides." *Electrochimica Acta*, V. 54 (22), pp. 5190-5198.
- Dupoiron, F., and Audouard, J. P. (1996). "Duplex stainless steels: a high mechanical properties stainless steel family." *Scandinavian Journal of Metallurgy*, V. (25), pp. 95-102.
- Edvardsen, C. (1999). "Water Permeability and Autogenous Healing of Cracks in Concrete." *ACI Materials Journal*, V. 96 (4), pp. 448-456.
- Ehlen, M.A. (2009). *Life 365* (Version 2.0.1) [Software]. <http://www.life-365.org>
- Ehlen, M.A., et. al. (2009). "Life 365 Service Life Prediction Model Version 2.0," *Concrete International*, V. 31, pp. 41-46.
- Elices, M., Cabllero, L., Valiente, A., Ruiz, J., and Martin, A. (2008). "Hydrogen Embrittlement of Steel for Prestressing Concrete: The FIP and DIBt Tests." *CORROSION* V. 64 (2), pp. 164-174.
- Federal Highway Administration (2006). "Status of the Nation's Highways, Bridges, and Transit: Report to Congress." FHWA, 436.
- FIP, C., (1992). "Design Guide for Durable Concrete Structures." T. T. Publishers, ed., Comité Euro-International du Béton - Fédération Internationale du Béton, Lausanne, Switzerland.
- Frederiksen, J. M. and Geiker, M.R. (2008). "Chloride ingress prediction: Part 1: Analytical model for time dependent diffusion coefficient and surface concentration," CONMOD 08, Delft, the Netherlands.
- Garcia-Alonso, M. C., Escudero, M. L., Miranda, J. M., Vega, M. I., Capilla, F., Correia, M. J., Salta, M., Bennani, A., and Gonzalez, J. A. (2007). "Corrosion behaviour of new stainless steels reinforcing bars embedded in concrete." *Cement & Concrete Research*, V. 37 (10), pp. 1463-1471.
- Glass, G. K., and Buenfeld, N. R. (2000). "The influence of chloride binding on the chloride induced corrosion risk in reinforced concrete." *Corrosion Science*, V. (42), pp. 329-344.
- Griggs, R. D. (1987). "Structural Concrete in the Georgia Coastal Environment." GDOT, Atlanta, GA.

- Hamilton III, H. R. (2007). "St. George Island Bridge Pile Testing." FDOT.
- Hansson, C. M. (2005). "Effects of High Performance Concrete on Corrosion of Reinforcement." PCA, ed., Portland Cement Association, Skokie, IL.
- Hansson, C. M. (2005). "Effects of High Performance Concrete on Corrosion of Reinforcement." P. C. Association, Skokie, IL.
- Hansson, C. M., Poursaei, A., and Laurent, A. (2006). "Macrocell and Microcell Corrosion of Steel in Ordinary Portland Cement and High Performance Concretes." *Cement and Concrete Research*, V. 36, pp. 2098-2102.
- Hartt, W. H. (2005). "Jobsite Evaluation of Corrosion Resistant Alloys for use as Reinforcement in Concrete." Florida Atlantic University, 82.
- Hartt, W. H., and Nam, J. (2004). "Critical Parameters for Corrosion Induced Deterioration of Marine Bridge Substructures in Florida." Florida Atlantic University, 69.
- Hartt, W. H., Kumria, C. C., and Kessler, R. J. (1993). "Influence of Potential, Chlorides, pH, and Precharging Time on Embrittlement of Cathodically Polarized Prestressing Steel." *CORROSION*, V. 49 (5).
- Hartt, W. H., Powers, R. G., Leroux, V., and Lysogorski, D. K. (2004). "Critical Literature Review of High-Performance Corrosion Reinforcements in Concrete Bridge Applications." Florida Atlantic University, 53.
- Hartt, W. H., Powers, R. G., Lysogorski, D. K., Liroux, V., and Virmani, Y. P. (2007). "Corrosion Resistant Alloys for Reinforced Concrete." Florida Atlanta University, 135.
- Heide, N. t. (2005). "Crack healing in hydrating concrete." M.S. , Delft University of Technology, Delft, Netherlands.
- Hope, B. B., and Nmai, C. K. (2001). "Corrosion of Prestressing Steels." American Concrete Institute Committee 222, 43.
- Hopkins, S.E. (1962). "Distribution of the species of *Cliona* (boring sponge) on the eastern shore of Virginia in relation to salinity," *Chesapeake Science*, V. 3, pp. 121-125.
- <http://www.life-365.org>
- Hurley, M. F. (2006). "Threshold Chloride Concentrations of Selected Corrosion-Resistant Rebar Materials Compared to Carbon Steel." *CORROSION*, V. 62 (10), pp. 892-904.
- Insteel Industries, I. (2002). "1/2" 240K Stainless Steel Strand." Sanderson, FL.
- Isecke, B. (1982). "Collapse of the Berlin Congress Hall Prestressed Concrete Roof." *Materials Performance*, V. 21 (12), pp. 36-39.

Izumida, H., Kawabe, N., Takamura, S., Morita, H., and Murai, T. (2005). "Development of High-tensile-strength Stainless Steel Wire." *Sumitomo (SEI) Steel Wire Corp. Technical Review*, V. 60.

Jenkins, J. F. (1987). "Validation of Nitronic 33 in Reinforced and Prestressed Concrete." Naval Facilities Engineering Command.

Johnson, D., et. al. (1996). "Determining Chloride Diffusion Coefficients for Concrete using Accelerated Test Methods," *Proceedings on Performance of Concrete in a Marine Environment*, New Brunswick, Canada.

Jones, D. A. (1996). *Principles and Prevention of Corrosion*, Prentice Hall, Upper Saddle River, NJ.

Kaid, H., Cyr, M., Julien, S., and Khelafi, H. (2009). "Durability of concrete containing a natural pozzolan as defined by a performance-based approach." *Construction and Building Materials*, V. 23, pp. 3457-3467.

Kalina, R. D. (2009). "Comparative Study of the Corrosion Resistance of Different Prestressing Strand Types for use in Post-Tensioning of Bridges." MS, University of Texas at Austin, Austin, TX.

Kanaya, M., et. al. (1998). "Diffusion of Chloride Ions in Concrete Exposed in the Coastal Area," *Concrete Under Severe Conditions 2: Environment and Loading*, E & FN Spon, pp. 242-249.

Khatib, J. M. and Wild, S. (1998). "Sulphate resistance of metakaolin mortar." *Cement and Concrete Research*, V. 28, pp. 83-92.

Knudson, A., and Skovsgaard, T. (1999). "The Optimal Use of Stainless Steel Reinforcement in Concrete Structures." Ramboll Arminox, 8.

Koch, G. H., Brongers, M. P. H., Thompson, N. G., Virmani, Y. P., and Payer, J. H. (2008). "Corrosion Costs and Preventive Strategies in the United States." NACE, Houston, TX, 12.

Kreyszig, E. (1967). *Advanced Engineering Mathematics*, John Wiley & Sons, Inc., New York, NY.

Kurth, J.C. (2008). *Mitigating Biofilm Growth through the Modification of Concrete Design and Practice*. Master's Thesis. Georgia Institute of Technology. pp. 234.

Kurtis, K. E. (2007). "Materials Science of Concrete." Georgia Institute of Technology.

Kurtis, K. E., and Mehta, K. "A Critical Review of Deterioration of Concrete Due to Corrosion of Reinforcing Steel." *Proc., Durability of Concrete*, ACI, 535-554.

- Kurtis, K.E., et. al. (2001). "Accelerated Test for Measuring Sulfate Resistance of Calcium Sulfoaluminate, Calcium Aluminate, and Portland Cements," *Journal of Materials in Civil Engineering*, May/June Edition, pp. 216-221.
- Landolt, D. (2007). *Corrosion and Surface Chemistry of Metals*, EPFL Press, Lausanne, Switzerland.
- Landolt, D. (2007). *Corrosion and Surface Chemistry of Metals*, EPFL Press, Lausanne, Switzerland.
- Lean, S. M. (2008). "Comparison of the Corrosion Resistance of New and Innovative Prestressing Strand Types used in the Post Tensioning of Bridges." MS, University of Texas at Austin, Austin, TX.
- Lewis, A. F. G. (1969). *Steel for Prestressing*, Lowe & Brydone Limited, London, UK.
- Li, L., and Sagues, A. A. (2002). "Chloride corrosion threshold of reinforcing steel in alkaline solutions - Cyclic polarization behavior." *CORROSION*, V. 58 (4), pp. 305-316.
- Luping, T. (1995). "On Chloride Diffusion Coefficients Obtained by Using the Electrically Accelerated Methods," *Rilem International Conference*, Paris, France.
- Luping, T., and Nilsson, L.O. (1992). "Chloride Diffusivity in High Strength Concrete at Different Ages," *Nordic Concrete Research*, V. 11, pp. 162-171.
- Manera, M., Vennesland, Ø., and Bertolini, L. (2008). "Chloride Threshold for Rebar Corrosion in Concrete with Addition of Silica Fume." *Corrosion Science*, V. 50 (2), pp. 554-560.
- Mangat, P. S. and El-Khatib, J. M. (1992). "Influence of initial curing on sulphate resistance of blended cement concrete." *Cement and Concrete Research*, V. 22, pp. 1089-1100.
- Mangat, P.S., and Molloy, B.T. (1994). "Prediction of Long Term Chloride Concentration in Concrete," *Materials and Structures*, V. 27, pp. 338-346.
- Markeset, G., Rostam, S., and Klinghoffer, O. (2006). "Guide for the use of stainless steel reinforcement in concrete structures." Norwegian Building Research Institute.
- Matco Inc. (2008). "Pier Cap Spalling of Cover Concrete."
<http://www.matcoinc.com/files/New/Home/WhatsNew/Bridge3.jpg>
- Matta, Z. G. (1993). "More Deterioration of Concrete in the Arabian Gulf." *Concrete International*, V. November, pp. 50-51.
- Mehta, P. K. (1991). *Corrosion in the Marine Environment*, Elsevier Applied Science.
- Mehta, P. K., and Monteiro, P. J. M. (2006). *Concrete: Microstructure, Properties, and Materials*, McGraw-Hill Companies Ltd.

- Mehta, P. K., and Monteiro, P. J. M. (2006). *Concrete: Microstructure, Properties, and Materials*, McGraw-Hill Companies Ltd.
- Mehta, P.K. (1991). *Concrete in the Marine Environment*, Elsevier Science Publishers, New York, NY, pp. 214.
- Mietz, J. (2000). "Investigations on Hydrogen-Induced Embrittlement of Quench and Tempered Prestressing Steels." *Materials and Corrosion*, V. 51, pp. 80-90.
- Mietz, J., and Isecke, B. (2002). "Assessment of test methods for evaluation stress corrosion cracking susceptibility of prestressing steels." *Materials and Corrosion*, V. 53 (6), pp. 373-384.
- Mietz, J., Elsener, B., and Polder, R. (1997). *Corrosion of Reinforcement in Concrete - Monitoring, Prevention, and Rehabilitation*, The Institute of Materials, London, UK.
- Milad, M., Zreiba, V., Elhalouani, F., and Baradai, C. (2008). "The effect of cold work on structure and properties of AISI 304 stainless steel." *Journal of Materials Processing Technology*, V. 203 (1-3), pp. 80-85.
- Miller, A.N., et. al. (2010). "Effects of Heat and Salinity Stress on the Sponge *Cliona celata*," *Internation Journal of Biology*, V. 2, pp. 3-16.
- Mohammed, T.U. and Hamada, Hidenori. (2003). "Corrosion of Steel Bars in Concrete at Joints under Tidal Environment." *ACI Materials Journal*. V. July-Aug, pp. 265-273.
- Mohammed, T.U., and Hamada, H. (2003). "Relationship between free chloride and total chloride contents in concrete," *Cement and Concrete Research*, V. 33, pp. 1487-1490.
- Morrison, S. R. (1990). *The Chemical Physics of Surfaces*, Plenum Press, New York, NY.
- Moser, R. D., Singh, P. M., Kahn, L. F., and Kurtis, K. E. (2010). "Chloride-Induced Corrosion of Prestressing Steels Considering Crevice Effects and Surface Imperfections." *CORROSION*, In Review.
- Murata, K., et. al. (1997), "Determination of sulfate in brackish waters by laser Raman spectroscopy," *Analytica Chimica Acta*, 344, pp 153-157.
- NACE (2007). "Corrosion of Concrete Pier."
<http://www.nace.org/nace/content/library/photogallery/showLarge.asp?PhotoID=145>
- NACE (2008). "How Much Can a Bridge Take?," National Association of Corrosion Engineers.
- Nawy, E. G. (2000). *Prestressed Concrete - A Fundamental Approach*, Prentice Hall, Upper Saddle River, NJ.
- Neumann, A.C. (1966). "Observations on Coastal Erosion in Bermuda and Measurements of the Boring Rate of the Sponge, *Cliona lampa*," *Limnology and Oceanography*, V. 11, pp. 92-108.

- Neville, A.M. (1997). *Properties of Concrete*, 4 ed., John Wiley and Sons, New York, NY, pp. 844.
- Nicol, W.L. and Reisman, H.M. (1976). "Ecology of the Boring Sponge (*Cliona celata*) at Gardiner's Island, New York," *Chesapeake Science*, V. 17, pp. 1-7.
- Nilsson, L.-O. (2009). "Models for chloride ingress into concrete - from Collepardi to today." *International Journal of Modeling, Identification, and Control*, V. 7 (2), pp. 129-134.
- Nuernberger, U. (1995). *Korrosion und Korrosionsschutz im Bauwesen*, GmbH, Berlin.
- Nuernberger, U. (2002). "Corrosion Induced Failures of Prestressing Steels." *Otto-Graf Journal*, V. 13.
- Nürnberg, U. "Hydrogen Induced Cracking of Prestressing Steel in Concrete Constructions." *Proc., EUROCORR*.
- Nürnberg, U. (2002). "Corrosion induced failure mechanisms of prestressing steel." *Materials and Corrosion*, V. 53 (8), pp. 591-601.
- Nürnberg, U. (2003). "High Strength Stainless Steel - Alternative Materials for Tension Members in Civil Engineering." *Otto-Graf-Journal*, V. 14, pp. 45-66.
- Nürnberg, U., and Wu, Y. "High-Strength Stainless Steel in Prestressed Concrete." *Proc., Workshop of COST on NTD Assessment and New Systems in Prestressed Concrete Structures*, Institute for Terotechnology, 33-38.
- Nürnberg, U., and Wu, Y. (2008). "Stainless steel in concrete structures and in the fastening technique." *Materials and Corrosion*, V. 59 (2), pp. 144-158.
- Osborn, A. E. N., Lawler, J. S., and Connolly, J. D. (2008). "Acceptance Tests for Surface Characteristics of Steel Strand in Prestressed Concrete." NCHRP.
- Page, C., and Vennesland, Ø. (1983). "Pore solution composition and chloride binding capacity of silica-fume cement pastes." *Materials & Structures*, V. 16 (1), pp. 19-25.
- Papadakis, V.G. (2000). "Effect of supplementary cementing materials on concrete resistance against carbonation and chloride ingress." *Cement and Concrete Research*, V. 30, pp. 291-299.
- Papadakis, V.G., et. al. (1991). "Fundamental Modeling and Experimental Investigation of Concrete Carbonation." *ACI Materials Journal*, V. 88, pp. 363-373.
- PCA (2007). "Corrosion of Embedded Metals." Portland Cement Association.
- Pedersen, V., and Arntsen, B. (1998). Effect of Early-Age Curing on Penetration of Chloride Ions into Concrete in the Tidal Zone," *Concrete Under Severe Conditions 2: Environment and Loading*, E & FN Spon, pp. 468-477.

Perez, N. (2004). *Electrochemistry and Corrosion Science*, Kluwer Academic Publishers, Norwell, MA.

Polder, R.B. (1995) "Chloride Diffusion and Resistivity Testing of Five Concrete Mixes for Marine Environment," *Rilem International Conference*, Paris, France.

Pourbaix, M. (1974). *Atlas of Electrochemical Equilibria in Aqueous Solutions*, NACE International, Houston, TX.

Poursaei, A., and Hansson, C. M. (2007). "Reinforcing steel passivation in mortar and pore solution." *Cement & Concrete Research*, V. 37 (7), pp. 1127-1133.

Poursaei, A., and Hansson, C. M. (2007). "Reinforcing steel passivation in mortar and pore solution." *Cement & Concrete Research*, V. 37 (7), pp. 1127-1133.

Presuel-Moreno, F., Scully, J. R., and Sharp, S. R. (2010). "Literature Review of Commercially Available Alloys That Have Potential as Low-Cost Corrosion-Resistant Concrete Reinforcement." *CORROSION*, V. 68 (8), pp. 1-13.

Proverbio, E., and Bonaccorsi, L. M. (2002). "Failure of Prestressing Steel Induced By Crevice Corrosion in Prestressed Concrete Structures." *9th International Conference on Durability of Materials and Components* Brisbane, Australia.

Raharinaivo, A. "Galvanised Carbon Steel Tendons." *Proc., Workshop of COST on NTD Assessment and New Systems in Prestressed Concrete Structures*, Institute for Terotechnology, 41-48.

Reve, R. W. (2000). *Uhlig's Corrosion Handbook*, John Wiley & Sons Inc.

Rodriguez, O. G., and Hooton, R. D. (2003). "Influence of Cracks on Chloride Ingress into Concrete." *ACI Materials Journal*, V. 100 (2), pp. 120-126.

Rossi, A., Tulifero, R., and Elsener, B. (2001). "Surface analytical and electrochemical study on the role of adsorbed chloride ions in corrosion of stainless steels." *Materials and Corrosion*, V. 52 (3), pp. 175-180.

Rourke, D. (2008). "Galvanized Rebar Resource Center." <http://www.galvanizedrebar.com/>

Sagüés, A. A., Lee, J. B., Chang, X., Pickering, H., Nystrom, E., Carpenter, W., Kranc, S. C., Simmons, T., Boucher, B., and Hierholzer, S. (1994). "Corrosion of Epoxy Coated Rebar in Florida Bridges." University of South Florida, 135.

Salas, R. M., Schokker, A. J., West, J. S., Breen, J. E., and Kreger, M. E. (2004). "Conclusions, Recommendations and Design Guidelines for Corrosion Protection of Post-Tensioned Bridges ", Center for Transportation Research Austin, TX, 85.

Salas, R. M., Schokker, A. J., West, J. S., Breen, J. E., and Kreger, M. E. (2008). "Corrosion risk of bonded, post-tensioned concrete." *PCI Journal*, V. 53 (1), pp. 89-107.

Sandberg, P., Tang, L., and Andersen, A. (1998). "Recurrent Studies of Chloride Ingress in Uncracked Marine Concrete at Various Exposure Times and Elevations." *Cement and Concrete Research*, V. 28 (10), pp. 1489-1503.

Schaeffler, A. L. (1949). "Constitution diagram for stainless steel weld metal." *Metals Progress*, V. 56 (11), pp. 680.

Schiessl, P., and Raupach, M. (1997). "Laboratory Studies and Calculations on the Influence of Crack Width on Chloride-Induced Corrosion of Steel in Concrete." *ACI Materials Journal*, V. 94 (1), pp. 56-62.

Schmuki, P. (2002). "From Bacon to barriers: a review on the passivity of metals and alloys." *Journal of Solid State Electrochemistry*, V. 6 (3), pp. 145-164.

Schroeder, R. M., and Müller, I. L. (2003). "Stress Corrosion Cracking and Hydrogen Embrittlement Susceptibility of an Eutectoid Steel Employed in Prestressed Concrete." *Corrosion Science*, V. 45, pp. 1969-1983.

Schroeder, R. M., and Müller, I. L. (2003). "Stress Corrosion Cracking and Hydrogen Embrittlement Susceptibility of an Eutectoid Steel Employed in Prestressed Concrete." *Corrosion Science*, V. 45, pp. 1969-1983.

Schupack, M. (2001). "Prestressing Reinforcement in the New Millennium." *Concrete International*, V. 23 (12), pp. 38-45.

Schupack, M., and Suarez, M. G. (1982). "Some Recent Corrosion Embrittlement Failures of Prestressing Systems in the United States." *PCI Journal*, V. March-April, pp. 38-55.

Schweitzer, P. A. (2003). *Metallic Materials: Physical, Mechanical, and Corrosion Properties*, Marcel Dekker, Inc., New York, NY.

Scott, P.J.B., et. al. (1988). "Bioerosion of Concrete and Limestone by Marine Organisms," *Marine Pollution Bulletin*, V. 19, pp. 219-222.

Shanina, B. D., Gavriljuk, V. G., Berns, H., and Schmalt, F. (2002). "Concept of a new high-strength austenitic stainless steel." *Steel Research International*, V. 73 (3), pp. 105-113.

Sharland, S. M. (1992). "A Mathematical-Model of the Initiation of Crevice Corrosion in Metals." *Corrosion Science*, V. 33 (2), pp. 183-201.

Sharp, S. R., and Virmani, Y. P. (2006). "Factors That Influence the Efficiency of Electrochemical Chloride Extraction During Corrosion Mitigation in Reinforced Concrete Structures." Virginia Transportation Research Council, 30.

Shirahama, S., Fang, S., Kobayashi, T., and Miyagawa, T. (1999). "Basic Properties of Duplex Stainless Prestressing Steel and Flexural Behaviors of Prestressed Concrete Beams Using the Tendon." *Journal of the Society of Materials Science of Japan*, V. 48 (10), pp. 1199-1206.

Simmons, J. W. (1996). "Overview: High-nitrogen alloying of stainless steels." *Mater. Sci. Eng. A-Struct. Mater. Prop. Microstruct. Process.*, V. 207 (2), pp. 159-169.

Singh, P. M. (2008). "Environmental Degradation." Georgia Institute of Technology.

Skalny, J., et. al. (2002). *Sulfate Attack on Concrete*, Spon Press, New York, NY, pp. 217.

Skorchelletti, V. V. (1976). *Theory of Metal Corrosion*, Israel Program for Scientific Translations, Jerusalem, Israel.

Stanish, K.D. and Thomas, Michael. (2003). "The use of bulk diffusion tests to establish time-dependent concrete chloride diffusion coefficients." *Cement and Concrete Research*. V. 33, pp. 55-62.

Stanish, K.D., et. al. (1997). *Testing the Chloride Penetration Resistance of Concrete: A Literature Review*, FHWA contract report, pp. 33.

Steffens, A., et. al. (2002). "Modeling carbonation for corrosion risk prediction of concrete structures." *Cement and Concrete Research* V. 32, pp. 935–941.

Stein, G., and Witulski, H. (1990). *High Nitrogen Steels*, Verlag Stahleisen GmbH, Aachen, Germany.

Suryavanshi, A., Scantlebury, J. D., and Lyon., S. B. (1996). "Mechanism of Friedel's Salt Formation in Cements Rich in Tri-Calcium Aluminate." *Cement & Concrete Research*, V. 26 (5), pp. 717-727.

Talbot, D., and Talbot, J. (1998). *Corrosion Science and Technology*, CRC Press LLC, Boca Raton, FL.

Thaesler, P., Kahn, L., Oberle, R., and Demers, C. E. (2005). "Durable Repairs on Marine Bridge Piles." *Journal of Performance of Constructed Facilities*, V. 19 (1), pp. 88-92.

Thangavel, K., and Rengaswamy, N. S. (1998). "Relationship Between Chloride/Hydroxide Ratio and Corrosion Rate of Steel in Concrete." *Cement & Concrete Composites*, V. 20, pp. 283-292.

Thomas, D. (2003). "Fundamentals of Electrochemistry." University of Guelph.

Thomas, M. and Bamforth, P. (1999). "Modelling chloride diffusion in concrete: Effect of fly ash and slag." *Cement and Concrete Research*. V. 29, pp. 487-495.

Thomas, M. D. A., Bamforth, P. B., and Banerjee, M. K. (1999). "Modelling chloride diffusion in concrete effect of fly ash and slag." *Cement & Concrete Research*, V. (29), pp. 487-495.

Thomas, M. D. A., Bentz, E. C., and Ehlen, M. A. (2009). "Life-365 v. 2.0.1." Life-365 Consortium.

Torii, K. and Kawamura, M. (1994). "Effects of fly ash and silica fume on the resistance of mortar to sulfuric acid and sulfate attack." *Cement and Concrete Research*, V. 24, pp. 361-370.

Trejo, D., Monteiro, P. J. M., Ben C. Gerwick, J., and Thomas, G. (2000). "Microstructural Design of Concrete Reinforcing Bars for Improved Corrosion Performance." *ACI Materials Journal*, V. 97 (1), pp. 78-84.

USGS Surface Water Information Pages, United States Geological Survey, June 3rd, 2010, from <http://water.usgs.gov/osw/>.

Virmani, Y. P., and Clemena, G. G. (1998). "Corrosion Protection: Concrete Bridges." Turner-Fairbank Highway Research Center.

Virmani, Y. P., and Clemena, G. G. (1998). "Corrosion Protection: Concrete Bridges." Turner-Fairbank Highway Research Center.

West, J. S., Larosche, C. J., Koester, B. D., J. E. Breen, and Kreger, M. E. (1999). "State-of-the-Art Report about Durability of Post-Tensions Bridge Substructures." University of Texas at Austin, Austin, TX.

Wierig, H. J. (1984). "Long-Time Studies on the Carbonation of Concrete Under Normal Outdoor Exposure." *Durability of Concrete Structures Under Normal Outdoor Exposure*, RILEM, Hannover.

Wight, J. K. (2005). "ACI 318-05 Building Code Requirement for Structural Concrete and Commentary." American Concrete Institute Farmington Hills, MI.

Winitzki, S. (2006). "A handy approximation for the error function and its inverse," Lecture note, Ludwig-Maximilians University, Munich, Germany.

Winitzki, S. (2006). "A handy approximation for the error function and its inverse," Lecture note, Ludwig-Maximilians University, Munich, Germany.

Wu, Y., and Nürnberger, U. (2009). "Corrosion-technical properties of high-strength stainless steels for the application in prestressed concrete structures." *Materials and Corrosion*, V. 60 (10), pp. 771-780.

Young, J. F., Mindess, S., Gray, R. J., and Bentur, A. (1998). *The Science and Technology of Civil Engineering Materials*, Prentice Hall, Upper Saddle River, NJ.

Zea, S. and Weil, E. (2003). "Taxonomy of the Caribbean excavating sponge species complex *Cliona caribbaea* – *C. Aprica* – *C. langae* (Porifera, Hadromerida, Clionaidae)," *Caribbean Journal of Science*, V. 39, pp. 348-370.

Zemajtis, J., Weyers, R. E., and Sprinkel, M. M. (1999). "Performance Evaluation of Corrosion Inhibitors and Galvanized Steel in Concrete Exposure Specimens." Virginia Transportation Research Council, 74.

Zumdahl, S. S. (2000). *Chemistry*, Houghton Mifflin Company, Boston, MA.